



# High temperature and high electrical resistance multilayer polyimide nanodielectrics for electric motors insulation

Shakeel Akram

## ► To cite this version:

Shakeel Akram. High temperature and high electrical resistance multilayer polyimide nanodielectrics for electric motors insulation. Electronics. Université Montpellier, 2020. English. NNT : 2020MONT028 . tel-03191962

**HAL Id: tel-03191962**

**<https://theses.hal.science/tel-03191962>**

Submitted on 7 Apr 2021

**HAL** is a multi-disciplinary open access archive for the deposit and dissemination of scientific research documents, whether they are published or not. The documents may come from teaching and research institutions in France or abroad, or from public or private research centers.

L'archive ouverte pluridisciplinaire **HAL**, est destinée au dépôt et à la diffusion de documents scientifiques de niveau recherche, publiés ou non, émanant des établissements d'enseignement et de recherche français ou étrangers, des laboratoires publics ou privés.

# THIS THESIS IS SUBMITTED TO OBTAIN THE GRADE OF DOCTOR DEGREE FROM UNIVERSITY OF MONTPELLIER

– High Voltage Engineering Insulation –

Doctoral School of Information, Structures and Systems  
Research Institute of Electronics and Systems UMR 5214

## PhD THESIS

High temperature and high electrical resistance multilayer  
polyimide nanodielectrics for electric motors insulation

Presented by Shakeel AKRAM  
May 2020

Under the direction of Jérôme CASTELLON  
& Serge AGNEL

Devant le jury composé de

M. David FABIANI, Associate Professor, Università di Bologna

M. Sombel DIAHAM, Associate Professor HDR, Paul Sabatier University - Toulouse III

M. Zhou KAI, Professor, Sichuan University

M. Juan MARTNEZ VEGA, Professor, Université de Toulouse

M. Jean Pierre HABAS, Professor, Université de Montpellier

M. Jérôme CASTELLON, Associate Professor HDR, Université de Montpellier

M. Serge AGNEL, Professor, Université de Montpellier

Rapporteur

Rapporteur

Examineur

Examineur

Examineur

Directeur de thèse

Co-directeur de thèse



UNIVERSITÉ  
DE MONTPELLIER



### Paper Publications

**Shakeel Akram**, Guoqiang Gao, Yang Liu, Jian Zhu, Guangning Wu, Kai Zhou “Degradation Mechanism of Al<sub>2</sub>O<sub>3</sub> Nano Filled Polyimide Film due to Surface Discharge under Square Impulse Voltage”, IEEE Transactions on Dielectrics and Electrical Insulation, vol. 22, no. 6, pp. 3341-3349, 2015.

**Shakeel, Akram**, Guangning Wu, GuoQiang Gao, Yang Liu, “Cavity and Interface effect of PI-Film on Charge Accumulation and PD Activity under Bipolar Pulse Voltage” Journal of Electrical Engineering & Technology, vol. 10, no. 5, pp. 2089-2098, 2015.

**Shakeel Akram**, Guangning Wu, GuoQiang Gao, Yang Liu, “Effect of surface discharge on nano filled polyimide film under square voltage” IEEE Electrical Insulation Conference (EIC), USA, 2015.

**Shakeel Akram**, Jérôme Castellon, Serge Agnel, M. Zeeshan Khan, “Space Charge Analysis of Multi-Structure Polyimide Films using TSM”, IEEE Conference on Electrical Insulation and Dielectric Phenomena (CEIDP), Cancun, Mexico, 2018.

**Shakeel Akram**, Yan Yang, Xin Zhong, Shoaib Bhutta, Guangning Wu, Jerome Castellon, Kai Zhou, “Influence of nano layer structure of polyimide film on space charge behavior and trap levels”, IEEE Transactions on Dielectrics and Electrical Insulation, vol. 25, no. 4, pp. 1461-1469, 2018.

**Shakeel Akram**, Jérôme Castellon, Serge Agnel, Jean-Pierre Habas, Zhou Kai, M. Tariq Nazir, “Impact of Nanocomposite Thin Layer on Nanoparticles Dispersion and their Dielectric Properties”, IEEE Conference on Electrical Insulation and Dielectric Phenomena (CEIDP), USA, 2019.

**Shakeel Akram**, Jérôme Castellon, Serge Agnel, Kai Zhou, Jean-Pierre Habas, Muhammad Tariq Nazir, “Multilayer polyimide nanocomposite films synthesis process optimization impact on nanoparticles dispersion and their dielectric performance”, Journal of Applied Polymer Science, 49715, 2020.

**Shakeel Akram**, Jérôme Castellon, Serge Agnel, Jean-Pierre Habas, Zhou Kai, M. Tariq Nazir, “Dielectric properties and modeling of multilayer polyimide nanocomposite to highlight the impact of nanoparticles dispersion”, IEEE Transactions on Dielectrics and Electrical Insulation, vol. 27, no. 4, pp. 1238-1246, 2020.

**Shakeel Akram**, Tariq Nazir, Jerome Castellon, Serge Agnel, Kai Zhou, M Shoaib Bhutta, “Preparation and distinguish dielectric properties of multi-layer nanoparticles-based polyimide films”, Materials Research Express, vol. 6, no. 12, pp. 125092, 2019.

**Shakeel Akram**, Wang Peng, M. T. Nazir, Kai Zhou, M. S. Bhutta, H. Hussaine, “Impact of impulse voltage frequency on the partial discharge characteristic of electric vehicles motor insulation”, Engineering Failure Analysis, 104767, 2020.

### Book Chapter

**Shakeel Akram**, Jérôme Castellon, Serge Agnel and Jean-Pierre Habas (August 20th 2020). Synthesis Process Optimization of Polyimide Nanocomposite Multilayer Films, Their Dielectric Properties, and Modeling [Online First], IntechOpen, DOI: 10.5772/intechopen.91206.

## Table of contents

<b>List of figures.....</b>	<b>ix</b>
<b>Abstract .....</b>	<b>xv</b>
<b>Chapter 1 Introduction .....</b>	<b>2</b>
1.1 Background .....	3
1.2 Electric traction motors.....	3
1.2.1 Electric traction drive systems .....	4
1.2.2 High voltage high frequency pulse power.....	5
1.2.3 Motor insulation.....	7
1.2.4 Motor insulation failure mechanism.....	9
1.2.4.1 Thermal aging of insulation .....	10
1.2.4.2 Electrical aging of insulation.....	10
1.2.4.3 PD turns-insulation .....	11
1.3 From polyimide to nanodielectrics multicoated polyimide films .....	12
1.3.1 Polyimide insulation .....	12
1.3.2 Nanodielectrics based polyimide .....	13
1.3.3 Fluorination coated polyimide .....	14
1.4 Motivation.....	14
1.5 Objective and novel contribution .....	15
1.6 Description of the dissertation outline .....	15
<b>Chapter 2 Physical properties and synthesis optimization of polyimide nanodielectrics .....</b>	<b>18</b>
2.1 Introduction .....	20
2.2 Organic polymers .....	20
2.3 Physical properties of polyimide.....	21
2.3.1 Polyimide.....	21
2.3.2 Chemical properties of polyimide .....	21
2.3.3 Thermal properties.....	21
2.3.4 Mechanical strength.....	22

---

2.3.5 Properties of polyimide in electrical engineering .....	22
2.3.5.1 Conduction current .....	22
2.3.5.2 Dielectric constant and dielectric loss.....	23
2.3.5.3 Dielectric breakdown strength .....	25
2.3.5.4 Charge transport phenomena .....	25
2.3.5.5 Corona discharge resistance and material degradation .....	26
2.4 Physical properties of nanodielectric based polyimide in high voltage engineering .....	27
2.4.1 Inorganic filling particles .....	28
2.4.2 Particles size shape and types.....	28
2.4.3 Nanoparticles dispersion and distribution .....	30
2.4.4 Nanoparticles surface treatment .....	31
2.4.4.1 Coupling agents .....	31
2.4.4.2 Plasma treatment .....	31
2.4.5 Polymer nanocomposite materials .....	32
2.5 Synthesis of polyimide .....	32
2.5.1 Preparation mechanism for poly amic acid (PAA) .....	32
2.5.2 Monomers reactivity conditions .....	33
2.5.3 Synthesis of PAA/nanoparticles composite solution .....	35
2.5.4 PI film casting .....	35
2.5.4.1 Casting PI films using glass and brass substrate.....	35
2.5.4.2 Casting PI films using a spin coating technique.....	35
2.5.5 Controlling the thickness.....	35
2.5.6 Casting PI and nanocomposite/PI multi-layer films .....	36
2.5.7 Thermal imidization of a poly amic acid (PAA) .....	36
2.6 Synthesis process optimization.....	37
2.6.1 Factors involved in the molecular weight of PAA .....	37
2.6.2 Determination of the degree of imidization .....	38
2.6.3 Changes in the mechanical strength during thermal imidization .....	38

---

2.6.4 Crystallinity and the glass transition temperature .....	38
2.6.5 Avoid side reactions .....	39
2.7 Summary .....	39
<b>Chapter 3 Experimental techniques and methodology .....</b>	<b>42</b>
3.1 Introduction .....	43
3.2 General description of samples .....	43
3.3 Microscopy morphology characterization .....	44
3.3.1 Scanning electron microscopy (SEM) .....	44
3.3.2 Transmission electron microscopy (TEM) .....	45
3.4 Fourier transform infrared spectroscopy .....	46
3.5 Dielectric spectroscopy characterization .....	47
3.6 Corona resistance property tests under PWM waveform .....	48
3.6.1 Lifetime and electrical breakdown tests under corona discharge .....	48
3.6.2 PD and surface discharge test setup .....	49
3.7 Conduction currents .....	50
3.8 Thermal and mechanical characterization .....	56
3.8.1 Rheological test using dynamic mechanical analyzer (DMA) .....	56
3.8.2 Thermal diffusivity test .....	58
3.9 Space charges measurement setups .....	59
3.9.1 Thermal step method (TSM) .....	59
3.9.2 Pulse electro acoustic method (PEA) .....	62
3.10 Thermal stimulated current (TSC) .....	63
3.11 Summary .....	65
<b>Chapter 4 Experimental results and analysis .....</b>	<b>68</b>
4.1 Introduction .....	69
4.2 Microscopic and chemical characterization .....	69
4.2.1 Scanning and transmission electron microscopy analysis .....	69
4.2.2 FTIR analysis .....	72
4.3 Thermomechanical analysis of rheological tests .....	75



---

4.4 Thermal conductivity analysis.....	78
4.5 Dielectric constant and dielectric loss .....	80
4.6 Dielectric breakdown strength .....	83
4.7 Current-voltage characteristics.....	87
4.8 Space charges and trap levels analysis .....	99
4.8.1 Space charge analysis using TSM technique .....	99
4.8.2 Space charge analysis using PEA technique .....	106
4.8.3 Total charge decay and trap levels distribution analysis .....	108
4.8.4 Discussion .....	113
4.9 Summary .....	116
<b>Chapter 5 Simulation and modeling .....</b>	<b>120</b>
5.1 Introduction .....	121
5.2 Numerical modeling description.....	121
5.3 General sample description .....	121
5.4 Multi-layer PI/nanocomposite model using real experimental boundary conditions ....	122
5.4.1 Boundary conditions .....	124
5.4.2 Domain equations .....	125
5.4.3 Electric field distribution for PI nanocomposite models.....	126
5.4.4 Effect of permittivity and agglomeration on electric field enhancement .....	127
5.4.5 Role of the interface and inter-particle distance .....	128
5.5 Summary .....	131
<b>Conclusion and future perspectives .....</b>	<b>133</b>
<b>Conclusion.....</b>	<b>133</b>
<b>Outcome of the research work .....</b>	<b>136</b>
<b>Future works.....</b>	<b>136</b>
<b>Acknowledgement .....</b>	<b>140</b>
<b>References .....</b>	<b>142</b>

**List of figures**

Figure 1.1 Richard Trevithick 1802 world-first steam engine locomotive .....	3
Figure 1.2 Structure configurations of AC-DC traction drive system .....	4
Figure 1.3 Electric traction drive system to convert electrical power into mechanical power .....	5
Figure 1.4 PWM inverter output voltage and current waveforms.....	5
Figure 1.5 (a) Time $t=t_r$ (at the end of the rise time of the pulse) (b) Time $t=t_r+t_p$ (after one cable propagation time).....	6
Figure 1.6 (a) Time $t=2t_r+2t_p$ (after two cable propagation times) (b) Time $t=2t_r+3t_p$ (after three cable propagation times) .....	7
Figure 1.7 First coil voltage distribution against incident voltage rise times [11] .....	7
Figure 1.8 (a) Form-wound stator coil insulation structure for multiple slots. (b) Single slot semi conductive grading. Grading is applied to the coil around the first bend and the first end of the winding insulation .....	8
Figure 1.9 Thermal hot spots, in the end, winding under (a) pulsed and (b) sinusoidal voltages [9].....	10
Figure 1.10 Dismantle magnetic wires turn insulation on the left and its microscopic image on the right .....	12
Figure 1.11 Stator slot cavities after the operation .....	12
Figure 2.1 Several polarization mechanisms with varying electric field frequency [65].....	23
Figure 2.2 Dielectric loss vs frequency .....	24
Figure 2.3 Layers structure, holes injection layer (HIL), holes transport layer (HTL), electrons transport layer (ETL), electrons injection layer (EIL) .....	26
Figure 2.4 Fillers types, sizes and shapes .....	29
Figure 2.5 Change in composite material properties w.r.t (define w, r and t) particles size	30
Figure 2.6 Synthesis process of PAA solution.....	32
Figure 2.7 Generalized reaction mechanism of aromatic imide formation .....	33
Figure 2.8 Film thickness variation at different spin coater speed (a) PAA solution high molecular weight (b) PAA solution slight less molecular weight .....	36
Figure 2.9 Polyimide films synthesis process .....	37

Figure 3.1 (a) Three-layer sample with less chance of nanoparticles agglomeration (b) Single-layer PI film with a higher chance of nanoparticles agglomeration .....	43
Figure 3.2 Final composition of PI/SiO <sub>2</sub> -PI-PI/SiO <sub>2</sub> three-layer structure .....	44
Figure 3.3 FEI inspect S50 Scanning electron microscope.....	45
Figure 3.4 SEM image of surface topography of PI/SiO <sub>2</sub> .....	45
Figure 3.5 TEM image of 1wt% of SiO <sub>2</sub> nanoparticles dispersion in PI.....	46
Figure 3.6 Fourier Transform Infrared Spectroscopy (FTIR) instrument.....	46
Figure 3.7 Dielectric spectroscopy measuring setup.....	47
Figure 3.8 (a) Pulse voltage waveform and PD (b) Breakdown test system in the presence of PD.....	48
Figure 3.9 PD test system .....	49
Figure 3.10 Scheme of surface discharge (PD) and corona-resistance measurement.....	49
Figure 3.11 Conduction current density vs voltage .....	53
Figure 3.12 Metal and insulator energy gap (a) before and (b) after the applied electric field .....	54
Figure 3.13 PI film view and guard ring gold electrode deposition.....	55
Figure 3.14 Guard ring electrode setup to measure conduction current .....	56
Figure 3.15 I(t) characteristics of polarization and depolarization current .....	56
Figure 3.16 Measuring modes offered by an MCR rheometer .....	57
Figure 3.17 Schematic of the DMA chamber.....	58
Figure 3.18 Thermal diffusivity measuring instrument .....	59
Figure 3.19 TSM electrode setup in short circuit conditions .....	60
Figure 3.20 Principle of TSM (a) equilibrium state at T <sub>0</sub> (b) Equilibrium modified at T <sub>1</sub> .....	60
Figure 3.21 (a) Schematic diagram of PEA system (b) Space Charge distribution profile.....	63
Figure 3.22 TSC measuring system electrode.....	64
Figure 3.23 Polarization and depolarization process .....	64
Figure 4.1 SEM image of surface topography of single and multi-layer nanoparticles dispersion Left column showing single layer PI/SiO <sub>2</sub> films and right column showing multilayer PI/SiO <sub>2</sub> films .....	70

(a) SEM image of two-layer PI-PI/SiO <sub>2</sub> film	(b) TEM image of three-layer PI/SiO <sub>2</sub> -PI-PI/SiO <sub>2</sub> film	
Figure 4.2 SEM image of surface topography of single and multi-layer nanoparticles dispersion .....		71
Figure 4.3 SEM image of surface topography of single and multi-layer nanoparticles dispersion .....		71
Figure 4.4 PI molecule structures and bonding interaction between PI and SiO <sub>2</sub> .....		72
Figure 4.5 Modified and unmodified SiO <sub>2</sub> nanoparticles .....		73
Figure 4.6 (a) Half cured PI film at different temperatures and times (b) Fully cured PI film .....		74
Figure 4.7 Schematic representation of the plane-plane geometry (diameter 25 mm) .....		76
Figure 4.8 Thermomechanical analysis of (a) ODA-ODPA based PI nanocomposite films (b) ODA-PMDA based PI nanocomposite films .....		78
Figure 4.9 Thermal conductivity of different samples as a function of temperature .....		79
Figure 4.10 Dielectric response (a) dielectric constant (b) dielectric loss as a function of frequency .....		81
Figure 4.11 Dielectric response (a) dielectric constant (b) dielectric loss as a function of frequency .....		82
Figure 4.12 (a) Dielectric constant as a function of temperature at 100 Hz (b) Dielectric loss as a function of temperature at 100 Hz .....		82
Figure 4.13 Electrical breakdown strength at different temperatures .....		84
Figure 4.14 Breakdown Weibull statistic at different temperatures (a) PI (b) PI/Al <sub>2</sub> O <sub>3</sub> .....		84
Figure 4.15 Breakdown Weibull statistic for all samples at 25 °C temperatures .....		85
Figure 4.16 PI and PI/Al <sub>2</sub> O <sub>3</sub> corona resistant lifetime tests .....		86
Figure 4.17 Conduction current density versus electric field at different temperatures .....		88
Figure 4.18 SCLC conduction mechanism at different temperatures .....		90
Figure 4.19 Poole-Frenkel conduction mechanism at different temperatures .....		92
Figure 4.20 Schottky injection mechanism at different temperatures .....		95
Figure 4.21 Current-Voltage characteristics of J vs E plots in log/linear scale at (a) 50 °C (b) 100 °C (c) 150 °C .....		96

Figure 4.22 Hopping conduction model curve fitting line with experimental symbols data at hopping distance $\alpha=2.6\text{nm}$ for (a) PI (b) FPI (c) PI/SiO <sub>2</sub> (d) PI-PI/SiO <sub>2</sub> at 50 °C .....	97
Figure 4.23 Hopping conduction model curve fitting line with experimental symbols data at hopping distance $\alpha=2.6\text{nm}$ for (a) PI (b) FPI (c) PI/SiO <sub>2</sub> (d) PI-PI/SiO <sub>2</sub> at 100 °C .....	98
Figure 4.24 Hopping conduction model curve fitting line with experimental symbols data at hopping distance $\alpha=2.6\text{nm}$ for (a) PI (b) FPI (c) PI/SiO <sub>2</sub> (d) PI-PI/SiO <sub>2</sub> at 150 °C .....	98
Figure 4.25 TS current for PI and FPI samples (a) after poling at 50 °C (b) maximum and minimum values after poling at 50 °C (c) after poling at 100 °C (d) maximum and minimum values after poling at 100 °C (e) after poling at 150 °C (f) maximum and minimum values after poling at 150 °C .....	102
Figure 4.26 (a) TS current for single layer PI/SiO <sub>2</sub> (b) TS current for two layers PI-PI/SiO <sub>2</sub> films.....	104
Figure 4.27 (a) Electric field calculation using TS current (b) Charge density calculation using TS current.....	105
Figure 4.28 Space charge profile for different samples after 30 kV/mm during 180 min (a) PI/Al <sub>2</sub> O <sub>3</sub> -PI-PI/Al <sub>2</sub> O <sub>3</sub> (b) PI/SiO <sub>2</sub> -PI-PI/SiO <sub>2</sub> (c) PI/Al <sub>2</sub> O <sub>3</sub> -PI/SiO <sub>2</sub> (d) PI/Al <sub>2</sub> O <sub>3</sub> (e) PI/SiO <sub>2</sub> (f) PI.....	108
Figure 4.29 Total charge decay profile after Voltage off for pre-conditioned 30 kV/mm during 180 min at 25°C .....	111
Figure 4.30 TSC measurement of preconditioned samples at 30 kV/mm (b) Trap level distribution using TSC data .....	113
Figure 4.31 Layers structure, holes injection layer (HIL), holes transport layer (HTL), electrons transport layer (ETL), electrons injection layer (EIL) .....	115
Figure 5.1 Change of sample capacitance and interface permittivity due to nanoparticles agglomeration: (a, c) three-layer structure with less chance of agglomeration, (d) single-layer structure with a higher chance of agglomeration, (b) two-layer structure with interface thickness and permittivity. ....	122
Figure 5.2 Model building algorithm .....	123
Figure 5.3 (a, d, g) SEM/TEM images (b, e, h) Image processing binary conversions (c, f, i) Model in COMSOL using MATLAB Live Link (j) Cross-sectional view using SEM .....	124
Figure 5.4 Electric field boundary conditions.....	125
Figure 5.5 Electric field distribution (a) Top agglomeration (b) Bottom agglomeration (c) Three-layer homogenous dispersion (d) Three-layer original homogenous distribution .....	127

Figure 5.6 Calculation of (a) Electric field enhancement factor and (b) Polarization charge density.....	128
Figure 5.7 Model for inter-particle distance .....	130



**Abstract**

Electrical insulations are key components of electrical machines such as motors that are used in aircrafts and electric trains. Polyimide films as an insulating material are used in such rotating machines that are commercially available in single or multi-coated layer forms. To fulfill the demand for high-speed trains, the railway industry is using fast switching pulse power, which has reduced the motor insulation lifetime. Therefore, there is a strong urgency to improve the motor insulation system to fulfill the demand for high-speed trains. We are always looking towards new dielectric materials, which could meet the required conditions. With the advancements in nanotechnology, nanoparticles are getting scientific attraction due to its large surface to volume ratio. It has a controlled interaction region known as interphase region, which can influence polymer nanocomposite properties. But dealing with nanoparticles is not an easy task because these nanoparticles are very small in size and have a strong tendency to agglomerate. We can only improve its properties if these nanoparticles are well dispersed and distributed inside the polyimide matrix. We proposed a multilayer PI/nanocomposite insulation structure to improve the nanoparticles dispersion and thereafter improve its dielectric properties.

In this thesis, the multilayer PI/nanocomposite films were prepared using an optimized synthesis process. The synthesis of PI nanocomposite is a complex process with many variables are involved. A detailed synthesis process optimization for multilayer PI/nanocomposites films is presented in this thesis. Several factors, which can influence the molecular weight of the PAA during the synthesis process are discussed in detail. The synthesized samples are characterized by experiments and simulations. The experimental protocols and the best diagnostic techniques are presented to evaluate the performance of samples.

First, the samples degradation mechanism was explored under the corona discharge generated from the square power pulse source. Second, electrical properties such as insulation lifetime, dielectric strength, corona discharge, space charge and thermal stimulated current (TSC) are investigated. Third, trap levels are calculated using total charge decay data and TSC data. In the end, multilayer PI/nanocomposite 3D models based on actual boundary conditions obtained from SEM/TEM images of synthesized samples were constructed in COMSOL Multiphysics software. The impact of nanoparticle dispersion on the electric field enhancement is explicitly described in this model. The electrical properties of these synthesized multi-layer PI/nanocomposite films are also measured through experimental results. Our results demonstrate that the chances of nanoparticles agglomeration are reduced by using multi-layers system composed by a thin layer of PI/nanocomposite on PI film instead of using one single layer of PI/nanocomposite film. In consequence, less space charge and low electrical fields are observed in multilayer films. Our methods will help to reliably predict the dielectric strength of



polymer/nanocomposite insulating materials. Additionally, the new synthesized multilayer PI/nanocomposite insulating material will ensure reliable operation for electric motors and increase its lifetime.

# Chapter-1

---

Introduction

**Chapter 1 Introduction**

1.1 Background .....	3
1.2 Electric traction motors.....	3
1.2.1 Electric traction drive systems .....	4
1.2.2 High voltage high frequency pulse power.....	5
1.2.3 Motor insulation.....	7
1.2.4 Motor insulation failure mechanism.....	9
1.2.4.1 Thermal aging of insulation .....	10
1.2.4.2 Electrical aging of insulation.....	10
1.2.4.3 PD turns-insulation .....	11
1.3 From polyimide to nanodielectrics multicoated polyimide films .....	12
1.3.1 Polyimide insulation .....	12
1.3.2 Nanodielectrics based polyimide .....	13
1.3.3 Fluorination coated polyimide .....	14
1.4 Motivation.....	14
1.5 Objective and novel contribution .....	15
1.6 Description of the dissertation outline .....	15

## 1.1 Background

In the early days, only ways to travel were by foot and carriages. The trend started to change with the development of the first steam engine in the early 19<sup>th</sup> century by Richard Trevithick, a British builder and mining engineer as shown in Figure 1.1 [1]. By the end of the century, the railway had started to get popularity all over the world. In early, it was primarily utilized in mines in Europe by applying a different source of traction power [2]. Since then, rapid development has been seen until the 21<sup>st</sup> century and currently, railway transportation is the most convenient and speedy way to travel domestically. High speed, safety and environmental impact were the main factors that have steered the enormous advancement in railway. The modern materials used to manufacture railway tracks were the decisive factors in its developments. In the beginning, it was made of cast iron but later steel starts being used because of its high mechanical strength and less fragile nature. The rubber was also added between the tracks to reduce the noise and mechanical vibration. Furthermore, the track size was standardized to produce the same gauge tracks globally.

The main progress in the railway industry was the birth of the steam engine. However, the enormous evolution in the railway industry was the use of electric motors powered by electric lines. The first locomotive electrification arose late 19<sup>th</sup> century, while the first diesel engine-based locomotive was introduced in the early 20<sup>th</sup> century [2]–[4]. The speed of diesel locomotives was far less than the speed of electric locomotives. The electric locomotives are energy efficient and environmentally friendly but a huge investment is required in infrastructure to electrify the line. Due to the development in electric locomotive technology, excessive rise in high-speed trains has been seen in the late 20<sup>th</sup> century and the first decade of the 21<sup>st</sup> century. To accelerate these high-speed trains an electric traction system is used in which motors are the main components of electric multiple unit (EMU) in the locomotive.

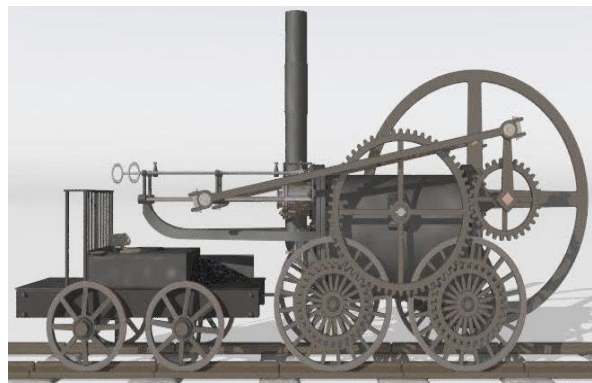


Figure 1.1 Richard Trevithick 1802 world-first steam engine locomotive

## 1.2 Electric traction motors

To accelerate the wheels of the train, a propulsion force is required which is achieved using an electrification line system. For this purpose, an electric traction motor is used to drive heavy

vehicles such as locomotives [2], [4], [5]. These motors are also used in elevators, electric road cars, roller coasters, conveyors and other vehicles with electrical transmission systems. In rail industry, motors fed by inverters are the main components to control the speed of trains [6], [7]. In the beginning, some traditional DC motors were used for this purpose at normal speed. Improvements in power electronics have now made it possible for the use of AC induction motors to achieve high speed. These AC motors are also being utilized in the French TGV. Due to the advancements in power electronics, such high-speed trains speed can be controlled.

### 1.2.1 Electric traction drive systems

Electric drive technology was established in the 19<sup>th</sup> century and is widely used in industries such as agriculture, transport and daily life in the 20<sup>th</sup> century [8]. The electric motors actuators can be driven by the DC or AC drive system, as shown in Figure 1.2 [9]. The speed of the electric drive can be constant or variable, depending on the load variation. In 1960, with the advancement in power electronics and the success of frequency invertors have made it a hot research topic for scientists [10]. In the middle of 1970, energy saving was the main concern for scientists. In the 1990s, the semiconducting devices and the application of modern control theory technology have made breakthroughs in the AC motor drive system for adjustable speed. Nowadays, as an excellent drive and control technology AC motor drive system has been widely used in the railway traction system applications. After the development of power electronics and the availability of semiconductor based high-speed power switching devices, such as IGBTs, most of the companies are using PWM inverters in their AC voltage source drive systems; these are now the industrial standard device because of their reliability and low switching losses [11].

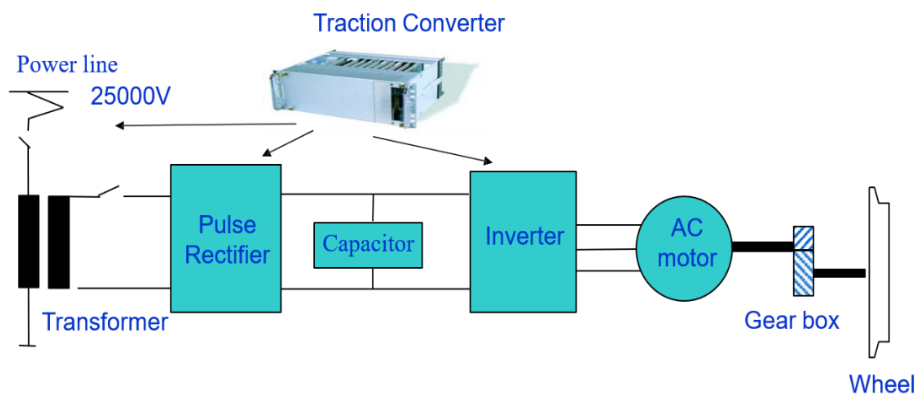


Figure 1.2 Structure configurations of AC-DC traction drive system

These PWM inverters are reliable and low switching loss devices, which have industrial standards to use them globally. In order to control the speed of motors, these PWM inverters provide alternating pulses after a complete rectification process from incoming AC voltage to DC using a rectifier, filtering the DC to remove ripples by using RC filters and inverting back to an alternating pulse [9], [12]–[14]. These short pulse width and high frequency voltage

waveforms from PWM can increase the electric field stresses on the motor used in the locomotive, as shown in Figure 1.3, which can cause serious damage to the motor insulation system [15].

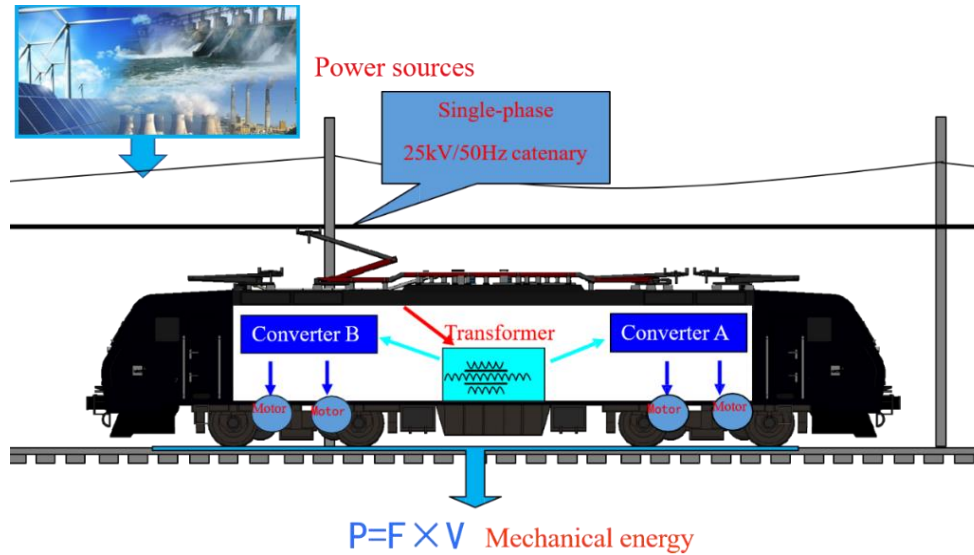


Figure 1.3 Electric traction drive system to convert electrical power into mechanical power

### 1.2.2 High voltage high frequency pulse power

The resulting current from these short width high frequency pulses converters are modified significantly by the inductance of motor and cable length. Some numbers of ripples are superimposed on the sinusoidal waveform of the output current from PWM converters. The simplified form of current and the voltage for one cycle is illustrated in Figure 1.4. The rise time of the pulse is so steep that their propagation can produce a voltage overshoot [16].

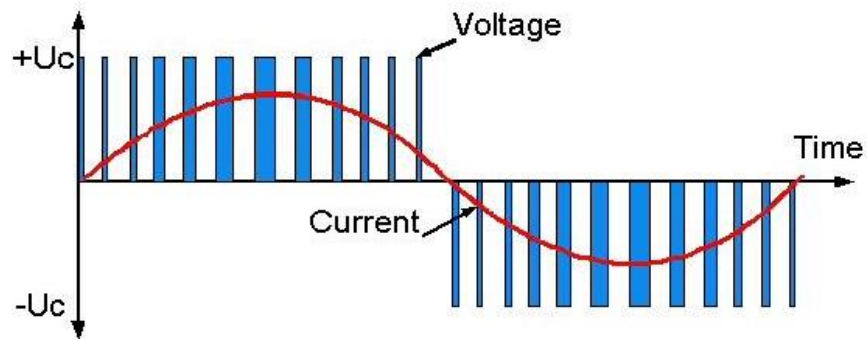


Figure 1.4 PWM inverter output voltage and current waveforms

The transmission cable equivalent circuit consists of series and parallel combination of inductors and capacitors. The energy of each pulse from the drive is used to charge these capacitors and inductors. The traveling speed of pulse, in a typical PVC cable insulation, is equal to  $1/\sqrt{LC}$  m/s, where "C" is the capacitance and "L" is the inductance of cable and the propagation velocity of each pulse is about  $1.7 \times 10^8$  m/s. It changes little according to the type

of cable and mainly it varies with the permittivity of cable insulating material. The pulse propagation mechanism is illustrated in Figure 1.5 and Figure 1.6 [17]. In PWM waveform, the pulse starts rises at  $t=0$  and reaches to voltage  $V$  at  $t = t_r$ . In an ideal situation cable length of about 30 m, the rise time ( $t_r$ ) is lower than the propagation time ( $t_p$ ). The pulse moves from the drive towards the motor and when it arrives the motor, it reflected back due to higher impedance of motor than cable, as illustrated in the schematic diagram in Figure 1.5(b). It increases the voltage peak twice; because both the forward and the reflected pulses have the magnitude  $V$ . The returned pulse from the motor is reflected back again in a negative direction due to the low impedance of drive. The voltage remains the same at drive because the drive clamps the voltage to  $V$ . The reflected pulse again reflected back in the reverse polarity, as shown in Figure 1.7, and makes the voltage level double at the motor terminal. Therefore, the actual voltage at the motor terminal is raised [18].

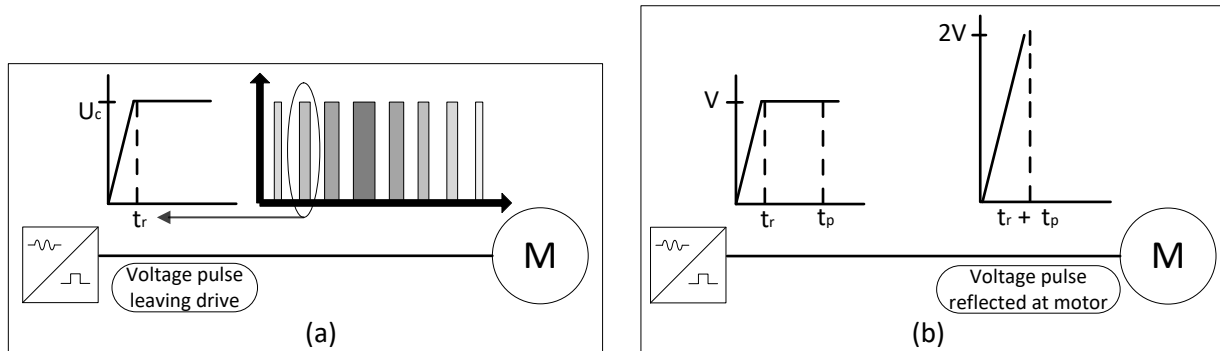


Figure 1.5 (a) Time  $t=t_r$  (at the end of the rise time of the pulse)  
(b) Time  $t=t_r+t_p$  (after one cable propagation time)

In short length cable, the voltage will never approach to  $2V$  because  $2t_p$  is less than  $t_r$ , while in long length cable, the reflected pulse is delayed and the voltage peak reduced, as described here. In the ideal conditions, these reflection peaks may cause the voltage to oscillate frequently which increases the voltage rise time and causes losses in the cable [17]. These losses and overshoot voltage peaks change the shape of the original waveform. The features of the typical output pulse waveform and the motor terminal voltage waveform are shown in Figure 1.7. It shows that the voltage at the motor terminal depends upon both the cable length and the rise time. Some measured pulse voltage waveforms at a supply voltage of 460 V show some overvoltage even with 4 m cable length. The motor insulation winding system is protected from such overshoot voltages [14]. The overshoot of the voltage pulse with sequence of voltage peaks travels towards the motor winding with a measurable propagation time as illustrated above. In later coils, this effect reduces to a uniform voltage distribution to high frequency inductive and capacitive losses [9]. These overshoot voltage stresses can increase the chances of partial discharge (PD) occurrence and damage the turns insulation, due to the short rise time. This short rise time will also increase the PD occurrence because, due to

the short rise time, the statistical time lag will reduce and the availability of free electrons will start ionization for PD. Another effect due to the short rise time under pulse voltage is the memory effect for space charges, accumulated within the insulation. Furthermore, with the reduction in rise time,  $dV/dt$  will increase. Hence  $\Delta V$  will increase with the same statistical time lag. Voltage in the aged defected areas during the time lag may exceed inception voltage  $V_i$  by an overvoltage  $\Delta V$ , and PD ignites at a voltage  $V_i = V_i + \Delta V$ . After discharge, voltage drops to the residual value and this residual value help for the next discharge due to memory effect.

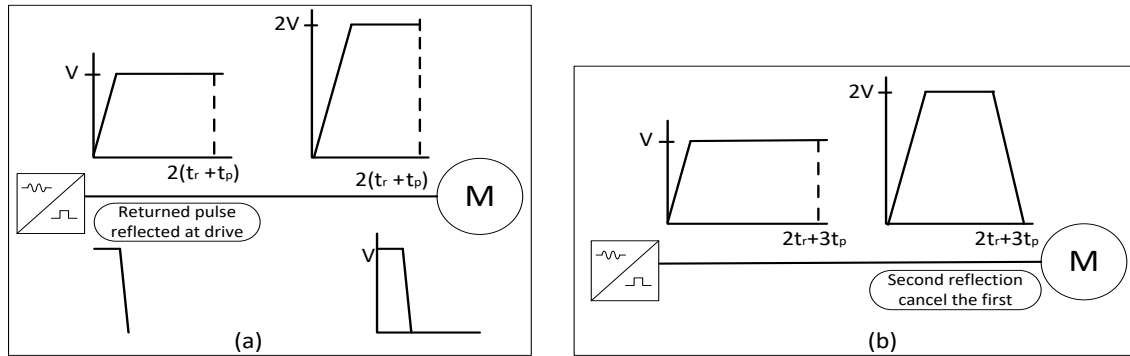


Figure 1.6 (a) Time  $t = 2t_r + 2t_p$  (after two cable propagation times)

(b) Time  $t = 2t_r + 3t_p$  (after three cable propagation times)

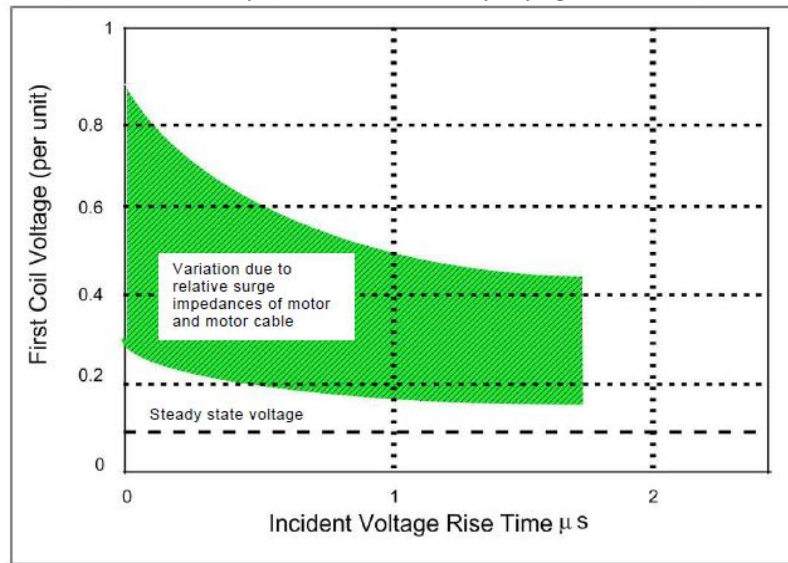


Figure 1.7 First coil voltage distribution against incident voltage rise times [11]

### 1.2.3 Motor insulation

It is mentioned in the above section how the voltage waveforms of PWM inverters changes and how it can damage the motor insulation [19]. To resist to nanosized width high frequency and high voltage stresses from PWM inverters, the International Electrotechnical Commission (IEC) has released two technical specifications name as IEC-60034-18-41 and IEC-60034-18-42, for type I and type II motors respectively [20]. These technical specifications have improved the



insulation of the motor. These standards are used to maintain specific prerequisites for motor insulation. Therefore, motors with a form-wound insulation system have different aging conditions compared to motors with random-wound stators insulation supplied by PWM waveforms and motors insulation supplied by sinusoidal voltage waveforms. Depending on the particular insulation winding design, it can be affected significantly by several factors such as aging due to the high voltage stresses, PD and temperature rise. IEC-60034-18-41 addresses the requirements of a low voltage insulation system known as Type I motors, which are designed to work in an environment without PD [21]. IEC TS 60034-18-42 covers the Type II motors insulation system [22]. These motors have form wound coils structure and are rated higher than 2400 V, therefore, such motors experience PD during operation. The occurrence of PD and other aging factors during operation can reduce the lifetime of the insulating material [13], [22]–[26]. The designers must keep in mind the information of high frequency, high voltage and short rise time of the PWM waveform to design better insulation for PWM applications, because these parameters can strongly impose great stress on motor insulation. To decrease the surface discharge at the slot, semiconductive silicon coated layer is used to lower the electrical stress, as shown in Figure 1.8.

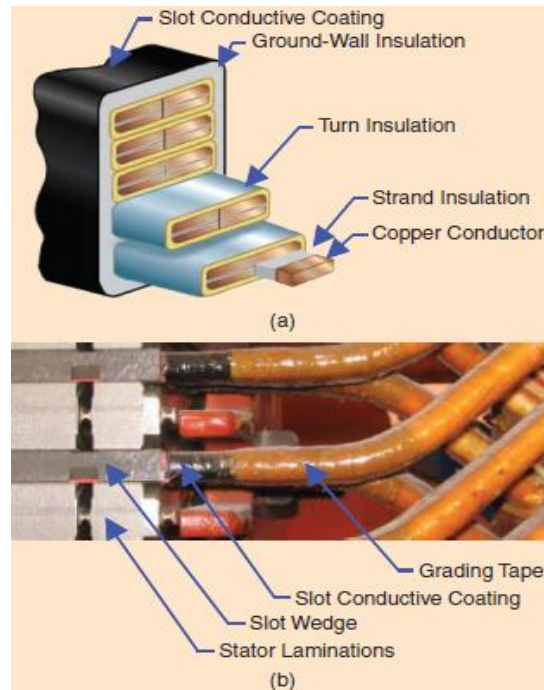


Figure 1.8 (a) Form-wound stator coil insulation structure for multiple slots. (b) Single slot semi conductive grading. Grading is applied to the coil around the first bend and the first end of the winding insulation

After carefully considering the IEC standards, as shown in Figure 1.8, an insulation system of form wound coil consists of the following parameters for better performance [27]:

- 1) In order to reduce the skin effect losses and eddy current losses, strand type conductors are used which help to reduce these losses and enhance efficiency. The insulation used on these strand type conductors is a thin film coated with a Dacron material.
- 2) To separate the copper turn from each other, turn insulation is used on each turn. The mica sheet and Dacron are used as an insulating material for copper turns.
- 3) To isolate the copper turns from the stator, ground-wall insulation is used. The insulating material used for this purpose is a composite of mica sheet and epoxy.
- 4) To avoid PD in cavities between the slots and grounded-wall, semi conductive material (slot-conductive coating) is used. Many motor companies are using carbon loaded tape or paint as a coating material for motors rated above 3 kV [21].
- 5) For further protection of end winding a stress grading insulating layer is superimposed on the outer edge of the slot, which is coated with a conductive material.
- 6) A tape loaded with silicon carbide powder is specially designed to mitigate the surface electric field stress from the line voltage.

#### **1.2.4 Motor insulation failure mechanism**

The main failure reason for form wound motors is the deterioration of the insulating material due to the continuous thermal and fast switching electrical stresses during operation [21], [24]. The heat is generated due to the losses, such as copper loss and core loss. The temperature may rise to higher values during operation due to the overloading and insufficient motor cooling system. Extreme temperature conditions may tend to shorten the insulation life span. Contamination can be another way of thermal aging, as it can reduce the thermal conductivity from the coils and increase the internal temperature. Thermal aging, combined with mechanical vibrations can enhance the insulating material delamination process from the winding. Furthermore, if the heat generated in the winding is not dissipated on time, it can increase the rate of oxidation, which helps the chemical bonds to break and therefore reduce its electrical and mechanical strength. The delamination of the insulating material can create voids that may initiate PDs when the applied voltage is higher than the inception voltage. The chances of PD occurrence increase at higher voltages, which further degrade the insulation. Contamination can also cause electrical failure due to electrical tracking because these contaminations can be semiconducting, leading to a small amount of surface current on coils. These electrical tracking discharges leave carbon track with higher electrical conductivity, cause further discharges and decompose the insulation. With the passage of time, these electrical tracking can cause different to phase faults. Such insulation failures become even severe under PWM power supplies where steep rise time and high frequency pulses increase the chances of electrical discharges and weaken its electrical strength [16], [25], [28].

### 1.2.4.1 Thermal aging of insulation

For high-speed motors, the required high voltage, short rise time and high frequency pulses of PWM based motor drives generate heats in the winding, increase the overall motor stator working temperature and lead to thermal aging, as mentioned in the above section. In an ideal condition, when voltage is applied to the pure capacitive dielectric insulation, having minimum or zero dielectric loss causes a negligible amount of power loss in the form of heat. But, in a normal condition, where epoxy-based mica sheet is used as dielectric insulation, having dielectric loss due to internal dipoles movements under alternate electric field generates a high amount of power loss in the form of heat. According to the literature, about 0.5% power of 60 Hz applied voltage is due to dielectric loss [29]. In PWM drive motors the copper ( $I^2R$ ) and core losses are higher than the conventional AC drives motors. This effect added to harmonics increases with the increase in switching frequency, develop more heat in the stator insulation winding. Another reason to increase winding temperature is by using a coating layer to suppress PD; such coatings increase the capacitive currents through the ground-wall. The thermal deterioration due to this coating under PWM and sinusoidal voltage are shown in Figure 1.9 [7], [26]. At higher frequency, these defects are aggravated, degrade the silicon carbide materials around the coils surface and induce hot spots accumulation near the core and around the bending area [26]. Literature work has demonstrated that if the heat dissipation is low in the insulation system, then the temperature may rise up to 75 °C or even higher than the normal operating temperature at 50 Hz sinusoidal voltage drive motors [18]. Such localized heat from the coating accelerates its thermal aging.

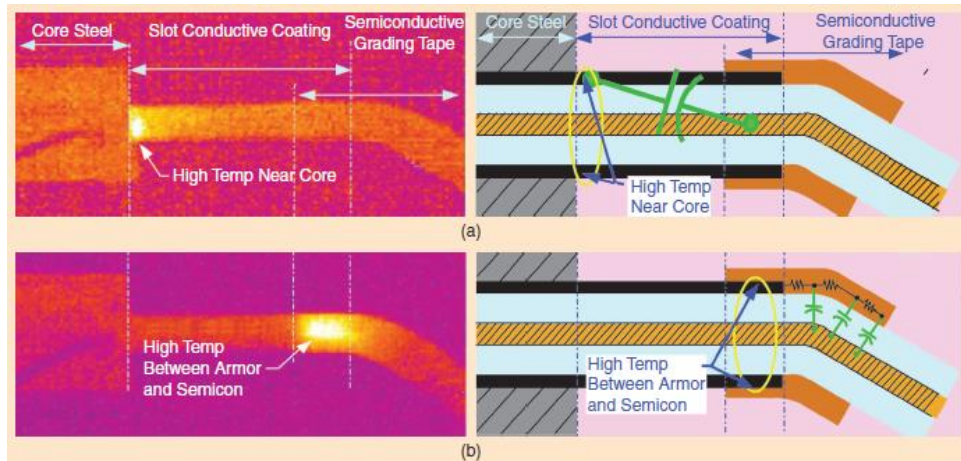


Figure 1.9 Thermal hot spots, in the end, winding under (a) pulsed and (b) sinusoidal voltages [9]

### 1.2.4.2 Electrical aging of insulation

Electrical aging of insulation can be due to the PD, space charges and electric field enhancement around interfaces and voids. The motors, which are operated at 3 kV or above, may have internal PDs even if micro size air gaps are present in stator magnetic bars insulation.

As mentioned above, such kinds of voids can be formed due to the insulation delamination. The characteristics of pulses from inverter intensify the above-mentioned effects [30]. When PD occurred, it generates ultraviolet rays, high energy electrons, and breaks the chemical bonds, which speed up the material degradation [31]. The degradation of polymer starts with the breakage of polymer chains under corona discharge electric stresses. To measure the corona resistance property is meaningful in the sense that it can be used to predict the life span of the insulation. It is obvious that high temperature elevates such degradation process. The electrical aged insulation reduces the safety operation and leads to electrical breakdown. Indeed, comprehensive research has been done to understand the electrical aging process due to PDs and charges injections from electrodes inside dielectric materials, measuring space charges, interfacial defects and traps. The electrical aging of insulation can be due to the following main:

- 1) Localization of electric field and PD occurrence in the dielectric materials.
- 2) Interfacial polarization and corona or surface discharges.
- 3) Charge trapping at interface and injected charges mobility.

#### **1.2.4.3 PD turns-insulation**

For PDs, the following two main conditions should be fulfilled:

- 1) The applied voltage must be higher than the PDIV (partial discharge inception voltage).
- 2) Availability of free electrons to initiate discharges.

As mentioned in section 1.2.2, the first coil of turn insulation faces 50 % overshoot voltage peaks due to fast-switching frequencies [28], [32]. The value of overvoltage in the first coil depends on the applied pulse voltage. These overvoltage short rise time peaks provide more PD pulses available per second, due to memory effect. These PD activities happen in air gap cavities within the turns of the insulation system. Although these turns insulating magnetic wires are VPI processed, but still, some micro size voids remain in these insulation wires which cases PDs. The PDs erode the insulation around the surface of the electrode, as shown in Figure 1.10 and Figure 1.11 below. Mica paper made up of polyimide material is widely used insulating material in these magnetic bars, these PI films are highly PD resistance materials, but sometimes they failed due to high PD magnitude and repetition of occurrence. The significance of such failures due to PD activities depends on the rise time and frequency of voltage pulse inverters [33]. Once the PD happened, it generates more cavities and interforms new interfaces due to material degradation. The dissipation of heat energy in such newly formed interfaces and micro-sized airgaps becomes difficult. The charges may trap in these interfaces and become deep traps after gaining some thermal energy from high temperature; these trap charges help to obtain the initial free electrons for further discharge, decrease the required discharge time,

and make it easier for ionization. Hence, PDIV decreases at a higher temperature and PD occurrence accelerates.

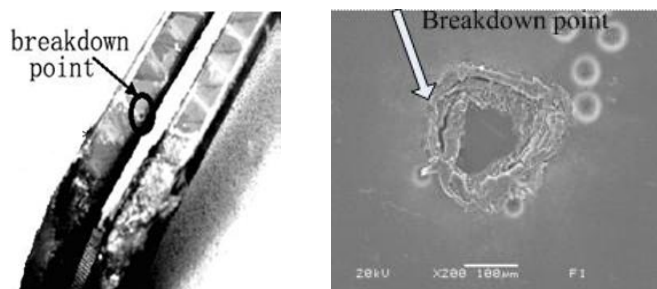


Figure 1.10 Dismantle magnetic wires turn insulation on the left and its microscopic image on the right

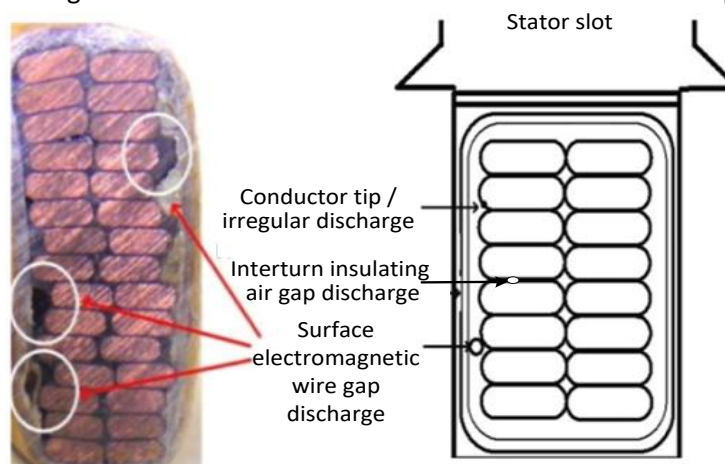


Figure 1.11 Stator slot cavities after the operation

### 1.3 From polyimide to nanodielectrics multicoated polyimide films

#### 1.3.1 Polyimide insulation

Thermo-oxidative polyimide (PI) films by DuPont are in the market since 1960s. These low dielectric constant thin films are highly corona resistive, thermally stable and have higher breakdown strength electrically and mechanically [27]. Such unique characteristics have made PI films to use in large industrial applications such as aerospace, automotive and microelectronics devices. Multiple monomers are available to synthesize PI films that provide a wide range of high glass transition temperatures depending on the monomer used to synthesize. The fire resistance property of PI and low dielectric constant has made it possible to isolate metal lines and reduce electromagnetic interference effect in electronics and signal processing devices. Polyimide is also used in electric motors insulation for high-speed trains. These PI films undergo high electric field stresses due to the pulse power supplies to control the speed of trains [34]. Under high electric field and temperature environment, electric charges known as space charges tend to accumulate within PI films [31]. These electrical charges induce a local electric field which can be superimposed to the electric field applied to the dielectric material under normal operating conditions [35]. Thus, the resulting value of the electric field can approach and even exceed the early breakdown threshold, leading to local material degradation and, as a result, to a possible failure of the insulation. The risk is increased when

high voltages are applied to the insulation component having nonhomogeneous insulating materials. Hence, developments in PI films are compulsory so that it could perform better under high voltage and high temperature environments. The properties of common PI are shown in Table 1.1.

Table 1.1 Physical properties of PI film

Properties	Typical value at 25 °C	Test method
Tensile strength (MPa)	231	ASTM D-882-91
Density (g/cc or g/ml)	1.42	ASTM D-1505
Glass transition temperature $T_g$ (°C)	360-410	Differential calorimetry
Thermal conductivity (W/m.K)	0.12	ASTM F-433
Electrical breakdown strength (kV/mm)	280	ASTM D-149
Dielectric constant at 1 kHz	3.4	ASTM D-150
Dissipation factor at 1 kHz	0.0020	ASTM D-150
Volume resistivity ( $\Omega$ .cm)	$1.5 \times 10^{17}$	ASTM D-257

### 1.3.2 Nanodielectrics based polyimide

Composites with superior properties may be formed when two different materials are combined. Within the vast group of inorganic-organic hybrid materials, composites received a great deal of attention in the last decade. Nano-size particles and micro-size particles are commonly used with organic polymers due to their large surface area which helps composite material to improve its electrical, mechanical and/or thermal properties contrasting with the conventional polymer materials [36]. Nanocomposites are formed by adding nanometer-size particles into the base polymer matrix. They are used to provide resistance to the charges injection from the electrodes and reduce the free path for electrical tree initiations in the bulk of polymer nanocomposite materials [37]. Various results of nanodielectric polymeric composites can be invaluable when a small number of nanoparticles are properly chosen and dispersed/distributed into the polymer matrix [13], [38], [39]. However, adopting a traditional way to mix nanoparticles in the host polymer matrix is not an easy task because these tiny particles can easily agglomerate and increase the nonhomogeneous nature of the insulating material. Therefore, their homogeneous dispersion and distribution is an obligatory condition to improve their dielectric properties [40], [41]. Conventionally fillers are materials in the form of particles (calcium carbonate, silica), fibers (glass fibers), sheets (clays). Several kinds of nanoparticles such as  $\text{SiO}_2$  [35],  $\text{Al}_2\text{O}_3$  [31],  $\text{TiO}_2$  et al, have been used with polyimide. The concentrations of the fillers, as well as their proper dispersion, are the main parameters.

### 1.3.3 Fluorination coated polyimide

Coating PI films with such a material that can increase its surface conductivity can help to speed up the surface charge dissipation and reduce the space charge accumulation. For this purpose, the coating of the fluorination layer on both sides of PI films is being used to modify the surface chemistry without altering its bulk properties [42]. Some research has demonstrated that the mobility of charges and the trap depth of charges can be influenced by using fluorination on the surface. It can change the surface energy of polyimide film and therefore change the electrical properties [43]. The FTIR studied has shown that fluorination can alter the surface chemistry of polymer. It breaks the C-H bond of polymer and forms new C-F, C-F<sub>2</sub> and C-F<sub>3</sub> bonds, as the C-F bond is highly electronegative, which make the C-F bond highly polarized and increase surface conductivity. The C-F bond dissociation energy is 544 kJ/mol, which is much higher than the C-H bond dissociation energy of 414 kJ/mol [44]. The intensity of fluorination depends on the treatment conditions such as temperature, surface nature of the polymer, reaction time and pressure of the reaction gases inside the chamber. The fluorination can lead to the in-phase and out of phase stretching of aromatic groups C=O and C-N bonds and the in-plane deformation of phenyl-H [45]. The thickness of the samples and the thickness of the fluorination coated layer can have some degree of impact on the bulk conductivity of the sample. In the case of PI, the thickness is very small, around 25  $\mu\text{m}$ , so it is certain that it will change its bulk conductivity to some extent.

### 1.4 Motivation

Nowadays, it is known that electrical insulations are key components of such motors that are used in aircrafts and electric trains. Polyimide films as an insulating material are used in such rotating machines, which are commercially available in single or multi-coated layer forms. Over the past few years, the global market has shown a great interest in the application of nanodielectrics, especially in the field of electrically insulating material. Various research results have claimed that polymer nanocomposites materials can improve dielectric properties for electrical insulation applications. The key role, played by the nanoparticles dispersion and interface region, is an essential part of these improvements. Further conditions to improvements are the size and type of nanoparticles properly chosen and distributed into the polymer matrix. Initially, it seemed like magic that everything is possible by using nanodielectrics, which later proved wrong after understanding the exact working principles of polymer-based nanocomposites, though several questions still need to be solved. This has motivated us to explore in this field further and find those principles, by using experimental and simulation work, on improving the dielectric properties of the PI-based nanocomposite.

### 1.5 Objective and novel contribution

The main objectives of this thesis work were to synthesize the multi-layer PI nanocomposites films, analysis and simulation, taking into account the nanoparticles dispersion to improve their dielectric properties. The multi-layer PI nanocomposite films are synthesized specifically for the electric motor insulation used in the high-speed trains. This investigation thoroughly examines the effect of inorganic nanoparticles in the form of multilayer PI films on space charge accumulation, conduction current, dielectric loss, thermomechanical and thermal conductivity. The objectives and novel contribution from this research work are as follows:

- 1) Synthesis protocol and chemical characterization of multilayer PI nanocomposite films.
- 2) Rheological characterization of polyimides and derived nanocomposites.
- 3) Nanoparticles dispersion in PI nanocomposite films and their modeling using real experimental boundary conditions.
- 4) Space charge analysis of multi-structure PI films using TSM (thermal step method).
- 5) Influence of nanolayer structure of PI film on space charge behavior and trap levels.
- 6) Electrical performance and dielectric properties of multilayer PI nanocomposite films for motor insulation.
- 7) Simulation and modeling to calculate electric field distribution.

### 1.6 Description of the dissertation outline

The organization of this thesis is as follows:

**Chapter 1** introduces the background importance on the basis of literature review, applications, motivations and objectives of this research. Novel contributions by the author and the structure of the thesis are also illustrated in the end.

**Chapter 2** provides the physical properties of polyimide and their derived nanocomposites, synthesis process optimization to prepare single and multi-layer polyimide-based nanocomposite films.

**Chapter 3** deals with the description of experimental techniques and methodology to characterize PI nanocomposite films.

**Chapter 4** investigates the performance of single and multi-layer polyimide films on the basis of data collected from experimental results. Physical, chemical, electrical and thermomechanical characterizations of these films are discussed in detail.

**Chapter 5** presents the numerical simulation of single and multilayer PI film models built in COMSOL Multiphysics software. In order to build the model COMSOL to MATLAB, live link platform is utilized. The FEM is used to calculate the electric field distribution in films.





## Chapter-2

---

Physical properties and optimize synthesis process of  
polyimide nanodielectrics

**Chapter 2 Physical properties and synthesis optimization of polyimide nanodielectrics**

2.1 Introduction .....	20
2.2 Organic polymers .....	20
2.3 Physical properties of polyimide.....	21
2.3.1 Polyimide.....	21
2.3.2 Chemical properties of polyimide .....	21
2.3.3 Thermal properties.....	21
2.3.4 Mechanical strength.....	22
2.3.5 Properties of polyimide in electrical engineering .....	22
2.3.5.1 Conduction current .....	22
2.3.5.2 Dielectric constant and dielectric loss.....	23
2.3.5.3 Dielectric breakdown strength.....	25
2.3.5.4 Charge transport phenomena .....	25
2.3.5.5 Corona discharge resistance and material degradation .....	26
2.4 Physical properties of nanodielectric based polyimide in high voltage engineering .....	27
2.4.1 Inorganic filling particles .....	28
2.4.2 Particles size shape and types.....	28
2.4.3 Nanoparticles dispersion and distribution.....	30
2.4.4 Nanoparticles surface treatment .....	31
2.4.4.1 Coupling agents .....	31
2.4.4.2 Plasma treatment .....	31
2.4.5 Polymer nanocomposite materials .....	32
2.5 Synthesis of polyimide .....	32
2.5.1 Preparation mechanism for poly amic acid (PAA) .....	32
2.5.2 Monomers reactivity conditions .....	33
2.5.3 Synthesis of PAA/nanoparticles composite solution .....	35
2.5.4 PI film casting .....	35
2.5.4.1 Casting PI films using glass and brass substrate.....	35

Chapter 2      Physical properties and optimize synthesis process of polyimide nanodielectrics

2.5.4.2 Casting PI films using a spin coating technique.....	35
2.5.5 Controlling the thickness.....	35
2.5.6 Casting PI and nanocomposite/PI multi-layer films .....	36
2.5.7 Thermal imidization of a poly amic acid (PAA) .....	36
2.6 Synthesis process optimization.....	37
2.6.1 Factors involved in the molecular weight of PAA .....	37
2.6.2 Determination of the degree of imidization .....	38
2.6.3 Changes in the mechanical strength during thermal imidization .....	38
2.6.4 Crystallinity and the glass transition temperature .....	38
2.6.5 Avoid side reactions .....	39
2.7 Summary .....	39

## **2.1 Introduction**

This chapter begins with a description of the physical properties of polyimide and the derived nanodielectrics. Afterward, a detailed synthesis process of PI nanocomposite single and multilayer films is outlined, leading to the synthesis process optimization. Polyimide nanocomposites are the leading component in the advancement of electric motors and generators insulating materials. But nanoparticles dispersion is the main concern to improve polymer nanocomposite dielectric properties. In this work, PI-based nanocomposite single and multi-layer films are synthesized and characterized in detail. The preparation of PI nanocomposite is a complex process with many variables involved; therefore, it is very important to know the right chemistry when dealing with it. Many methods were probed before an optimal synthesis process was found. A detailed synthesis process optimization is described at the end of this chapter to understand all variables, which can influence the dielectric properties of the final product.

## **2.2 Organic polymers**

The polymers are made up of long-chain repeating monomers; for example, polyethylene consists of ethylene as repeating units. Most of the polymers used in electrical engineering applications are made of long carbon chain repeating units, such as polytetrafluoroethylene (PTFE), polyvinyl chloride (PVC), polymethyl methacrylate (PMMA) and polyethylene (PE). The PE is further divided into low-density polyethylene (LDPE) and nonbranched high-density polyethylene (HDPE); both have excellent dielectric properties and very common to use in electrical cables insulation. Polymer dielectric films have shown high dielectric strength, low dielectric losses and excellent mechanical flexibility. Based on chemical groups, organic polymers are categorized into three main classes such as plastics, biopolymers and rubbers. Plastics can be further divided into thermoset and thermoplastic polymers based on their response towards the temperature [46]. Thermoset polymers are irreversible plastics and resin, which are cured of soft solid or solution, by applying heat. The strong bond and hard structure make such material suitable for high-temperature applications, while thermoplastic polymers become soft when the heat is applied and change to the fluid when extra heat is applied. The thermoplastic polymers are fully reversible due to weak cross-linking of chemical bonds. They can be remolded and recycled without altering their physical properties [47]. Electric and magnetic energy storage and dissipation in ceramics and polymer nanodielectrics were the most common topic for researchers in the last decade [48]. Fully cured PI is a thermoset polymer that cannot be reversible due to the structure of its fully closed and thermally stable monomers such as ODA, PMDA, ODPA. Epoxies are highly reactive thermoset polymers, which are cured by applying heat and using a hardener. LDPE and HDPE are thermoplastic polymers that can be reversible by applying heat above the melting point. Therefore, PE nanocomposite

materials can be self-healing, if such nanoparticles are well chosen, which can increase the internal temperature of material [49], [50].

## 2.3 Physical properties of polyimide

### 2.3.1 Polyimide

Polyimide is a high-temperature organic class of polymer which is mechanically tough, and thermally stable based on stiff aromatic backbones [51]. The main functional groups in PI structure are aromatic ring, amide and ether groups. There are several monomers and methods available to synthesize the polyimide; therefore, the mechanical strength and thermal stability of polyimide films can vary by using different available monomers. In order to obtain different mechanical and thermal strength, we used two dianhydrides (PMDA and ODPA) to react with diamine (ODA) to synthesize the PAA solution. A slight change in monomers structure and synthesis process can alter the dielectric properties of PI films significantly.

### 2.3.2 Chemical properties of polyimide

Polyimides are chemically closed structure polymers that are non-reactive to many chemicals, such as solvents and oils. Polyimides are intrinsically resistant to heat and flame-retardants. Polyimide is also resistive to acids but avoids using in alkalis and inorganic acid environment. Polyimide, such as CP1 and CORIN XLS, are soluble in the solvent and exhibit transparent and lightweight properties useful for materials in the glass and photovoltaic sheets [52]. The remarkable radiation resistant property of PI has made it an ideal material to use in outer space radiations environment and in nuclear reactors, where PI is used both alone and in composite forms.

### 2.3.3 Thermal properties

The changes in the dimension of material per 1 °C rise in temperature are called the thermal expansion coefficient. Polyimide exhibits higher values of thermal expansion coefficient than other polymers. Polyimides undergo numerous phase changes to 400 °C during the imidization process from poly amic acid solution to thin solid films. The thermal expansion coefficient for different materials is mentioned in Table 2.1.

Table 2.1 Thermal expansion coefficient

Material	Thermal expansion coefficient (ppm/°C)
Si, SiC	3
SiO <sub>2</sub>	4
Alumina	6
Gold	14

Copper	17
Aluminum	24
Polyimide	40-50

Polyimide is a thermally stable polymer with a very high value of  $T_g$  and only 5 % weight loss above 400 °C [51], [53], [54]. Therefore, it is a very suitable material for packaging applications [55]. Due to the availability of different monomers, the  $T_g$  of PI can vary depending on the type and structure of dianhydride used. For rigid and ordered PI, the  $T_g$  usually exists around 300 °C, but for those of interlayer dielectrics 400 °C or above  $T_g$  are preferred [56]. Polyimide has rubbery flow above  $T_g$  and if an external force is applied during rubbery flow, the film can be deformed; therefore, it is important to measure its mechanical strength [56], [57].

### 2.3.4 Mechanical strength

The stress-strain tests are used to assess the capacity of insulation material to withstand the mechanical strength limit. A deformity free material can prolong the equipment life. Polyimide films have higher mechanical strengths. The stress-strain results have shown that the flawless PI films have mechanical strength between 100-200 MPa and the elongation at break in between 10-25 % [58]–[60]. The mechanical vibrations in electric motors and metal conductor's contact in electronics packaging applications can cause serious damage to the mechanical strength of PI films [51]. If the films are brittle and the applied force due to mechanical vibrations crosses the fracture limit, then the internal cracks or defects can break the insulation [55]. The brittleness of PI films can be controlled during the synthesis process by using different monomers and imidization temperature and time [61]. During the thermal imidization process, when temperature starts exceeding 150 °C, the phase changes from poly amic acid ring to imide ring; if the first crack appeared in PI films during this process, then the final films will be brittle after completing the imidization process and elongation at break value would be less than 10% [55], [62]. The brittleness of PI films does not depend only on curing, but also depends on the molecular weight of PAA solution which can be controlled during the synthesis process. The ODA and PMDA based PI films have relatively less mechanical strength compared to ODA and ODPA based PI films.

### 2.3.5 Properties of polyimide in electrical engineering

#### 2.3.5.1 Conduction current

When a dielectric material is submitted to an electrical constraint, conduction current due to different polarization and depolarization process occurs inside the material. The complete polarization process can be presented as equation (2.1) and shown in Figure 2.1 [63].

$$i_p = i_i + i_a + i_c \quad (2.1)$$

Where  $i_i$  is the instantaneous current due to the displacement polarization,  $i_a$  represents the relaxation polarization current and  $i_c$  presents the conduction current due to the conductivity of the specimen. The Simons and Tam theory represents that the depolarization current is a superposition of different relaxation processes depending on the trap levels [64]. There are several polarizations due to dipole relaxation process may take place in a dielectric material. They are given as [65], [66]:

- 1) Electronic polarization.
- 2) Ionic polarization.
- 3) Orientation polarization.
- 4) Interfacial/space charge polarization.
- 5) Hopping polarization.

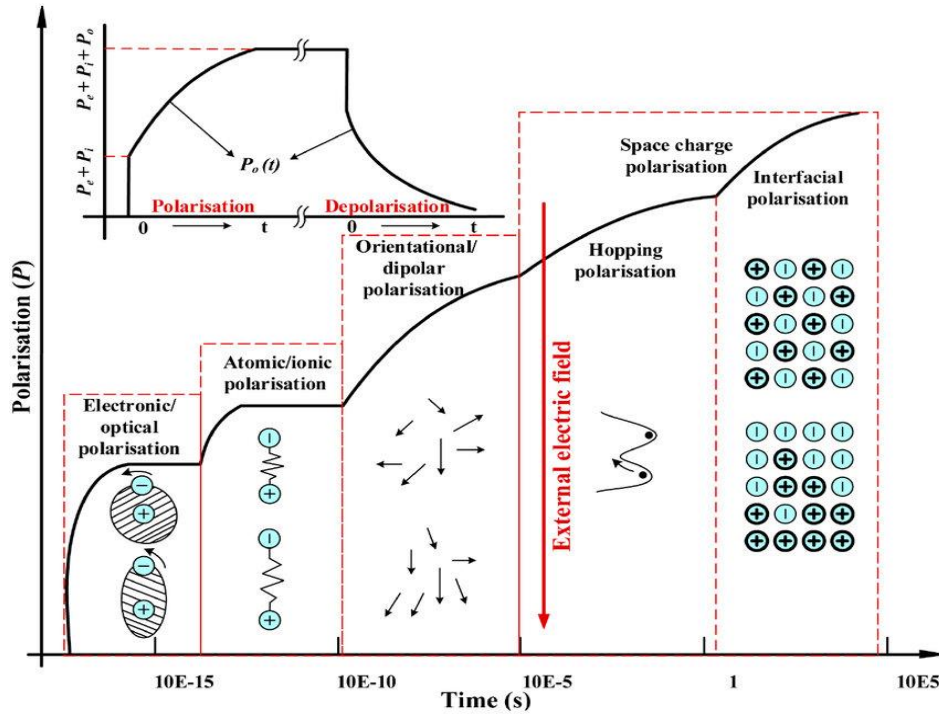


Figure 2.1 Several polarization mechanisms with varying electric field frequency [65]

### 2.3.5.2 Dielectric constant and dielectric loss

When an external electric field is applied to a dielectric material, it becomes polarized due to the movement of induced and permanent electric dipoles [55], [67]. For ideal insulation, the movement of dipoles should be zero or very low to block the conduction current. The value of dielectric constant ( $\epsilon'$ ) defines the polarization ability of dielectric material. The movement of dipoles in an alternating electric field causes the loss of energy known as a dielectric loss ( $\epsilon''$ ). The conduction loss and dielectric loss are two major losses that are responsible for energy loss



in a dielectric material. The movement of charges determines the conduction loss, while the movement of dipoles determines the dielectric loss; the movement of dipoles causes the energy dissipation as the polarization switches its direction in an alternating electric field. The polarization lags the alternate electric field to produce heat and dielectric loss increases at the relaxation frequencies. Therefore, the value of dielectric constant reduces quickly at relaxation frequencies because the polarization is not able to keep pace with the alternating electric field as illustrated in Figure 2.2. An efficient insulating dielectric material blocks the conduction with minimum energy dissipation. The materials with a higher value of dielectric constant normally have a higher dielectric loss. The energy loss in dielectrics can be used to heat up the food in a microwave oven. The orientational polarization in water frequency is utilized for this process, which is close to the relaxation or resonance frequency. It means water molecules absorb a lot of energy, which later dissipated to heat up the food. The dielectric constant of PI films varies from 3.0 to 3.8, according to the structure and composite fillers added into it [68], [69].

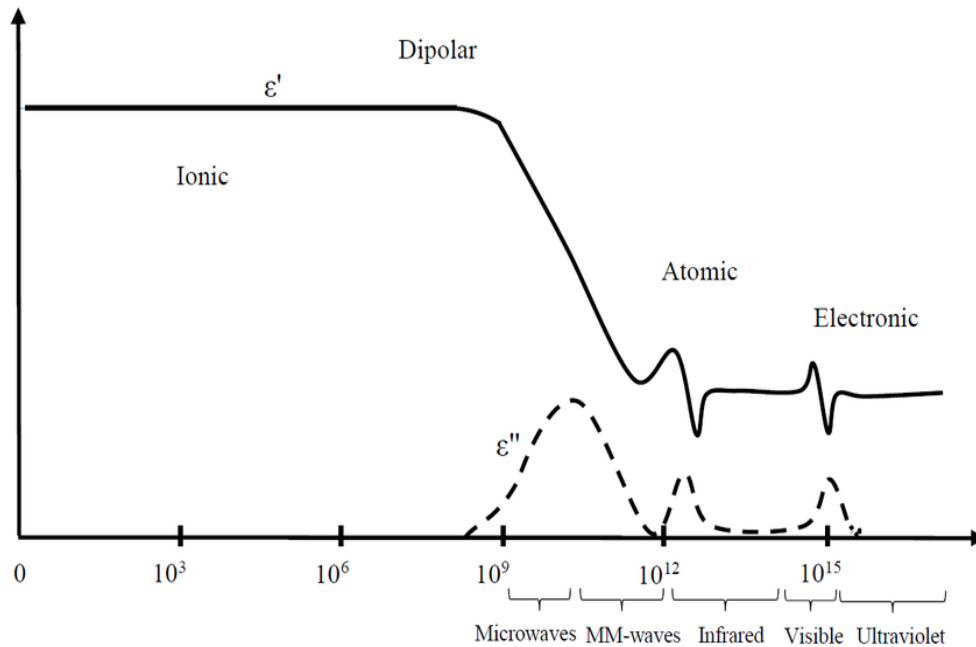


Figure 2.2 Dielectric loss vs frequency

The relative permittivity is composed of two parts: the real part denoted as  $\epsilon'$  and imaginary part denoted as  $\epsilon''$ . The ratio of these two values is defined as the dissipation factor and given as:

$$\tan \delta = \frac{\epsilon''}{\epsilon'} \quad (2.2)$$

Normally, PI films have dissipation loss in between 0.001-0.02 [53], [55], [69]. The low  $\tan \delta$  value indicates that PI loses less electrical energy. The low dielectric constant and low dielectric

loss make PI films suitable to use in electrical signal packaging applications to avoid signal interference.

### **2.3.5.3 Dielectric breakdown strength**

The breakdown strength is the ability of dielectric material to oppose electric field stresses without any insulation breakage or passing a certain amount of leakage current. The value of dielectric breakdown strength can be found as the applied voltage at which the electric breakdown occurred. The breakdown strength may vary by varying the temperature, moisture and defects inside the material. The PI films that we synthesized have breakdown strength between 150-260 kV/mm under DC electric field [70], [71]. Due to its high electrical breakdown strength and mechanically tough properties, PI insulation can be useful to utilize in a high voltage industry environment, where electrical instruments can produce strong electrical field and leakage current to damage the insulation. Dielectric strength can vary due to the following reasons:

- 1) Non-homogenous nature of sample thickness.
- 2) Decreases with the increase in temperature.
- 3) Decreases with an increase in frequency.
- 4) Decreases with an increase in humidity.

### **2.3.5.4 Charge transport phenomena**

The PI films can be amorphous or crystalline depending on their synthesis chemistry. In these regions, the band structure is responsible for the distribution of trap energy spectrum of electrons [72]. Trap levels generate due to the disorder change in the atomic structure under high electric field stress, which is common at the top and bottom surface of samples near electrodes. The density of such damage reduces towards the interior regions. In Figure 2.3, a thin PI sample is a sandwich between two electrodes. The layer near to anode can act as holes transport layer and layer near cathode can act as an electrons transport layer. The intersection region of these layers can provide enough space for the recombination of electrons and holes that are injected by electrons injection layer (EIL) and holes injection layer (HIL) respectively.

As illustrated in Figure 2.3, the injection of holes from HIL and injection of electrons from EIL move towards holes transport layer (HTL) and electrons transport layer (ETL) respectively. The charges are transported and attracted to opposite electrodes, and during the mobility some the charge trapping, de-trapping and recombination may happen in this interfacial region [70]. Some charges already exist due to defects present in this region. The interface area can be the same or opposite charge polarity junction compares to the nearest electrode depending on the electronic state of the interface. In the case of two layers PI structure, the electrons accumulate near the anode interface because the mobility of electrons is higher than holes

[35]. In the case of three layers structure, the same polarity charges accumulate in this region [35]. There can be three reasons for these phenomena. Firstly, distinctive charge barriers at the interface for electrons and holes influence the charge injection rate. Secondly, the differences between holes and electrons carrier mobility of PI and nanocomposite give rise to the accumulation of charges at interfaces. Finally, the presence of interface charge polarity further restricts or recombines charge carriers transport. Due to permittivity/conductivity difference at interface and bond linkage between different composite layers, electronic states at interface changes from the rest of the bulk material. Therefore, the discontinuity of electronic state distribution causes an additive trap at the interface for the transportation of charge.

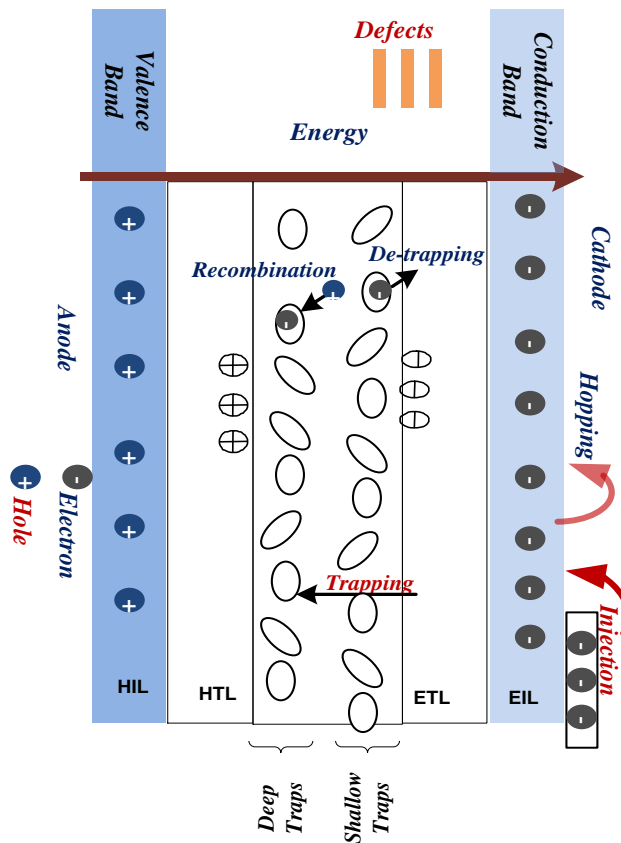


Figure 2.3 Layers structure, holes injection layer (HIL), holes transport layer (HTL), electrons transport layer (ETL), electrons injection layer (EIL)

#### 2.3.5.5 Corona discharge resistance and material degradation

The ionization of air in the form of electrical discharge is known as corona discharge. This ionization occurs when the electric field crosses the threshold value of air breakdown. Partial or surface discharge is also a kind of corona discharge, because it is half discharged to bridge between the electrodes [72], [73]. Corona discharge appears in the form of a lightning color. In high voltage laboratory, corona discharge can be originated using a simple rod to plane

electrodes with an air gap between them. Extensive research work has been studied on the appropriate electric field stress to set up corona discharge [74]. Corona discharge depends on the following parameters:

1. Air or gas Ionization limit and free path for gas molecules.
2. Electrodes geometry and surface conditions.
3. Distance between the electrodes.
4. Insulation structure design flaws.

Corona discharges can damage the insulation significantly. With the growing demand for high voltage power supplies, it is becoming common that the insulating materials face severe corona discharges. Corona discharge produces eminently energized plasma of charged species and emits UV light. These plasma discharges emit charged particles on the surface of the insulation and deteriorate the surface physically and chemically. The increase in temperature and humidity can accelerate the corona discharge intensity.

#### **2.4 Physical properties of nanodielectric based polyimide in high voltage engineering**

For the last decade, the research has shown that when two materials in which one part is inorganic nanoparticles are combined to form a nanodielectric material, this new material may have superior properties than single ones. If one is polymer matrix and the other is a nanometer-sized particle, it is known as a polymer nanocomposite. Polymer nanocomposites have been used widely in academic research and industry [56]. The properties of nanocomposites change due to the large surface to volume ratio of the nanoparticles. The addition of nanoparticles into the host polymer matrix modifies the physical properties of composites. If the size of the nanoparticles is less than the critical length scale, then the physics of nanocomposite changes significantly. It has become one of the most reliable materials in electrical engineering since the first time the term nanocomposite was introduced in 1984 and since then it has been warmly accepted by the scientific community [36]. “Nanometric dielectrics”, later named “Nanodielectrics” in 2004 by M. F. Frechette, is a nowadays popular term in the research community, also known as nanocomposites made by the inclusion of nanometer size nanoparticles in a polymeric matrix for dielectric applications [36], [65]. In the beginning, the glass and ceramics were very common to use as solid dielectrics materials. But, over time the power supplies demand increased abruptly and these insulating materials were not enough to fulfill the demand. Therefore, new dielectric materials such as natural and synthetic polymers successfully overcome conventional dielectric materials. These new polymers based dielectric materials have superior properties and lighter in weight to use in different applications [38], [43].

### 2.4.1 Inorganic filling particles

Fillers are often fine-grained nanometer or micrometer size particles and fibers, which can be made of organic or inorganic materials. Generally, such particles and fibers are named as conventional sized fillers according to their size range [75], [76]. Composites formed by using these fillers are labeled as conventional size filled composites, for example, nanocomposites and micro composites [75], [77]. Recently, filler materials have been used to improve electrical, mechanical strength and thermal properties [78]. Polymers are chosen in electrical engineering according to the required application and their properties can be modified by adding inorganic fillers in it [78]. The quantity of fillers in the host polymer matrix is still under question from the literature that which amount by weight is most suitable to improve the desired properties [79]. Therefore, in this work, we only use very low quantity of nanoparticles into the base polyimide.

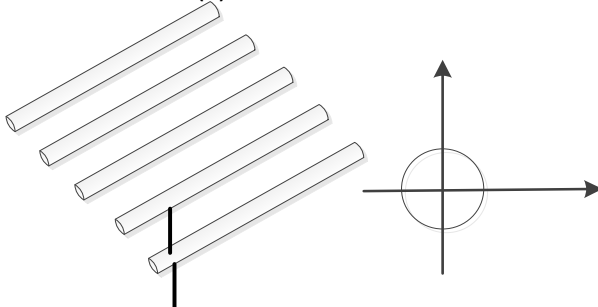
### 2.4.2 Particles size shape and types

Various results of electrical, mechanical and thermal properties have announced that the polymeric nanocomposites can be invaluable, when a small number of nano-size particles are appropriately chosen and dispersed into the base polymer matrix [80]. Composite material properties change dramatically due to the size, shape and type of nanoscale particles. These nanoparticles have individual mechanical, electrical and thermal properties [62], [81]. Based on the size of particles, nanomaterial can be categorized as:

- 1) Zero-dimensional (0-D).
- 2) One-dimensional (1-D).
- 3) Two-dimensional (2-D).
- 4) Three-dimensional (3-D).

1-D

Two dimensions (x, y) at nanoscale,  
other dimension (L) is not

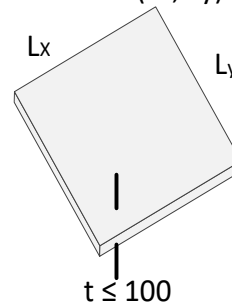


Nanowires, nanorods and nanotubes

(a)

2-D

One dimensions (t) at nanoscale, other  
two dimensions (Lx, Ly) are not

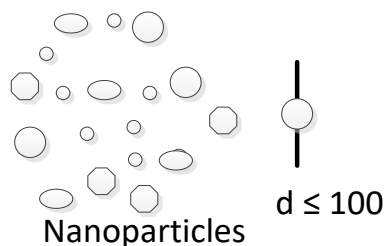


Nanocoatings and nanofilms

(b)

0-D

All dimensions (x, y, z) at nanoscale



Nanoparticles

(c)

Figure 2.4 Fillers types, sizes and shapes

If the number of the dimensions (ND) that are in the nano-range is considered, exfoliated clay will be regarded as 1ND nanofiller, since the thickness of an exfoliated layer is around 1 nm. In order to utilize the ceramic nanoparticles in a better way with polymers, a potential study has been done recently, especially in the field of the synthesis process and surface science. The most common studied ceramic nanoparticles are silica (silicon dioxide -  $\text{SiO}_2$ ), alumina ( $\text{Al}_2\text{O}_3$ ), titania ( $\text{TiO}_2$ ), zirconia ( $\text{ZnO}$ ), or silicon carbide ( $\text{SiC}$ ).

Table 2.2 Organic, inorganic fillers and their chemical family

Chemical family	Examples
<b>Inorganics</b>	
Oxides	$\text{Al}_2\text{O}_3$ , $\text{SiO}_2$ , $\text{MgO}$ , $\text{ZnO}$ , $\text{TiO}_2$ , glass
Hydroxides	$\text{Al}(\text{OH})_3$ , $\text{Mg}(\text{OH})_2$
Silicates	Talc, mica, nano clays, asbestos
Salts, compounds	$\text{CaCO}_3$ , $\text{BaSO}_4$ , $\text{CaSO}_4$ , $\text{BaTiO}_3$ , $\text{SrTiO}_3$
Metals	Al, Ag, Sn, Au, Cu
Nitrides, carbides	$\text{AlN}$ , $\text{BN}$ , $\text{Si}_3\text{N}_4$ , $\text{SiC}$
<b>Organics</b>	
Carbon	Carbon fibers, carbon black, graphite fibers, carbon nanotubes
Natural polymers	Cellulose fibers, wood flour, flax
Synthetic polymers	Polyimide, polyester, polyethylene, polypropylene

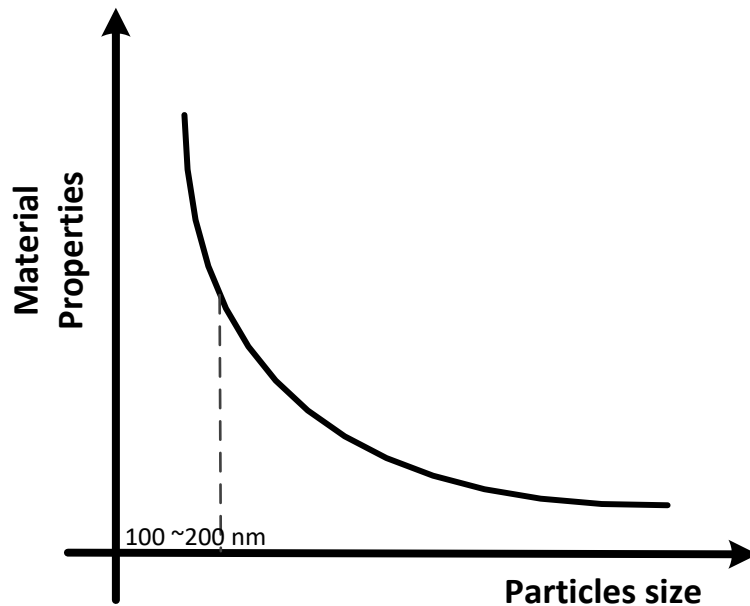


Figure 2.5 Change in composite material properties w.r.t (define w, r and t) particles size

#### 2.4.3 Nanoparticles dispersion and distribution

The homogenous dispersion and distribution of nanoparticles is the major factor to improve nanocomposite dielectric material properties. A vital part of preparing nanocomposites is the nanoparticles dispersion. They have heterogeneous surfaces, which cause variability in contact with the PI matrix. For better dispersion, several methods have been used, such as the orientation of nanoparticles by applying an electric field, chemical treatment by using coupling agents and plasma treatment [81]–[83]. All these methods are adopted to solve the problems of heterogeneous agglomeration and the compatibility between the PI matrix and the nanoparticles. The nanoparticles mixing techniques, such as mechanical milling, ultrasonication, high-speed stirrer, liquid dissolving or heat melting, can also affect the nanoparticles dispersion level. The size of particles and filler loading percentage can also influence the dispersion level [14]. Particles smaller than 80 nm tend to agglomerate and form more significant chunks of particles. The intermolecular forces keep nanoparticles together. The following particles parameters can influence the overall properties of polymer composites:

- 1) The size and shape of particles.
- 2) The degree of particles dispersion.
- 3) The surface modification of the particles.
- 4) The particles-matrix interaction.

#### **2.4.4 Nanoparticles surface treatment**

The interlinking of the PI and the nanoparticles depends on the functional groups and the surface energy of PI and nanoparticles. Some hydroxyl (OH) functional groups can be formed on nanoparticles after surface modification, which provide a better interface and tightly bound with the PI matrix. To modify nanoparticles surface, different methods have been presented in recent papers, such as modify by deposition reactions, modify by chemical surface treatment, high energy such as plasma source modification and intercalation modification [58]. Affinity and polarity compatibility can also be used to create materials with homogenous dispersion of nanoparticles. For better interlink between the silica nanoparticles and PI matrix, the surface of polar silica nanoparticles is modified using the KH550 coupling agent. Silica nanoparticles are hydrophilic and PI is nonpolar, which is not compatible with mixing. Therefore, the surface of the silica is modified to make it hydrophobic with hydroxyl (OH) functional groups on its surface, which are easy to bond with aromatic PI functional groups [34], [35]. This surface modification is adopted to ensure success in the application. The interphase region around nanoparticles can be controlled using surface treatment [84].

##### **2.4.4.1 Coupling agents**

KH-550 silane coupling agent chemically, known as 3-(2,3-epoxypropoxy) propyl trimethoxy silane, is selected for silica nanoparticles surface modification. It contains an organic functional group, a linker, a silicon and a hydroxyl group. The organic functional group can bond to the organic aromatic polyimide ring. The general chemical formula for the silane group and the hydrolyzable functional group, typically alkoxy, amine, or chlorine, involved in the reaction with the inorganic silica substrate. The silanol groups of the nano-silica surface can react with the hydroxyl groups of the silane after hydroxylation through hydrogen bonding. The covalent bond improves interfacial adhesion between inorganic silica particles and organic monomer molecules.

##### **2.4.4.2 Plasma treatment**

Non-thermal plasma technique is also prevalent these days to modify the surface of nanoparticles. This plasma technique enhances the compatibility between nanoparticles and polymer by modifying the interfacial area of nanoparticles. The plasma is produced by using a dielectric barrier discharge, which generates ions and reactive high-energy electrons that interact with the surface of nanoparticles to modify their surface characteristics [66], [85], [86]. Therefore, higher surface reactivity and stronger interactions between the nanoparticles and the surrounding polymers can be acquired, compared with traditional coupling agent modification.



## 2.4.5 Polymer nanocomposite materials

When two materials are combined, in which one is polymer matrix and the other is nanometer-sized particles, the new material is known as a polymer nanocomposite. Polymers have been widely used with the nanoparticles to form nanocomposite materials over the past few decades [87], [88]. Polymer nanocomposites have a wide range of applications in academic research and industry [56]. The nanocomposites have extraordinary properties due to a bigger surface to volume ratio of the nanoparticles [89]. The addition of nanoparticles into the host polymer matrix modifies the physical properties of composites. These physical properties have a critical length scale, and if the size of a nanoparticle is lower than that critical length, then the physics of nanocomposite changes significantly.

## 2.5 Synthesis of polyimide

When one monomer reacts with other monomers, it forms a carbon chain of the polymer. In the case of polyimide, the monomers such as diamine (ODA) react with another monomer, such as dianhydride (PMDA) form poly amic acid solution (PAA). The synthesis process of the PAA solution is shown in Figure 2.6. In this reaction, an oxygen atom of diamine reacts with the hydrogen atom of dianhydride and the hydrogen of dianhydride reacts with the carbon of diamine to give a repeated unit of poly amic acid. To obtain PI film, thermal heat is applied for several hours to evaporate DMAC solvent. The chemistry and the properties of PI can vary due to the availability of several monomers. The ratio of monomers can affect the molecular weight of PAA and change the molar mass of the final PI film [61], [90].

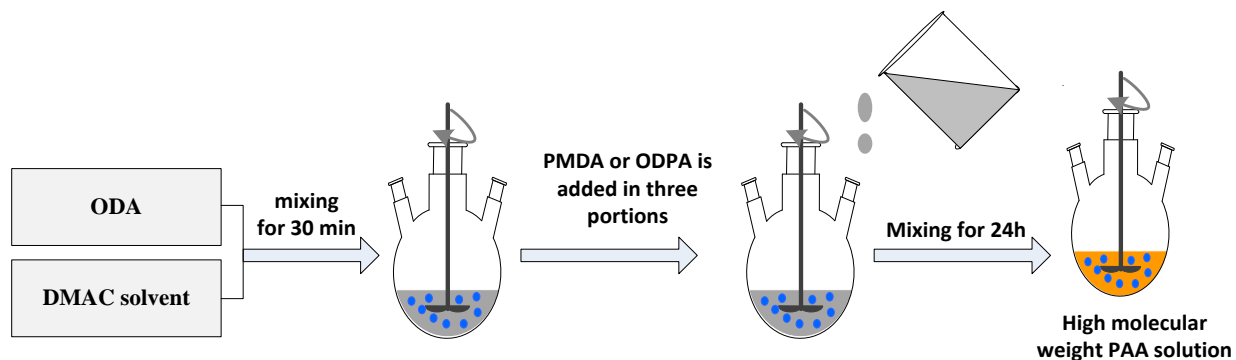


Figure 2.6 Synthesis process of PAA solution

### 2.5.1 Preparation mechanism for poly amic acid (PAA)

The aromatic PI film can only be synthesized from the solvent route using a two-steps method. The reaction between dianhydride (pyromellitic dianhydride PMDA) and diamine (4,4'-oxydianiline ODA) at room temperature in dipolar aprotic solvents, such as N-methyl pyrrolidone (NMP) or N, N-dimethylacetamide (DMAC) to synthesize PAA, which later converted into the final PI films after evaporating solvent, as explained in Figure 2.7. To make

sure that PMDA did not absorb any moisture, it was heated for 2 hours at 150 °C. ODA was added into the beaker and mixed with DMAC for half an hour, the mechanical stirrer was used to stir the solution, then PMDA was added into the solution in three parts. The solution was further stirred for 24 hours to get yellow color high molecular weight PAA solution, as shown in Figure 2.7.

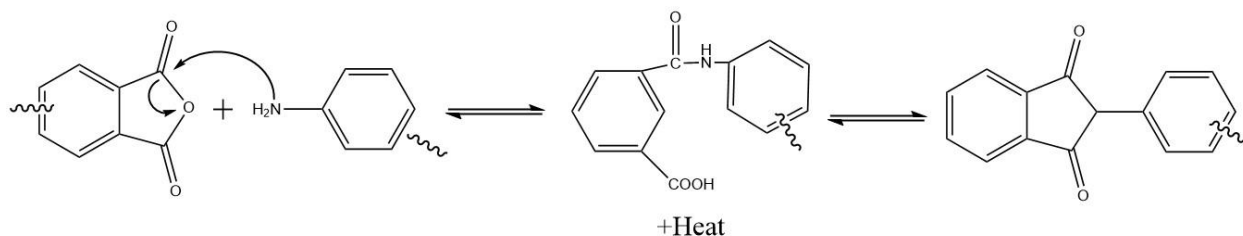


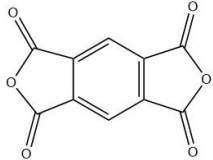
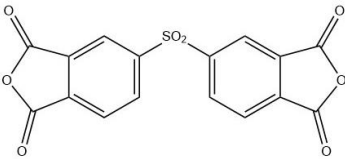
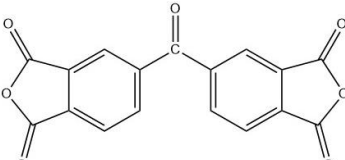
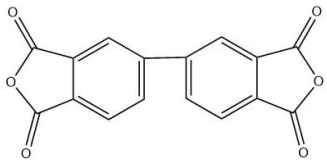
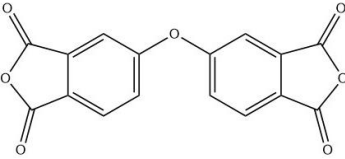
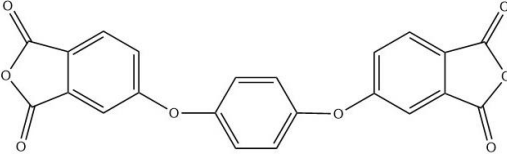
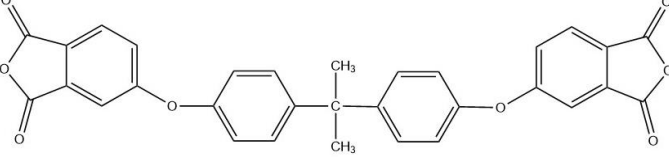
Figure 2.7 Generalized reaction mechanism of aromatic imide formation

The reaction between monomers to obtain viscous PAA solution is strongly dependent on the precise measurements. The following discussion will highlight important factors to select the monomers, solvents and reaction conditions to get better results and avoid side reactions. The formation of the PAA solution may also involve some reversible reaction, which leads to the opening of the anhydride ring. Despite that, the forward rate of reaction is larger than the reverse rate depending on the purity of reagents. The molecular weight of the PAA product is also relying on the rate of difference between the forward and reverse reactions. Reverse reaction provokes when carboxyl group strikes to the adjacent poly acid group. Some reagents can be used to stop the reverse reaction and provokes a forward reaction. The amino group basicity and PMDA electrophilicity in different solvents can change the equilibrium constant and the reaction takes place is exothermic, therefore it should carry out at room temperature to minimize the equilibrium constant effect.

### 2.5.2 Monomers reactivity conditions

As explained in the above section, the PAA solution is formed by nucleophilic substitution of the carbonyl carbon atom of the dianhydride with a diamine. Therefore, electrophilicity of carbonyl group carbon atom and nucleophilicity of amino group nitrogen atom can be controlled using electron affinity measurement of both dianhydride and diamine [61]. PMDA has the highest electron affinity, as illustrated in Table 2.3 that shows strong reactivity with diamines compares with other dianhydrides such as DSDA, BTDA, BPDA and ODPA. The change in the structure of the diamines and dianhydride can affect the reaction significantly. These highest electron affinity dianhydrides can easily absorb moisture; therefore, they must keep a moisture-free environment.

Table 2.3 Electron affinity of different dianhydrides

Dianhydride structure	Name	Electron affinity (eV)
	PMDA	1.90
	DSDA	1.57
	BTDA	1.55
	BPDA	1.38
	ODPA	1.30
	HQDA	1.19
	BPADA	1.12

### **2.5.3 Synthesis of PAA/nanoparticles composite solution**

The PAA/SiO<sub>2</sub> nanocomposite solution was synthesized by applying the in-situ polymerization method, as elaborated in Figure 2.9. For the better link between PI and nanoparticles, SiO<sub>2</sub> was treated with a KH-550 coupling agent to modify its surface. Altered surface SiO<sub>2</sub> nanoparticles and dimethylacetamide (DMAC) were dispersed by applying ultrasonication and high-speed stirring, then Oxy dianiline (ODA) was added into the solution and mixed for 1 hour. After that, Pyromellitic dianhydride (PMDA) was added into two portions. For the first portion, almost 90% PMDA was added and mixed for 30 minutes, then the remaining 10% PMDA was added and mixed for 2-6 hours until yellowish color high molecular weight PAA solution was obtained.

### **2.5.4 PI film casting**

Higher molecular weight poly amic acid solution dissolved in dimethylacetamide based solvent is suitable for PI film casting using multiple substrates and metal surfaces such as Teflon, alumina, glass, silicon wafers, brass and copper. After coating the PAA solution on the substrate, the precursor is thermally cured into aromatic polyimide film.

#### **2.5.4.1 Casting PI films using glass and brass substrate**

Both static and dynamic casting techniques can be used depending on the final product size and available tooling. In static casting, glass was used as a substrate to cast the PAA solution on it using a glass rod. Typically, this technique is easy but it requires more material per substrate and difficult to control the thickness of PI films.

#### **2.5.4.2 Casting PI films using a spin coating technique**

Spin coating is the most common dynamic technique to deposit PAA solution onto substrates, such as silicon wafers and brass. The dynamic deposition technique uses less material, but it requires precision to control the operation. Another important thing to assure that the solution is poured in the center of the wafer. Typically, a PAA solution is dispensed on the surface of the substrate, followed by rapidly spinning on a vacuum chuck at high speeds up to 6,000 rpm. The solution is evenly distributed over the surface during spinning. Acceleration to final spin speed should be as slow as possible to allow the coating to flow across the substrate. Often one or more intermediate spin speeds steps can be used to allow the solution to gradually cover more than 80% of the substrate before continuing on to the final speed.

### **2.5.5 Controlling the thickness**

The thickness of the casted PI film depends on several factors, such as the viscosity, molecular weight of the PAA solution and the spin speed of spin coater. Varying PI film thickness in the range of 10 μm to 150 μm can be achieved by using a spin coating method. Two different viscosity solutions of PAA are used to obtain PI films, as shown in Figure 2.8. The film

thickness decreases with increasing spin rate. To avoid the bubbles and the accumulation of excessive blocks of PAA solution, spin cycle time should increase because prolonger spin times improve film coating uniformity but, at the same time, it can reduce the film thickness.

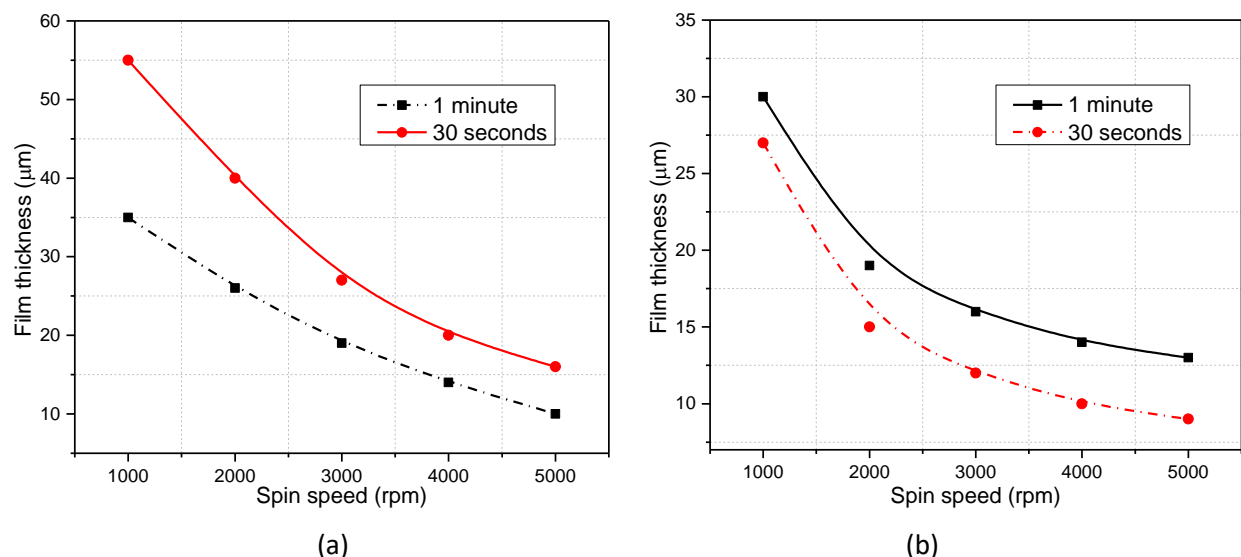


Figure 2.8 Film thickness variation at different spin coater speed (a) PAA solution high molecular weight (b) PAA solution slight less molecular weight

### 2.5.6 Casting PI and nanocomposite/PI multi-layer films

In order to cast the PI based nanocomposite multi-layer films, two different spin speeds were used for the two-layer structure. After calibrating the right speed to get right thickness, we select 20 seconds at speed of 500 rpm to get around 60  $\mu\text{m}$  thick first base layer of PI film and soft bake for 30 minutes at 60 and 100  $^{\circ}\text{C}$  temperature, then we use 30 seconds of 1000 rpm to get second PI based nanocomposite 20  $\mu\text{m}$  thick layer.

### 2.5.7 Thermal imidization of a poly amic acid (PAA)

The PI films can be cured of the PAA solution after applying thermal imidization. After casting the PAA solution onto the substrate, thermal steps with temperature from 100  $^{\circ}\text{C}$  to 350  $^{\circ}\text{C}$  were used to evaporate the solvents. According to the literature, various thermal steps and different temperature range have been utilized to achieve 100% imidization from PAA to PI. Two mains thermal imidization ways are as follows:

1. Baking films with slowly increasing in temperature up to 350  $^{\circ}\text{C}$ , according to the flexibility and  $T_g$  of the PI film.
2. Start baking PAA with the temperature 100  $^{\circ}\text{C}$  for one hour, then baking at 200  $^{\circ}\text{C}$  for one hour, then baking at 300  $^{\circ}\text{C}$  and keeping for one hour and slowly cool down to room temperature.

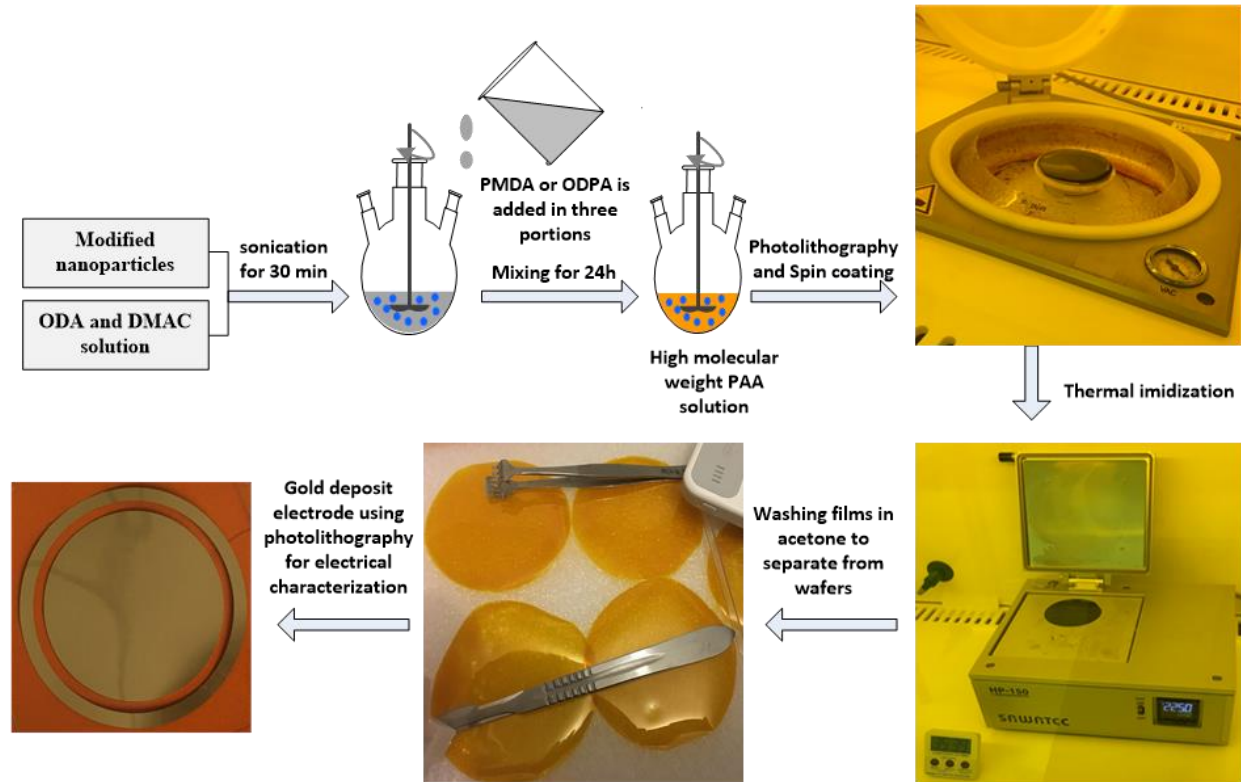


Figure 2.9 Polyimide films synthesis process

Several arduous factors are involved in the above simple-looking thermal imidization process to predispose the degree of imidization of PI films. During imidization, the remaining solvent at the later stages determines the stability of PI films. In early stages, the imidization process is faster and several dynamic changing in physical properties happen due to the basicity of the amide solvent to accept protons and the amicable conformation of the amic acid to increase the mobility of the reacting functional groups [90]. At later stages, the rate of imidization slows down due to the decyclohydration of the open amic acid group into the closed imide ring, which decreases the chain mobility and the  $T_g$  approaches the reaction temperature.

## 2.6 Synthesis process optimization

### 2.6.1 Factors involved in the molecular weight of PAA

The following factors are involved to increase or decrease the molecular weight of PAA:

- 1) A slight increase of dianhydride quantity and the addition of solid dianhydride into the diamine solution can increase the molecular weight of PAA.
- 2) The order and the mode of the monomer addition; the solid mode of dianhydride addition into diamine solution can avoid an immediate reaction and minimize the side reactions with water and impurities.

- 3) Minimize the side reactions to avoid dianhydride reaction with water and impurities.
- 4) Lesser quantity of solvent will help to reduce the impurities and water contents, and increase the concentration of the monomer.
- 5) Storage of PAA solution for a long time can decrease the molecular weight; it can be due to the initiative of hydrolysis process and chemical breakdown of a compound. The other reason for this low viscosity can be the reverse reaction.
- 6) The solvents can also slightly affect the molecular weight. The universal dipolar aprotic amide solvents are DMF, DMAC, and NMP. The reaction is exothermic in which monomers for the reaction are basic aromatic amines and protic anhydrides, and the final product is an acid. Therefore, the strong rate of the reaction is expected for more basic and more polar solvents.

### 2.6.2 Determination of the degree of imidization

Fourier Transform Infrared spectroscopy (FTIR) is used to determine the degree of imidization. The major chemical bonds are imide group near  $1780\text{ cm}^{-1}$  (C=O asymmetrical stretching),  $1380\text{ cm}^{-1}$  (C-N stretching) and  $725\text{ cm}^{-1}$  (C=O bending). The carboxylic band of PAA at  $1700\text{ cm}^{-1}$  (C=O) also overlaps at  $1720\text{ cm}^{-1}$  (C=O symmetrical stretching). The bands at  $1780\text{ cm}^{-1}$  and  $725\text{ cm}^{-1}$  imide bands are also possible with the absorption of anhydrides occurring at  $1780\text{ cm}^{-1}$  and  $720\text{ cm}^{-1}$ . The peaks at  $2800\text{--}3200\text{ cm}^{-1}$  (OH) and amide bands at  $1660\text{ cm}^{-1}$  (C=O),  $1550\text{ cm}^{-1}$  (CNH) and  $3200\text{--}3300\text{ cm}^{-1}$  (N-H) are important for qualitative assessment during imidization process.

### 2.6.3 Changes in the mechanical strength during thermal imidization

Some changes in the mechanical strength appear as the PAA solution is converted to the PI film during imidization. The flexibility in the PI film mainly depends on the molecular weight of the PAA solution during monomers reaction. If the viscosity of the PAA solution is less than 0.2, then the PI films obtained are brittle. PAA solution with the viscosities in the range of 0.2-1.0 produced tough and creasable PI films, that became brittle between  $150\text{ }^{\circ}\text{C}$  and  $200\text{ }^{\circ}\text{C}$ . PAA solution with the viscosity above 1.0 remained tough and flexible over  $300\text{ }^{\circ}\text{C}$ . These variations in the mechanical strength are mainly due to the variations in the molecular weight and the changes in the molecular weight is due to the amic acid groups, that regenerate anhydride and amine at temperatures around  $150\text{ }^{\circ}\text{C}$ . As the temperature increases, the bonds break and the molecular weight is reduced.

### 2.6.4 Crystallinity and the glass transition temperature

The glass transition temperature of PI films mainly depends upon the chemical structure of the monomers used and several factors are involved in determining the  $T_g$  of the final polyimide. The chain stiffness is the main parameter to influence the  $T_g$ . Other factors such as

isomeric attachments of the flexible/rigid groups and the presence of the side groups can also affect the chain-chain interactions. The crystallinity and molecular weight of the PAA solution can also influence the T<sub>g</sub> [91]. Another feature related to the ability of the PI to crystallize is the nature of the dianhydride and the availability of different monomers to synthesize the PI films provides a wide range of T<sub>g</sub>. For most polyimides, using common dianhydrides, the ability to crystallize often goes with BTDA>PMDA>BPDA~ODPA.

### **2.6.5 Avoid side reactions**

During PAA solution synthesis, multiple side reactions can occur, which can lead to unwanted side products and affect the molecular weight. Therefore, it is very important to avoid such type of side reactions. Avoid the reverse reaction from PAA to the dianhydride and the diamine. Another important side reaction may take place is the reaction of dianhydride with water. Impurities in the solvent can also have a destructive effect on the main chain synthesis reaction. The moisture absorbed by monomers as an impurity is not the only source of water before reactions; during thermal imidization of PAA solution to PI films at ambient temperature, some water may absorb from atmosphere as a side product due to reactions occurring at ambient conditions, if poly(amic acid) is left at these conditions for a long time. A slight increase in the dianhydride quantity, that sometimes has to be used to give high molecular weight products, can also initiate some side reactions. This is more likely to happen when the highest electron affinity dianhydrides, such as PMDA, are used because it is strongly dehydrating agents and can easily absorb moisture. The slight increase in dianhydride may attack the amic acid group leading to the formation of a diacid and an imide. The ortho-dicarboxylic acid group, which remains as a chain end group, limits the molecular weight of the PAA solution.

## **2.7 Summary**

A brief introduction of the physical properties of polyimide films and the nanoparticles, including the single and multilayer PI/nanocomposite films synthesis process optimization, is described in this chapter. The synthesis of PI based nanocomposite is a complex process with many variables are involved. Several methods were probed before an optimal synthesis process was found. A detailed synthesis process to prepare PI and PI/nanocomposite and synthesis process optimization of multi-layer PI based nanocomposites films is described in this chapter to understand all variables, which can influence the dielectric properties of the final product. Several factors in the synthesis process, which can influence the molecular weight of the PAA solution and the quality of the PI films, are discussed in detail. To control the thickness of the single and multilayer films, spin coating method is adopted and compared with glass substrate mechanical spreading method.





## Chapter-3

---

Experimental techniques and methodology

**Chapter 3 Experimental techniques and methodology**

3.1 Introduction .....	43
3.2 General description of samples .....	43
3.3 Microscopy morphology characterization .....	44
3.3.1 Scanning electron microscopy (SEM) .....	44
3.3.2 Transmission electron microscopy (TEM) .....	45
3.4 Fourier transform infrared spectroscopy .....	46
3.5 Dielectric spectroscopy characterization .....	47
3.6 Corona resistance property tests under PWM waveform .....	48
3.6.1 Lifetime and electrical breakdown tests under corona discharge .....	48
3.6.2 PD and surface discharge test setup .....	49
3.7 Conduction currents .....	50
3.8 Thermal and mechanical characterization .....	56
3.8.1 Rheological test using dynamic mechanical analyzer (DMA) .....	56
3.8.2 Thermal diffusivity test .....	58
3.9 Space charges measurement setups .....	59
3.9.1 Thermal step method (TSM) .....	59
3.9.2 Pulse electro acoustic method (PEA) .....	62
3.10 Thermal stimulated current (TSC) .....	63
3.11 Summary .....	65

### 3.1 Introduction

This chapter describes the diagnostic techniques to characterize the synthesized single and multilayer PI nanocomposite samples. The physical properties were carried out using SEM and TEM microscopic facilities available in the MEA laboratory of UM. FTIR tests were performed in the ICGM laboratory of UM, to characterize the chemical bonds and functional groups present in PI. Furthermore, the dielectric and thermal properties were carried in a high voltage laboratory (IES-GEM) of UM. The sample description and all experimental testing details are explained in this chapter.

### 3.2 General description of samples

The materials to fabricate samples were mainly bought from two companies. Bis(4-aminophenyl) ether 98% purity 500 gram product number (AL-A16815-500G), pyromellitic dianhydride 97% purity 500 gram product number (AL-A12712-500G), silicon(IV) oxide, amorphous, nano-powder 80 nm size 99.9% (metals basis) 25 gram product number (AL-44781-25G) were bought from Alfa-Aesar chemicals company and 3-AMINOPROPYLTRIETHOXYSILANE 99% PURITY 100ML product number (SI-440140-100ML) were bought from Sigma-Aldrich company. The achievement of desired results and the performance of nanocomposite are not only dependent on the nature of the material we used but also depend on the samples synthesis process, nanoparticles dispersion and characterization techniques. Polyimide nanocomposite is thin nanofilms, which have complex chemical synthesis process to achieve 100 microns or thicker samples. The schematic diagram of sample composition is shown in Figure 3.1 and its final composition is shown in Figure 3.2.

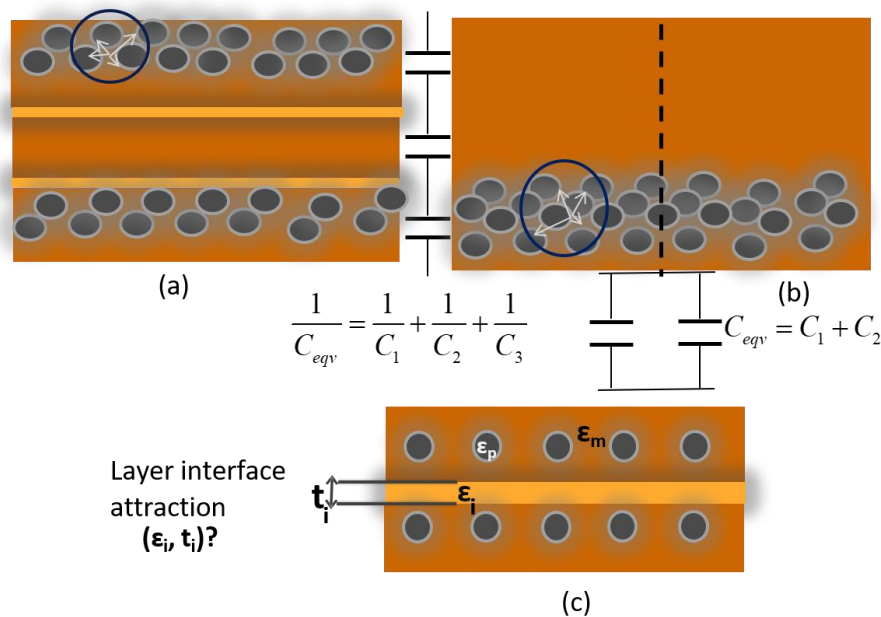


Figure 3.1 (a) Three-layer sample with less chance of nanoparticles agglomeration  
(b) Single-layer PI film with a higher chance of nanoparticles agglomeration

PI is obtained using the curing method in which the solvent is evaporated with the increase of temperature. During the PI film curing process from polyamic acid (PAA) solution, there is a strong tendency of nanoparticles to get agglomerated [53], [54], [69]. They may float on the surface or decant, as presented in Figure 3.1(b). Both effects can increase the chances of agglomeration and may influence the interface thickness and permittivity of samples, as shown in Figure 3.1(c), and result in lower electrical, mechanical and thermal properties of PI films. Keeping this in mind, we prepared a two-layer insulating material structure in which the top consists of a very thin PI/nanoparticle (NPI) layer and the bottom is composed of pure PI layer [32]. By doing this, we are giving less space for nanoparticles to get agglomerated, as shown in Figure 3.1(a).

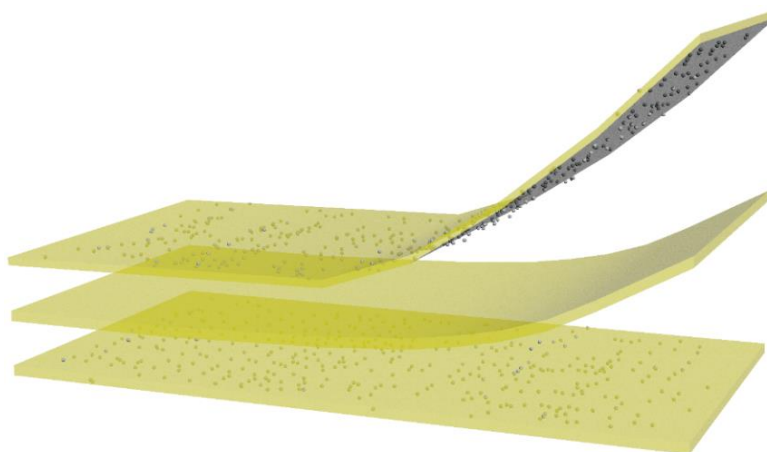


Figure 3.2 Final composition of PI/SiO<sub>2</sub>-PI-PI/SiO<sub>2</sub> three-layer structure

### 3.3 Microscopy morphology characterization

In order to investigate the nanoparticles dispersion and surface nature of nanocomposite samples, SEM and TEM microscopy were performed. The sample internal microscopic morphology was characterized by TEM, while the sample's surface composition and cross-section view were characterized by SEM. TEM can be operated in high-resolution mode in the range of 1 nm with the holography, morphology and crystallization information of the samples. The EDS can be performed in SEM to obtain the chemical bond energy differences.

#### 3.3.1 Scanning electron microscopy (SEM)

JEOL JSM 6460 and FEI inspect S50 SEM at CTM-IES of UM, as shown in Figure 3.3, were used to scan PI and multi-layer PI/SiO<sub>2</sub> samples. Scattered secondary electrons are used in SEM for surface topography and composition of samples. The electron beam scans the surface and overcomes the surface barrier energy of samples between 5 eV to 50 eV. In SEM, the sample is coated with conductive material or pasted on conductive metals, such as gold and aluminum. SEM can also provide surface roughness information of aged samples. The surface area ranging from 1 cm to 5  $\mu\text{m}$  can be imaged in a scanning mode of SEM with amplification from 20X to

30,000X, and spatial resolution of 50 to 100 nm. The surface topography of the PI/SiO<sub>2</sub> sample is shown in Figure 3.4 [92].



Figure 3.3 FEI inspect S50 Scanning electron microscope

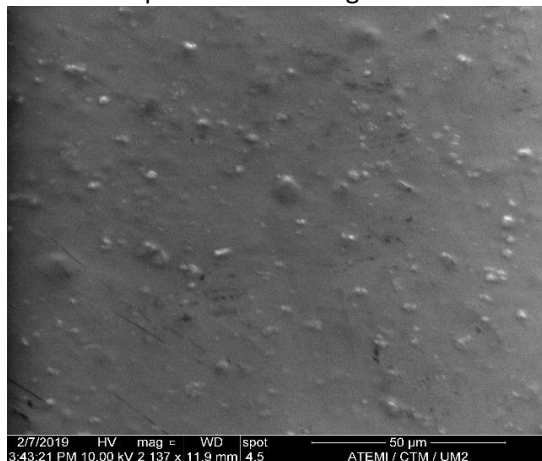


Figure 3.4 SEM image of surface topography of PI/SiO<sub>2</sub>

### 3.3.2 Transmission electron microscopy (TEM)

The nanoparticles dispersion level for single PI/SiO<sub>2</sub> and multilayer PI-PI/SiO<sub>2</sub> was analyzed by transmission electron microscope (TEM) at the MEA laboratory of UM. In TEM, electrons are transmitted using a filament. These electrons are transmitted with the voltage range of 60-120 kV. Some electrons interact with the atoms of the subjected area, while others cross the area without any interaction. Most electrons reach the target lens which magnifies the image that is projected through other lenses and gives us information about the sample, such as crystallization or internal morphology [93], [94]. The information of the thin section of the PI

sample filled with 80 nm size of silica nanoparticles was obtained using TEM. The image shown in Figure 3.5 provides the 1wt% silica nanoparticles dispersion in PI. We can see the homogeneous dispersion of silica oxide nanoparticles with few agglomeration spots presented in the sub-micron range.

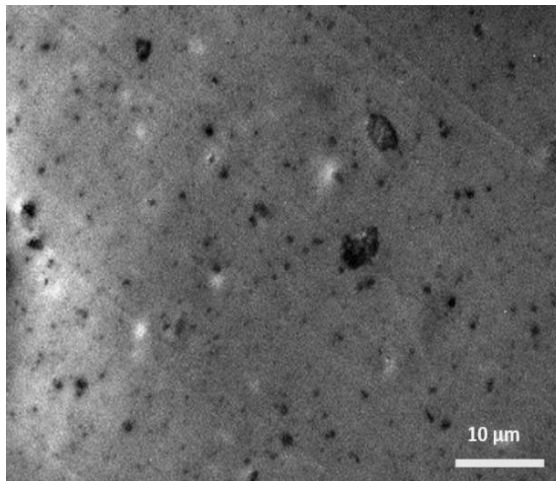


Figure 3.5 TEM image of 1wt% of  $\text{SiO}_2$  nanoparticles dispersion in PI

### 3.4 Fourier transform infrared spectroscopy

FTIR uses the basic physics of spectroscopy bypassing IR radiation from the sample to obtain a unique spectrum, representing the chemical composition of a particular material. These IR rays can be absorbed or transmitted from the sample creating a unique molecular spectrum. This unique spectrum for different materials makes FTIR capable to evaluate the chemical composition and conditions of material [31], [95]. The device to measure the FTIR spectroscopy is shown in Figure 3.6 [96], [97].



Figure 3.6 Fourier Transform Infrared Spectroscopy (FTIR) instrument

In this study, the PAA solution was synthesized and thin solid PI films were cured at different temperatures. These different curing temperatures and fabrication process conditions

make PI versatile for different applications. Therefore, to understand both the physical and chemical properties of PI films modified at different conditions, the FTIR spectrum was studied at each condition to see the change in chemical bonds and make sure at which temperature the imide ring is obtained. These influences were then qualitatively correlated to chemical changes within the polyimide's chemical structure.

### 3.5 Dielectric spectroscopy characterization

Dielectric spectroscopy measures the dielectric and electrical properties of samples as a function of frequency. It is based on the interaction of an applied electric field with the dipole movement of the material. Dielectric properties measurement can provide critical design parameter information for many electronics applications [98]. For example, the dielectric loss, the impedance and the dielectric relaxation process at different frequencies. It can provide changes in the material at molecular scale, which are important for heterogeneous materials such as nanocomposites. A material is known as dielectric when it is placed between a parallel plate capacitor under an electric field. These dielectric materials have the ability to store electrical energy depending on the permittivity value of the material [99]. This permittivity value and dielectric loss can be measured using dielectric spectroscopy instruments, such as the Solartron analytical impedance analyzer, as shown in Figure 3.7. We used the device to measure the dielectric constant and dielectric loss of PI and multi-layer PI/SiO<sub>2</sub> samples.

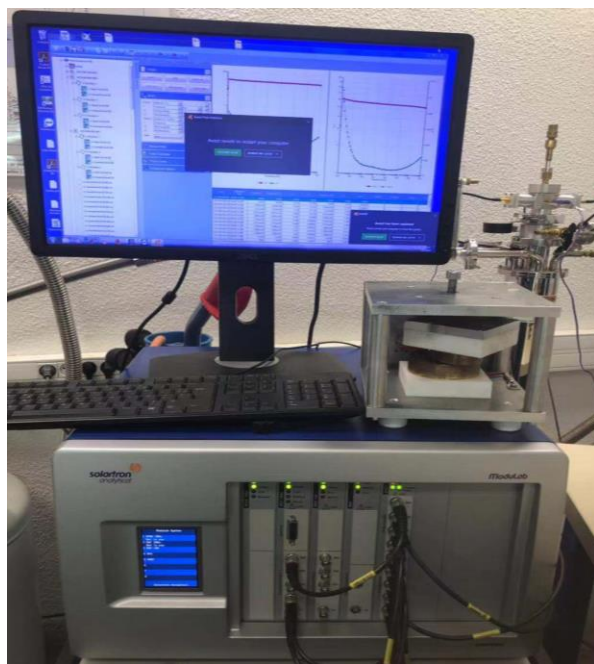


Figure 3.7 Dielectric spectroscopy measuring setup

When consecutive isothermal scans are performed, a dielectric relaxation map can be obtained. These maps will provide important information about the molecular mobility of the polymeric chains as influenced by the frequency and the temperature. The rates with which



polarization can occur are limited so that as the frequency of the applied electric field is increased, some polarization will no longer be able to attain their values. The dipole moments are just not able to orient fast enough to keep in alignment with the applied field and the total polarizability falls. This fall, with its related reduction of permittivity, and the occurrence of energy absorption, is referred to as dielectric relaxation or dispersions.

### 3.6 Corona resistance property tests under PWM waveform

The corona resistance property tests such as PD, surface discharge, lifetime and electrical breakdown tests were performed with a bipolar square impulse voltage waveform generator in high voltage laboratory of Sichuan University in Chengdu, China.

#### 3.6.1 Lifetime and electrical breakdown tests under corona discharge

According to the standard of IEC 60034-18-42, laboratory-produced bipolar continuous square impulse voltage (BCSIV) generator can be used as a replacement of PWM inverters for testing purposes [10], [20], [22]. The generator is capable to generate a square voltage waveform up to 10 kV peak to peak, duty cycles up to 50 %, switching frequency 200 Hz-20 kHz, peak to peak rise time 50ns-10 $\mu$ s. In this study, the measured average partial discharge inception voltage (PDIV) for different samples was about 800 V, therefore, applied voltage for aging is set to be 1200 V, frequency 1 kHz, duty cycle 0.5, and rising time 1  $\mu$ s was used for corona resistance testing purposes as shown in Figure 3.8. Electrodes are designed according to the IEC-60343 standard and ASTM-2275 standard. The top electrode is a rod-type cylindrical shape having a diameter of 6 mm and edge radius 1 mm, as shown in Figure 3.8. The bottom electrode is a plate shape having a diameter of 50 mm. Both electrodes are made of stainless steel. Furthermore, electrical breakdown tests were carried out in a vacuum oven using a rod-plate electrode system. Pulse voltage of 1 kHz, 0.5 duty cycles and 60 ns rise time was applied during the test. Five samples are used for each test.

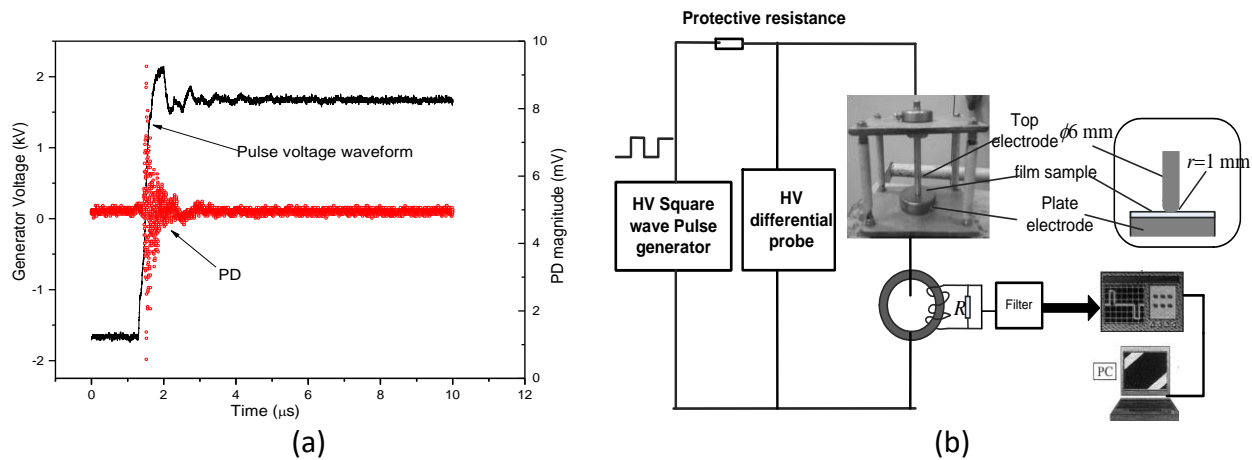


Figure 3.8 (a) Pulse voltage waveform and PD (b) Breakdown test system in the presence of PD

### 3.6.2 PD and surface discharge test setup

PD measuring test setup using the square wave voltage waveform is shown in Figure 3.9 and its schematic diagram is shown in Figure 3.10 [18], [28], [30], [100]. PD signal was collected using the Archimedean spiral antenna as a sensor. The antenna was designed in the high voltage laboratory of Sichuan University. The antenna sensor has the ability to collect 300 MHz to 3 GHz bandwidth of electromagnetic waves without distortion.

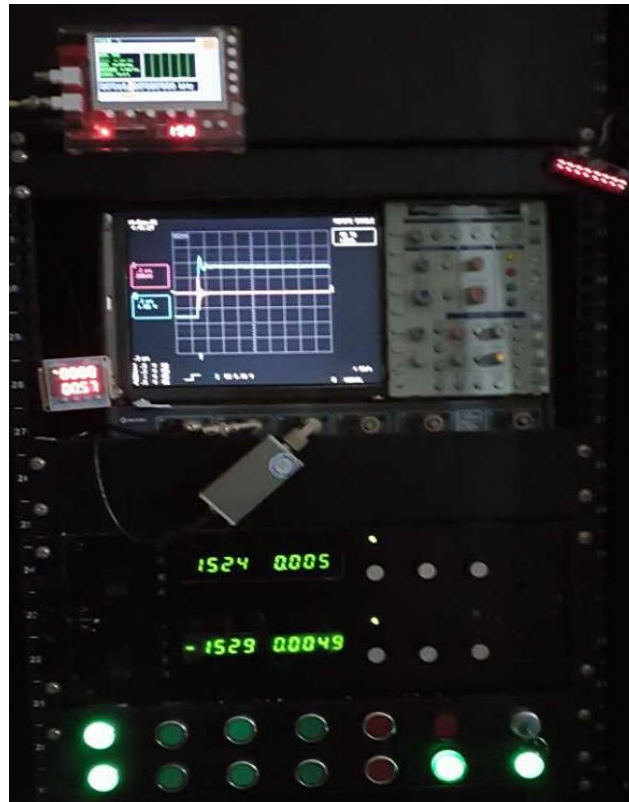


Figure 3.9 PD test system

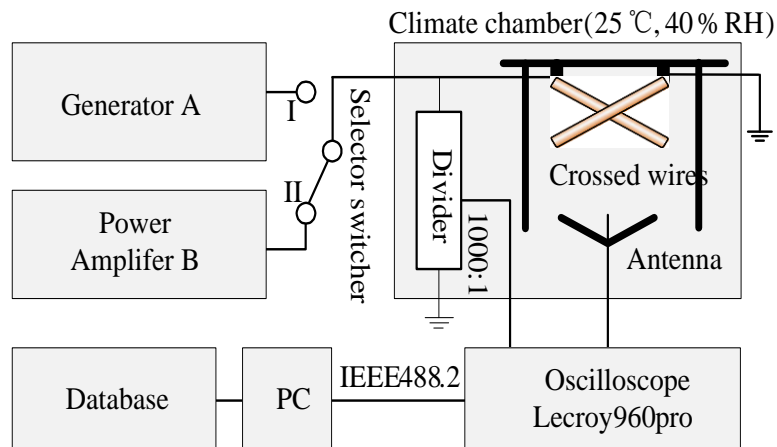


Figure 3.10 Scheme of surface discharge (PD) and corona-resistance measurement

In addition, a high voltage differential probe is used to acquire a phase resolved PD pattern at the square waveform. Due to high frequency square waveform having steep rise edge (high  $dv/dt$ ), PD signal contains interfering signal components. For the exact investigation of PD, it needs to deal with the original partial discharge signal. The dB6 [18] wavelet packet method can adequately disintegrate low frequency segments and high frequency segments of signals, so it is used to separate PD signals from interference signals. After surface discharge aging, PD signals are obtained at a sampling rate of 500 MHz for 10 times for PD statistics each half cycle time of voltage waveform [18].

PD test setup has the following main parts:

- 1) **Antenna:** UHF gain > 5.0 dB, frequency domain 0.8-2 GHz, positioned 20 cm.
- 2) **Filter:** 500 MHz, high-pass, filtering out the generator interferences.
- 3) **Divider:** 50 MHz bandwidth, 1000:1 ratio, as the phase synchronization signal.
- 4) **Oscilloscope:** 2.0 GHz bandwidth, 16 Gs/s max sampling rate, GPIB bus.

### 3.7 Conduction currents

Conduction current is attributed to different polarization and depolarization process happening inside the material. The complete polarization process can be presented as equation (3.1) [101], where  $i_i$  is the instantaneous current due to the displacement polarization,  $i_a$  represents the relaxation polarization current and  $i_c$  is the conduction current due to the conductivity of the specimen. The Simons and Tam theory represents that the depolarization current is a superposition of different relaxation processes depending on the trap levels and given as [102]. For all the measurements, the samples and electrodes were placed in a temperature-control chamber. The electric field (up to 50 kV/mm) was applied by a low residual ripple voltage power supply which has a maximum limit of 35 kV HVDC (Fug HCP140-35000). The quasi-steady state polarization current, that is also known as conduction current, was obtained after the transient regime of the absorption during 3000-5000 seconds.

$$i_p = i_i + i_a + i_c \quad (3.1)$$

We can use equation (3.2) to describe the conduction phenomena. The time needed to reach the steady state current depends on the type of the material, the applied electric field and the temperature. Normally at higher temperatures and electric fields, the steady state is achieved earlier.

$$\sigma_t = \sum n.q.\mu \quad (3.2)$$

Where  $n$  is the concentration of charge carrier,  $q$  is the fundamental charge and  $\mu$  represents the mobility of the respective charge carrier. Under the electric field, the charge carrier moves either in the direction of the field or the opposite direction depending on the

dominant carrier polarity. For higher temperatures, the charge carriers and the charge mobility increase because of the molecular motion increases with temperature. So, the following Arrhenius law from equation (3.3) can describe the relationship between charge density, mobility and specific temperature  $T$ :

$$n \cdot q \sim \exp\left(\frac{-E_A}{kT}\right) \quad (3.3)$$

Where  $E_A$  is the thermal activation energy and  $k$  is the Boltzmann constant. According to this law, the conductivity increases with the increase in temperature. The field strength can also affect the density and the mobility of the carriers, but it is generally believed that it is true only for electrons, so that the measurement of conductivity as a function of field strength provides a way to distinguish between mechanisms controlled primary electronically and secondly by ions or dipoles [103], [104]. The electrical conductivity increases with the increase in temperature and electric field, but, at the same time, it can be limited by the presence of intrinsic space charges, due to the fact that all the intrinsic charges could be seen as traps for the moving charges [105], [106]. If homocharges are injected at the interface between the dielectric and the metal electrode, the local field is lowered, which will determine an increase in injection phenomena. Mott and Gurney have proved that the maximum current density  $J$  that corresponds to space charge saturation (completely filled traps) inside the material, in a perfect dielectric without intrinsic carriers and without electron holes, will be given by equation (3.4) [107].

$$J = \frac{9}{8} \varepsilon \mu \frac{V^2}{d^3} \quad (3.4)$$

This equation is valid only if the electric field at the interface between the dielectric and the metal is completely canceled by the internal field due to the presence of space charges. If the interfacial field is present, then the maximum current density  $J$  will be from equation (3.5).

$$J = \frac{9}{8} \varepsilon \mu V^2 \left[ (d + x_0)^{3/2} - x_0^{3/2} \right]^{-2} \quad (3.5)$$

With  $x_0$  being the number of free electrons at the anode. For the case of a perfect dielectric, if the external field is low, the current density has an ohmic behavior as presented in equation (3.6).

$$J = \sigma \frac{V}{d} = q n_0 \mu \frac{V}{d} \quad (3.6)$$

If we compare the previous case with that of perfect insulation, the current density will be reduced with a specific factor  $\theta$ , which corresponds to the fraction of carriers that are injected and trapped in the dielectric, as shown in equation (3.7).

$$J = \frac{9}{8} \varepsilon \mu \theta \frac{V^2}{d^3} \quad (3.7)$$

In the case of trapped charges, the depth level of the trapped charges is also needed to be considered [101], [108]. If the sample containing only one level of charge traps, the transition between the ohmic conduction and the space charge limited conduction is possible under the influence of a high field, because part of the injected charges will be trapped. But, when all the charge traps are filled, for a specific electric field (given by the  $V_{TFR}$  applied voltage), a sudden increase in current will be observed, because the current will tend to approach the current density of material without traps. The two phenomena may be repeated if the material has several trap levels. The value of the  $V_{TFR}$  voltage is given by equation (3.8).

$$V_{TFR} = \frac{q d^2 n_t}{2 \varepsilon} \quad (3.8)$$

Where  $n_t$  represents the density of the traps found in the material. The polarization current for the PI/nanocomposite samples increases with the increase in the electric field because the charge injection and the charge mobility depend on the applied electric field. Similar results have been obtained and, in order to compare the different materials, the conduction current density versus the applied field was analyzed. The presence of space charge inside the bulk of the samples can act as traps for the moving charges and can limit the charge transport phenomena. Two phenomena can be used to describe the conduction for dielectric materials, the Poole-Frenkel effect, which explains the Schottky gap variation, and the space charge limited current (SCLC), which explains the charge trapping phenomenon [106], [109]. If the applied electric field is low and the charge injection is neglected, as Coelho explains, the variation of the current density as a function of the electric field corresponds to an ohmic behavior [103], [110]. But, as the applied electric field increases, after a certain threshold voltage, the type of conduction changes, and the initial ohmic conduction is changed to space charge conduction. The conduction is also known as space charge limited current conduction (SCLC), which depends on the depth of the trapped charges. When all the charge traps are filled, for a specific electric field, a sudden increase in current should be observed and the current will tend to reach the current density of material without traps. The schematic diagram of conduction current density phenomenon versus the applied field is represented in Figure 3.11.

The basic theory of conduction bands was first applied to semiconducting materials and later was applied to polymers. This theory explains the basic conduction mechanism that happens in polymeric materials [111]. According to the band theory, every material possesses a valence band for the fixed electrons and a conduction band for the free moving electrons. These two bands are separated by the forbidden gap. In an ideal insulator, electrons are

present only in the valence band and no free electrons available in the conduction band. These electrons need some energy to jump from valence band to conduction band, which they can get from temperature or electric field. For an ideal insulator, the forbidden gap is large ( $> 1$  eV) and the chances for an electron to jump from the valence band to conduction band are small. In polymers, groups of atoms are chemically bonded together in molecules, in which weak molecular motion is responsible for electronic conduction. In a dielectric material, when an electric field is applied, the energy barrier at the electrode-insulation interface can be given by the Schottky and the Fowler-Nordheim two injection phenomena [112].

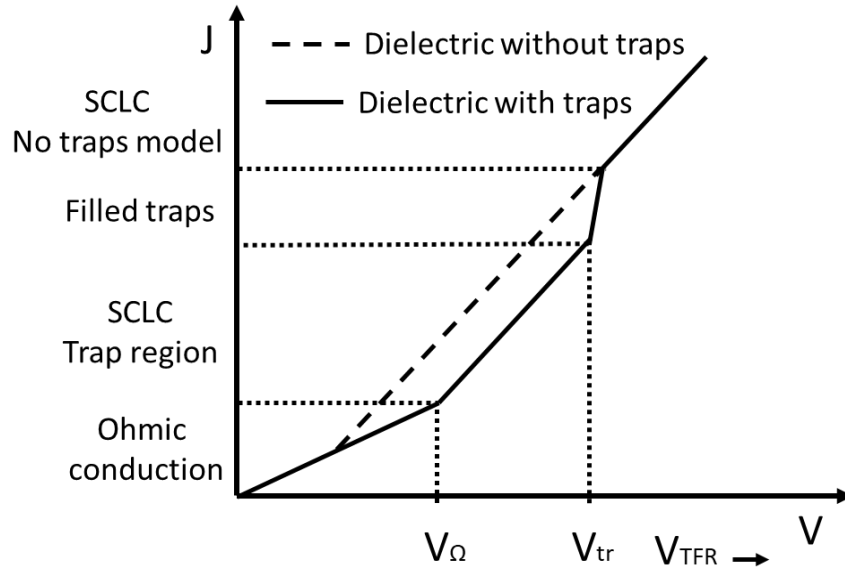


Figure 3.11 Conduction current density vs voltage

Consider that the energy gap between the metal and the insulator  $X$  is given by the difference between the forbidden gap of the metal  $\varphi_m$  and the forbidden gap of the insulator  $\varphi_i$  (difference also called Fermi energy level). This difference has its maximum value when no external force is applied, as shown in Figure 3.12(a). But, in the presence of an electric field, the energy gap of the insulator is reduced, as shown in Figure 3.12(b) [101]. The reduced energy gap  $\varphi_0$  represents the difference between the energy gap of the metal and the initial energy gap between the metal and the insulator. If this energy barrier is weak ( $\varphi_0 < 0.3$  eV), then a weak electric field is enough to allow the conduction current [101]. In the case of a pure dielectric, the energy barrier is superior to 2 eV, so the electric field has to be increased ( $> \text{kV/mm}$ ). As a consequence, charges coming from the metal electrode will be injected in the material, and, after a specific time, the number of the injected charges may pass the number of the intrinsic charges. In this case, due to the accumulation of injected charges, the local contact field between the metal and the insulator will be reduced (as a consequence of the Coulomb force), which will reduce even more the energy gap between the metal and the dielectric.

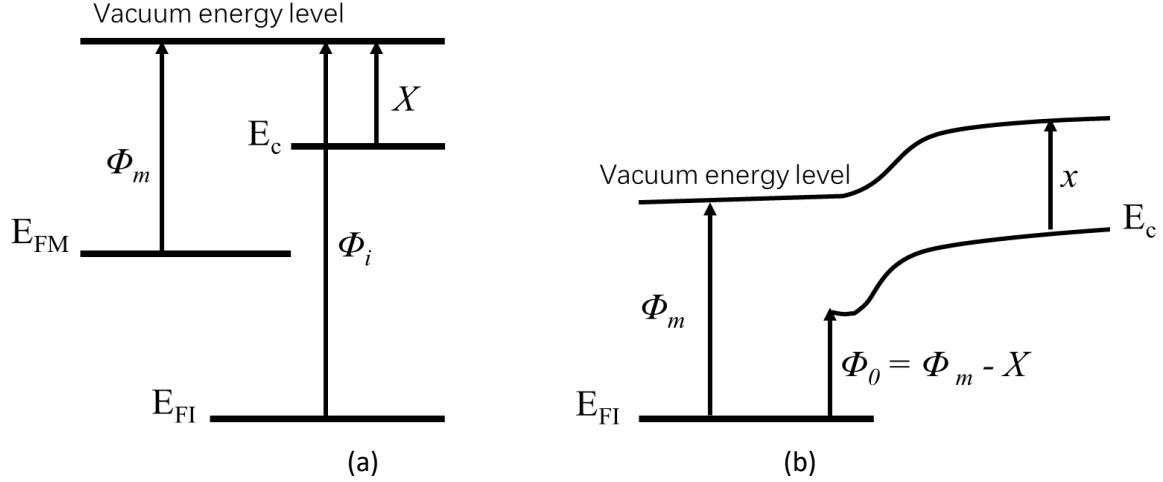


Figure 3.12 Metal and insulator energy gap (a) before and (b) after the applied electric field

Actually, the potential energy of an electron, placed at a certain distance  $x$  with respect to the contact field at the cathode  $E_c$ , will attenuate the energy barrier at the contact, as given in equation (3.9) [111]:

$$\phi(x) = -E_c x \frac{-q^2}{16\pi\epsilon_0\epsilon_r x^2} \quad (3.9)$$

Where  $\phi$  is the energy barrier attenuation,  $E_c$  represents the contact field and  $\epsilon_0$  and  $\epsilon_r$  represent respectively the permittivity of the vacuum and the relative permittivity of the dielectric. In this case, the effect of field strength on electron conductivity phenomena is known as the Schottky effect that is characterized by equation (3.10).

$$\Delta\phi = \sqrt{\frac{q^3 \cdot E}{4\pi \cdot \epsilon_0 \cdot \epsilon_r}} \quad (3.10)$$

The density of the injected current can then be given as equation (3.11).

$$J_s = A_s T^2 \exp \left[ \frac{\phi - \beta_s \left( \gamma \frac{V}{d} \right)^{1/2}}{kT} \right] \quad (3.11)$$

$A_s$  is the Richardson constant:

$$A_s = \frac{4\pi qmk^2}{h^3} = 1.2 \times 10^6 \text{ A/m}^2 \text{K}^2 \quad (3.12)$$

$\beta_s$  is the Schottky constant:

$$\beta s = \sqrt{\frac{q^3}{4\pi\epsilon_0\epsilon_r}} \quad (3.13)$$

Where  $m$  is the mass of the electron,  $T$  is the temperature,  $h$  is Plank's constant and  $k$  is the Boltzmann's constant.  $V$  represents the applied voltage and  $d$  is the thickness of the sample. The  $\gamma$  coefficient, also called the electric field distortion coefficient is an experimental parameter, which could be either  $\gamma > 1$  in the case of an injection dominated by heterocharges or  $\gamma < 1$  in the case of a dominant homocharges injection at the contact [103].

The PI film with guard ring electrode deposition is shown in Figure 3.13. Conduction current measurements, the samples and electrodes were placed in a temperature-control chamber, as shown in Figure 3.14. The electric field (up to 50 kV/mm) was applied by a low residual ripple voltage power supply, which has a maximum limit of 35 kV HVDC (Fug HCP140-35000). The quasi-steady state polarization current, that is also known as conduction current, was obtained after the transient regime of the absorption during 3000-5000 seconds, as shown in Figure 3.15. When we apply an electric field to the thin sample of PI films, there is slight current conduction through the samples. This current conduction can be due to multiple reasons [103], [113], such as:

- 1) Orientation of dipoles.
- 2) Displacement of the positive and negative charges.
- 3) Shifting of mobile positive and negative carriers (MWS polarization).
- 4) Space charge injection from electrodes and their accumulation in the bulk of the sample.



Figure 3.13 PI film view and guard ring gold electrode deposition



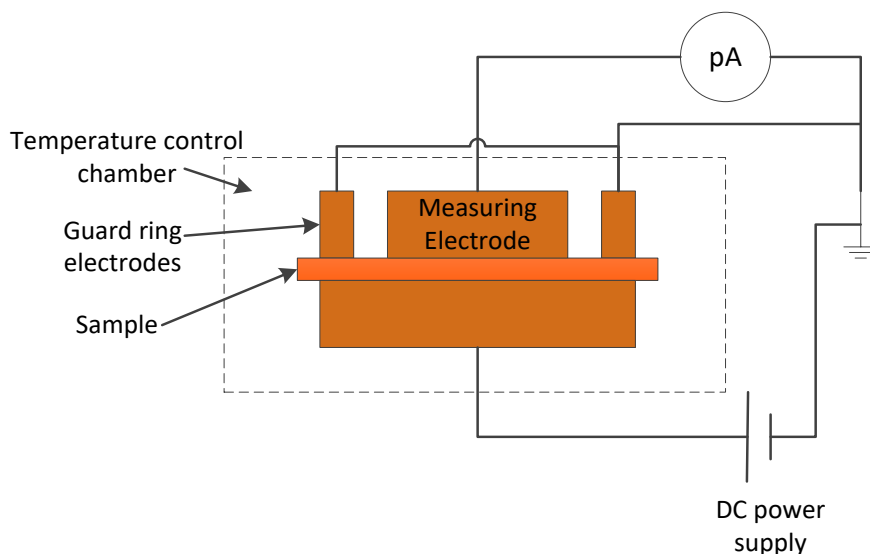
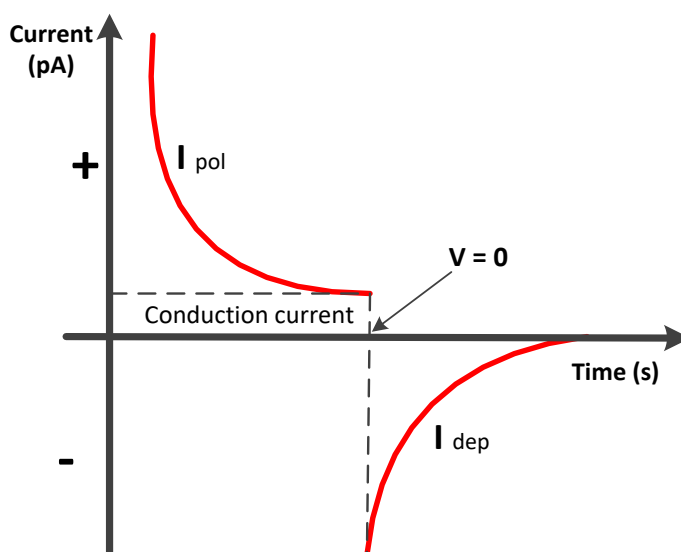


Figure 3.14 Guard ring electrode setup to measure conduction current

Figure 3.15  $I(t)$  characteristics of polarization and depolarization current

### 3.8 Thermal and mechanical characterization

In order to evaluate the flexibility and  $T_g$  of PI and PI/SiO<sub>2</sub> nanocomposite samples, the mechanical strength is characterized using DMA test, and thermal diffusivity was measured using NETZSCH LFA-447 Nano flash, as described hereafter.

#### 3.8.1 Rheological test using dynamic mechanical analyzer (DMA)

Due to their macromolecular structure, polymeric materials such as PI films are known as viscoelastic because they exhibit a combination of elastic and viscous properties. Depending on the temperature, a characteristic of material can be changed from solid to rubbery to liquid. Rheology test allows the study of the viscoelastic behavior of a material. DMA is a vastly used

material characterizing scientific technique, which can measure mechanical rigidity of material as a function of temperature as shown in Figure 3.16. In this method, a small deformation force is subjected to the samples and the change in the material is observed as a function of temperature. The deformation is belonged to the stiffness of the material. A motor is used to generate the sinusoidal force and this is transmitted to the sample with the help of drive shaft. To fix and stabilize the position of sample, bearing is used with the drive shaft [114]. A schematic of the analytic train of the DMA is shown in Figure 3.17.

	Shear rheology	Extensional rheology	DMA torsion	DMA extension	DMA reaction
Measuring system					
Polymer solutions					
Polymer melts					
Solid polymers					
Elastomers					
Reactive systems (resins)					

Figure 3.16 Measuring modes offered by an MCR rheometer

Relaxation steps during the softening process of a solid may become visible in the glass transition region. Various evaluation methods enable the quantification of a material's transition from its solid to its rubbery state. The melting point  $T_m$ , the glass transition temperature  $T_g$ , the secondary  $\beta$ - and  $\gamma$ -relaxations, the shear modulus at a given temperature, can be provided by an MCR rheometer with DMA accessories, at the push of a button. DMA measures stiffness and damping; these are reported as modulus and  $\tan \delta$ . Because we are applying a sinusoidal force, we can express the modulus as an in-phase component, the storage modulus, and an out of phase component, the loss modulus. The storage modulus, either  $E'$  or  $G'$ , is the measure of the sample's elastic behavior. The ratio of the loss to the storage is the  $\tan \delta$  and is often called damping. It is a measure of the energy dissipation of a material [115].

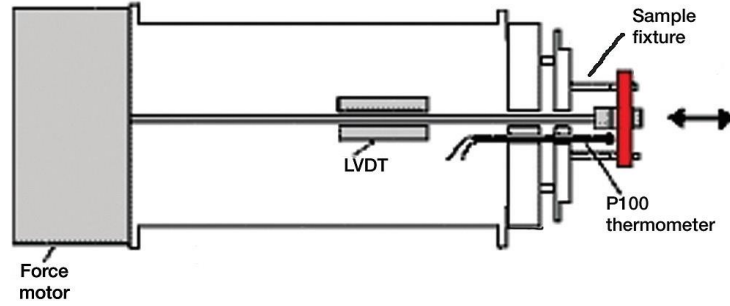


Figure 3.17 Schematic of the DMA chamber

### 3.8.2 Thermal diffusivity test

Thermal conductivity  $\lambda$  is an important property of a material to transfer heat from one material to another or to atmosphere. Higher thermal conductivity materials are required in electric motors and generators to dissipate heat from motors conductors to atmosphere. NETZSCH- LFA-447 Nano flash was used to measure thermal diffusivity  $D$ , and thermal conductivity  $\lambda$  was calculated by dividing the product of density  $\rho$  and specific heat capacity  $C_p$ , as given in equation (3.14). The LFA-447 Nano flash is equipped with a furnace capable of operation from room temperature to 300 °C. The system is equipped with a software-controlled automatic sample changer allowing measurement of up to 4 samples at the same time. The temperature rise on the back face of the sample is measured using an In-Sb detector [116], [117]. Data acquisition and evaluation are accomplished using a comprehensive 32-bit MS-Windows software package. Various analysis models are integrated in the software [118]. The data can be corrected for finite pulse and heat loss effects (radial and facial). The schematic diagram of the measuring instrument is shown in Figure 3.18 [119].

$$D(T) = \frac{\lambda(T)}{\rho(T)C_p(T)} \quad (3.14)$$

$$D = 0.13 \frac{d^2}{t^{1/2}} \quad (3.15)$$

Where  $d$  is the thickness of the sample and  $t^{1/2}$  represents the half-rise time (the time for the back face of the temperature to reach 50 % of the maximum value). Actually, both thermal diffusivity and specific heat can be determined simultaneously. For our measurements, the width of the light pulse was of 0.3 ms and it was applied on circular shaped samples of about 100  $\mu\text{m}$  thickness and half inch in diameter. A standard aluminum pan was used for holding the sample. Temperature-dependent measurements were performed up to 573 K. The measurement of the temperature increase on the rear of the sample is carried out with a liquid-nitrogen-cooled In-Sb (Indium-Antimonide) infrared detector. Both the detector and amplifier components are designed for measurements with data acquisition rates of 500 kHz.

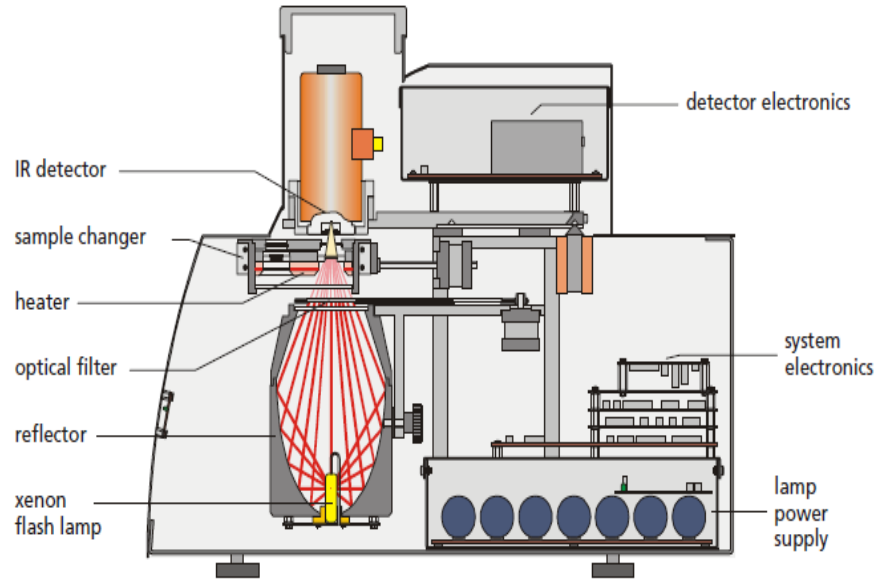


Figure 3.18 Thermal diffusivity measuring instrument

### 3.9 Space charges measurement setups

It is obvious reason that when an insulating material is subjected to high electric field, the charges accumulate in the bulk of material, known as space charges. These space charges disturb the local internal field that overstress locally the material and may lead to early breakdown due to material degradation. Measuring the space charge inside the dielectric material is meaningful in a sense that it can be used to calculate the local electric field enhancement. The determination of electric field and charge density are helpful to design better insulating material. Numerous nondestructive techniques are available to measure space charges in the dielectric insulating materials. In these, two famous techniques are Pulse-Electro-Acoustic (PEA) and Thermal Step Method (TSM) [120]–[122].

#### 3.9.1 Thermal step method (TSM)

In the TSM technique, a thermal wave diffuses through the sample and causes thermal expansion and contraction of dielectric, through which space charges in a dielectric slightly fluctuates for a short time. This fluctuation adjusts the induced charges at the electrodes, causing a short circuit current in the external circuit. The short circuit current is recorded through current amplifier and mathematical calculation of this current permits to determine the distribution of the residual electric field and charge density across the sample. In TSM, the top electrode is a cylindrical shape of 5 cm diameter while the bottom electrode is the thermal diffuser. Both electrodes are made up of copper. The arrangement of TSM measurements is presented in Figure 3.19. Keithley-428 current amplifier connected to a data acquisition card is used to record the current that is controlled by a Lab-View program in PC [39]. Suppose a sample of thickness  $d$ , surface area  $S$  is placed between two short circuited electrodes of distance  $x = 0$  to  $x = d$  in the direction of sample thickness, as shown in Figure 3.20.

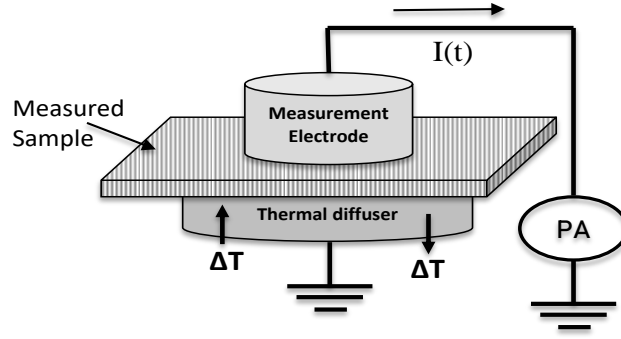
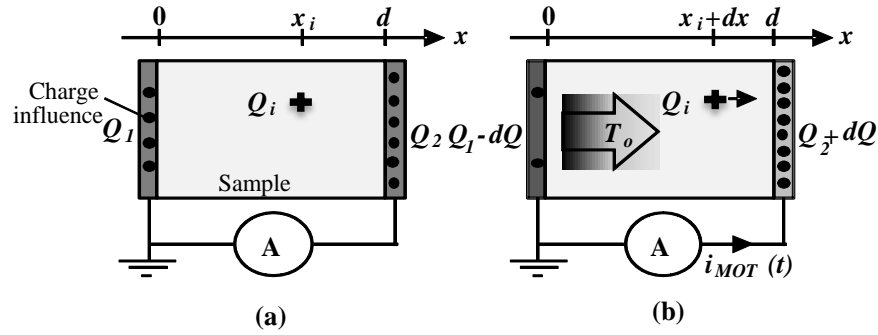


Figure 3.19 TSM electrode setup in short circuit conditions

Figure 3.20 Principle of TSM (a) equilibrium state at  $T_0$  (b) Equilibrium modified at  $T_1$ 

Considered the material is homogeneous and infinitely plane ( $d \ll \sqrt{S}$ ); thus, the electric field is assumed to be constant in any plane parallel to the electrodes. As the system consist of sample, electrode and conducting wire is in electrostatic equilibrium, a charge  $Q_i$  located in the bulk of the sample at the distance of thickness  $x_i$  induces charges of  $Q_1$  and  $Q_2$  at the electrodes, as presented in equation (3.16). The dependence of the induced charges on the space charge  $Q_i$  and on the geometrical dimensions of the sample can be obtained with the help of the short circuit conditions  $\int_0^d E(x)dx=0$ , the electric charge conservation law  $Q_1+Q_2+Q_3 = 0$  and the conservation of the electric displacement at the electrode-dielectric interface  $\text{div}_s(\epsilon \vec{E})=Q/S$ :

$$Q_1 = -\frac{d-x_i}{d}Q_i, \quad Q_2 = -\frac{x_i}{d}Q_i \quad (3.16)$$

If a temperature step  $\Delta T = T - T_0$  is applied to one side of the sample, the propagation  $\Delta T(x, t) = T(x, t) - T_0$  of the thermal wave across the sample will give rise to local variations of the permittivity and the thickness (expansion or contraction), which can be given as equation (3.17).

$$\epsilon = \epsilon_{T_0}(1 + \alpha_\epsilon \Delta T), \quad dx = dx_0(1 + \alpha_d \Delta T) \quad (3.17)$$

Where  $\alpha_\epsilon$  is the rate of change of the material permittivity with the temperature and  $\alpha_d$  is its rate of thermal expansion,

$$\alpha_\varepsilon = \frac{1}{\varepsilon} \frac{d\varepsilon}{dT}, \quad \alpha_d = \frac{1}{x} \frac{dx}{dT} \quad (3.18)$$

The variations of the thickness and permittivity modify the induced charges, which can be given as (3.19):

$$\begin{aligned} Q_1(t) &= -Q_i \int_{x_i}^d \frac{dx}{\varepsilon(x,t)} / \int_0^d \frac{dx}{\varepsilon(x,t)}, \\ Q_2(t) &= -Q_i \int_0^{x_i} \frac{dx}{\varepsilon(x,t)} / \int_0^d \frac{dx}{\varepsilon(x,t)} \end{aligned} \quad (3.19)$$

Use the above expression and putting (3.16)

$$\alpha = -\frac{1}{C} \frac{dC}{dT} \approx \frac{1}{x} \frac{dx}{dT} - \frac{1}{\varepsilon} \frac{d\varepsilon}{dT} = \alpha_d - \alpha_\varepsilon \quad (3.20)$$

We get expression for  $Q_2(t)$  as presented in equation (3.21):

$$Q_2(t) = -Q_i \frac{x_i}{d} \left[ 1 + \frac{\alpha}{x_i} \int_0^{x_i} \Delta T(x,t) dx - \frac{\alpha}{d} \int_0^d \Delta T(x,t) dx \right] \quad (3.21)$$

As the system tends to rebalance, the induced charges on the electrodes are redistributed. Hence, charge transport occurs between the electrodes. This corresponds to an external current, known as thermal step current (TS) given by  $I(t)$  as presented in equation (3.22) [121]:

$$I(t) = -\frac{dQ_2(t)}{dt} \quad (3.22)$$

If the value of the TS current and the spatial distribution of the temperature are known for every instant  $t$ , the value of the charge  $Q_i$  and its position  $x_i$  can be determined using equation (3.23).

$$I(t) = -\alpha C \int_0^d E(x) \frac{\partial \Delta T(x,t)}{\partial t} dx \quad (3.23)$$

Where  $\alpha$  is the constant of material related to thermal expansion and contraction of the sample and variation in permittivity.  $C$  is the electrical capacitance of the sample and  $E(x)$  is the remaining electric field in the sample. To find the space charge density distribution, the current is recorded and then mathematically processed in order to find the remaining electric field distribution  $E(x)$  [6, 7]. Then, space charge density distribution is calculated by applying the Poisson equation, as shown in equation (3.24):

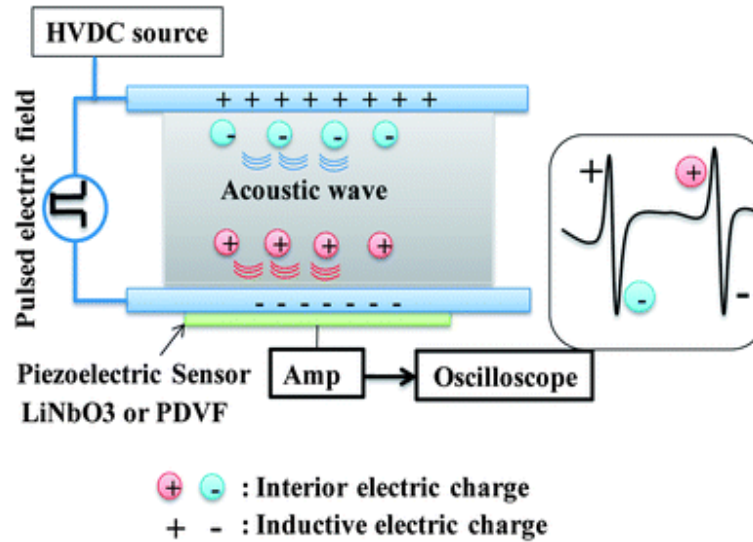
$$\rho(x) = \varepsilon \frac{\partial E(x)}{\partial x} \quad (3.24)$$

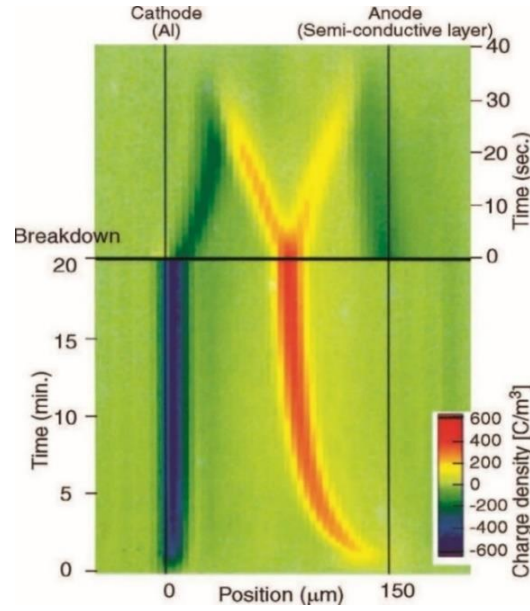
### 3.9.2 Pulse electro acoustic method (PEA)

In PEA, an electric pulse of nanosecond width is applied to the sample. A perturbation force is induced and when this force is interacted with the charges, it generates an acoustic wave with the speed of sound, that is proportional to the distribution of space charges inside the sample and then a piezoelectric transducer is used to convert this wave into an electric signal. PEA technique is used to evaluate the space charge behavior and effects of nano filler type interface with PI film. In PEA, the spatial resolution depends on the thickness of the sample  $d$ , the duration of the pulse voltage  $\Delta T_p$ , which is given as in Equation (3.25) [123].

$$\eta = \frac{\Delta T_p}{d/u_s} \times 100\% \quad (3.25)$$

The division of  $d/u_s$  is the transit time at which the acoustic pulse propagates through the PI film samples. Here,  $u_s$  is the acoustic velocity of the PI sample. For a PI, acoustic velocity is 2200 m/s. A pulse generator of 10 ns pulse width and 0 to 0.2 kV voltages is used. PVDF sensor of 9  $\mu\text{m}$  thickness is used. Negative DC voltage source is connected with upper electrode, which is made of copper, while bottom electrode, which is made of aluminum, is connected with ground, as shown in schematic diagram in Figure 3.21(a) [123]. The sensor is connected below the bottom electrode with impedance matching backing material. Conducting gel is used on sample for good contact between electrodes. DC voltage source with range of 0 to 20 kV is used. DC electric field of 30 kV/mm is applied to measure space charge density according to thickness of samples for 0 to 180 minutes, then LabVIEW based program is used to observe charges behavior, as shown in Figure 3.21(b).





(b)

Figure 3.21 (a) Schematic diagram of PEA system (b) Space Charge distribution profile

### 3.10 Thermal stimulated current (TSC)

TSC is a thermally stimulated current technique that is used to locate trap charges energy levels in semiconductor or insulating material. First, energy levels are filled by electrical infusion generally at low temperature, then heating at higher temperature to emit electrons and holes. Data of emitted current will be recorded and plotted against temperature, resulting as TSC spectrum [124]. By analyzing TSC spectra, data can be acquired with respect to energy levels. TSC measuring system with electrode is shown in Figure 3.22. To get experimental TSC data, the tested sample is first polarized under 3 kV/mm at 120 °C for 20 min, then cooled down to -20 °C at -10 °C/min according to equation (3.26) and equation (3.27). After a delay of 3 min, the sample is depolarized for 10 min to release the polarization charges. Finally, a linear heating at 4 °C/min is performed with the depolarization current recorded, as shown with curve in Figure 3.23 expressed in equation (3.28) and equation (3.29).

Polarization process

$$P(t) = P_e [1 - \exp(-t / \tau)] \quad (3.26)$$

$$P_e = \frac{aNp^2 E_p}{kT_p} \quad (3.27)$$

Depolarization process

$$P(t) = P_e \exp(-t / \tau) \quad (3.28)$$



$$P(t) = P_e \left[ \exp\left(-\int_0^t \frac{dt}{\tau}\right) \right] \quad (3.29)$$



Figure 3.22 TSC measuring system electrode

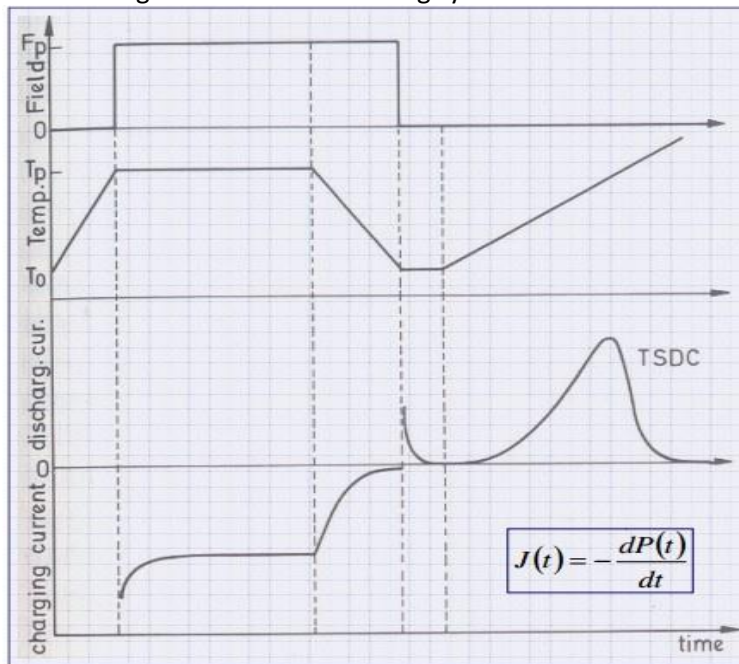


Figure 3.23 Polarization and depolarization process

### 3.11 Summary

In this chapter, we made the general description of our samples and their characterization techniques. The methodology and the working principle about the techniques to characterize the samples are presented. However, more specific details about the experimental conditions will be presented in the experimental results chapter. PI/nanocomposites single and multilayer samples were made using silicon and aluminum dioxide nanoparticles ( $\text{SiO}_2$ ,  $\text{Al}_2\text{O}_3$ ). To change the surface properties, some samples were fluorinated, which are called FPI samples. The experimental protocols are chosen according to the international standards and the best diagnostic techniques are presented to test the performance of materials.



## Chapter-4

---

Experimental results and analysis

**Chapter 4 Experimental results and analysis**

4.1 Introduction .....	69
4.2 Microscopic and chemical characterization.....	69
4.2.1 Scanning and transmission electron microscopy analysis .....	69
4.2.2 FTIR analysis .....	72
4.3 Thermomechanical analysis of rheological tests .....	75
4.4 Thermal conductivity analysis.....	78
4.5 Dielectric constant and dielectric loss .....	80
4.6 Dielectric breakdown strength .....	83
4.7 Current-voltage characteristics.....	87
4.8 Space charges and trap levels analysis .....	99
4.8.1 Space charge analysis using TSM technique .....	99
4.8.2 Space charge analysis using PEA technique.....	106
4.8.3 Total charge decay and trap levels distribution analysis .....	108
4.8.4 Discussion .....	113
4.9 Summary .....	116

## 4.1 Introduction

This chapter presents the experimental characterization of PI and PI nanocomposites films. After synthesis of samples, microscopic analysis and chemical characterization using Scanning Electron Microscopy “SEM” and Fourier Transform Infrared Spectroscopy “FTIR” are presented to analyze the composition of samples. Findings on the corona discharge resistance properties and the impact of surface discharge degradation are discussed. Furthermore, the most striking outcomes of this chapter describe the impact of improved nanofiller dispersion on space charge and electric breakdown results. The space charge density and electric field, by using the Thermal Step method, were calculated and compared for single and multi-layer PI nanocomposites films. Moreover, dielectric loss and thermal conductivity are analyzed to check the material energy loss and heat transfer ability respectfully.

## 4.2 Microscopic and chemical characterization

### 4.2.1 Scanning and transmission electron microscopy analysis

Surface and a cross-sectional view of single and multilayer PI/nanocomposite films using SEM/TEM are shown in Figure 4.1, Figure 4.2 and Figure 4.3. The left column SEM images in Figure 4.1 are showing nanoparticles dispersion for single layer PI/SiO<sub>2</sub> films while the right column deals with multilayer PI/SiO<sub>2</sub> films. White regions in these figures are corresponding to the nanofiller inclusions and darker ones to the polyimide matrix. We observed a better nanoparticles dispersion in PI/SiO<sub>2</sub> multilayer films, as shown in the right column SEM images of Figure 4.1, compared to PI/SiO<sub>2</sub> single-layer film with few nanoparticles agglomeration spots, as shown in the left column SEM images. We can also notice the relatively clean composition of the two-layer and three-layer structure, as shown in Figure 4.2(a, b). Cross-section of three-layer structure with top and bottom layers in PI/Al<sub>2</sub>O<sub>3</sub> nanocomposite, with a middle layer in PI, are shown before and after aging in Figure 4.3(c) and Figure 4.3(d), respectively. White regions in these figures are corresponding to the inclusions of nanofillers and darker ones to the polyimide. To investigate the failure mechanism of nanocomposite PI films under square impulse voltage, SEM was used to obtain a direct surface view after corona discharge aging under square wave pulse voltage [31], [86]. Figure 4.3(a, b) is showing the microscopic view of the sample around top electrode; sign I is the surface below the top electrode that is almost smooth and sign II is the surface around electrode that is rough, after PD. It tells that most of the discharge occurs around the edges of the electrode. The surface in this region is corroded and prompts the surface roughness and variation in the microstructure. Therefore, the electric field intensity may increase in these areas and causes a breakdown. Figure 4.3(a) PI film showing roughness is scattered all way around the electrode surface, while Figure 4.3(b) is showing that the PI/Al<sub>2</sub>O<sub>3</sub> sample has non-homogenous roughness. This non-homogeneity may be due to the presence of nanoparticles. Some voids can be seen due to insulation degradation.

The increase in aging time under pulse voltage enhances chemical erosion and enlarges the voids.

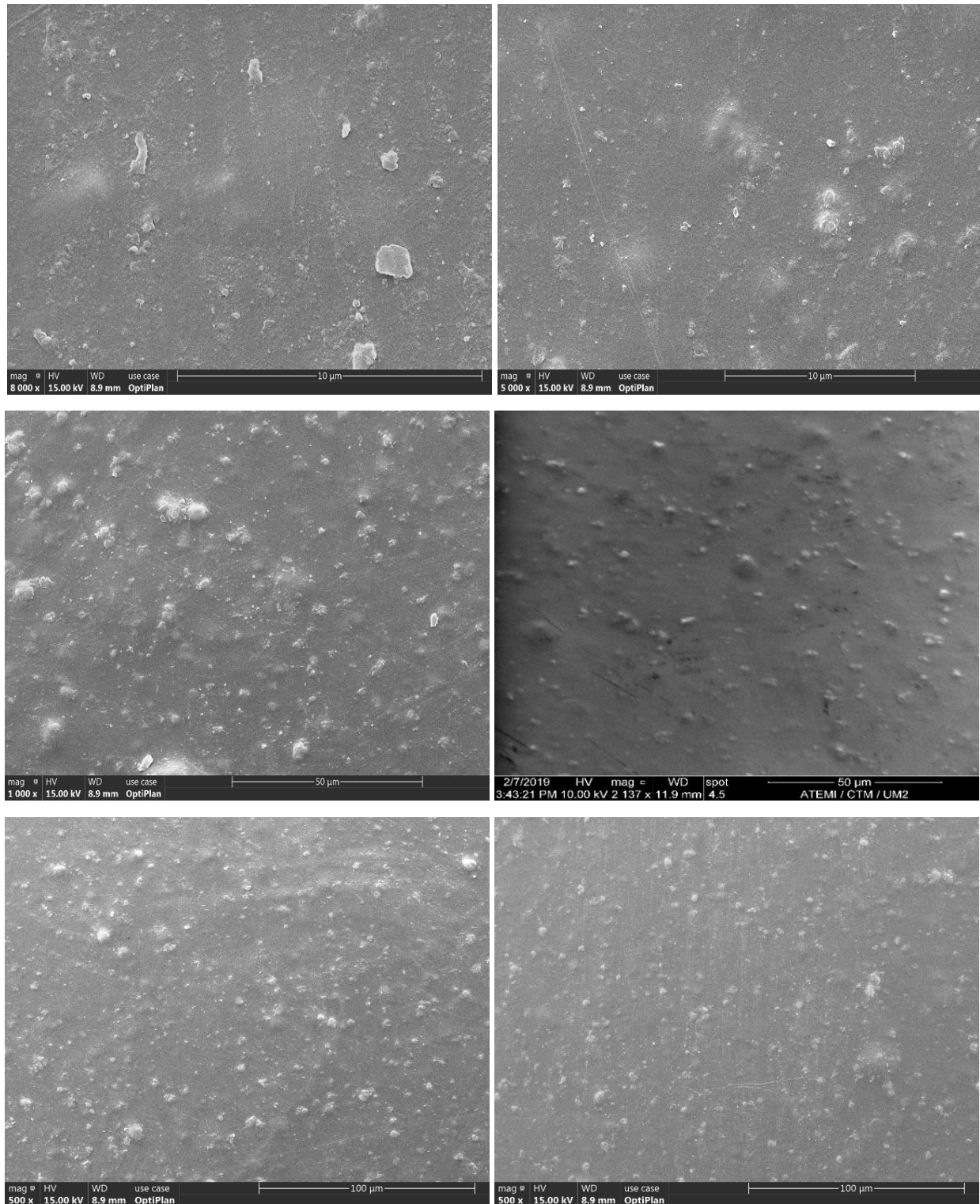


Figure 4.1 SEM image of surface topography of single and multi-layer nanoparticles dispersion  
Left column showing single layer PI/SiO<sub>2</sub> films and right column showing multilayer PI/SiO<sub>2</sub> films

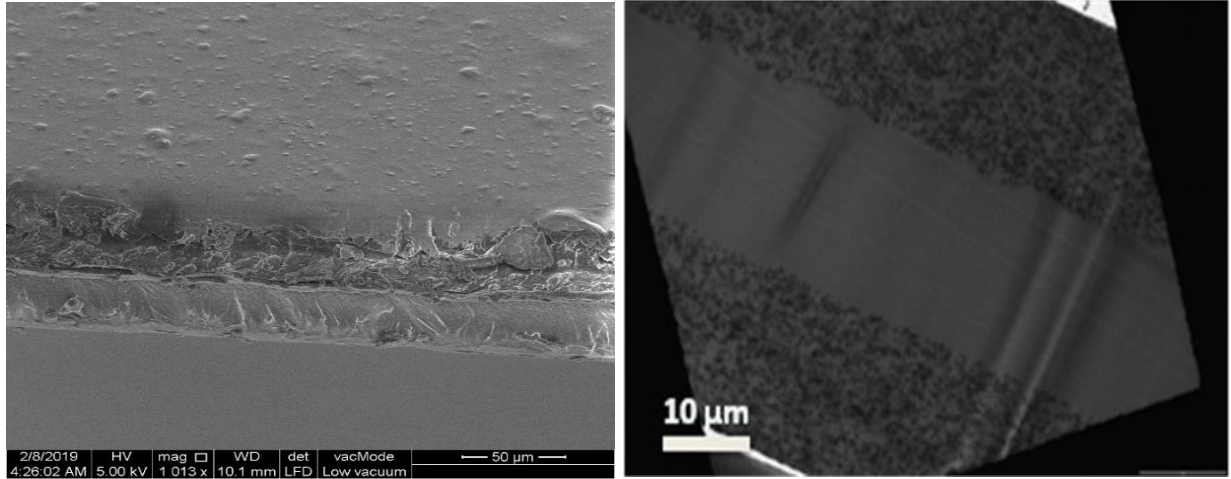
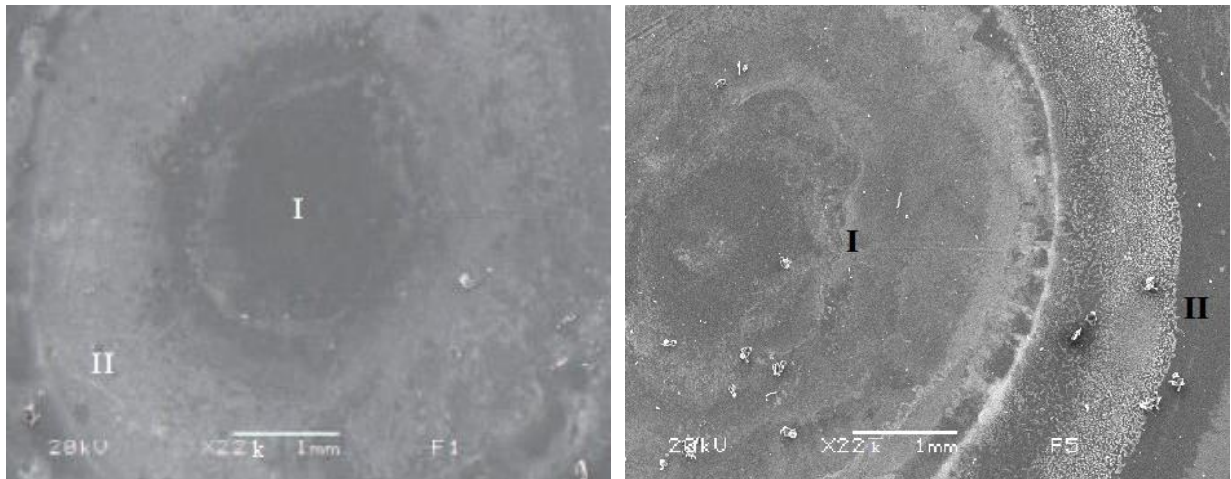
(a) SEM image of two-layer PI-PI/SiO<sub>2</sub> film(b) TEM image of three-layer PI/SiO<sub>2</sub>-PI-PI/SiO<sub>2</sub> film

Figure 4.2 SEM image of surface topography of single and multi-layer nanoparticles dispersion



(a) PI film after surface discharge aging

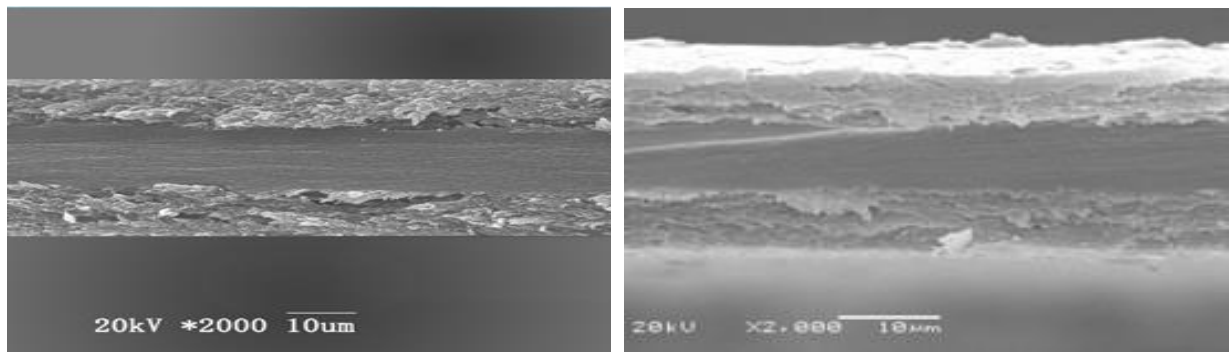
(b) PI/Al<sub>2</sub>O<sub>3</sub> multilayer surface discharge aging(c) PI/Al<sub>2</sub>O<sub>3</sub> before aging cross-section view(d) PI/Al<sub>2</sub>O<sub>3</sub> cross-section view after aging

Figure 4.3 SEM image of surface topography of single and multi-layer nanoparticles dispersion

The chances to occur PD increase due to the presence of voids. Apparently, if these voids are subjected consistently to a higher voltage than PDIV, material deterioration is certain, and



chances of failure will increase. After applying pulse voltage aging, despite nanocomposite or pure PI film, the surface of the top layer of the film becomes rough and some mesh occurs, as shown in Figure 4.3(c, d). The microscopic structure changing in the center layer of film is not obvious after aging. Therefore, surface corona discharge and charge injection from electrodes are the main factors that result in the failure of PI films. Damage of film under the pulse electric field begins at the surface of the film and penetrates deeper into the material.

#### 4.2.2 FTIR analysis

When one monomer reacts with another monomer, it forms a carbon chain of the polymer. In our case, a single unit of two monomers, such as diamine (ODA) and dianhydride (PMDA), reacts with each other to form a single unit of poly amic acid (PAA) solution. In this reaction, the oxygen atom of diamine reacts with the hydrogen atom of dianhydride and the hydrogen atom of dianhydride reacts with the carbon atom of diamine, to give us a repeated unit of PAA. After obtaining PAA, thermal imidization was applied to cure PI and PI/SiO<sub>2</sub> films. The composition of the PI atomic structure was studied by FTIR spectroscopy to analyze the chemical bonds present in PI and PI/SiO<sub>2</sub> films. This part describes the chemical characterization of half cured and fully cured PI and PI/SiO<sub>2</sub> films. The range of wavelength used was from 650 cm<sup>-1</sup> to 4000 cm<sup>-1</sup>. The repeated molecular structure of PI and possible bonding interaction of PI polymer chains and the surface of SiO<sub>2</sub> nanoparticles are sketched below in Figure 4.4.

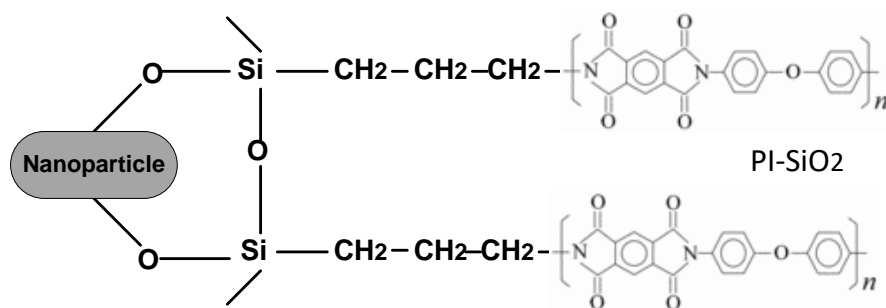


Figure 4.4 PI molecule structures and bonding interaction between PI and SiO<sub>2</sub>

The PI sub-atomic structure is composed of a molecular chain containing the functional groups such as aromatic rings, imide rings, and some non-cyclic ether rings. These functional groups have discrete chemical bonds such as C-N-C, C=O, benzene (C<sub>6</sub>H<sub>n</sub>), ether link (C-O-C), and -OCH<sub>2</sub>-CH<sub>2</sub> deformation. The functional groups of PI polymer chains provide the level of linkage with sub-atoms, as well as the linkage with silicon oxide nanoparticles. In FTIR, infrared radiation was passed through the samples. Some of the rays were absorbed by the samples and some were passed through the samples to provide a specific spectrum. The resulting spectrum expresses the fingerprint of the sample with absorption peaks, which correspond to the occurrence of vibrations between the bonds of sub-atoms of the material. Hence, FTIR can distinguish the types of chemical bonds and determine the material type. Figure 4.6(a, b) are

showing the FTIR spectra of half cured and fully cured bonds of PI at different temperatures and different times. In fully cured PI films, the bonds are grouped into imide rings, aromatic rings, and noncyclical stretching on the basis of atoms vibrations [95]. The strength of the absorption band at  $3364\text{ cm}^{-1}$ , which corresponds to stretching vibration of  $\text{-OH}$  and the bending vibration of  $\text{H-O-H}$  at  $1625\text{ cm}^{-1}$ , is increased for the modified  $\text{SiO}_2$  nanoparticles, as shown in Figure 4.5. These could indicate interactions between  $\text{-OH}$  groups and the modified  $\text{SiO}_2$  nanoparticles.

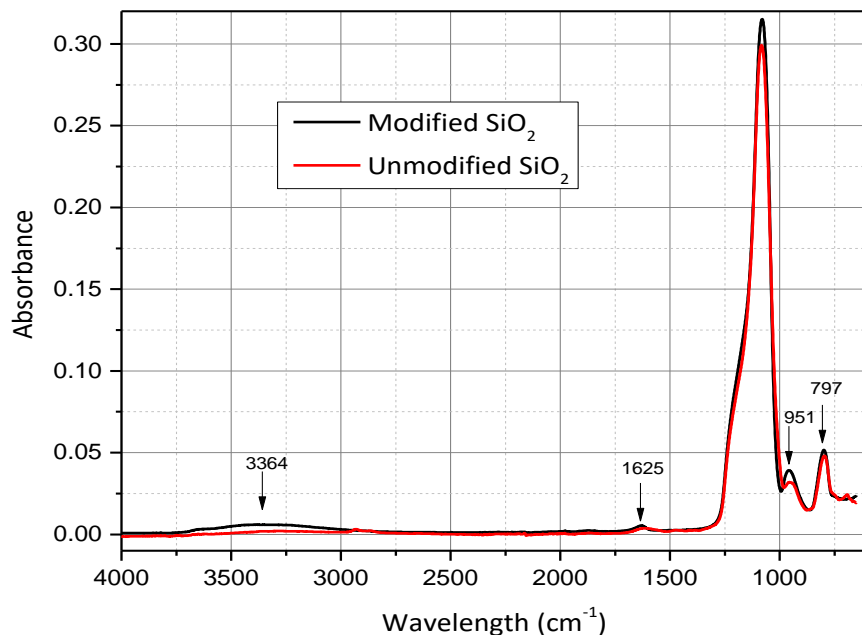
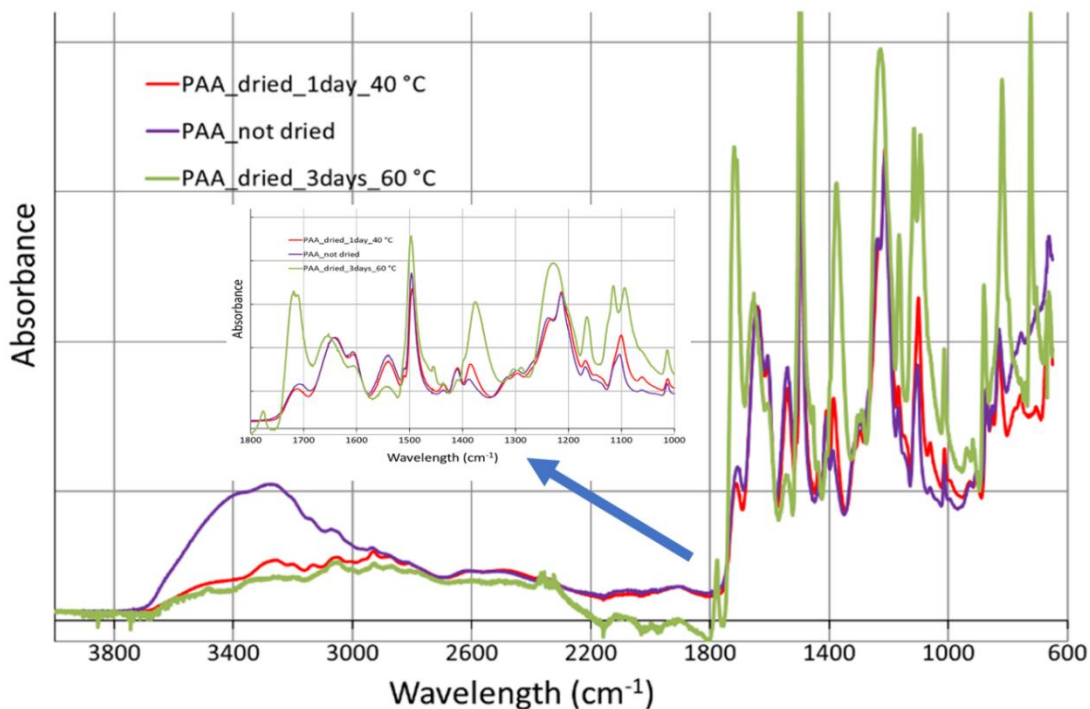


Figure 4.5 Modified and unmodified  $\text{SiO}_2$  nanoparticles



(a)

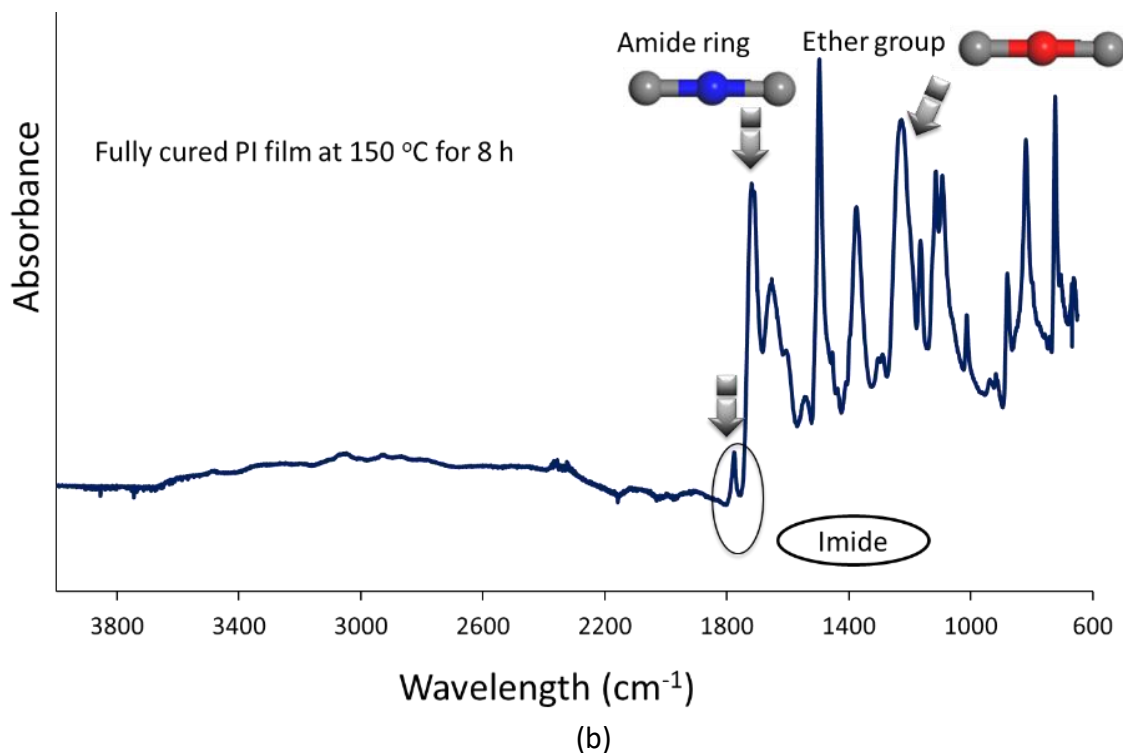


Figure 4.6 (a) Half cured PI film at different temperatures and times (b) Fully cured PI film

### 1) Imide ring

This group contains imide carbonyl in phase and out of phase stretching, the C-N-C axial, transverse and out of plane stretching. The absorbance peaks at  $1371\text{ cm}^{-1}$ ,  $1112\text{ cm}^{-1}$ , and  $721\text{ cm}^{-1}$  indicate the transverse and axial stretching of the C-N-C bond; the reason of  $1774\text{ cm}^{-1}$  and  $1712\text{ cm}^{-1}$  peaks are in-phase and out-of-phase stretching of C=O in imide ring, as shown in Table 4.1.

Table 4.1 FTIR spectrum for imide ring

Group	Chemical bond	Wavenumber ( $\text{cm}^{-1}$ )
Imide ring	C-N-C out of phase bending	721
	Imide C-N-C transverse stretching	1112
	C-N-C axial stretching	1371
	C=O out of phase vibration	1712
	C=O in-phase vibration	1774

### 2) Aromatic ring

It is divided on the basis of tangential, radial skeletal and out of plane vibrations. The peak at  $1590\text{ cm}^{-1}$  relates to tangential C-C vibrations. The peak at  $1280\text{ cm}^{-1}$  is tangential phenyl ring vibrations. The others  $1480\text{ cm}^{-1}$ ,  $1168\text{ cm}^{-1}$ ,  $1087\text{ cm}^{-1}$ ,  $1011\text{ cm}^{-1}$ ,  $843\text{ cm}^{-1}$ ,  $788\text{ cm}^{-1}$  peaks describe the tangential, radial skeletal and out-of-plane bending vibrations of  $\text{C}_6\text{H}_n$  in the aromatic ring, as shown in Table 4.2.

Table 4.2 FTIR spectrum for aromatic ring

Aromatic ring	Tangential vibrations	C <sub>6</sub> H <sub>4</sub>	1012
		C <sub>6</sub> H <sub>4</sub>	1087
		C <sub>6</sub> H <sub>3</sub>	1164
		C <sub>6</sub> H <sub>3</sub>	1286
		C <sub>6</sub> H <sub>4</sub>	1303
		C <sub>6</sub> H <sub>5</sub>	1496
		C <sub>6</sub> H <sub>4</sub>	1596
	Radial skeletal vibrations	C <sub>6</sub> H <sub>3</sub>	565
		C <sub>6</sub> H <sub>4</sub>	634
		C <sub>6</sub> H <sub>5</sub>	752
	Out of plane bending vibrations	C <sub>6</sub> H <sub>3</sub>	601
		C <sub>6</sub> H <sub>4</sub>	703
		C <sub>6</sub> H <sub>4</sub>	775
		C <sub>6</sub> H <sub>4</sub>	800
		C <sub>6</sub> H <sub>4</sub>	815
		C <sub>6</sub> H <sub>3</sub>	881
		C <sub>6</sub> H <sub>3</sub>	914
		C <sub>6</sub> H <sub>4</sub>	937

### 3) Non-cyclical ether vibrations

The peaks at 1234 cm<sup>-1</sup> and 1454 cm<sup>-1</sup> relate to the bond of ether link (C-O-C) and 1416 cm<sup>-1</sup> peak corresponds to -OCH<sub>2</sub>-CH<sub>2</sub> deformation, as shown in Table 4.3.

Table 4.3 FTIR spectrum for ether group

Non-cyclic	C-O-C	1234
	-OCH <sub>2</sub> -CH <sub>2</sub> deformation	1454

### 4.3 Thermomechanical analysis of rheological tests

A thermomechanical analysis makes it possible to determine the morphology of the polymer (amorphous or semi-crystalline) and allows to define the limits of the characteristic thermal domains (glassy state, rubbery or flow zone) as well as the associated temperature limits (glass transition temperature) [115]. The exploitation of viscoelastic quantities allows after calculation to go back to other key data. For example, from the stiffness measured in the rubber plate, it is possible to define the density of tangles (in the case of thermoplastics) or of crosslinking (in the case of thermosets). In the end, it should be remembered that rheological analysis is a powerful and versatile characterization tool that is often essential in any subject aimed at establishing "structure-property" relationships. On a technical level, the study of rheology in dynamic mode consists in determining the viscoelastic properties of a system by subjecting the sample to sinusoidal stress [125], [126]. If the experiment is carried out with imposed constraint and that the latter is applied in a sinusoidal way with time, one can write it in the form as equation (4.1).

$$s = s_0 \sin(\omega t) \quad (4.1)$$

With  $\omega$  (rad/s) the pulsation. The resulting deformation is itself sinusoidal with the same pulsation but is phase shifted by an angular value. Its mathematical expression is in equation (4.2).

$$\gamma = \gamma_0 \sin(\omega t - \delta) \quad (4.2)$$

The phase shift angle between the deformation and the stress has a value between  $0^\circ$  (characteristic of an elastic solid) and  $90^\circ$ , in the case of a viscous liquid. By associating to each quantity its complex component, it is possible to define the complex shear modulus in equation (4.3).

$$G^* = \sigma^* / \lambda^* = \frac{\sigma_0 e^{j\omega t}}{\gamma_0 e^{j(\omega t - \delta)}} = G_0 \cos(\delta) + jG_0 \sin(\delta) \quad (4.3)$$

Which can ultimately be written in the form:

$$\text{with } G' = G_0 \cos(\delta) \text{ and } G'' = G_0 \sin(\delta)$$

We call the real contribution  $G'$  as the "conservation modulus"; it characterizes the elastic behavior of the material and its rigidity, while  $G''$  is designated as the loss module and characterizes the dissipative component.

In this work, we used two dynamic rheometers with imposed stress (respectively an AR2000 from TA Instruments and an MCR102 or even 301 from Anton Paar). The latter has numerous measurement geometries, in order to be able to measure various materials from the liquid state to the solid-state. The Figure 4.7 illustrates the concept of the experiment in parallel plate geometry.

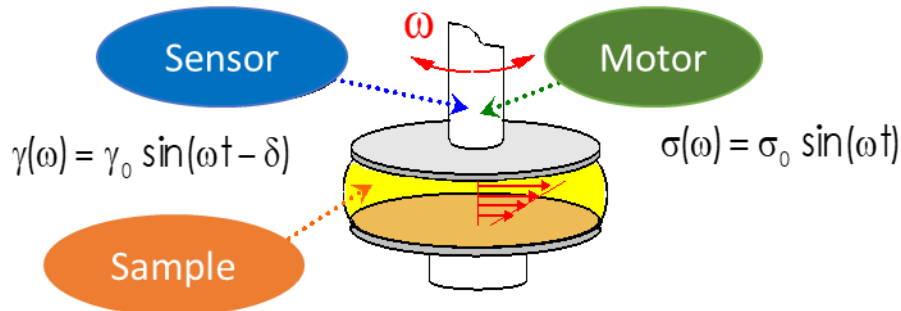
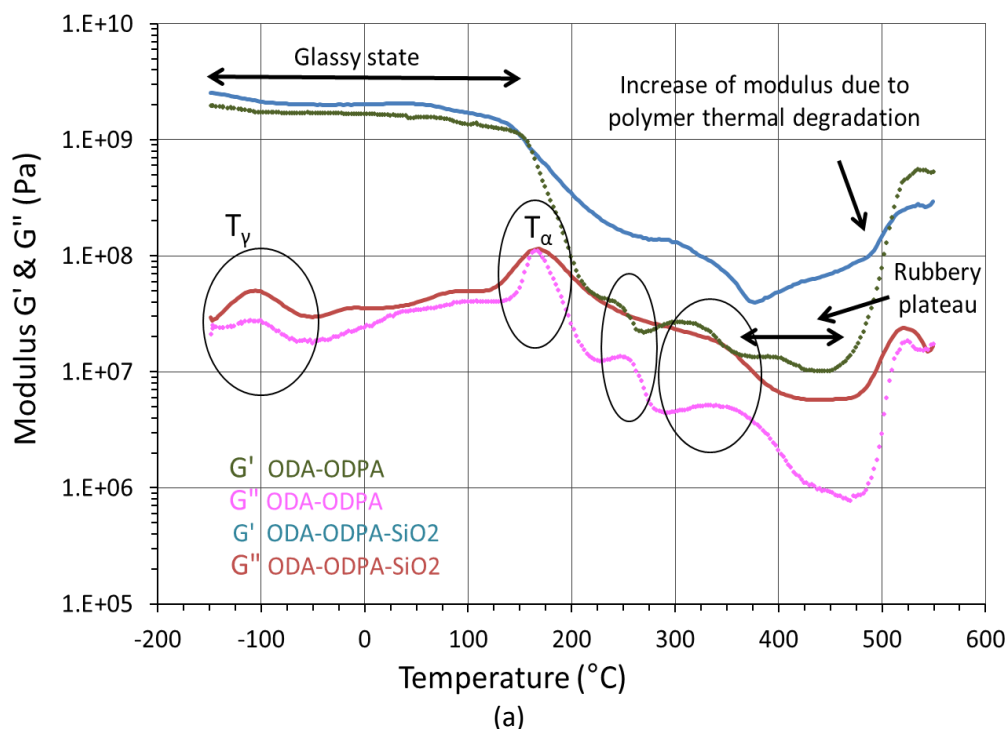


Figure 4.7 Schematic representation of the plane-plane geometry (diameter 25 mm)

Thermomechanical analysis of polyimide and their derived nanocomposites was performed using the rheological test. Two monomers ODPA and PMDA dianhydride were compared to check the mechanical flexibility and glass transition state. MCR rheometer equipped with DMA accessories was used to find the relaxation peaks during the sample softening process, which

become visible in the glass transition region. The analysis technique enables the quantification of PI nanocomposite sample transition from its solid state to the rubbery plateau state. The thermomechanical results provide all information such as the melting point  $T_m$ , the glass transition temperature  $T_g$ , the secondary  $\beta$ - and  $\gamma$ -relaxations, and the shear modulus at a given temperature. The glassy and rubbery states of PMDA and ODPA based PI nanocomposite films are shown in Figure 4.8. In Figure 4.8(a), the “ $T_\gamma$ ” peak is the secondary rheological relaxation due to the oscillation of the aromatic groups present in the polymer skeleton. The main  $T_\alpha$  process is the main rheological relaxation due to the glass transition temperature of the polymer.  $T_g \cong 162^\circ\text{C}$ . It seems corresponding to the diacid polymer  $T_g$  that remains predominant. The relaxation peak at  $247^\circ\text{C}$  (taken at the max of  $G''$ ) is due to the glass transition of the polyimide phase. In other words, the imidization seems not to be completed. The next relaxation peak around  $337^\circ\text{C}$  (taken at the max of  $G''$ ) is due to the glass transition of the polyimide, which showing again the imidization seems not to be completed. The thermomechanical profile of silica mixed PI films shows that the addition of 1% nano  $\text{SiO}_2$  to the PI films induces a slight increase of the mechanical rigidity: a broadening of the different mechanical relaxation peaks, but without any shift along the temperature axis. In Figure 4.8(b),  $T_\gamma$  process is the secondary rheological relaxation due to the oscillation of the aromatic groups present in the polyimide skeleton.  $T_\beta$  process in Figure 4.8(b) is the secondary rheological relaxation due to the cooperative motions of aromatic and imide cycles.  $T_\alpha$  process corresponds to rheological relaxation due to the glass transition temperature of the polymer. In this case, the polymer seems fully imidized.  $T_g \cong 357^\circ\text{C}$  is significantly higher than that characteristic of ODA-ODPA (PMDA is stiffer).



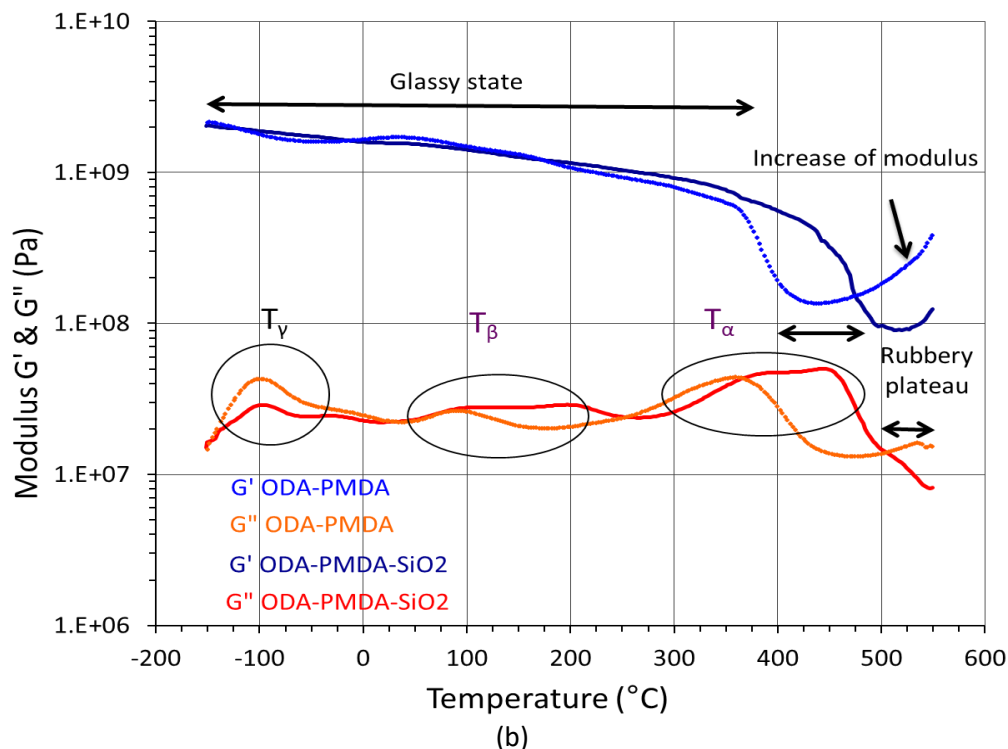


Figure 4.8 Thermomechanical analysis of (a) ODA-ODPA based PI nanocomposite films  
(b) ODA-PMDA based PI nanocomposite films

After the addition of 1% SiO<sub>2</sub> in PMDA based polyimide films, a reduction of the amplitude of the  $\gamma$ -relaxation is observed compared to the neat polyimide film: a split-up of the  $\beta$ - and  $\alpha$ -relaxations. For each relaxation, the lowest component is due to the rheological behavior of the classical macromolecular chains. It is unchanged compared to that characteristic of the neat polymer. The highest component is attributable to the more reduced molecular motion of the chains in the vicinity of the mineral filler. The reduction of the molecular mobility close to the filler induces an increase in the apparent glass transition temperature. The highest  $T_g$  value is taken at the maximum of  $G''$  is about 447 °C. Similar discrepancies are expected on dielectric properties.

#### 4.4 Thermal conductivity analysis

Thermal conductivity is the measure of heat transfer depending upon the radiation and convection property of the material. In convection material, direct contact is necessary to transfer heat, while in radiation the energy is transferred using emission and absorption phenomenon. The thermal conductivity is time-dependent and it is measured as the amount of heat that transfers through a unit cube of material in a unit of time, when the temperature difference between the opposite sides of the cube is 1 K [117].

The first relation between heat transfer and temperature difference came in 1822 by Fourier. When the heat is transferred through the material, a temperature gradient is produced

in the direction of the heat flow. The relation between temperature gradient and heat transfer is given as the equation (4.4) [127], [128].

$$q = -\lambda \frac{dT}{dx} \quad (4.4)$$

Where  $\lambda$  is the thermal conductivity of the material and measured in unit of W/m·K [182]. In dielectric materials such as polyimide films, the heat is transmitted using heat carriers such as electrons, phonons, and photons. The intensity of heat transmission depends on the scattering of phonons. For higher thermal conductivity, the phonon should be scattered closely. The thermal conductivity for single and multilayer PI, FPI and PI/nanocomposite samples were measured and results are compared with each other, as shown in Figure 4.9. The pure PI and fluorination PI films show less value of thermal conductivity compared to single and multilayer PI/nanocomposite films. Most polymers including the PI have low thermal conductivity between 0.1 to 0.6 W/m·K. Adding high thermal conductive nanoparticles, such as  $\text{Al}_2\text{O}_3$  and  $\text{SiO}_2$ , in the polyimide matrix doubled the thermal conductivity of PI/nanocomposite films. The thermal conductivity for single layer PI/nanocomposite films is slightly lower than the multilayer PI/nanocomposite films. It can be due to the nanoparticles agglomeration in single layer films. The scattering of phonons in single layer PI/nanocomposite films faces some barriers and flaws due to nanoparticles agglomeration and impurities.

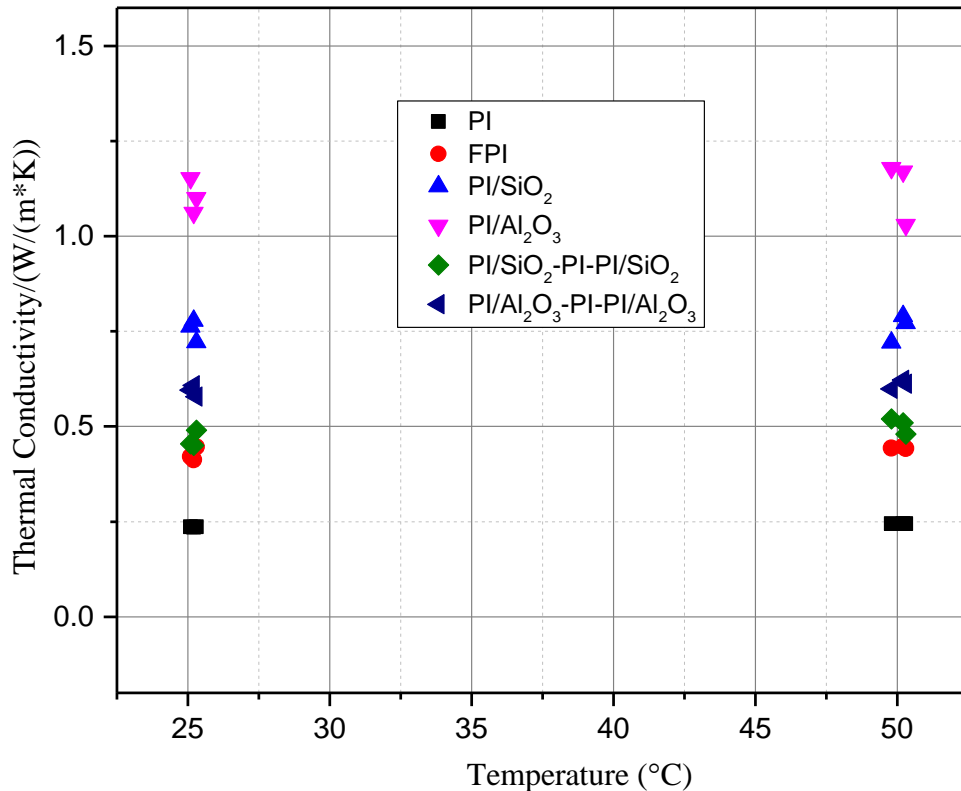


Figure 4.9 Thermal conductivity of different samples as a function of temperature



The size of the nanoparticles and the structure of the sample put a significant impact on heat transfer. Adding nanoparticles on the top and bottom layer of composite samples improves the heat transfer of composites, since heat is mainly transferred through the surface of the nanoparticles. The nanoparticles can form a percolation chain to take heat from the conductor and transfer to the atmosphere. Since the thermal conductivity of  $\text{Al}_2\text{O}_3$  is higher than  $\text{SiO}_2$ , microparticles of alumina will transfer heat much faster in the micro composite compare to nanocomposite, but at the same time, it will affect its electrical properties. Phonons, which are responsible for heat conduction in dielectric materials, are scattered at the interface between two different types of materials. The heat dissipates on the surface of nanoparticles to a higher degree than on the surface of microparticles.

After nanoparticles surface modification using the coupling agent, an interphase region is formed on the surface of nanoparticles, which links inorganic nanoparticles and the polyimide organic matrix; the heat transfer can be controlled by this interphase region. Furthermore, these interphases can extend the corroded path caused by corona discharge and enhance the corona resistance lifetime. The thermal conductivity of pure PI film is 0.15 W/m.K, but the thermal conductivity of  $\text{Al}_2\text{O}_3$  nanoparticles is about 30 W/m.K. With the addition of nanoparticles, the thermal conductivity of PI molecular chain can be increased [31]. The measured thermal conductivity of multilayer PI/ $\text{Al}_2\text{O}_3$ -PI-PI/ $\text{Al}_2\text{O}_3$  samples is around 0.56 W/m.K. High thermal conductivity of PI/ $\text{Al}_2\text{O}_3$  is valuable to dissipate the heat in the bulk, which can decrease the thermal aging effects.

#### 4.5 Dielectric constant and dielectric loss

Higher dielectric constant will lead to slower propagation of light to insulation and thus enhance insulation polarization. Within the area of an electric field, the polarized molecules or atoms in the medium become dipole moments. This effect can lower the electric field intensity and energy loss. The dielectric constant and the dielectric loss for all types of samples at different temperatures and frequencies were measured and the results are shown in Figure 4.10, Figure 4.11 and Figure 4.12. In general, we observed a decrease of dielectric constant with the increase of frequency for all samples. This can be explained that the dielectric constant of the insulation is determined by the numbers of oriented dipoles and their capacity to align in the direction of the electric field [71], [98], [129]. At low frequency, more aligned dipoles will give rise to high dielectric constant, while with the increase of frequency, it is difficult for dipoles to align in the direction of the electric field, which will lead to relatively low dielectric constant [67].

Another observation from Figure 4.10(a) is that the dielectric constant increases with the addition of nanocomposite layers on the top and bottom side of PI film, whatever the frequency. This is attributed to the formation of new bonds due to the presence of nanoparticles on the surface, which are easy to polarize in the presence of the electric field. The

dielectric constant of nanocomposite increases with the increase of nanoparticles volume fraction [130]–[132]. Nanocomposite has higher permittivity compared with the PI matrix, because two types of interface exist in the multilayer structure. One kind exists between PI matrix and nanoparticles and the other type exists between layers (composite layer and pure PI layer). In the presence of an external electric field, a number of negative and positive charges accumulate at the interfaces region of multilayer samples, which will increase the interfacial polarization phenomenon and thus lead to a higher dielectric constant. The type and size of filler particles can have a significant effect on the dielectric constant of the material.  $\text{Al}_2\text{O}_3$ -PI- $\text{Al}_2\text{O}_3$  nanocomposite has a higher dielectric constant compared with  $\text{SiO}_2$ -PI- $\text{SiO}_2$  structure nanocomposite due to the fact that  $\text{Al}_2\text{O}_3$  has higher inherent permittivity ability [71]. Therefore, it can be concluded that  $\text{Al}_2\text{O}_3$  based samples show a higher dielectric constant than  $\text{SiO}_2$  based samples. Dielectric loss is the reciprocal of the ratio between the resistance of the insulating material to its capacitive reactance at a certain frequency. After becoming polarized, PI or any dielectric material stores the electrical energy under AC field applications. Some of these stored electrical energies can be lost in the form of heat. Therefore, both the real and imaginary part of dielectric property is important to be measured. Tan delta loss of samples, as a function of frequency in the log-log coordinate axis, is shown in Figure 4.10(b) and Figure 4.11(b). Whenever there is a change in permittivity, a peak will be observed belong to a specific change. Layered nanocomposite dielectrics exhibit higher energy loss than single-layer samples. This phenomenon may be related to the incorporation of the nanoparticles, which results in more ions, dipoles, charge carriers and interaction zones.

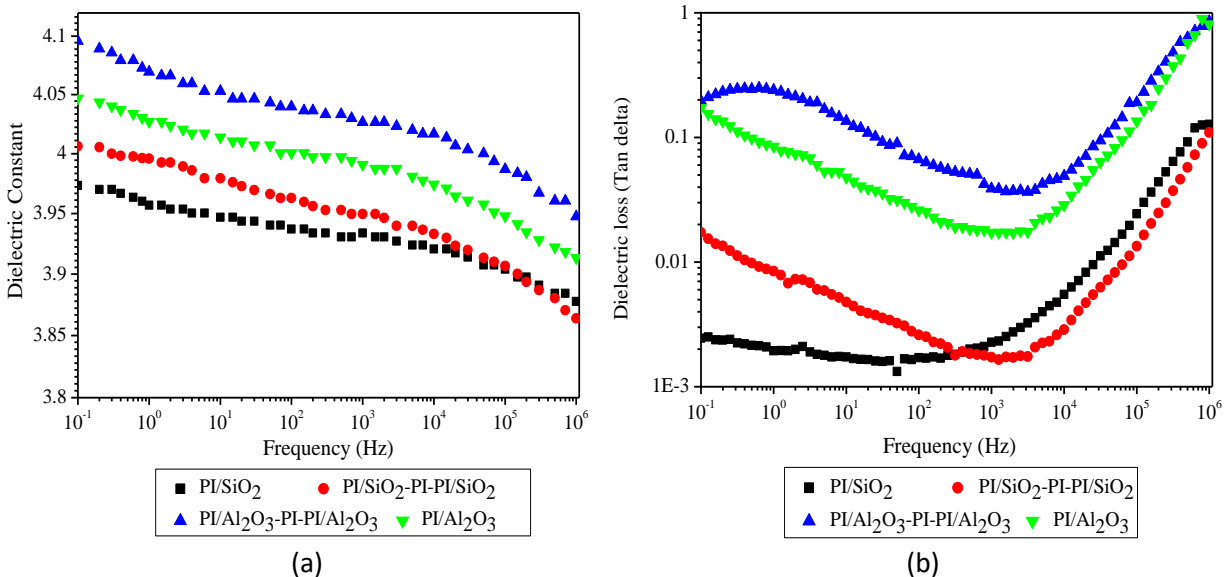


Figure 4.10 Dielectric response (a) dielectric constant (b) dielectric loss as a function of frequency

It can be apparently seen that two peaks occur in the studied frequency range of  $10^{-1}$  Hz- $10^6$  Hz, revealing two relaxations processes existing in these dielectrics, interfacial polarization

and dipole polarization, which correspond to the peak at around  $10^0$  Hz and  $10^3$  Hz, respectively. After the first high peak, the values show a decreasing tendency until  $10^3$  Hz and after it shows an increasing tendency. The real and imaginary parts of the complex permittivity for all samples at 100 Hz, as a function of temperature, are shown in Figure 4.12(a, b). We observed the beginning of the first peak in Figure 4.12(b) at 100 °C and maximum value around 150 °C, then another rising peak at 300 °C. In Figure 4.12(b), the high value of peak at 100 °C can be attributed to  $\alpha$ -relaxation.  $\gamma$ -relaxation peak is not clearly visible at high temperature because obscured by the DC conductivity, which increases for nanocomposite samples especially for alumina-doped samples around glass transition temperature.

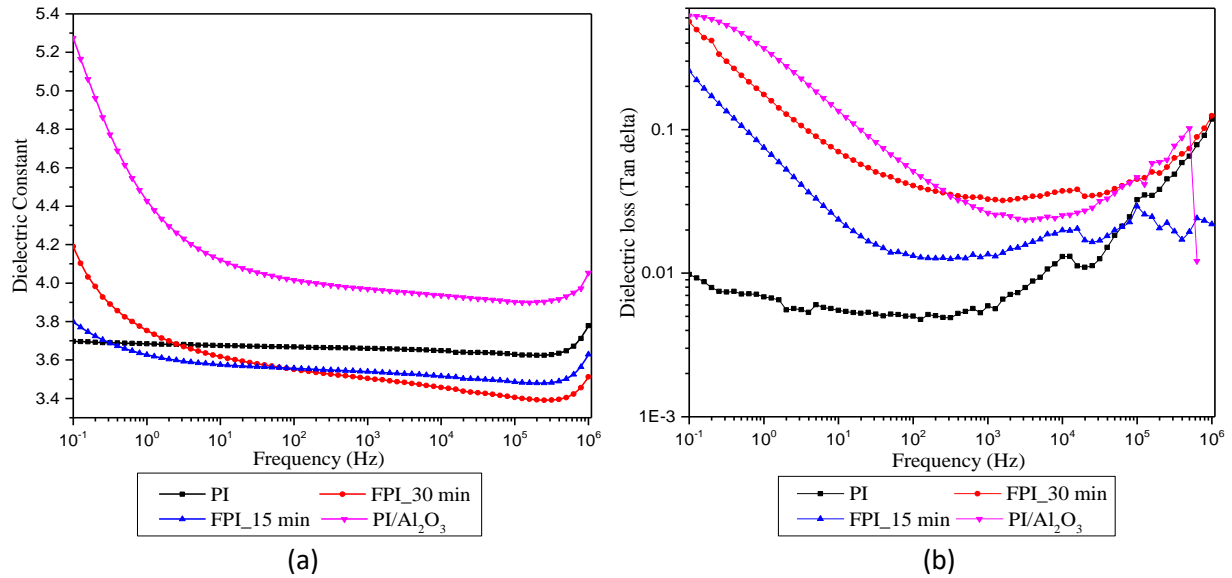


Figure 4.11 Dielectric response (a) dielectric constant (b) dielectric loss as a function of frequency

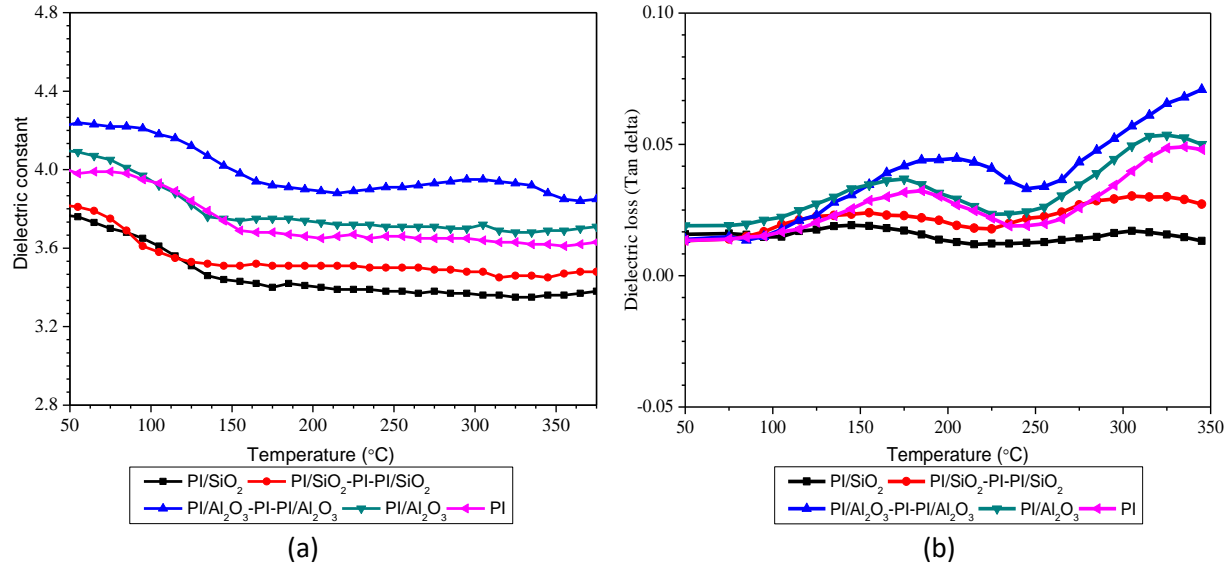


Figure 4.12 (a) Dielectric constant as a function of temperature at 100 Hz (b) Dielectric loss as a function of temperature at 100 Hz

The  $\beta$ -relaxation at low temperature is linked to the mobility of side chains in polyimide film. It can be apparently seen that two peaks for applied temperature range, revealing two relaxations, exist in dielectrics: interfacial polarization and dipole orientation. The surface functionalization of nanoparticles is crucial for nanocomposites [71]. The  $\beta$ -relaxation process for  $\text{Al}_2\text{O}_3$ -PI- $\text{Al}_2\text{O}_3$  is very similar to single layer alumina PI film, but the peak slightly shifted to higher temperatures. Composite with  $\text{SiO}_2$  on the other hand saw a shift of  $\beta$ -peak to lower temperature, compared to alumina filled samples.

#### 4.6 Dielectric breakdown strength

Weibull statistical probability method was used to compare the measured electrical breakdown strength, as shown in Figure 4.13, Figure 4.14 and Figure 4.15. The glass transition temperatures ( $T_g$ ) usually exist 350 °C for rigidly ordered polyimides, but those of 450 °C or above are preferred for multilayer dielectrics [133], [134]. In this experiment, temperature range between 25 °C to 400 °C is selected. The results in Figure 4.13 are showing the PI/nanocomposite film breakdown mechanism, mainly for the electric and thermal breakdown process. PI molecular chain structure is a tightly bond closed structure, that provides less flexibility to chain mobility; therefore it has a strong resistance to heat [90]. However, with the increase in temperature, the breakdown field strength is reduced. With the increase of temperature, the intensity of electric field under the same conditions enhances the mobility and injection of the electrons, and the number of charges in the localize region into PI film may increase, while heat provides internal excitation and makes electrons deep trap into the bulk of the material. High temperature reduces the interaction between the molecular chain and chain segments tend to break. These broken chain segments create free volume space in polymer chain and high temperature and high electric field will accelerate energy level of charge carriers. Therefore, the mobility and the chances of charge collision increase, which increase the localize electric field and the breakdown is certain. The effect of nanoparticles on electric breakdown has been investigated by several authors [71], [84], [135], [136]. The breakdown strength of nanoparticles due to changes in surface chemistry is illustrated in reference . From electrical breakdown results in Figure 4.13 and Figure 4.14, it is found that multilayer PI/nanocomposite films have higher electric breakdown strength as compared to nanocomposite of single-layer structure. Another interesting observation is that  $\text{SiO}_2$  gives higher breakdown strength as compared to  $\text{Al}_2\text{O}_3$ . This is because  $\text{Al}_2\text{O}_3$  permits higher relative permittivity and increases the ability to store charges, as compared to  $\text{SiO}_2$ . The electrical breakdown strength of PI/ $\text{SiO}_2$ -PI-PI/ $\text{SiO}_2$  samples is the highest among other types of samples till 200 °C. As the temperature increases above 200 °C, the breakdown strength of single-layer samples increases as compared to that of three-layer samples.

One reason can be the presence of defects between interfaces during sample synthesis, the other one is the breakage of new chemical bonds obtained from nano doped layers and PI

layer [31]. As the temperature increases, surface potential decay time decreases and hence the volume resistivity decreases and therefore breakdown strength also decreases; above 200 °C defects between interfaces and chemical bond breakage play a dominant role.

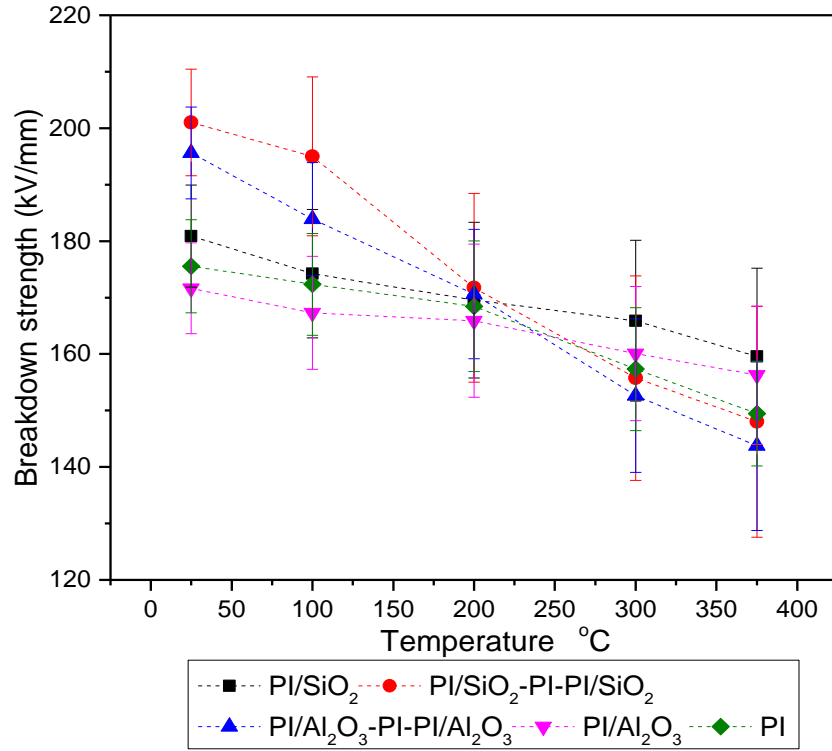


Figure 4.13 Electrical breakdown strength at different temperatures

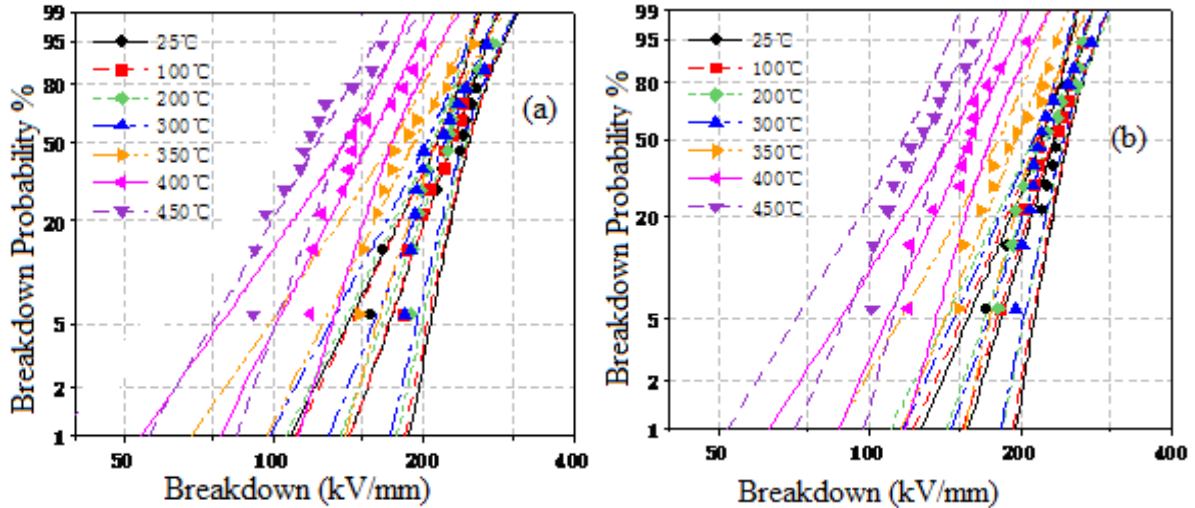


Figure 4.14 Breakdown Weibull statistic at different temperatures (a) PI (b) PI/Al<sub>2</sub>O<sub>3</sub>

Charges are injected from electrodes and accelerated by the applied electric field inside the film. When these charges collide with the outer layer of fillers that is bounded with the interfacial layer, they are decelerated. The decelerated charges would increase the tree initiation time. The tree propagation is impeded and blocked by the presence of nanoparticles.

Hence the total time increase for tree growth would result in an increase in electric breakdown strength. Therefore, it can be assumed that the nanoparticles on the top and bottom of surfaces act as a barrier against tree propagation. For further elucidation, it is important to combine chemical structure and charge dissemination together to pick up a more reliable mechanism for breakdown interpretation [86], [135], [137].

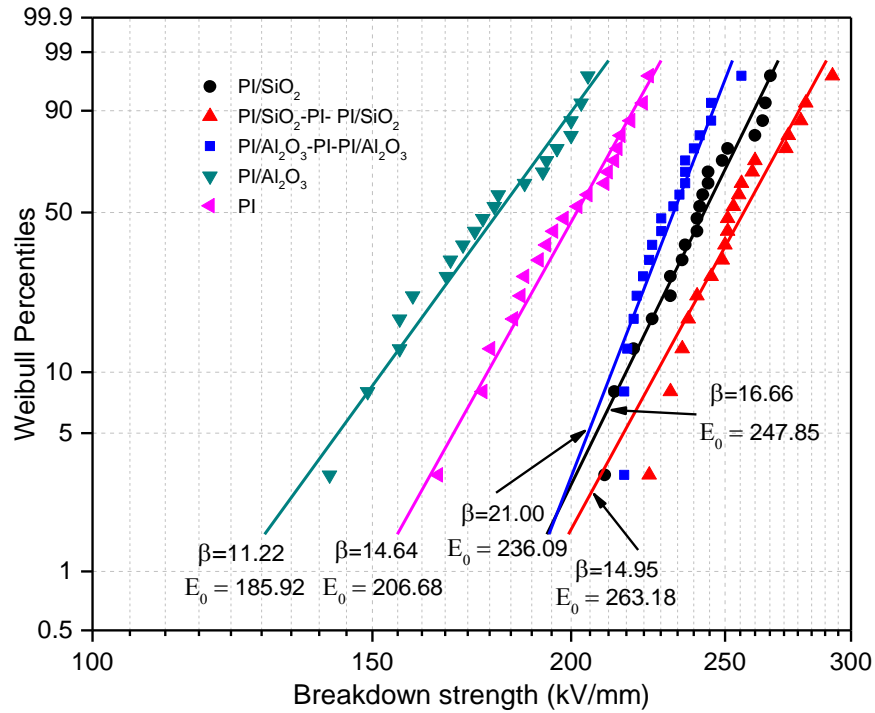


Figure 4.15 Breakdown Weibull statistic for all samples at 25 °C temperatures

In the case of surface discharge in our experiment, mostly corona discharge is shown up on the surface of samples around the top rod electrode. This kind of discharge could create ultraviolet rays, high-energy electrons, and high activity chemical groups, which would accelerate the degradation of insulation material. Where corona discharge exists, by measuring the corona resistance property, we can define the lifetime of insulating material in the application field. The failure of polymer dielectric is the fracture and degradation of the polymer chains, as described below in FTIR analysis. Figure 4.16 is showing the corona resistance lifetime of PI and PI/Al<sub>2</sub>O<sub>3</sub> aged and unaged samples, as a function of temperature. For each condition, five samples were tested for each temperature to get the average data points of lifetimes. It is shown that the corona resistance lifetime increases sharply with the addition of nano Al<sub>2</sub>O<sub>3</sub>. The PI/Al<sub>2</sub>O<sub>3</sub> presents excellent corona resistance ability. At 20°C, the lifetime of unaged PI samples is around 16 hours, and the lifetime of PI/Al<sub>2</sub>O<sub>3</sub> samples is around 97.5 hours, which is about 6 times longer than that of pure PI film [126], [127].

The corona resistance lifetime tests outcome demonstrate that the lifetime of samples decreases gradually with the increase in temperature, which makes it temperature dependent.

With the addition of nanoparticles into PI film, the composite material becomes thermal conductive, which will pass some heat from conductor to atmosphere and will improve the lifetime at higher temperatures. The lifetime of PI/ $\text{Al}_2\text{O}_3$  nanocomposites reduces with the increase in temperature, however, keeping up the perspective improvement compared to the pure PI sample. Despite of temperature level, the lifetime of aged PI film is the lowest. The corona resistance lifetime of samples with addition of  $\text{Al}_2\text{O}_3$  nanoparticles is about 6 times longer at  $25^\circ\text{C}$  comparing to the lifetime measured at  $230^\circ\text{C}$ . Other related conclusions of the temperature effects on voltage endurance are in reference [84]. Going into further details about results in Figure 4.16, it is concluded that nanoparticles can adequately improve the corona resistance property derived from the following perspectives. Firstly, surface discharge corroded the polymer chain during corona resistance testing. The  $\text{Al}_2\text{O}_3$  nanoparticles on the surface of films can constitute a protecting layer and oppose the harm of corona discharge directly, enhancing the corona resistance properties. Secondly, the reduction in corona energy due to interface layers between nanoparticles and PI chains plays an important role to decline the corroded effects on the dielectric surface. In addition, these interfaces can extend the corroded path caused by corona discharge and make longer the corona resistance lifetime [71]. Thirdly, the thermal conductivity of pure PI film is  $0.15\text{ W/m.K}$ , but the thermal conductivity of  $\text{Al}_2\text{O}_3$  nanoparticles is about  $30\text{ W/m.K}$ . By adding nanoparticles, the thermal conductivity of PI is increased. The thermal conductivity of PI/ $\text{Al}_2\text{O}_3$  samples is around  $0.51\text{ W/m.K}$ , measured by using the tester of thermal conductivity with the JTRG-III type. High thermal conductivity of PI/ $\text{Al}_2\text{O}_3$  is valuable to dissipate the heat in the bulk, which can decrease the thermal aging effects.

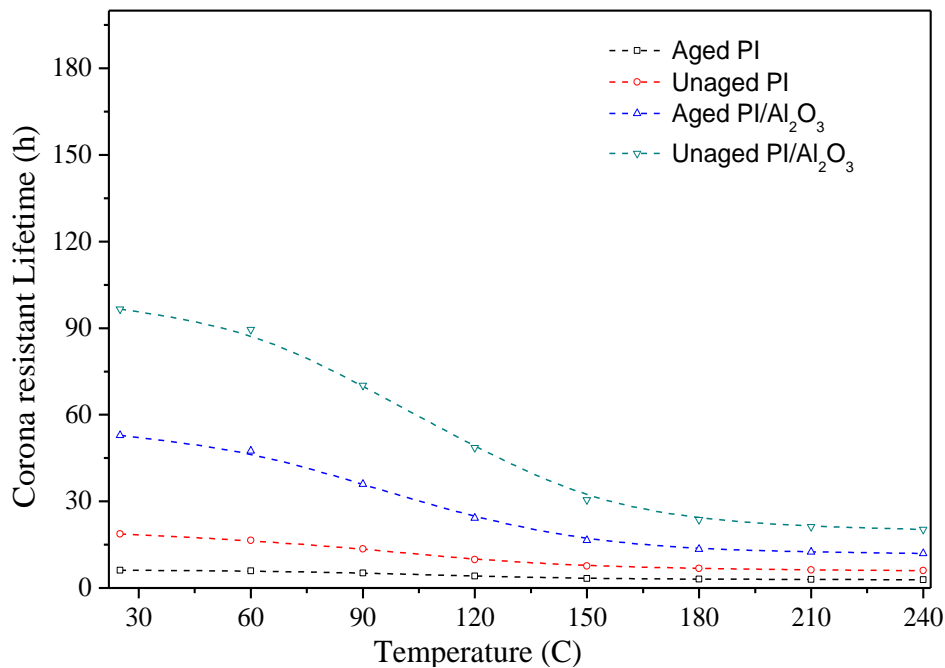
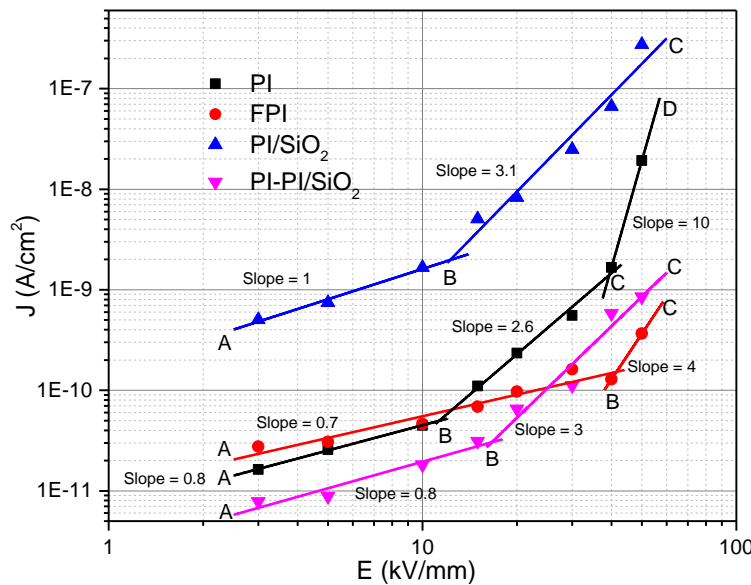


Figure 4.16 PI and PI/ $\text{Al}_2\text{O}_3$  corona resistant lifetime tests

#### 4.7 Current-voltage characteristics

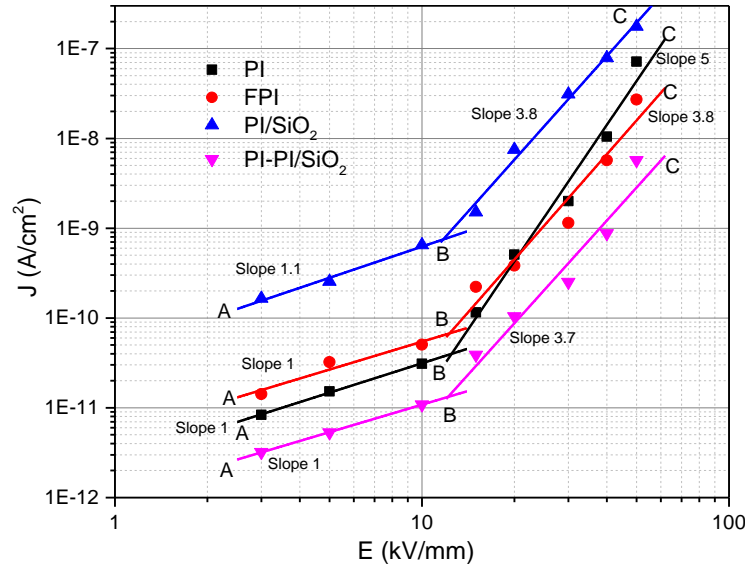
For the studied samples (films), the obtained conduction current density values versus the applied field are represented in Figure 4.17 (a, b and c). By analyzing the evolution of the conduction currents versus the applied electric field, we can observe an increase in conduction current, in case of fillers added in the polyimide matrix at low temperature, but conduction current decrease for nanocomposite samples at high temperature. All the materials show similar behavior at low electric fields ( $< 16$  kV/mm), but the single-layer PI/SiO<sub>2</sub> and fluorinated samples (FPI) seem to be more conductive at low electric fields compared to the pure PI and multilayer PI-PI/SiO<sub>2</sub> films. This could favor the charge flow and thus reduce its accumulation in the material [137], [138], [139]. Considering the change in the slope of the current density  $J$ , as shown in Figure 4.17, we observed that the films have at least two to three conduction types, depending on the electric field. At first, an ohmic behavior seems to be confirmed by a slope close to 1, corresponding to a linear variation of the current density versus the electric field. Normally, the ohmic current dependence is only due to the contribution of the intrinsic charges. At higher electric field the injection phenomenon increases, after a certain voltage threshold, the ohmic conduction is replaced by current-voltage dependence.



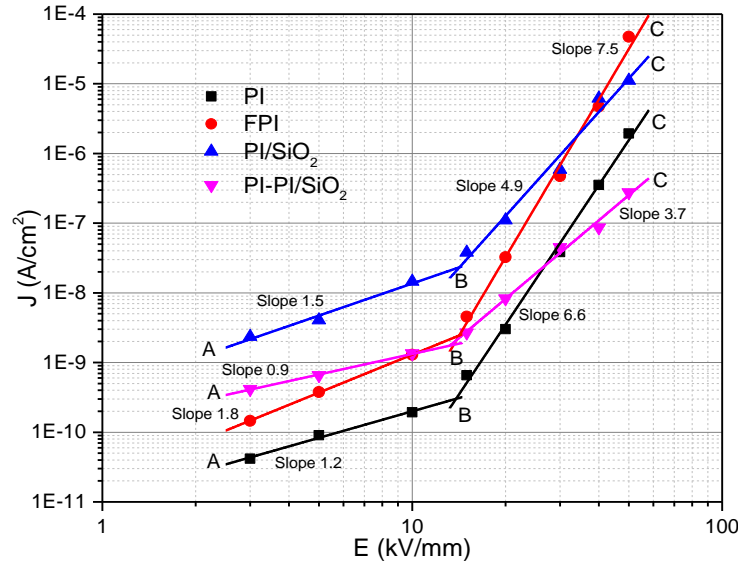
(a) Conduction current density versus electric field at 50 °C

In this particular case, dependence between the current density and the electric field confirmed by slopes higher than 1 was found and this behavior could be associated with the different conduction phenomena happening in the samples. It is interesting to observe that the current densities for the single-layer PI/SiO<sub>2</sub> samples are the highest, whatever the electric field and temperature, while multilayer PI-PI/SiO<sub>2</sub> samples show in most of the cases the lowest current densities except 150 °C. This could explain that the nanoparticles favor the charge flow when agglomerated and reduce charge flow when dispersing homogenously.





(b) Conduction current density versus electric field at 100 °C



(c) Conduction current density versus electric field at 150 °C

Figure 4.17 Conduction current density versus electric field at different temperatures

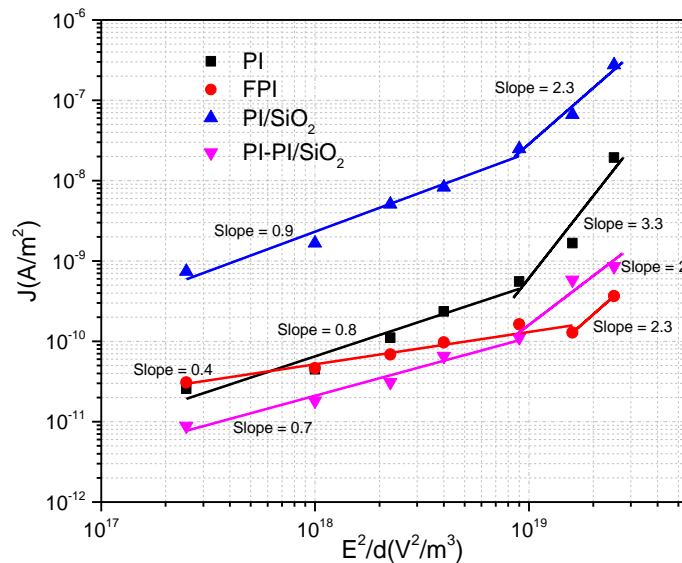
The results shown in Figures 4.17 are further analyzed to find the dominant injection or conduction mechanism in all samples, such as Schottky or Poole-Frenkel barrier injection. The Schottky injection can occur due to the activation energy of electrons at the electrode/dielectric interface due to the lowering of energy barrier at the interface. The Poole-Frenkel emission belongs to the conduction due to the electrons traps in the bulk of insulation. These trapped electrons can gain some activation energy to be de-trapped and participate in the conduction. Another conduction, which can increase the nonlinearity (Slope  $\geq 2$ ) in J-E plots, is due to the space charge limited current (SCLC), which can be influenced by the traps. Therefore, these models can apply to the experimental results to explain the conduction

mechanism. The results are analyzed using different representations of the conduction current density  $J$  with respect to the applied electric field  $E$ . After plotting the results in a log/log scale, as shown in Figure 4.17, we have observed an ohmic current in most of the samples with slope  $\leq 1$  at low field showing in the region AB. The applied threshold electric field of the order of 9 to 15 kV/mm, depending on the temperature, a nonlinearity in the conduction current rise with the slope  $> 1$ , indicating a nonohmic conduction mechanism. We divided the results into three regions marked as AB, BC and CD having different slopes, which implies that the  $J - E$  relation is of the type  $J \propto E^n$ , where  $n$  is the slope of the curve. The ohmic regions at 50 °C, 100 °C and 150 °C are shown with AB region in Figure 4.17. But for FPI and PI/SiO<sub>2</sub> films at 150 °C in Figure 4.17, the current density  $J$  is proportional to the square of the electric field in the first slope of region AB, which can be the characteristic of a Space Charge Limited Current (SCLC) regime, where the current density-electric field dependence is given by the equation 4.5 and plotted in Figure 4.18.

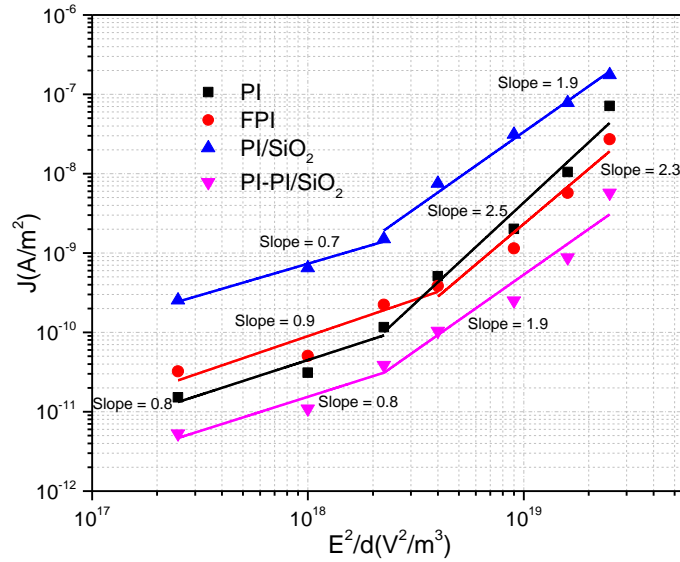
$$J = (9/8)\epsilon_r\epsilon_0\mu(V^2/d^3) \quad (4.5)$$

Where  $\mu$  is the carrier mobility,  $V$  is the applied voltage,  $d$  is the sample thickness,  $\epsilon_r$  is the relative permittivity of the material and  $\epsilon_0$  is the vacuum permittivity.

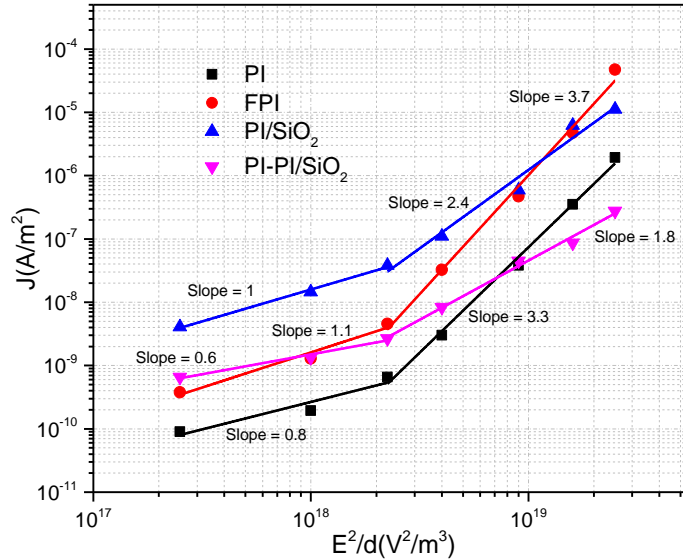
The slope of  $J$  vs.  $E^2/d$  line should be 1 to confirm the SCLC conduction. Slope  $< 1$  in Figure 4.18 are in area AB, in this area the dominant conduction mechanism is ohmic, thus it could not be SCLC mechanism. Slope 1 in fig. 4.18 represents the trap free SCLC, whereas the slope  $> 1$  represents the trap filled SCLC. From Figure 4.18 it can be seen that only for FPI and PI/SiO<sub>2</sub> at 150 °C temperature (better fit for FPI rather than PI/SiO<sub>2</sub>), the slope is equal to 1 which confirms the SCLC in this region [103]. Thus, it appears that SCLC mechanism is not the dominant mechanism in our samples in the studied conditions.



(a) Current/voltage characteristics in  $J$  vs  $E^2/d$  plots on log/log scale at 50°C



(b) Current/voltage characteristics in  $J$  vs  $E^2/d$  plots on log/log scale at 100°C



(c) Current/voltage characteristics in  $J$  vs  $E^2/d$  plots on log/log scale at 150°C

Figure 4.18 SCLC conduction mechanism at different temperatures

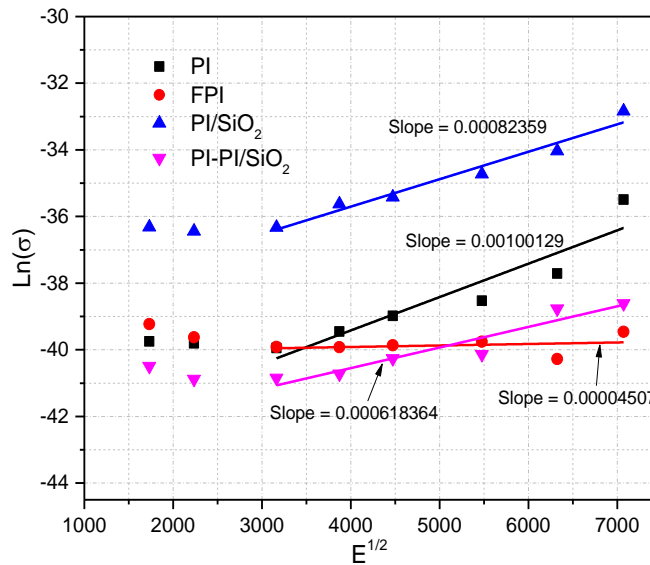
To conclude on it, it seems that SCLC would be only present at 150°C for FPI and PI/SiO<sub>2</sub> specimens. The second slope for PI, FPI, PI/SiO<sub>2</sub> and PI-PI/SiO<sub>2</sub> films obtained at high electric field has higher value which seems to correspond either to traps filled region or other conduction mechanism. The second slope of PI film at 50 °C and the second slope of PI and FPI films at higher temperatures 150 °C, is higher than 2, which could correspond to other conduction mechanism. The samples which have slopes region BC higher than 2 cannot be explained by the SCLC regime. The chemical and physical composition of sample related to the glass transition may affect the conduction in these regions. Thus, the conduction in these regions is mainly controlled by another mechanism. Other conduction mechanism, such as Schottky, Poole-Frenkel and hopping conduction have to be considered. The Poole-Frenkel

effect is a bulk conduction mechanism where the barrier between localized states is lowered due to the influence of the high electric field. The conductivity is given by equation (4.6) [143].

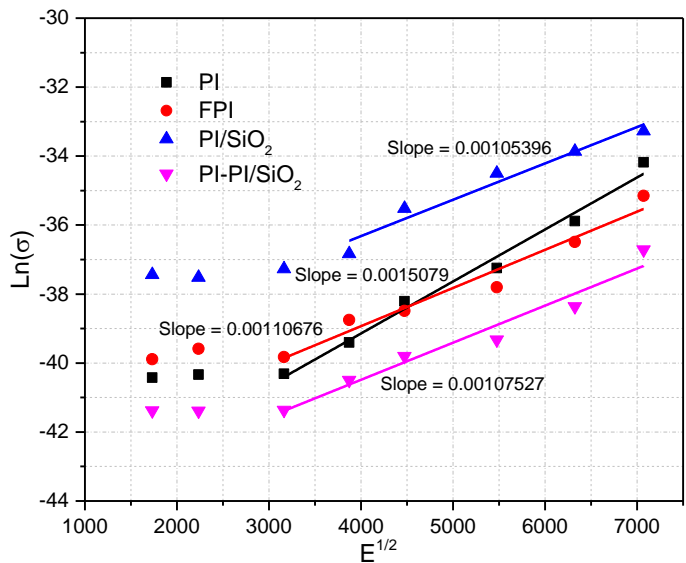
$$\sigma = \sigma_o \exp\left(\frac{\beta_{PF} \sqrt{E}}{kT}\right) \quad (4.6)$$

$$\beta_{PF} = (q^3 / \pi \epsilon_o \epsilon_r)^{0.5} \quad (4.7)$$

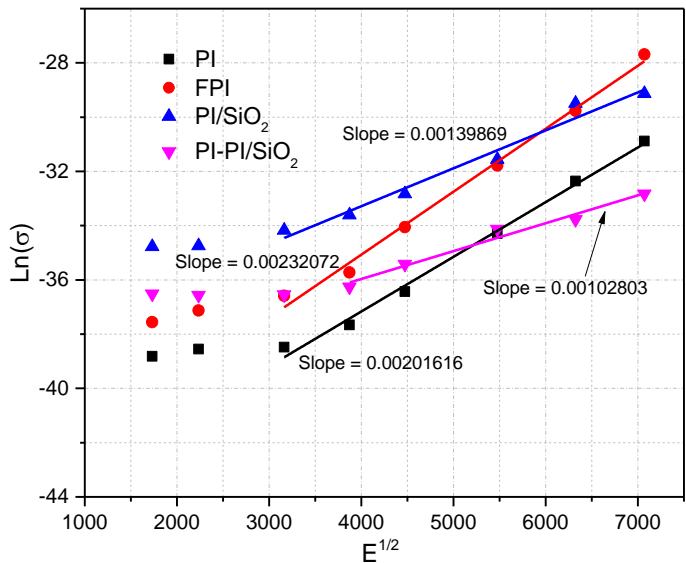
Where  $\sigma_o$  is the intrinsic conductivity of the material,  $\beta_{PF}$  is the Poole-Frenkel constant defined in equation (4.7),  $k$  is the Boltzmann constant and  $T$  is the absolute temperature. If this mechanism is dominant, the plot of  $\ln(J/E)$  versus  $E^{1/2}$  must be a straight line with a slope close to  $\beta_{PF}/(kT)$ . The  $\beta_{PF}$  coefficients are first calculated from the slope, and the dielectric constants are then estimated from these coefficients using Equation (4.7). If these dielectric constants agree with the values cited in the literature, it could be said that the samples follow the corresponding conduction mechanism. Representations in  $\ln(J/E)$  versus  $E^{1/2}$  coordinates are presented in Figure 4.19. These representations are not linear for FPI, PI/SiO<sub>2</sub> and PI-PI/SiO<sub>2</sub> films at 50 °C and their dielectric constant is in the range of 6 to 15, which is higher than the measured one. The slopes of these representations are also not linear for PI, FPI and PI/SiO<sub>2</sub> films at 150 °C and their dielectric constant is in the range of 0.8 to 2.2, which is lower than the measured one as shown in Table 4.4. Therefore, Poole-Frenkel conduction seems not to be the case for these films. But these representations can be seen linear for PI at 50 °C and linear for FPI, PI/SiO<sub>2</sub> and PI-PI/SiO<sub>2</sub> at 100 °C and their values are close to the calculated  $\beta_{PF}/(kT)$  values. It is also linear for multilayer PI-PI/SiO<sub>2</sub> nanocomposite films at 150 °C and their calculated dielectric constant from model is close to the measured one, which could confirm Poole-Frenkel conduction in these films.



(a) Current/voltage characteristics in  $\ln(\sigma)$  vs  $E^{1/2}$  plots at 50 °C



(b) Current/voltage characteristics in  $\ln(\sigma)$  vs  $E^{1/2}$  plots at 100 °C



(c) Current/voltage characteristics in  $\ln(\sigma)$  vs  $E^{1/2}$  plots at 150 °C

Figure 4.19 Poole-Frenkel conduction mechanism at different temperatures

Table 4.4 Comparison of slope value and calculated  $\beta_{PF}/kT$  value at various temperatures

Samples	$\epsilon_r$ (Measured)	Slope	$B_{PF}/kT$	$\epsilon_r$ (Calculated)	Temperature (°C)
PI	3.9	$1 \cdot 10^{-3}$	$1.4 \cdot 10^{-3}$	2.3	50
FPI	3.6	$0.4 \cdot 10^{-4}$	$1.4 \cdot 10^{-3}$	6.1	
PI/SiO <sub>2</sub>	3.95	$0.8 \cdot 10^{-3}$	$1.4 \cdot 10^{-3}$	9.2	
PI-PI/SiO <sub>2</sub>	3.98	$0.6 \cdot 10^{-3}$	$1.4 \cdot 10^{-3}$	15.1	
PI	4	$1.5 \cdot 10^{-3}$	$1.2 \cdot 10^{-3}$	2.4	
FPI	3.6	$1.1 \cdot 10^{-3}$	$1.2 \cdot 10^{-3}$	4.6	

PI/SiO <sub>2</sub>	3.65	1*10 <sup>-3</sup>	1.2*10 <sup>-3</sup>	5.5	100
PI-PI/SiO <sub>2</sub>	3.63	1*10 <sup>-3</sup>	1.2*10 <sup>-3</sup>	5.5	
PI	3.8	2*10 <sup>-3</sup>	1.1*10 <sup>-3</sup>	1	150
FPI	3.6	2.3*10 <sup>-3</sup>	1.1*10 <sup>-3</sup>	0.8	
PI/SiO <sub>2</sub>	3.5	1.4*10 <sup>-3</sup>	1.1*10 <sup>-3</sup>	2.2	
PI-PI/SiO <sub>2</sub>	3.58	1*10 <sup>-3</sup>	1.1*10 <sup>-3</sup>	4.3	

For the films which are not following Poole-Frenkel conduction, it is needed to explore other conduction mechanism. Therefore, the charge injection phenomenon previously mentioned, Schottky injection, is investigated for these films. In the case of Schottky injection, the potential barriers are reduced due to the applied electric field, and an electron can “jump” across the barrier [103].

The current density triggered by the Schottky effect is given by equation (4.8) and plotted in Figure 4.20.

$$J_s = A_s T^2 \exp\left(-\frac{\phi_0 - \beta_s \sqrt{E_c}}{kT}\right) \quad (4.8)$$

$$\beta_s = \sqrt{q^3 / 4\pi\epsilon_o\epsilon_r} \quad (4.9)$$

Where  $A_s$  is the Richardson-Dushman constant for thermionic emission,  $\phi_0$  is the height of the potential barrier at the metal-dielectric interface without any applied field,  $\beta_s$  is the Shottky constant and  $E_c$  is the field at the cathode. It is difficult to determine the electric field at the cathode during the measurement because it is distorted by space charge. We propose to quantify the electrical state at the contact by a parameter  $\gamma$  as suggested in equation (4.10):

$$E_c = \gamma \left(\frac{V}{d}\right) \quad (4.10)$$

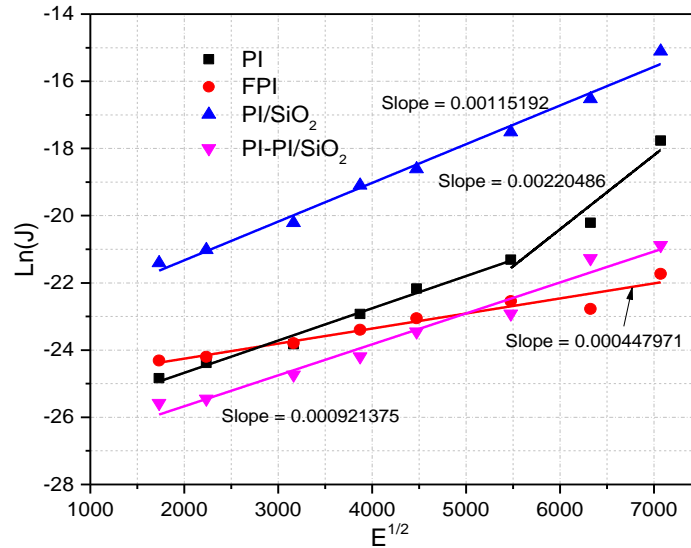
With  $\gamma < 1$  for a dominant contact homocharge and  $\gamma > 1$  for a dominant contact heterocharge. The expression of the Schottky current becomes, with the field distortion correction, as shown in equation (4.11):

$$J_s = A_s T^2 \exp\left(-\frac{\phi_0 - \beta_s \sqrt{\gamma \frac{V}{d}}}{kT}\right) \quad (4.11)$$

The  $\gamma$  parameter was calculated from the slope of each fitted curves given in Figure 20 by using equation (4.12). Knowing  $\epsilon_r$  and experimental slope, we can calculate  $\gamma$ , as shown in Table 4.5, while the extension of this straight line allows finding  $\phi_0$ . The high values of  $\gamma$  imply that heterocharge near the cathode strongly increases the local field and tends to decrease the energy barrier at the interface. The experimental slope values, the calculated  $\beta_s/kT$  values, the measured and calculated dielectric constants and the calculated  $\gamma$  values are given in Table 4.5.

$$\gamma = \frac{(\text{Slope} \times kT)^2 4\pi\epsilon_0\epsilon_r}{q^3} \quad (4.12)$$

If the conduction is mainly controlled by Schottky emission, then according to the Equation (4.8), a plot of  $\log(J)$  vs  $E^{1/2}$  should be proportional to each others and yield a straight line. The  $\beta_s$  coefficients are first calculated from the slope of  $\log(J)$  vs  $E^{1/2}$  plots, and the dielectric constants are then estimated from these coefficients using Equation (4.9). If these dielectric constants agree with the measured values, it can be said that the samples follow the corresponding conduction mechanism. Figure 4.20 shows that the slope of  $\ln(J)$  vs  $E^{1/2}$  is linear only for single and multilayer PI/SiO<sub>2</sub> films at 50 °C and their slope value is close to  $\beta_s/kT$  values. Also, the calculated dielectric constant values of these films are close to the measured value. Therefore, Schottky conduction could be valid for these films. But the  $\ln(J)$  vs  $E^{1/2}$  plots for other films are nonlinear and their dielectric constant is much lower than the measured one. The dielectric constant values calculated from the slopes in Figure 4.20 are lower than 1 which is not conceivable, whereas those from measurements in Table 4.5 and literatures are in range from 3.6 to 4.0 [143]. A comparison of these values indicates that Schottky conduction mechanism seems not to be the case for all the films except the PI/SiO<sub>2</sub> and PI-PI/SiO<sub>2</sub> films at 50 °C with dielectric constant 1.53 and 2.29 respectively. Therefore, it seems excluding the Schottky conduction and showing that some other conduction such as hopping may be occurring from one trapping site to another.



(a) Current/voltage characteristics in  $\ln(J)$  vs  $E^{1/2}$  plots at 50 °C

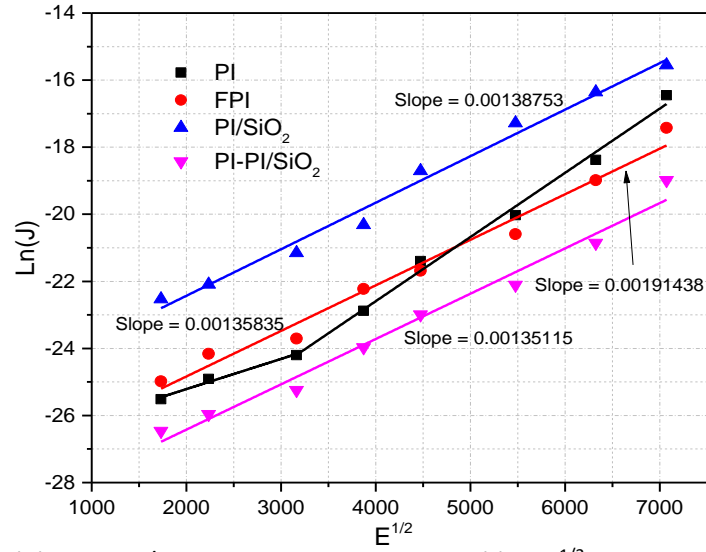
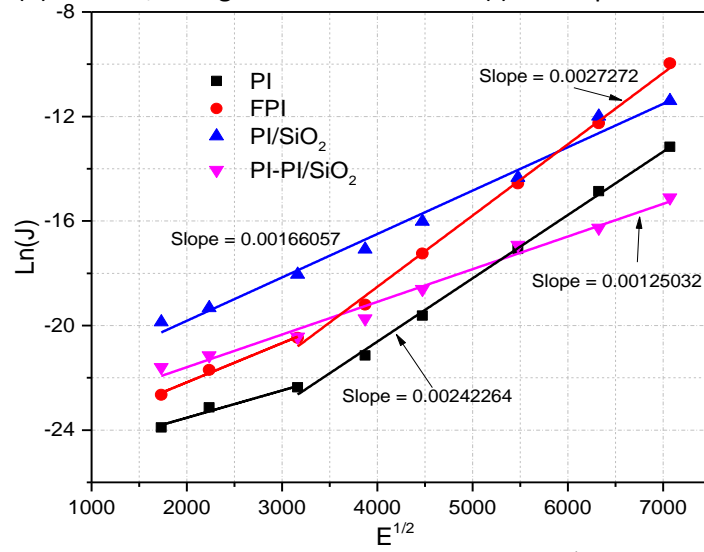
(b) Current/voltage characteristics in  $\ln(J)$  vs  $E^{1/2}$  plots at 100 °C(c) Current/voltage characteristics in  $\ln(J)$  vs  $E^{1/2}$  plots at 150 °C

Figure 4.20 Schottky injection mechanism at different temperatures

Table 4.5 The calculated  $\gamma$  values and the comparison of measured slope and  $\beta_s/kT$  values

Samples	$\epsilon_r$ (Measured)	Slope	$B_s/kT$	$\gamma$	$\epsilon_r$ (Calculated)	Temperature (°C)
PI	3.9	$2.2 \cdot 10^{-3}$	$0.69 \cdot 10^{-3}$	10.16	0.38	50
FPI	3.6	$0.4 \cdot 10^{-3}$	$0.71 \cdot 10^{-3}$	0.31	11.6	
PI/SiO <sub>2</sub>	3.95	$1.1 \cdot 10^{-3}$	$0.68 \cdot 10^{-3}$	2.57	1.53	
PI-PI/SiO <sub>2</sub>	3.98	$0.9 \cdot 10^{-3}$	$0.68 \cdot 10^{-3}$	1.73	2.29	
PI	4	$1.9 \cdot 10^{-3}$	$0.59 \cdot 10^{-3}$	10.36	0.38	100
FPI	3.6	$1.3 \cdot 10^{-3}$	$0.62 \cdot 10^{-3}$	4.36	0.82	
PI/SiO <sub>2</sub>	3.65	$1.3 \cdot 10^{-3}$	$0.61 \cdot 10^{-3}$	4.42	0.82	
PI-PI/SiO <sub>2</sub>	3.63	$1.3 \cdot 10^{-3}$	$0.62 \cdot 10^{-3}$	4.40	0.82	



PI	3.8	$2.4 \times 10^{-3}$	$0.53 \times 10^{-3}$	20.21	0.18	150
FPI	3.6	$2.7 \times 10^{-3}$	$0.54 \times 10^{-3}$	24.23	0.14	
PI/SiO <sub>2</sub>	3.5	$1.6 \times 10^{-3}$	$0.55 \times 10^{-3}$	8.2	0.42	
PI-PI/SiO <sub>2</sub>	3.58	$1.2 \times 10^{-3}$	$0.53 \times 10^{-3}$	4.76	0.75	

Finally, we can use the hopping conduction model to try explaining the conduction mechanism in the remaining films, which are unable to follow other models. The ions present in the films can gain some activation energy from electric or thermal source to participate in the conduction current, the current density  $J$  can be expressed in terms of ionic hopping conduction model from Equation (4.13) [143].

$$J_h = n\alpha v \exp\left(-\frac{U}{kT}\right) \sinh\left(\frac{eE\alpha}{2kT}\right) \quad (4.13)$$

Where  $e$ ,  $n$ ,  $\alpha$ ,  $v$ ,  $U$ ,  $k$ , and  $T$  are respectively the charge of electron, carrier density, hopping distance, attempt to escape frequency, activation energy, Boltzmann constant, and absolute temperature.

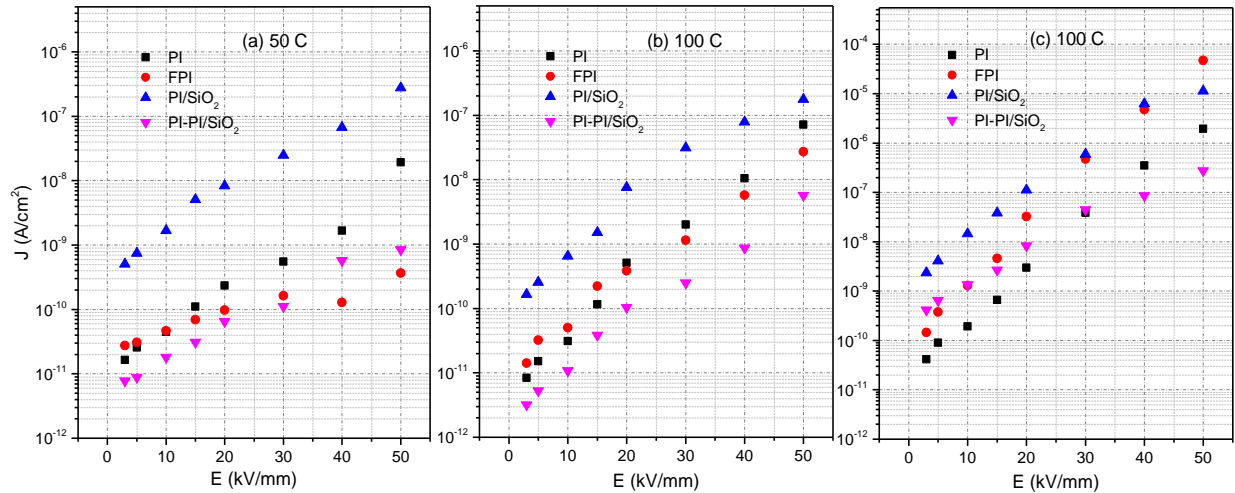


Figure 4.21 Current-Voltage characteristics of  $J$  vs  $E$  plots in log/linear scale at (a) 50 °C (b) 100 °C (c) 150 °C

The hopping conduction model curves are fitted with experimental data by adjusting constant parameters such as charge carrier density  $n$ , hopping distance  $\alpha$  and attempt to escape frequency  $v$  as shown in Figure 4.22, Figure 4.23 and Figure 4.24. These values are material dependent, in our case the main material is polyimide and these parameters can be easily estimated from experimental data and verify with the literature work [143]. The hopping distance  $\alpha$  can also be estimated from the slope of  $\ln(J)$  vs  $E$  plots presented in Figure 4.21 and the hopping distances for all samples were found to be in the range 2.6 nm to 5 nm. The range always vary little bit because of different temperature and material composition. So, one way is that we define a specific range and select each value according to the temperature and secondly, we can select one most suitable value for all temperature.

Although these small variation in value does not impact much on final calculation of current density. In our case, we select one value which is more suitable for all studied materials in the range from 2.6 to 5 nm which relate to 50 °C, 100 °C and 150 °C. To confirm the hopping conduction happening in the films, the model fitted curves must match with the experimental data. It can be seen from Figure 4.22 that FPI and PI-PI/SiO<sub>2</sub> films shown a good curve fitting for both datas at 50 °C. At 100 °C from Figure 4.23 no film shown a good curve fitting between model and experimental data which exclude hopping conduction. At 150 °C from Figure 4.24 PI and FPI shown best data match over the entire range of electric field, which confirms hopping conduction for them.

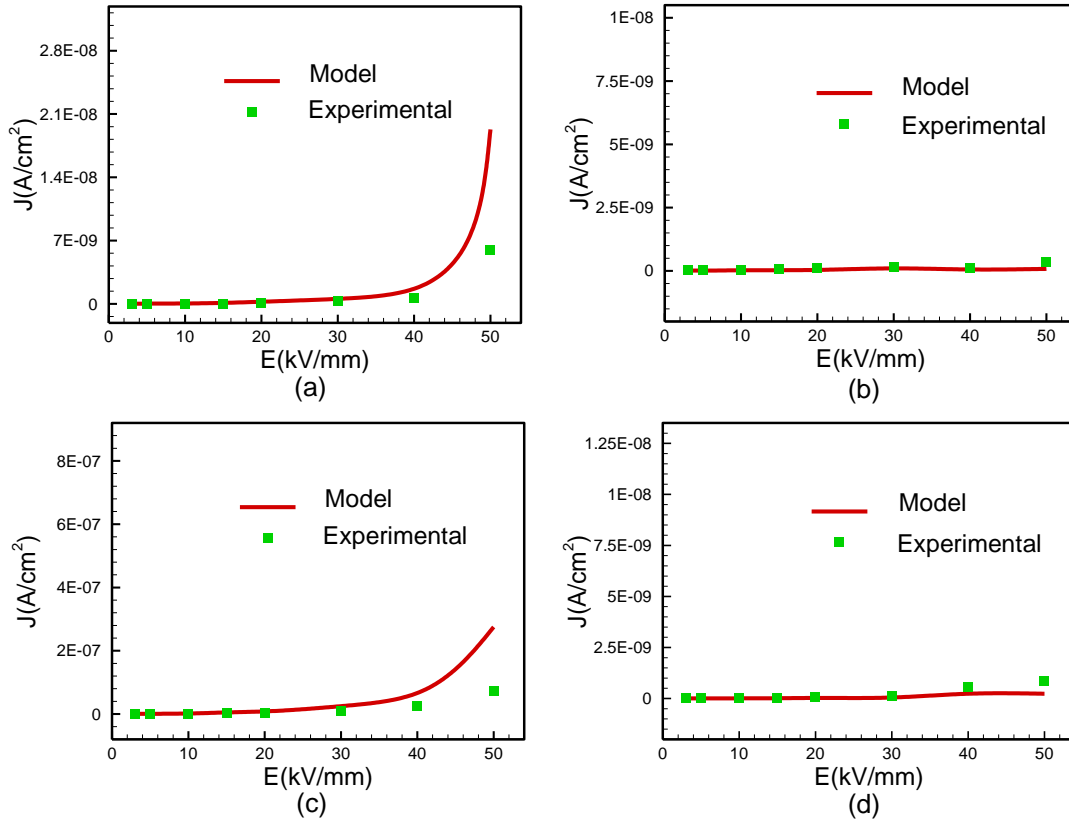


Figure 4.22 Hopping conduction model curve fitting line with experimental symbols data at hopping distance  $\alpha=2.6$ nm for (a) PI (b) FPI (c) PI/SiO<sub>2</sub> (d) PI-PI/SiO<sub>2</sub> at 50 °C

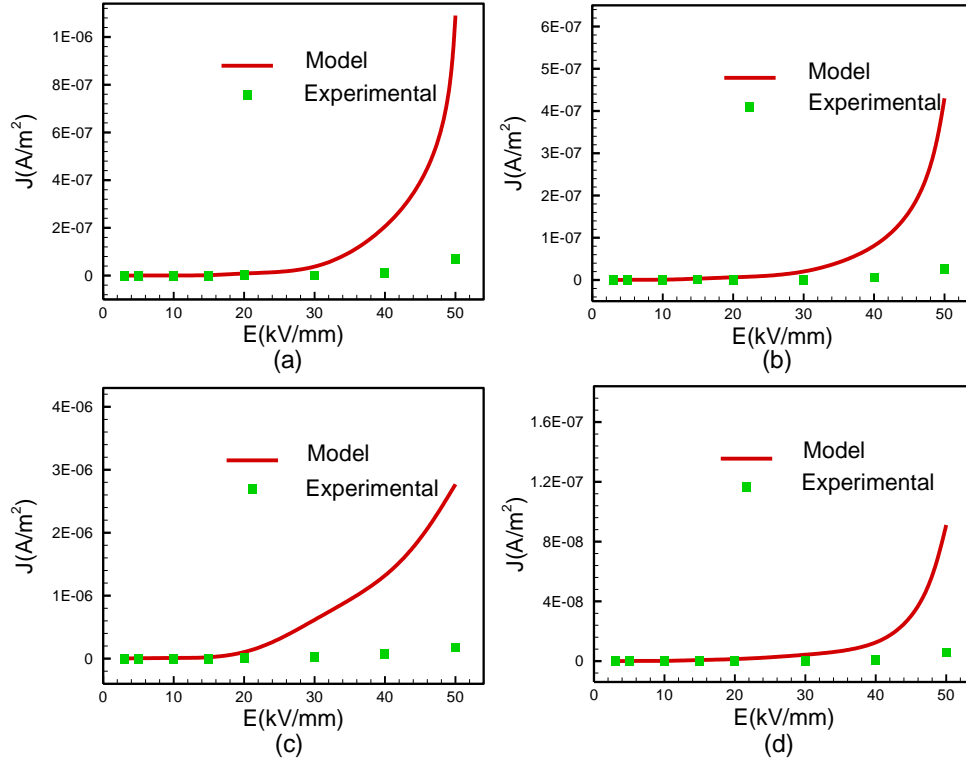


Figure 4.23 Hopping conduction model curve fitting line with experimental symbols data at hopping distance  $\alpha=2.6\text{nm}$  for (a) PI (b) FPI (c) PI/SiO<sub>2</sub> (d) PI-PI/SiO<sub>2</sub> at  $100^\circ\text{C}$

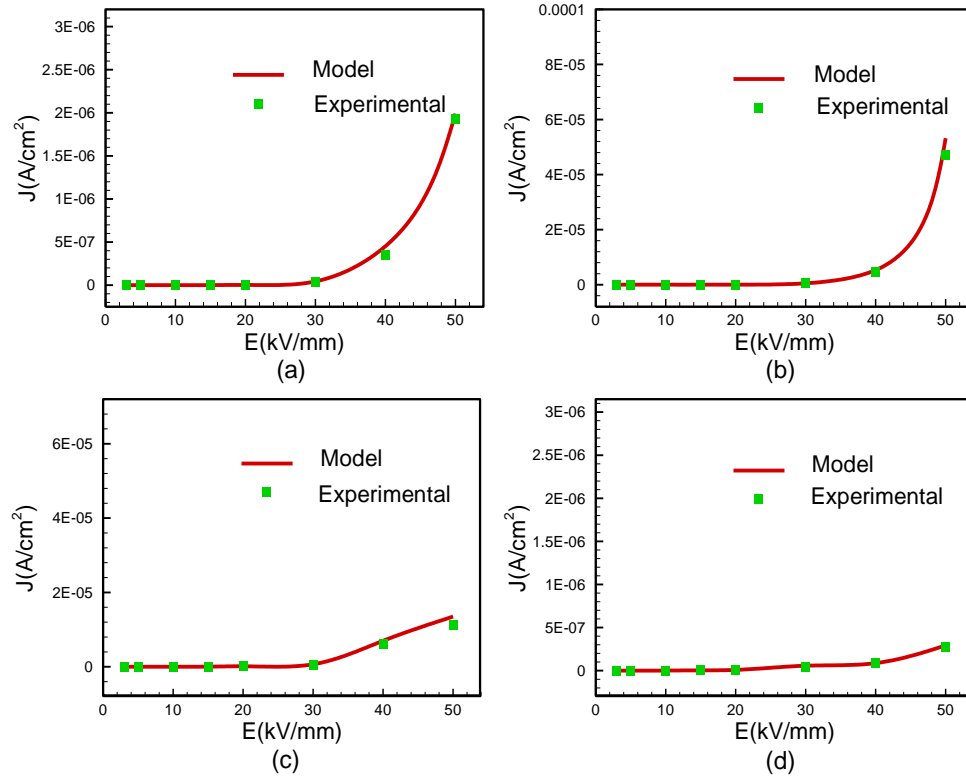


Figure 4.24 Hopping conduction model curve fitting line with experimental symbols data at hopping distance  $\alpha=2.6\text{nm}$  for (a) PI (b) FPI (c) PI/SiO<sub>2</sub> (d) PI-PI/SiO<sub>2</sub> at  $150^\circ\text{C}$

The Table 4.6 below summarizes the possible conduction phenomena for all the studied materials at different temperatures and the electric field ranges considered. At-least one possible conduction of each class either related to charge injection or bulk conduction should be present to describe the steady-state conduction current. But for some samples such as FPI and PI-PI/SiO<sub>2</sub> two different conduction mechanism from same bulk conduction class seem to be present at high temperature 150 °C as shown in Table 4.6.

In FPI films at 150 °C SCLC and hopping conduction both seem to be present, as SCLC relate to mobility of holes and electrons and hopping relate to ions donor and acceptor sites present in the bulk which need either thermal or electrical energy to participate in the conduction by giving their space to neighboring electrons or holes depending on their trap energy level. We are estimating these conduction phenomena by analyzing the slope of the current density over a certain range of electric field not just a point. Thus, it seems difficult to consider that this conduction is happening exactly at this electric field.

Table 4.6 Conclusion of possible conduction mechanism in all films

Samples	Possible conduction	Temperature (°C)
PI	Poole-Frenkel	50
FPI	Hopping	
PI/SiO <sub>2</sub>	Schottky	
PI-PI/SiO <sub>2</sub>	Schottky, Hopping	
PI	Poole-Frenkel	100
FPI	Poole-Frenkel	
PI/SiO <sub>2</sub>	Poole-Frenkel	
PI-PI/SiO <sub>2</sub>	Poole-Frenkel	
PI	Hopping	150
FPI	SCLC, Hopping	
PI/SiO <sub>2</sub>	Hopping	
PI-PI/SiO <sub>2</sub>	Poole-Frenkel, Hopping	

The study of conduction mechanisms in polymeric materials is not easy, and this is even more true when it concerns composite materials. It appears from this study, dominant conduction mechanisms strongly dependent on the electric field and the measurement temperature, whatever the type of studied material. Nevertheless, in the materials of this study based on polyimides, we can say that two volume conduction mechanisms seem to be predominant, Poole Frenkel and Hopping, especially at 100 and 150 °C.

## 4.8 Space charges and trap levels analysis

### 4.8.1 Space charge analysis using TSM technique

In order to study the space charge behavior for PI and FPI films, the TS currents (obtained by the TSM technique) were measured in short circuit conditions. The measured samples were pre-conditioned for one hour at 50 °C, 100 °C and 150 °C, under three voltage levels,

corresponding to 5, 15 and 25 kV/mm. The results presented in Figure 4.25 show that the amplitude of the TS current acquired for FPI films is lower than the PI films at all electric field and temperature conditions. The lower amplitude of TS currents having the same shape and dynamic is usually the attribute of the lower level of space charge accumulation. Moreover, two opposite TS current signs correspond to different dominant charges. At 50 °C, positive TS current is observed for PI and FPI films at all electric field levels, as shown in Figure 4.25. These positive signals correspond to the same dominant charge nature and show an increase in accumulated space charge when the poling applied field increases. Also, the FPI sample highlights lower TS currents, but this behavior is more visible for 15 and 25 kV/mm. Thus, the fluorination coating on both sides of samples acts as a barrier and reduces the charge injection from electrodes. These coated-layers are discharge resistive and increase the charge dissipation rate to reduce the space charge accumulation.

The charge transportation in material can be influenced by the trap depth and the conductivity of insulating material [37], [141]. The literature study has shown that the fluorination can not only decrease surface energy for polyimide film, but also change the electrical properties, such as the conductivity, the trap depth and higher charge dissipation rate [43]. The conductivity and charge dissipation rate of FPI film is higher than the PI film [37], [44], [141]. It is assumed that after poling, the charges were injected from electrodes and gradually accumulated, but higher conductivity and dissipation rate of FPI films reduced the overall space charge accumulation tendency. The TS current amplitudes at higher temperature were compared to the previous results obtained after poling at 50 °C. The negative peaks of TS current show a change in dominant trapped charges at higher temperature values, especially in the case of PI films. We can assume a shift from the dominant heterocharge to a dominant homocharge, but this can only be confirmed after the mathematical processing of the TS current signals. Indeed, this is not always the case, because we must also consider the conduction phenomena that can allow the injected charges (homocharges) to migrate to the opposite electrode and become a heterocharge. It is important to note that heterocharge near an electrode leads to an electric field enhancement at this electrode and an electric field reduction in the center of the sample, while homocharge leads to a decrease in electric field near the electrode and an electric field enhancement in the center. At higher level of poling electric field and temperature, the dominant phenomenon should normally correspond to a charge injection phenomenon, probably related to the presence of injected space charges at the electrodes during poling. It reveals that the temperature can influence the amount as well as the polarity of space charge accumulation significantly. The pure PI films tend to accumulate more space charge than the multi-coated FPI films. The negative sign of the TS currents presented in Figure 4.25(c, e) for PI films should normally correspond to the presence of injected electrons at this electrode [39], [144], [145].

In order to have a simplified overview of the different results, the maximum and minimum value of TS current is summarized from Figure 4.25(b, d, f) for all the samples, after the different poling conditions. From these results, it is clear that a minimum space charge accumulation in the FPI films and maximum space charge accumulation in PI films is observed, whatever the poling conditions are. The poling temperature seems to affect more significantly space charge accumulation than the poling electric field. For the higher applied electric field (25 kV/mm), a change in TS current sign is observed at lower poling temperature for PI sample (since 100 °C) than FPI one (since 150 °C). Thus, it could be assumed that, after the poling at higher temperatures, the injected charges at the cathode are gradually accumulated in the PI film. However, for the fluorinated film, which has a shallower trap and higher conductivity than the untreated sample, the injected charges dissipate. The decay for both negative charge and positive charge is improved by the fluorination layer present on the surface.

The space charge is also determined through the experimental results for single and multilayer PI nanocomposite films, after thermo-electrical poling. An electric field between 5 to 40 kV/mm is applied at 50 °C, 100 °C and 150 °C for 1 hour [14-19]. The results presented in Figure 4.26, for single layer PI/SiO<sub>2</sub> films in Figure 4.26(a) and multilayer PI-PI/SiO<sub>2</sub> films in Figure 4.26(b). The results illustrate that the amplitude of the TS current acquired for multilayer PI-PI/SiO<sub>2</sub> films is lower than the single-layer PI/SiO<sub>2</sub> films, at all electric field and temperature conditions. The current sign changes from positive to negative, from low temperature 50 °C to higher temperature 150 °C, especially for single layer PI/SiO<sub>2</sub> films. The sign of current corresponds to the same dominant charge injected from the electrode and shows an increase in accumulated space charge when the poling applied field increases. A thin layer of PI/SiO<sub>2</sub> on PI samples reduces the charge injection from electrodes inside the sample. Therefore, lower amplitude of TS currents is observed in multilayer PI/nanocomposite films and this behavior is more visible at higher electric fields due to high amount of charge emission and improve the signal to noise ratio. As can be seen from equation (3.23) in chapter 3, the amplitude of the TS current depends mainly on four parameters: the material constant  $\alpha$ , the electrical capacitance of the sample, the remaining electric field and the amplitude of the thermal step. It is obvious that the TS current would be much higher if the capacitance of the sample is large. PI is obtained using the curing method in which the solvent is evaporated by rising the temperature in oven; there is a high chance of nanoparticles agglomeration due to the change in density level and phase transition from liquid to solid.

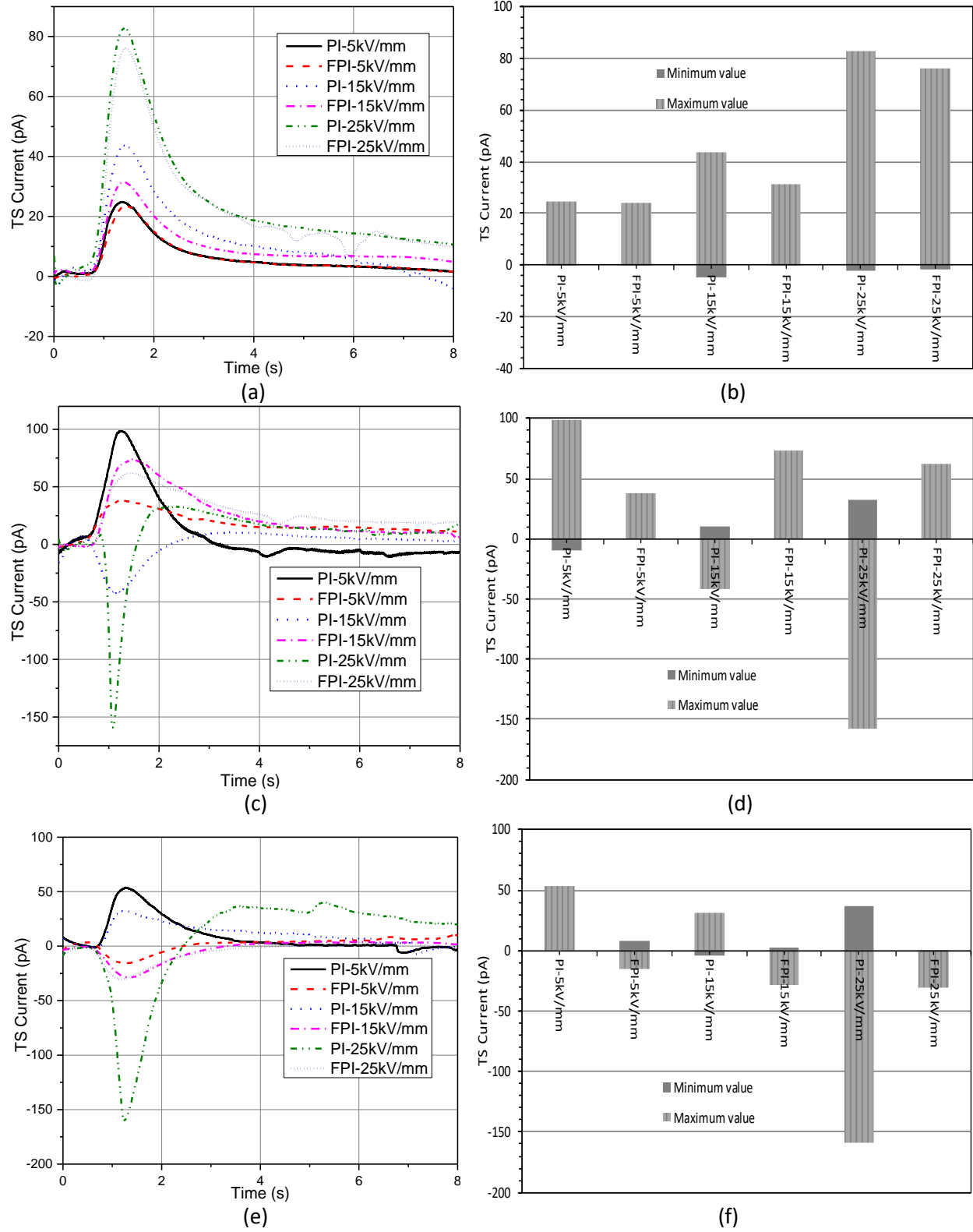


Figure 4.25 TS current for PI and FPI samples (a) after poling at 50 °C (b) maximum and minimum values after poling at 50 °C (c) after poling at 100 °C (d) maximum and minimum values after poling at 100 °C (e) after poling at 150 °C (f) maximum and minimum values after poling at 150 °C

As we have proposed in Figure 3.1, in the case of multilayer insulation structure, electrical capacitance of PI nanocomposite films with lower chances of nanoparticle agglomeration in series will reduce the equivalence capacitance of samples compared to single-layer PI nanocomposite films with parallel structure of capacitance and higher chance of nanoparticles agglomeration. This change in capacitance for single and multilayer films strongly impact on the measured TS currents. In multilayer films, less amount of TS current may attribute towards the lower value of equivalence capacitance of the sample.

The second main reason of lower amplitude of TS current in multilayer films can be due to the better nanoparticles dispersion, as we have observed in SEM images that adding the nanoparticles in the form of multilayer structure improves its dispersion. In multilayer structure, we are giving less space for nanoparticles to get agglomerated because if the same number of nanoparticles is contained in large volume of PAA solution, particles have higher chance of agglomeration. A thin layer restricting the nanoparticles to certain positions until the solvent is evaporated to get thin solid film. These thin nanocomposite layers coated on the main side of the magnetic wire can resist the charge injection from the electrodes, improve the nanoparticles dispersion level, improve the electrical capacitance of the sample and therefore suppress the charge accumulation. Residual electric field and space charge density are calculated using TS current data of pre-conditioned PI and FPI films plotted in Figure 4.27. Higher residual electric field and higher space charge are observed in PI films compared to FPI films at all electric fields. The charge mobility inside the bulk of sample can be affected due to the surface discharge nature of the material. By changing the chemical component (fluorination) in the surface layer of PI films, causes the corresponding change in electrical property such as space charge accumulation. The orbital shape of fluorine atom makes it possible to reduce its electron polarizability of F element and increase the surface energy of PI films. At the same time, it provides shallow traps for charges, which are easy to dissipate. These fluorine coated-layers are discharge resistive and increase the charge dissipation rate to reduce the space charge accumulation. Furthermore, positive and negative signs of current correlate to the leading charges (homocharges or hetrocharges). From Figure 4.27(b), it can be seen that homocharges are observed to the specific electrode. These leading charges for PI and FPI films represent the nature of charge accumulation near to a specific electrode, and an increased space charge accumulation trend is observed for all samples at higher electric field levels. For higher applied electric field (25 kV/mm), a change in TS current sign is observed at lower poling temperature for PI at 100 °C and for FPI at higher temperature value of 150 °C. Temperature influence on the amount as well as polarity of charges. Fluorination coating modifies PI films chemically increase its electronegativity by introducing C-F bonds on surface. C-F bond increases the overall surface conductivity and surface charge recombination rate of PI films, hence the space charge accumulation reduces for FPI films.



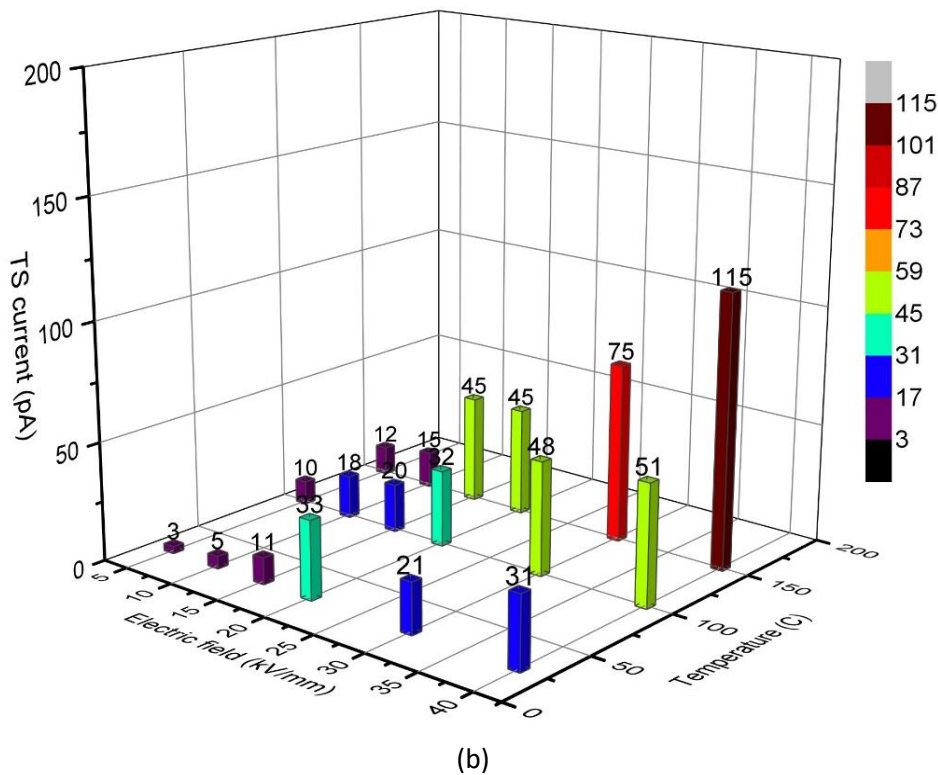
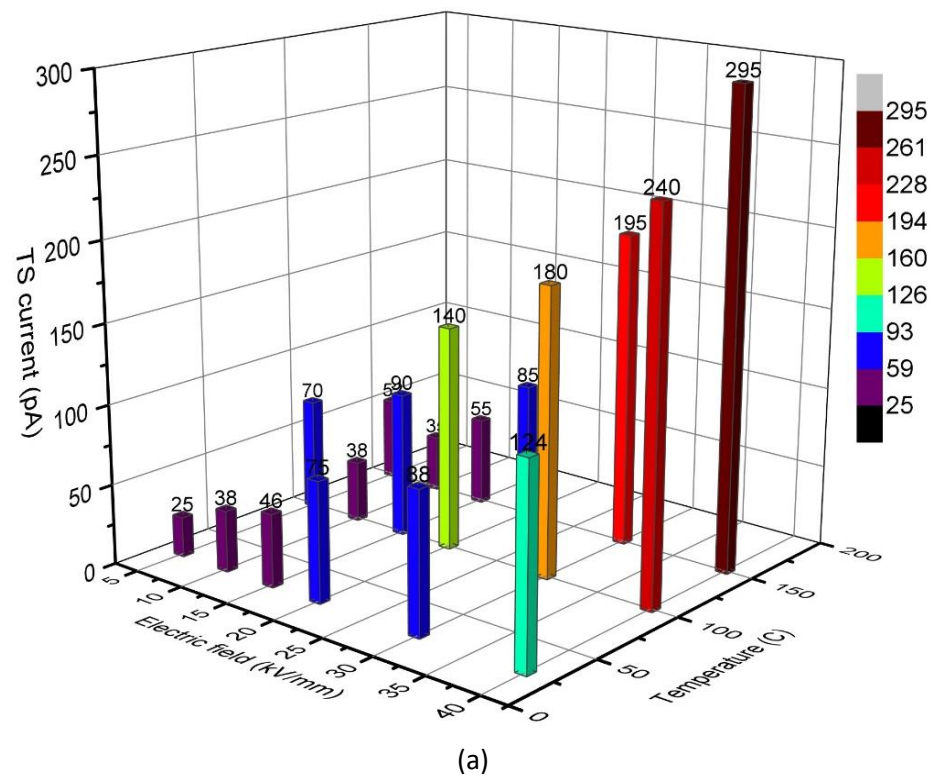
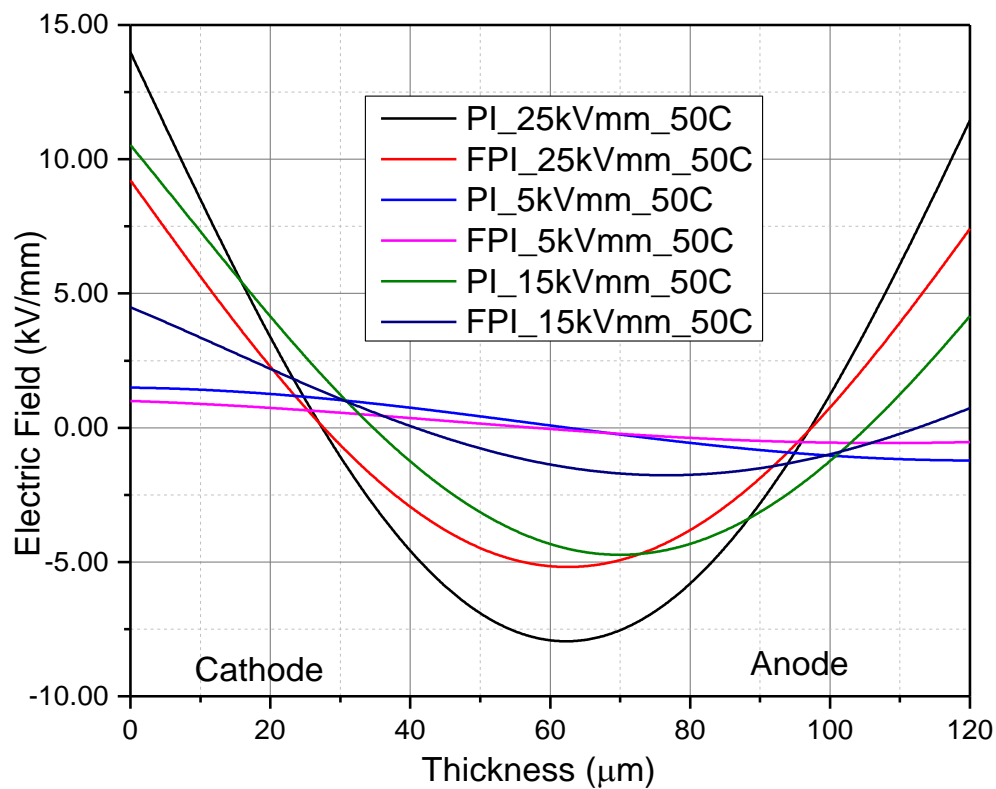
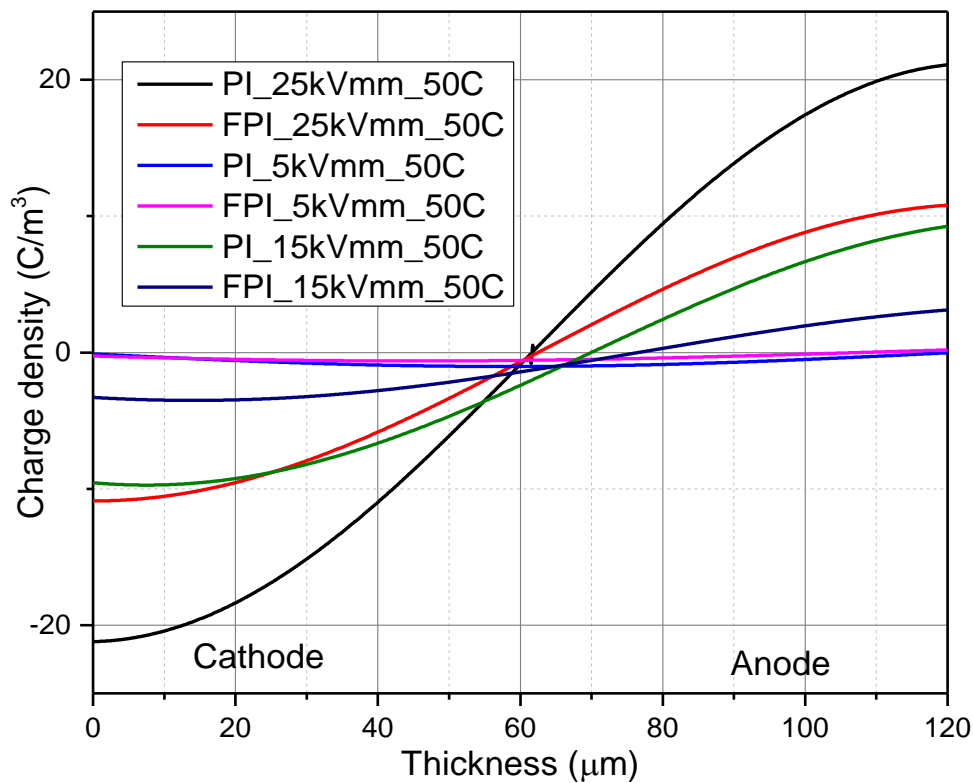


Figure 4.26 (a) TS current for single layer PI/SiO<sub>2</sub> (b) TS current for two layers PI-PI/SiO<sub>2</sub> films



(a)



(b)

Figure 4.27 (a) Electric field calculation using TS current (b) Charge density calculation using TS current

### 4.8.2 Space charge analysis using PEA technique

PEA technique is also used to measure the space charge accumulation for single and multilayer PI/nanocomposite films. The effects of the type of nanoparticles and their interface with a PI film are studied in this part. The detail of the experiment has been described in chapter 3. Negative DC electric field of 30 kV/mm at room temperature (25 °C) is applied to measure space charge density of one, two and three-layer samples from 0 to 180 minutes. The LabVIEW based program is used to observe the space charges behavior, as shown in Figure 4.28.

Structure of polymer/nanocomposite insulation is essential to suppress space charges and traps because sometimes it dominates other electrical properties. In layer samples, interfaces are made with different composite materials. Equation (4.14) can be used to explain interfacial charge density, present between two dielectrics [35], [146]. Although this theory cannot explain the amount of charge presents at the interface, but it is useful to explain the charge polarity at the interface.

$$\sigma = (\varepsilon_2 - \varepsilon_1 \gamma_2 / \gamma_1) E_2 = (\varepsilon_2 \gamma_1 / \gamma_2 - \varepsilon_1) E_1 \quad (4.14)$$

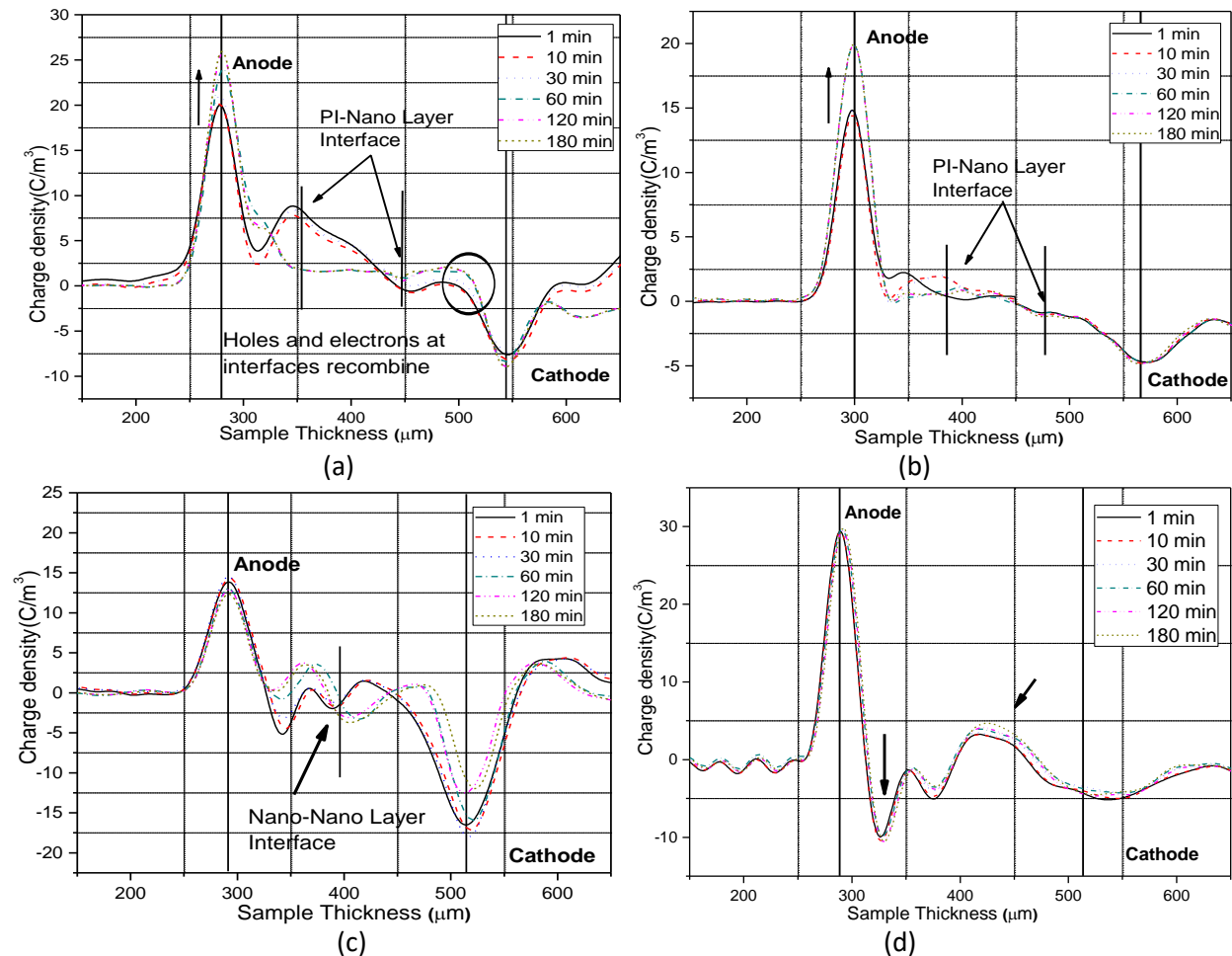
$$\varepsilon_2 / \varepsilon_1 = \gamma_2 / \gamma_1 \quad (4.15)$$

$\sigma_1$  and  $\varepsilon_1$  denote the conductivity and permittivity for material (1) and  $\sigma_2$  and  $\varepsilon_2$  are conductivity and permittivity of material (2) respectively. If the same material is involved, then the above equation (4.14) can be represented as the equation (4.15). The interfacial charge density of three-layer structure made up with similar nanoparticles material is almost negligible, as shown in Figures 4.28(a, b), for a time period of 60 minutes to 180 minutes. The charges behavior pattern agrees to the above theory because the three-layer structure has two-layer interfaces (top and bottom) made up with the same nanoparticles. In these interfaces, a small amount of homocharge accumulates besides both electrodes for a short time period (1 min to 30 min), and then disappears with the increase in time to 180 min. In two-layer structure, both layers are formed by two different nanoparticles ( $\text{Al}_2\text{O}_3$  and  $\text{SiO}_2$ ), in which electrons accumulate near the anode and at layer interface; the quantity of interface space charges increases and transport inside the bulk of the material.

To explain this in a better way, consider  $\text{Al}_2\text{O}_3$  as material 2 and PI as material 1. It means  $\varepsilon_2 > \varepsilon_1$  and  $\sigma_2 \ll \sigma_1$ , so according to equation (4.14), interfacial charge and electric field have similar charge polarity that holes near anode and electrons near cathode interfaces, as shown in Figure 28(a). In a similar way, consider  $\text{SiO}_2$  as material 2 and PI as material 1, hence,  $\varepsilon_2 > \varepsilon_1$  and  $\gamma_2 \ll \gamma_1$ , so according to equation (4.14), hole accumulates near positive electrode as shown in Figure 4.28(b). In the case of two-layer structures, heterocharges accumulate near anode and layer interface according to equation (4.14) and Figure 4.28(c) satisfies this condition. The

mobility of charges inside the bulk of the material can be influenced by the presence of traps. Particularly, broken bonds on the surface and at the interface of materials generate the traps, which accumulate charges. Therefore, the electronic state of the surface determines the polarity of accumulated charges and it dominates the charge trapped.

From these results, it is clear that the behavior of charges for three-layer films is quite different from that of two and single-layered films. Multilayer samples showed different space charge distribution tendencies when the time increases from 30 min to 180 min, compared with single layer samples in Figure 4.28(d, e, f). In three-layer samples, holes accumulate at interface near anode and electrons accumulate at interface near cathode for the first 30 min. From 60 min to 180 min, the interface charge disappears. Similar phenomena happen in two-layer samples; electrons accumulate at interface followed by holes but, instead of disappearing, interface charge increases from 60 min to 180 min. The maximum charge density increased in all samples as the electric stress time increased. It can be assumed from the results that the space charges were already trapped at the interfaces due to permittivity/conductivity difference, impurities ionization along with some other defects. By applying the electric field, these charges gain some energy and recombine with electrons from the other the electrode.



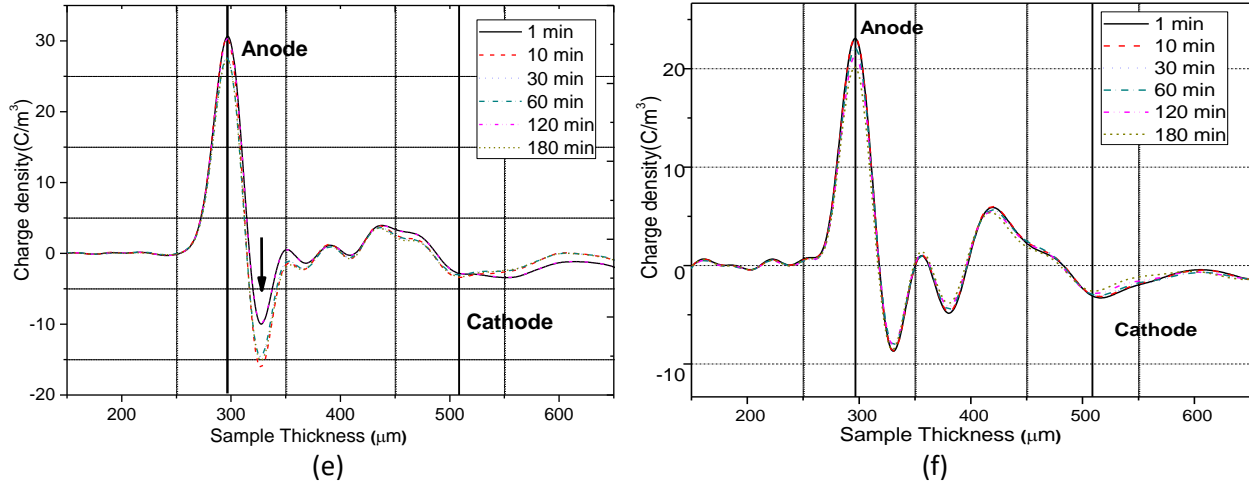


Figure 4.28 Space charge profile for different samples after 30 kV/mm during 180 min (a) PI/Al<sub>2</sub>O<sub>3</sub>-PI-PI/Al<sub>2</sub>O<sub>3</sub> (b) PI/SiO<sub>2</sub>-PI-PI/SiO<sub>2</sub> (c) PI/Al<sub>2</sub>O<sub>3</sub>-PI/SiO<sub>2</sub> (d) PI/Al<sub>2</sub>O<sub>3</sub> (e) PI/SiO<sub>2</sub> (f) PI

During the first 30 minutes of electric stress still, the energy of these static charges was not enough to jump and leave the trap level. By increasing the stress time to 180 minutes, trap charges gain some energy to leave its present state and move around to recombine with other opposite charges. This could be the reason that few space charges are seen in a three-layer structure between 60 min to 180 minutes. According to equation (4.14), depending on the value of material permittivity/conductivity, it can be homocharge or heterocharge, as proved from Figure 4.28(a, b). In the case of two-layer structures, the presence of heterocharges at the interface of Al<sub>2</sub>O<sub>3</sub>-SiO<sub>2</sub> will reduce the potential barrier for charge injection and increase the amount of space charge, as shown in Figure 4.28(c). This is the reason that charges already present will gain some energy from the electric field and move inside the bulk of insulation, while new charges injected from electrode accumulate at the interface, as shown with a new peak in Figure 4.28(c). In the case of a three-layer structure, the presence of homocharges at the interface of PI-Al<sub>2</sub>O<sub>3</sub> and PI-SiO<sub>2</sub> will increase the potential barrier for charge injection and repel charges coming from electrodes. Therefore, it could be concluded from these results that the conductivities of materials depend on the material structure and type of nanoparticles interface. It also depends on electric stress. Three-layer structure, in which nanocomposite layer is at the top and bottom side of the pure PI layer, will resist charge injection and suppress space charge. In contrast, the opposite phenomenon happens in the case of a two-layer structure. Conductivities of materials also depend on electric stress value and time [147], [148] [42], [44], [149].

#### 4.8.3 Total charge decay and trap levels distribution analysis

The traps are responsible for accumulating space charges inside the bulk of samples. The depth of these traps is both field-dependent and time-dependent. To specify the release of these trapped charges, we have to analyze the charges decay pattern. Therefore, total charge

decay data and TSC data are used to calculate the trap levels, and the results are compared. In the first step, the total charge  $Q$  is calculated according to equation (4.16).

$$Q(t) = \int_0^d \rho(x, t) S dx \quad (4.16)$$

Where  $Q$  is the total trapped charge,  $\rho(x, t)$  is the charge density,  $S$  is the electrode area, and  $d$  is the thickness of the sample. LabVIEW program is used to get the total charge decay with the help of charge density de-trapping at voltage off, as shown in Figure 4.29. The trap depth is continuous, and charge de-trapping is thermally activated. With the increasing charge decay time, the charges jump from a low energy trap level (shallow trap)  $E_{min}$  to a high-energy trap level (deep trap)  $E_{max}$ , and the rate of charge expulsion depends on the rate of charge decay. It has been shown that the charge decay can be used for a good approximation of the energy distribution of the traps [150]. Time-dependent charge decay and their density are shown in equations (4.17) to (4.23). The derivations of the below equations are given in references [35], [150].

For  $E_{min}$  and  $E_{max}$  :

$$\Delta Q / \Delta t = kT / h.e^{(-E_{min}/kT)} \quad (4.17)$$

$$\Delta Q = Q_1 - Q_0 \quad \cap \quad \Delta t = t_1 - t_0 \quad (4.18)$$

$$\Delta Q / \Delta t = kT / h.e^{(-E_{max}/kT)} \quad (4.19)$$

$$\Delta Q = Q_{n-1} - Q_n \quad \cap \quad \Delta t = t_{n-1} - t_n \quad (4.20)$$

$$\rho(t) = \rho(0) \quad t < [kT / h.e^{(-E_{min}/kT)}]^{-1} \quad (4.21)$$

$$[kT / h.e^{(-E_{min}/kT)}]^{-1} < t < [kT / h.e^{(-E_{max}/kT)}]^{-1} \quad (4.22)$$

$$\rho(t) = 0 \quad [kT / h.e^{(-E_{max}/kT)}]^{-1} < t \quad (4.23)$$

Where  $\Delta Q$  is the change in charge amount at time  $\Delta t$ ,  $\rho(t)$  is the time-dependent space charge density,  $Q_0$  is the initial charge amount at time  $t_0$  and  $Q_1$  is charge amount at time  $t_1$ .  $E_{min}$  is the energy of minimum trap depth, which releases the charge,  $k$  is the Boltzmann constant,  $h$  is the Planck constant and  $T$  is the temperature; the charges achieve steady-state after a certain period decay. Based on total trapped charge decay results in Figure 4.29, we calculate the energy of trap depth  $E_{min}$  and  $E_{max}$  from equation (4.17) and equation (4.19), respectively, as shown in Table 4.7. Values of charges  $Q_n$  are taken from the plot in Figure 4.29, at  $t_n$  where ( $n=0, 1, 2, \dots$ ). The trap levels obtained using the total charge decay date are shown in Table 4.7.

It can be interpreted that very little decay occurs until the time  $t_1$  at which the shallowest occupied traps  $E_{min}$  starts to be emptied, then the rest of the decay of the charge follows [148]. This phase of the decay ends when the deepest traps  $E_{max}$  start to be emptied at  $t_n$ . For a good

estimation of the energy distribution in thin samples and to avoid complications, we considered a single de-trapping approximation with negligible re-trapping. The following three possibilities may happen with charges. It may be de-trapped and move to another electrode for extraction. It may be recombined by space charge of opposite polarity at the interface and it may be neutralized by the charges injected from the other electrode. In these processes, three mechanisms are involved: charge de-trapping, transport, and injection. Each of these mechanisms may have a different period of operation. Depending on the trap distribution, the effective penetration depth of carriers will be both field-dependent and time-dependent. To specify the decay of these trapped charges, we have to analyze the release of carriers and their subsequent recapture, as they make their way through the sample.

An isothermal de-trapping process is considered in which charges are released at electrodes [150]. The transport of the charges from the injection electrode towards the extraction electrode involves multiple charges trapping and de-trapping. However, single de-trapping consideration provides very good estimations about the energy distribution of the trapping states [148]. For thin films, single de-trapping from a trap is dominated over multiple trapping and de-trapping. We adopted the Simmons and Tam method for the decay of trapped charges with negligible re-trapping [102]. In this method, thermal or demarcation energy  $E_m$  is used to describe the time dependency of energy distribution states. In these states above  $E_m$ , energy is emptied for electrons in the interval from the injection event to time  $t$ , whereas electrons in states below  $E_m$  remain frozen at that time. Therefore, electrons are excited from the vicinity of  $E_m$  and de-trapped at time  $t$  [147].

Table 4.7 Shallow and deep trap levels using total charge decay data and peak density trap level using TSC data

Samples	Trap Levels using Space Charge data		Trap Levels using TSC data
	$E_{\min}$ (eV)	$E_{\max}$ (eV)	$E_{\text{peak}}$ (eV)
PI/SiO <sub>2</sub> -PI-PI/SiO <sub>2</sub>	1.02	1.14	1.12
PI/SiO <sub>2</sub>	1.15	1.22	1.26
PI/Al <sub>2</sub> O <sub>3</sub> -PI-PI/Al <sub>2</sub> O <sub>3</sub>	1.10	1.21	1.13
PI/Al <sub>2</sub> O <sub>3</sub>	1.13	1.19	1.17
PI	1.14	1.18	1.16

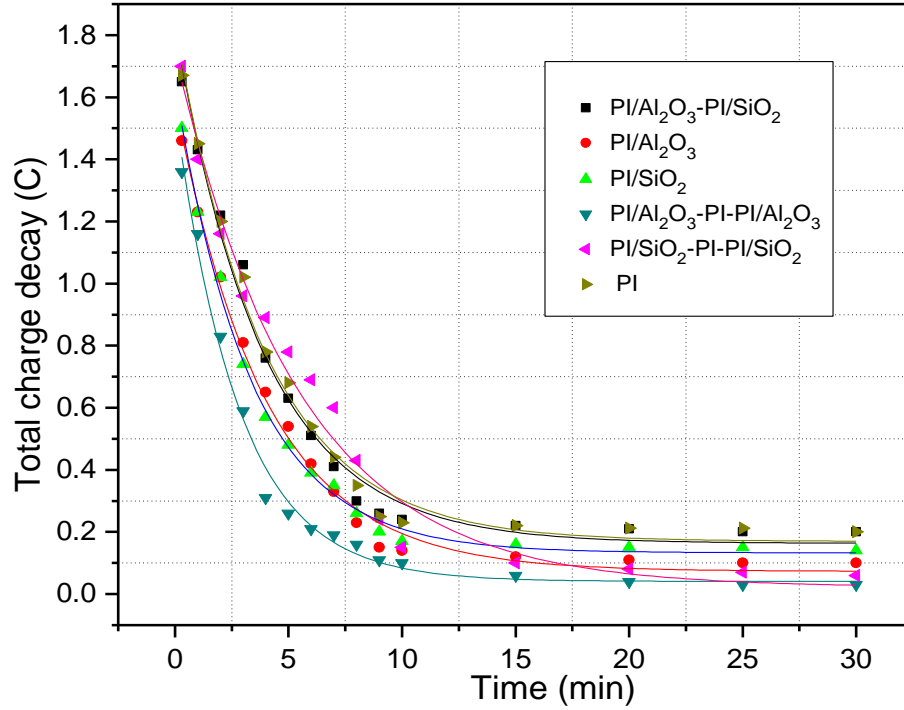


Figure 4.29 Total charge decay profile after Voltage off for pre-conditioned 30 kV/mm during 180 min at 25°C

The current obtained from TSC is plotted in Figure 4.30(a) and the trap levels obtained from the thermally stimulated depolarization current density by numerical calculation method [151] using MATLAB are shown in Figure 4.30(b). Peak density trap energy levels are noted from curves.

$$J = ex^2 / 2d \int_{E_v}^{E_c} r_0(E) N(E) ve(-E/kT) e^{-1/\beta \int_{T_0}^T ve(-E/kT) dT} dE \quad (4.24)$$

$$F1(E, T) = ve(-E/kT) e^{-1/\beta \int_{T_0}^T ve(-E/kT) dT} \quad (4.25)$$

$F1(E, T)$  attributes the electron at trap level  $E$  to the current at temperature  $T$ . Electrons that discharged from the traps in range of  $(E_m - 0.05\text{eV}) - (E_m + 0.05\text{eV})$  participate significantly to the current at the time of relaxation process at temperature  $T$ . When the temperature is increased,  $E$  moves away from low-level bands to the deep level. So, trap position above  $E_m$  becomes empty of electrons and trap at lower energy level  $E_m$  are still there as initial value at  $T$ , thus  $E_m$  can be used as the reference of demarcation energy [27, 28] and  $F1(E, T)$  can be approximated to be delta function, as shown in equation (4.26).

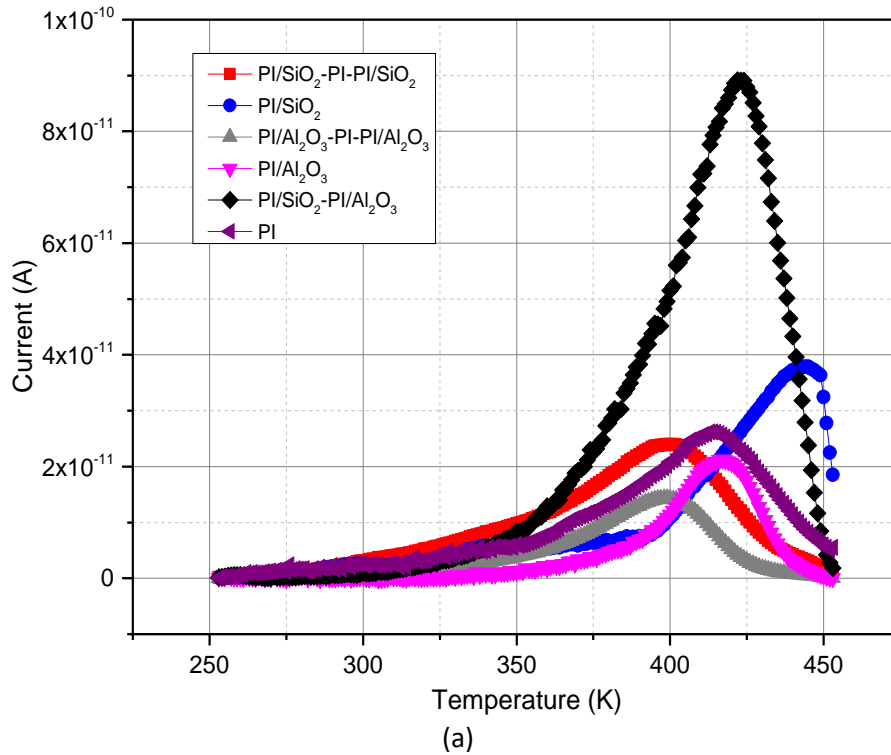
$$F1(E, T) = A(E_m \delta(E - E_m)) \quad (4.26)$$



$A$  is a function of  $E_m$ . The approximate analytical solution of  $A(E_m)$  described in the current discharge theory [152] can be replaced using a new method of using the trap level distribution from TSC experimental data. Traps level calculations are done using equation (4.26). Let suppose traps already filled and  $r_0=1$ , then we can use equations (4.24) and (4.26) directly to get a distribution of trap level, from the TSC measurement described in Table 4.6. The trap levels distribution factor can be calculated using equation (4.27), the solution of  $A(E_m)$  from theory [152].

$$r_0(E_m)N(E_m) = (2d / el^2)(J(T) / A(E_m)) \quad (4.27)$$

A noteworthy change is observed that the traps density of PI/Al<sub>2</sub>O<sub>3</sub>-PI/SiO<sub>2</sub> sample is five times larger than other samples. The trap levels energy range for all samples is between 0.9-1.3 eV and the density range is 10<sup>21</sup> to 10<sup>22</sup> (eV.m<sup>3</sup>)<sup>-1</sup>. These results are acceptable because the density of traps for polymers is in the range of 10<sup>14</sup>-10<sup>26</sup> (eV.m<sup>3</sup>)<sup>-1</sup> [29] and consistent with the discharge current theory [152]. Furthermore, as compared to the three-layer structure of both nanoparticles types (Al<sub>2</sub>O<sub>3</sub>, SiO<sub>2</sub>), deep trap levels are observed in two-layers structure (PI/Al<sub>2</sub>O<sub>3</sub>-PI/SiO<sub>2</sub>) and single layers of PI/SiO<sub>2</sub> and PI/Al<sub>2</sub>O<sub>3</sub> nanocomposite types. Polymer chain cooperating with the surface of the nanoparticles may change properties of composite material such as crystallinity, cross-linking, charge transportation, molecular structure, therefore traps level may influence too [153]. Thus, higher traps in two-layer structure are mainly the consequence of the above changes due to the two types of nanoparticles interface.



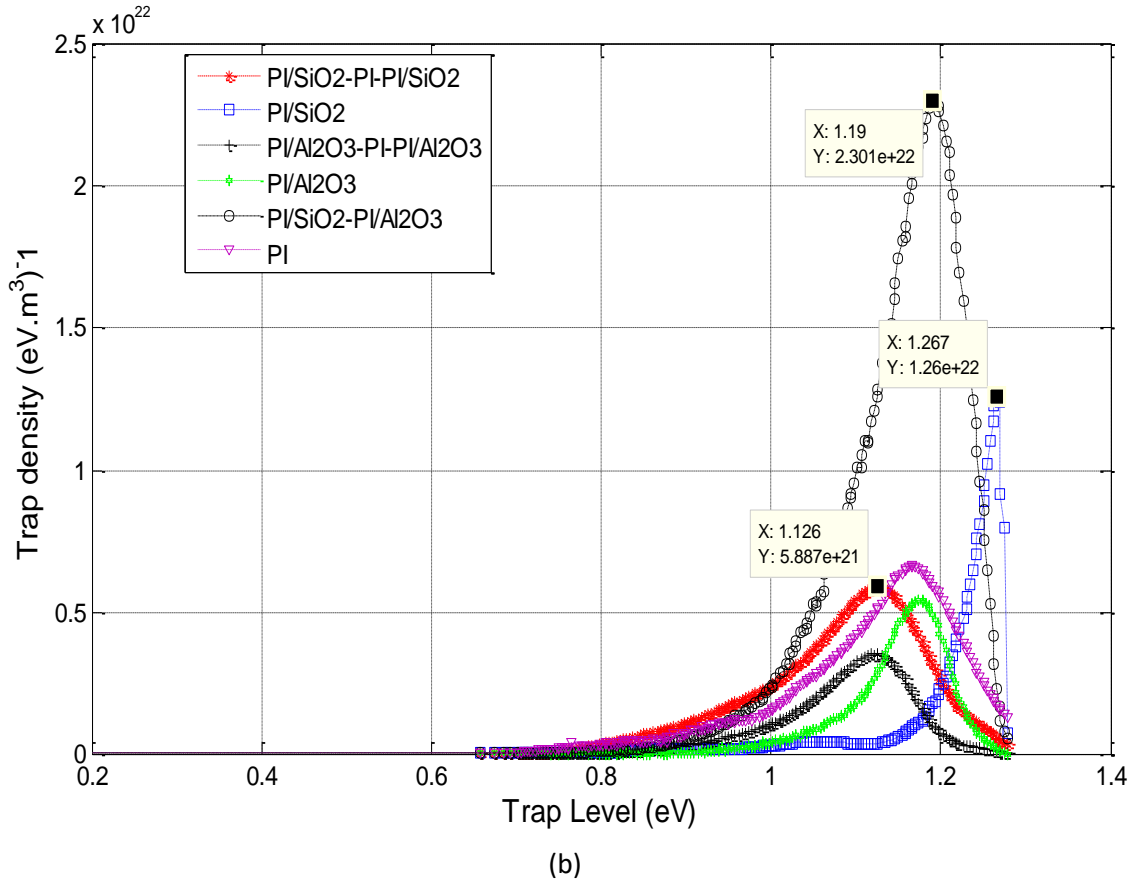


Figure 4.30 TSC measurement of preconditioned samples at 30 kV/mm (b) Trap level distribution using TSC data

#### 4.8.4 Discussion

The PI films can be amorphous or crystalline depending on their synthesis chemistry. In these regions, the band structure is responsible for the distribution of trap energy spectrum of electrons [72]. The traps are formed due to the disorder in the structure at the atomic level under a high electric field. These high electric field stresses are common at the top and bottom surface of samples near electrodes; the density of such damage reduces towards the interior regions. Charge mobility is influenced by the interaction between nanoparticles and polymer matrix. If the outer nanocomposite layers are discharged resistive, then the composite sample becomes discharge resistive, as a whole [154].

We observed space charge suppression due to the influence of the PI/nanocomposite layer structure. To explain this phenomenon, a model is presented in Figure 4.31 describing the influence of PI/nanocomposite layer interface on charge transportation, recombination and injection [35]. Thin layers sample is a sandwich between two electrodes. The layer near to anode acts as the holes transport layer and layer near cathode acts as the electrons transport layer. The interfacial region of such layers provides enough space for recombination for

electrons and holes that are injected by EIL and HIL respectively. The injection of holes from HIL and injection of electrons from EIL move towards holes transport layer (HTL) and electrons transport layer (ETL) respectively. The charges transported and attracted to opposite electrodes and, during the mobility, some the charge trapping, de-trapping and recombination may happen in this interface. Some charges already exist due to defects present in this region. The interface area can be the same or opposite charge polarity junction compared to the nearest electrode, depending on the electronic state of the interface. In the case of two layers, PI structure the electrons accumulate near the anode interface because the mobility of electrons is higher than holes. In the case of three-layer structure, the same polarity charges accumulate in the interface area. There can be three reasons for these phenomena. Firstly, distinctive charge barriers at the interface for electrons and holes influence the charge injection rate. Secondly, the differences between holes and electrons carrier mobility of PI and PI/nanocomposite give rise to the accumulation of charges at interfaces. Finally, the presence of interface charge polarity further restricts or recombines charge carriers transport. Due to permittivity/conductivity difference at interface and bond linkage between different composite layers, electronic states at interface change from the rest of the bulk material. Therefore, the discontinuity of electronic state distribution causes an additive trap at the interface for the transportation of charge.

In three-layer structure, the bond linkage is between PI/nanocomposite – PI layers, while in two-layer structure, the bond linkage is between PI/nanocomposite – PI/nanocomposite layers. According to the FTIR study, some new bonds appear between PI and nanoparticles layers, such as Al-O-Si, Si-C and strong hydrogen bonding due to using a silane coupling agent setting up a covalent bond. Physical and chemical structure change between layers arises new traps at interfaces containing different energy levels [74], [155]. It can either increase the charge carrier transportation or decrease depending on the trap energy levels present at the interface. The interfacial region and surrounding surface, with higher carrier transfer ability, lead to an increase in surface conductivity. The presence of nanoparticles on the top and bottom surface of insulation can restrict the charge injection, but at the same time provides a higher number of traps. We can consider that there are a large number of traps at the PI/nanocomposite – PI/nanocomposite interface region. Once the injected charges are captured by these traps, their release would be difficult. On the other hand, better bonding nature between the PI/nanocomposite layer and higher charge carrier mobility in the PI act as hopping sites for charge carrier and the charge could mitigate quickly. The charges achieve equilibrium state and most of the interface charges neutralized in three-layer structures. In the case of the PI/nanocomposite layer, the interface charge polarity acts as a barrier and makes further charge injection difficult. Depending on the nature of the interface, we can conclude from our results that a two-layer structure PI/nanocomposite – PI/nanocomposite interface mostly provides deep traps. Whereas three-layer structures provide shallow traps and charge injection

restriction phenomenon is dominant. The PI film has higher charge carrier mobility and better chemically linked with the nanocomposite layer rather nanocomposite/nanocomposite layer. The results showed that mostly deep trap levels present in two layers samples of PI/nanocomposite – PI/nanocomposite (PI/Al<sub>2</sub>O<sub>3</sub>-PI/SiO<sub>2</sub>) interface and charges can easily be trapped into these trap levels during the movement from one electrode to other. In the case of PI/nanocomposite interface, mostly shallow trap levels are observed with high charge mobility and low charge injection rate, as compared to PI/nanocomposite – PI/nanocomposite interface. A comparison of the results with distinctive layer structure and different types of nanoparticles gives evident proof that the structure and types of nanoparticles influence the interfacial charge accumulation. Besides, a noteworthy change in the amount of interfacial charge is observed, mostly because of the surface state of insulation material.

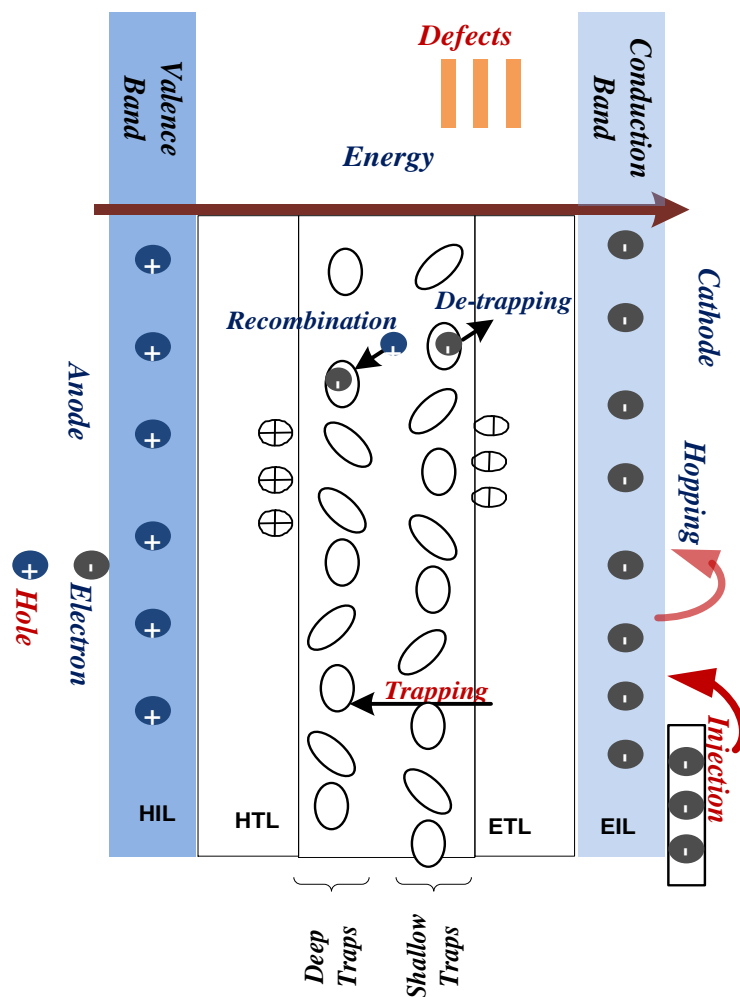


Figure 4.31 Layers structure, holes injection layer (HIL), holes transport layer (HTL), electrons transport layer (ETL), electrons injection layer (EIL)

#### 4.9 Summary

This chapter presents the experimental characterization of PI and PI/nanocomposites films. After synthesis of samples, microscopic analysis and chemical characterization using SEM and FTIR are presented to understand the composition of samples. FTIR spectroscopy was performed for full and half cured PI films to understand the chemical bonds and thermal imidization process. The microscopic morphology characteristics were performed using SEM/TEM scanning to obtain the nanoparticles dispersion and physical condition of samples after applying corona discharge PWM inverter pulses. Findings on the corona discharge resistance properties and the impact of surface discharge degradation are discussed.

A thermomechanical analysis is performed using rheological test which tells us the thermal phase changes states (glassy, rubbery) and relaxation peaks of polymer chain process happening for PI and nanocomposite-based PI films. The thermal conductivity of these films was also measured to obtain the heat transfer capacity of these films.

The dielectric properties of these films as a function of frequency and temperature were measured and analyzed. Also, to understand the polarization and depolarization process of these films, the conduction current versus applied electric fields were measured and different conduction mechanism related to charge injection and bulk conduction are analyzed using the slope of current densities/electric field characteristics.

Furthermore, the most striking outcomes of this chapter describe the impact of improved nanofiller dispersion on space charge and electric breakdown results. The electrical breakdown strength and lifetime were measured under bipolar square wave pulses conditions. Early breakdown phenomenon, such as space charge accumulation, was measured using TSM and PEA techniques. The effects of PI/nanocomposite – PI, PI/nanocomposite – PI/nanocomposite, PI – PI interfaces and the type of nanoparticles on the charge trapping and transporting were investigated. The space charge density and electric field on the basis of thermal step current were calculated and compared for single and multi-layer PI nanocomposites films. Moreover, dielectric loss and thermal conductivity are analyzed to check the material energy loss and heat transfer ability respectfully.

According to space charge and trap level results, the order of space charge accumulation ability in five types of samples is as follows:  $\text{PI}/\text{Al}_2\text{O}_3\text{-PI}/\text{SiO}_2 > \text{PI}/\text{SiO}_2 > \text{PI}/\text{Al}_2\text{O}_3 > \text{PI}/\text{SiO}_2\text{-PI-PI}/\text{SiO}_2 > \text{PI}/\text{Al}_2\text{O}_3\text{-PI-PI}/\text{Al}_2\text{O}_3$ . The two-layer structure of  $\text{PI}/\text{Al}_2\text{O}_3\text{-PI}/\text{SiO}_2$  interface acts as traps for electrons but not for holes.  $\text{PI}/\text{Al}_2\text{O}_3\text{-PI}/\text{SiO}_2$  interface accumulates charges with deep level traps, while  $\text{PI}/\text{Al}_2\text{O}_3\text{-PI-PI}/\text{Al}_2\text{O}_3$  and  $\text{PI}/\text{SiO}_2\text{-PI-PI}/\text{SiO}_2$  charges accumulate at interfaces then disappear with lower trap energy level. During depolarization, faster charge decay is observed in three-layer structure compared to the single-layer structure. This research illustrates a broad understanding of the influence of structure and type of nanoparticles on space charge

accumulation, transportation and suppression, which elaborate that the desirable structure design can increase the overall performance of electric motor insulation for high electric field applications.



## Chapter-5

---

Simulation and modeling



**Chapter 5 Simulation and modeling**

5.1 Introduction .....	121
5.2 Numerical modeling description.....	121
5.3 General sample description .....	121
5.4 Multi-layer PI/nanocomposite model using real experimental boundary conditions ....	122
5.4.1 Boundary conditions .....	124
5.4.2 Domain equations .....	125
5.4.3 Electric field distribution for PI nanocomposite models.....	126
5.4.4 Effect of permittivity and agglomeration on electric field enhancement .....	127
5.4.5 Role of the interface and inter-particle distance .....	128
5.5 Summary .....	131

### 5.1 Introduction

This chapter aims at discussing the impact of the nanocomposite thin layer on nanoparticles dispersion and their dielectric properties. The contents of this chapter describe the construction of a polyimide/nanocomposite 3D model based on actual boundary conditions, obtained from SEM/TEM images. Effect of nanoparticles agglomeration on the electric field distortion is explicitly described in this model. The agglomeration of nanoparticles is associated with the change in nanoparticles position and for that, each class of sample geometry and composition is defined in COMSOL Multiphysics software. Afterward, we investigate the electric field enhancement factor and electric potential.

### 5.2 Numerical modeling description

The effective permittivity of composite materials generally depends on the material microstructure, which includes the volume fraction, as well as the shapes and types of components. For homogeneous materials, the electric field distribution can be calculated using commonly used analytical solutions. However, if the material structure is nonhomogeneous composites, then analytical models cannot be used to precisely calculate electric field distribution. However, it can still be measured experimentally or calculated numerically. Few numerical models have been proposed for polymeric nanocomposites material structure, but no one describes the exact geometry and boundary conditions close to nature to the sample. In this part of the research, the electric field distribution of a polyimide-based nanocomposite model using real boundary conditions was calculated by numerical simulation in COMSOL Multiphysics software, which is based on the finite element method (FEM). The influence of dispersion, as well as the variation of the permittivity and radius (or the volume fraction) of inclusions on effective permittivity, is studied. The electric field and polarization distribution in the nanocomposite materials are also reported in this chapter.

### 5.3 General sample description

PI is obtained using the curing method, in which the solvent is evaporated with the increase of temperature. During the PI film curing process from poly amic acid (PAA) solution, there is a strong tendency of nanoparticles to get agglomerated, as presented in chapter 3 section 3.1, and may influence the permittivity, thus the capacitance of the sample. Keeping this in mind, we prepared a multi-layer PI nanocomposite model, in which the top layer consists of a very thin PI/nanocomposite (NPI) and the middle is composed of pure PI layer. By doing this, we are giving less space for nanoparticles to get agglomerated, because if the same number of nanoparticles is contained in a large volume of PAA solution, particles may get agglomerated easily, as shown hereafter in Figure 5.1.

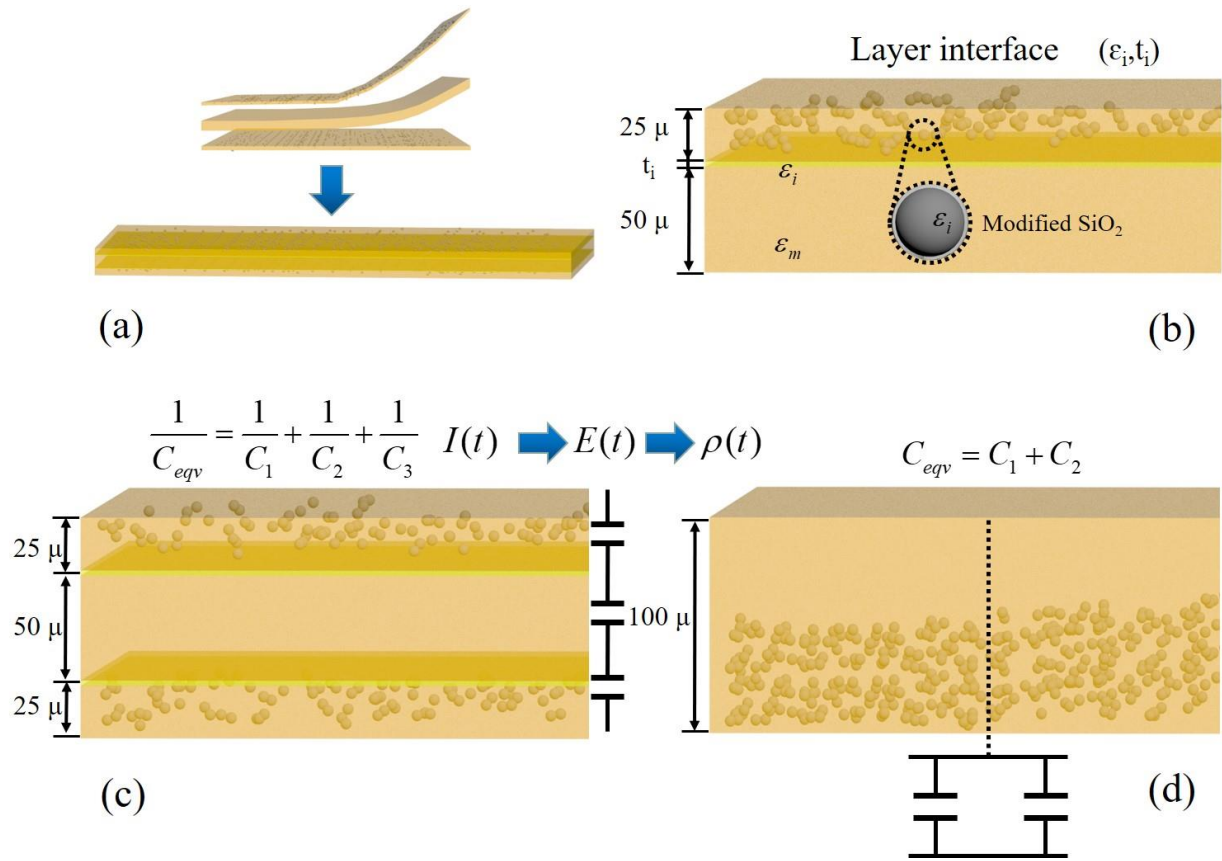


Figure 5.1 Change of sample capacitance and interface permittivity due to nanoparticles agglomeration: (a, c) three-layer structure with less chance of agglomeration, (d) single-layer structure with a higher chance of agglomeration, (b) two-layer structure with interface thickness and permittivity.

#### 5.4 Multi-layer PI/nanocomposite model using real experimental boundary conditions

PI/nanocomposite 3D model was built in COMSOL, on the basis of actual boundary conditions obtained from TEM/SEM images of laboratory produced samples, as shown in Figure 5.3(a, d, g) and it's respectfully constructed model, as shown in Figure 5.3(c, f, i), which is based on the actual nanoparticle's positions from TEM/SEM images. COMSOL-MATLAB Live Link and image processing tools are used to build the model. In the first two models shown in Figure 5.3(c, f), we assumed that the color intensity level from Figure 5.3(a, d), respectfully as the depth of nanoparticles, while in third model in Figure 5.3(i), we used SEM cross-view from Figure 5.3(j) to find the depth of nanoparticles inside the bulk of polymer. This information is used as a z-axis parameter to build the models. The detailed to construct the model is shown in Figure 5.2, picked up a clear TEM/SEM image, applied an image processing to remove background noise and finally converted it into the binary. In order to select the required data from the binary image, we adjusted the nanoparticles image to binary conversion threshold, nanoparticles size and circularity level. The data contained different information about the

particles size, shape and (x, y) coordinates position. The z-axis related to the depth of each particles, is obtained using a small code in MATLAB according to the intensity level of each particles. In this simulation model, the dielectric permittivity of the PI matrix is taken to be  $\epsilon_1 = 3.4$  and that of the silica nanoparticles is  $\epsilon_2 = 3.6$ . The average nanoparticles size of 10 nm radiuses has been calculated after image processing. The top surface of the 3D model was applied by the constant electric potential of (V = 10 V), and the bottom surface was grounded to 0 V. The volume fraction of nanoparticles is constant and set at 1% for single and multi-layer insulation structures.

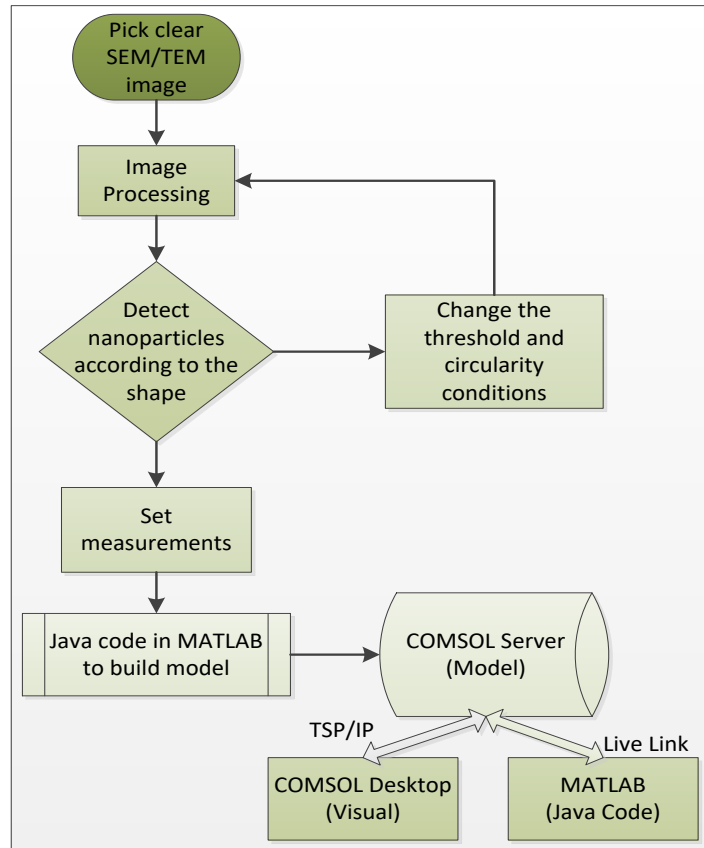
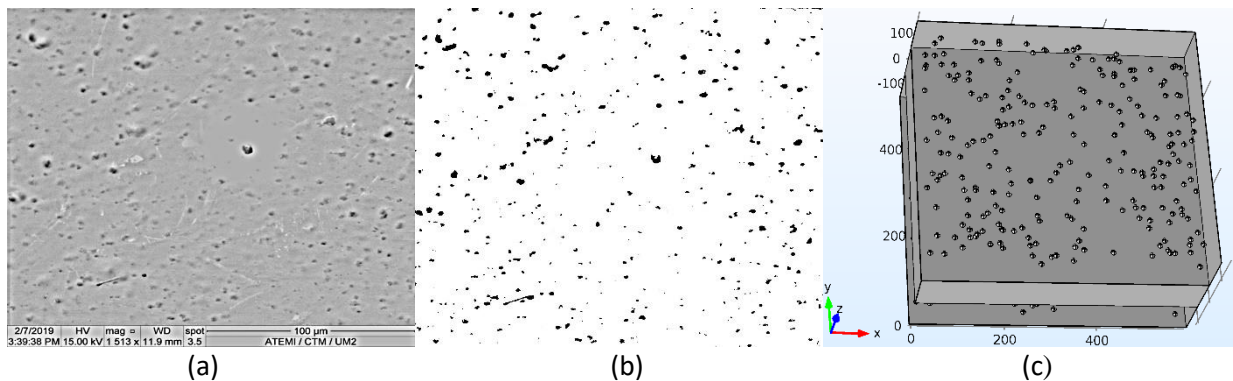


Figure 5.2 Model building algorithm



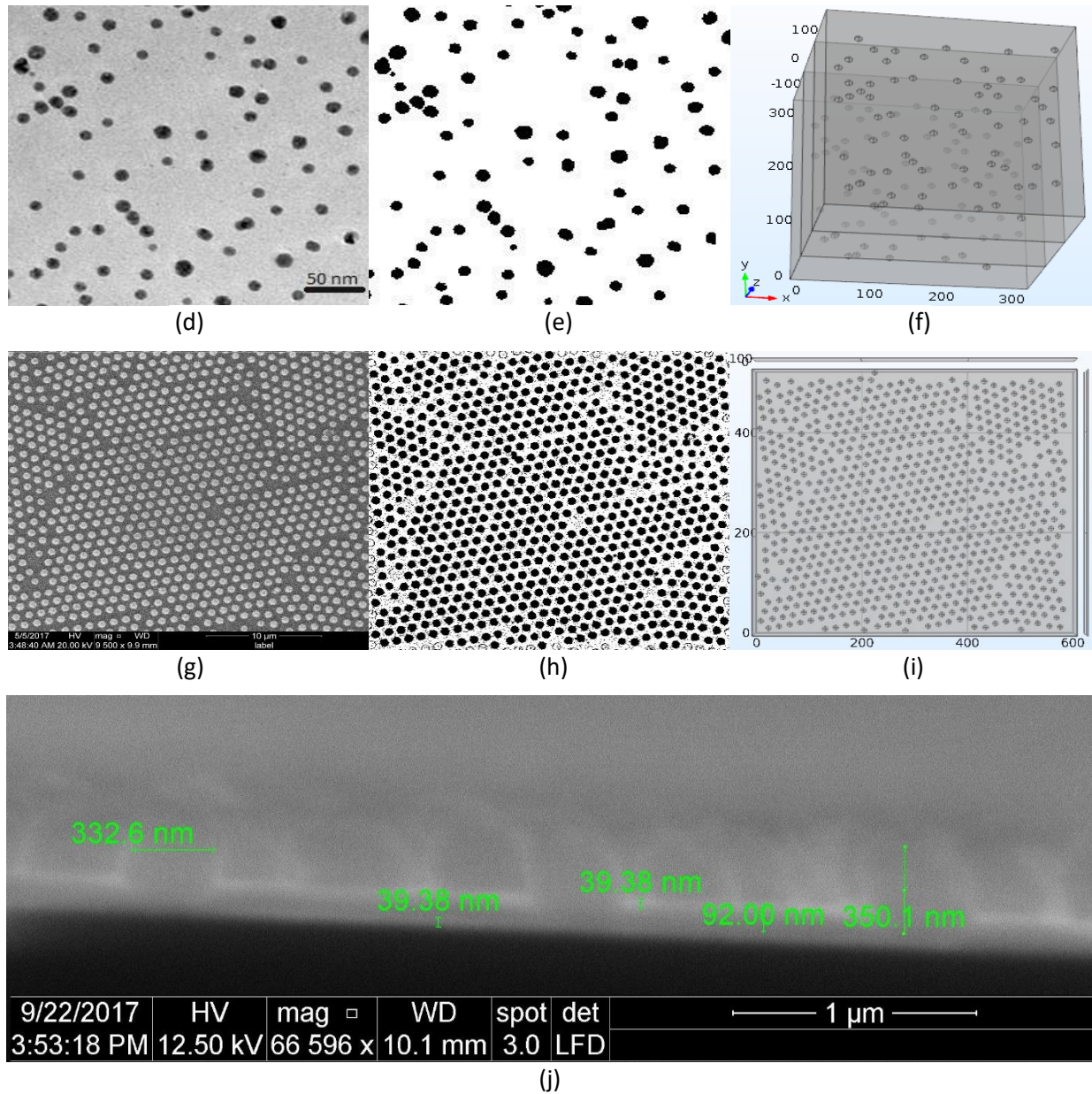


Figure 5.3 (a, d, g) SEM/TEM images (b, e, h) Image processing binary conversions (c, f, i) Model in COMSOL using MATLAB Live Link (j) Cross-sectional view using SEM

#### 5.4.1 Boundary conditions

When an electric field is applied to more than one dielectric material, then the boundaries between the two materials have some effects on the electric field components. The conditions exist at the boundaries of the materials when the same electric field spans over these materials is an interest of study. This is called the boundary conditions. The two conditions that exist at the boundary between a conducting medium and a dielectric medium are:

- 1) The tangential component of the electric field is zero ( $E_t = 0$ ).

- 2) The electric displacement or electric flux density  $D$  at the boundary of the dielectric medium is equal to the charge density  $\rho$  on the surface of the conductor medium at that point ( $D = \rho$ ).

The conditions that exist at the boundary between two different dielectric mediums are:

- 1) The tangential components of the electric fields are equal ( $E_{1t} = E_{2t}$ ).
- 2) The normal components of electric induction are equal ( $D_{1n} = D_{2n}$ ).

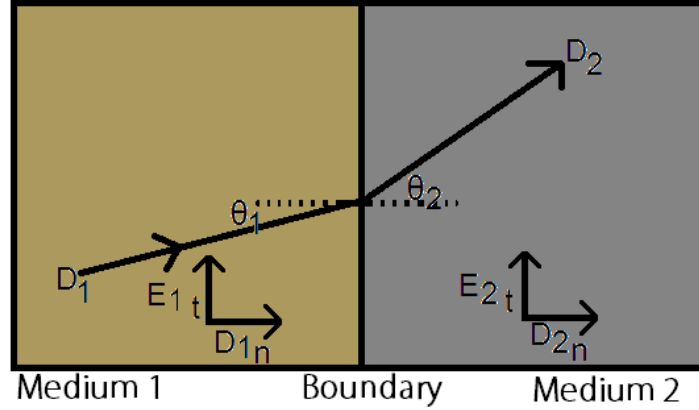


Figure 5.4 Electric field boundary conditions

The continuity conditions and simulation box boundaries for heterogeneous structure of two materials at the interfaces can be expressed as:

$$n \cdot D_1 = n \cdot D_2 \quad (5.1)$$

For neutral condition, charge density is set to negligible. Therefore, external box boundaries act as an insulator.

$$n \cdot D = 0 \quad (5.2)$$

Each nanoparticle (x, y) coordinates information was taken after converting the SEM/TEM image to binary. For z coordinate, intensity level and cross-sectional view of SEM images were used.

#### 5.4.2 Domain equations

COMSOL can be worked in a number of different ways, such as through graphical interface as well as applying basic java programming in order to extend the flexibility [156], [157]. In this work, an additional feature of COMSOL, such as COMSOL to MATLAB LiveLink, is explored. By applying MATLAB, several lines of java code were replaced with single statements. It also helped us to open both COMSOL desktop and to work with the code at the same time. By knowing the electric field vector distribution inside the nanocomposite material, it is possible to calculate the total effective permittivity, electric field enhancement factor and electric

polarization density of the PI nanocomposite samples. The AC-DC electrostatic physics study module of COMSOL was used in which the finite-element method (FEM) solves the Poisson's equation, maps the electrostatic potential ( $V$ ) distribution, and then calculates the resulting electrostatic electric field distribution at each position. The domain equations used in an electrostatic equilibrium state in which Poisson's equation is used to calculate the above parameters of the model, which are given as:

$$\vec{\nabla} \cdot \mathbf{D} = 0 \quad (5.3)$$

Where  $\mathbf{D} = \epsilon_0 \epsilon_r \mathbf{E}$ , is the electric displacement vector and  $\mathbf{E} = -\nabla V$  is the electric field vector

$$\vec{\nabla} \cdot (\epsilon_r \epsilon_0 \vec{\nabla} \varphi) = -\rho \quad (5.4)$$

Where  $\rho$  is the volume charge density,  $\epsilon_r$  is the relative permittivity of a material,  $\epsilon_0$  is the vacuum permittivity and  $\varphi$  is the electric field potential. If there is no charge ( $\rho = 0$ ), and if we consider electrical conductivity  $\sigma$  and dielectric loss into account, then above equation becomes as:

$$\vec{\nabla} \cdot (j\omega(\epsilon_r \epsilon_0 \vec{\nabla} \varphi)) = 0 \quad (5.5)$$

After knowing the material morphology and other information, we can solve equation (5.4) or equation (5.5) numerically using the finite elements method (FEM) in COMSOL Multiphysics software package [149], [156]. Once the electric field distribution is solved, the average effective permittivity, electric field enhancement factor and polarization density of the PI nanocomposite model can also be evaluated.

### 5.4.3 Electric field distribution for PI nanocomposite models

After constructing the continuum model in COMSOL, the Finite Element Method (FEM) was used to observe the nonlinear electric field distribution, as shown in Figure 5.5(a-d). The second aspect of nanodielectrics modeling with FEM is the prediction of dielectric strength based on electric field distribution. For that, FEM is used to calculate the electric field enhancement and polarization charge density, as shown in Figure 5.5(e, f). Even for the same insulating material, the breakdown strength varies from sample to sample. This simulation work can help to predict the nonhomogeneous nanocomposite materials breakdown strength and categorize the phase transition problems. Characteristic simulation breakdown strengths of a material can be predicted using the applied external electric field strength with the probability of 63% in the experiments.



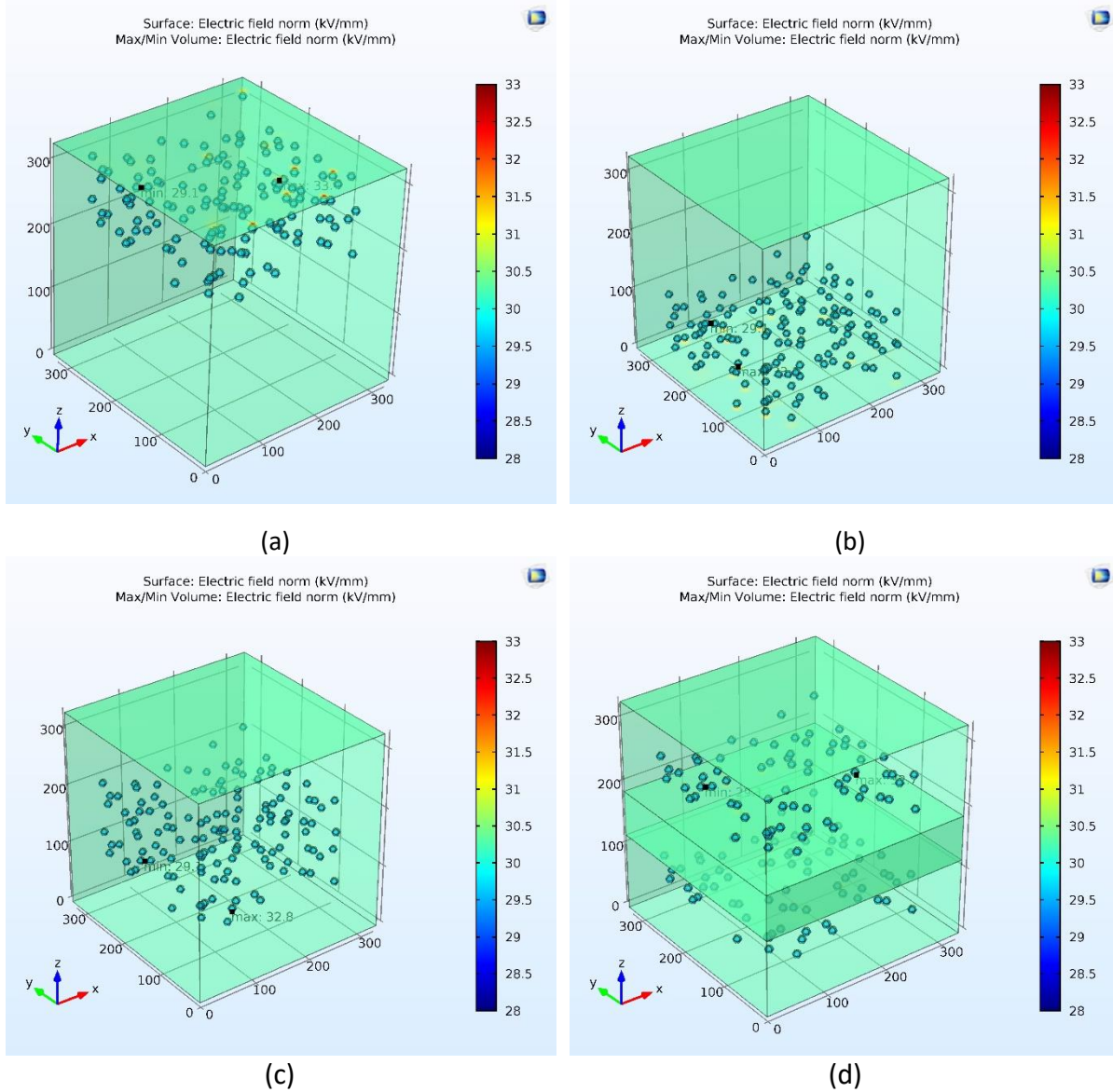


Figure 5.5 Electric field distribution (a) Top agglomeration (b) Bottom agglomeration (c) Three-layer homogenous dispersion (d) Three-layer original homogenous distribution

#### 5.4.4 Effect of permittivity and agglomeration on electric field enhancement

Single-layer, two-layer and three-layer PI/silica nanocomposite models were simulated with altered nanoparticles permittivity and position. The analysis is focused on calculating the peak electric field enhancement factor (peak EFEF) in the sample from equation (5.6)

$$\text{Peak EFEF} = \frac{\text{Maximum electricfield (kV / mm)}}{\text{Applied electric field (kV / mm)}} \quad (5.6)$$

The simulation results from Figure 5.6 demonstrate that the electric field enhancement factor (EFEF) varies with the increase in nanoparticles permittivity  $\epsilon_2$ ; low EFEF is observed in



multi-structure PI films compared with single-layer top and bottom agglomerated PI films. As shown in the simulation solution of Figure 5.6, an electric field enhancement is present at the interface between the nanoparticle and the PI matrix on the bottom and top sides in the  $z$ -direction, and the electric field is almost constant and lower in the rest of the inclusion area. The electric field decreases as the degree of dispersion of the nanoparticles increases, and the highest value of the electric field and polarization density is obtained in top agglomerated single layer PI film. The main reasons for such a reduction in EFEF can be the equivalent capacitance of sample due to nanoparticles distribution, interface thickness and permittivity ( $t_i$ ,  $\epsilon_i$ ) contrast of nanoparticles and PI matrix permittivity, which influence the effective permittivity of the overall sample. The electric field is also influenced due to the shape of the outer surface of nanoparticles because, if agglomeration happens, there is a chance that the combined particles may change the circularity level and transform the shape into the sharp edges, which increase the local electric field around those edges. Another reason for higher FEEF in agglomerated samples can be due to a decrease in the inter particles distance. PI is obtained using the curing method in which the solvent is evaporated with the increase of temperature. During the PI film curing process from poly amic acid (PAA) solution, there is a strong tendency of nanoparticles to get agglomerated. They may float on the surface or decant, as presented in Figure 5.1(b). Both effects can increase the chances of agglomeration and may influence the interface thickness and permittivity of samples, as shown in Figure 5.1(c), and result in worst electrical, mechanical and thermal properties of PI films.

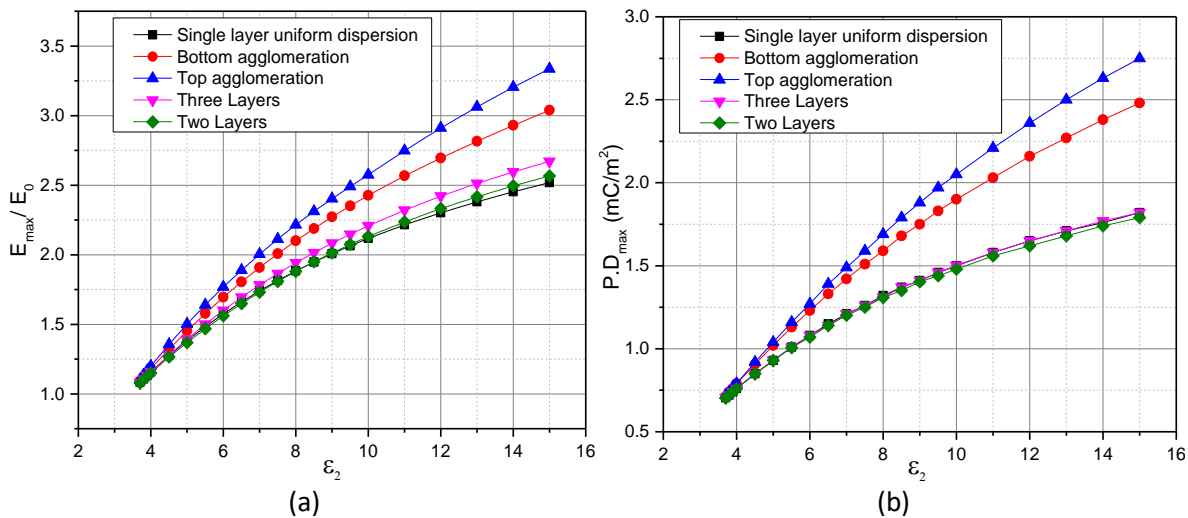


Figure 5.6 Calculation of (a) Electric field enhancement factor and (b) Polarization charge density

#### 5.4.5 Role of the interface and inter-particle distance

The performance of polymer nanocomposites is significantly dependent on parameters such as the size of nanoparticles, shape, types, contents of filling ratio, inter-particles distance and interface [158]. Nano saturation in the form of agglomeration is two main factors to

influence the interface interaction region and these factors change with the change of specimen structure. Conductivity and permittivity vary with the change of sample structure from a single layer to multi-layer, which influences the total surface area of nanoparticles and the interface polarization. In single-layer samples, inter particles distance is larger and homogenous than three-layer samples and therefore the surface to volume ratio for these saturated nanoparticles in single layer samples is lower compared to the three-layer model. We calculated surface area and inter-particle distance for different samples.

$$D = \left[ \left\{ \frac{\pi}{6} \left( \frac{\rho_{nano}}{\rho_{base}} \right) \frac{100}{wt\%} \left[ 1 - \frac{wt\%}{100} \left( 1 - \frac{\rho_{base}}{\rho_{nano}} \right) \right] \right\}^{0.3} - 1 \right] d \quad (5.7)$$

$$S = \frac{\pi d^2}{(D + d)^3} \quad (5.8)$$

A model is shown in Figure 5.7 to understand inter-particle distance and surface area, which is calculated on the basis of equations (5.6) and (5.7) [77], [154], [159]. It can be seen from Table 5.1 that due to different sizes of particles and nano distribution, the inter-particle spacing is reduced in triple layer samples and the total surface area interphase region of nanoparticles is increased.

Table 5.1 Inter-filler distance and surface area of composite films

Composite	Size of Nano Particles (nm)	Density $10^3(\text{kg/m}^3)$	Inter-particle distance (nm)	Surface area ( $\text{km}^2/\text{m}^3$ )
PI/ $\text{Al}_2\text{O}_3$ -PI-PI/ $\text{Al}_2\text{O}_3$	10	4	8.1	52.9
PI/ $\text{SiO}_2$ -PI- PI/ $\text{SiO}_2$	15	2.6	12.1	35.5
PI/ $\text{Al}_2\text{O}_3$	50	4	54.7	6.84
PI/ $\text{SiO}_2$	200	2.6	162	2.64
PI		1.7		

This is the main reason to influence the properties of nanocomposite materials. The small inter filler distance provides less free volume for electrons. Therefore, the less free path is available for electrons to accelerate and this increases the breakdown strength. Nanoparticles interface, on the top surface of three-layer samples, accounts for more surface area. In the same way, the surface area in a unit volume of  $\text{SiO}_2$  is larger than that of  $\text{Al}_2\text{O}_3$ , for the same size and hence the free volume is less. It clearly exhibits that the interface with various nanoparticles assumes an essential part of this microscopic area, which reflects the attributes of polymer nanocomposites [160]–[162].

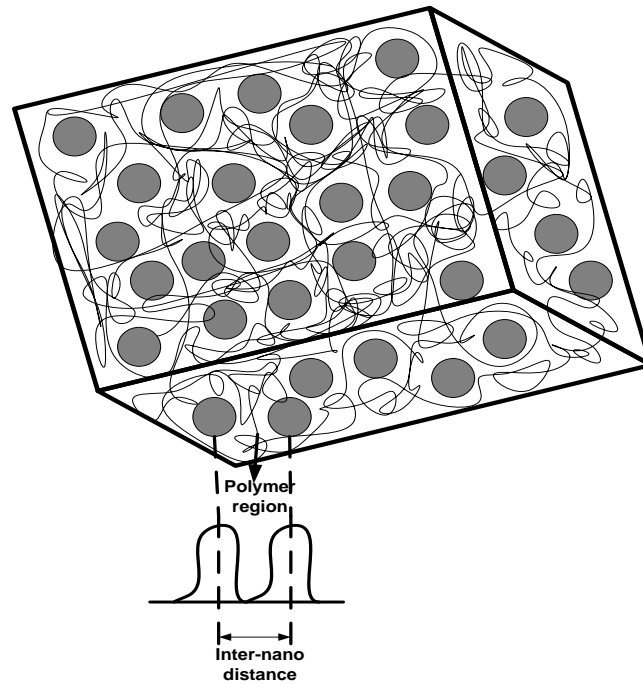


Figure 5.7 Model for inter-particle distance

Interfacial interaction of structure and type of nanoparticles are important factors to change dielectric constant and dielectric losses. The morphology of the PI film has amorphous and crystalline regions. In the crystalline regions, the band structure is responsible for the distribution energy spectrum of electrons [36]. Trap levels generated due to the disorder change in the atomic structure are commonly at the top and bottom surface of samples, near electrodes, and the density of these regions reduces towards the inferior regions. Three-layer sample consists of polymer and nano matrix, top layer consists of nanoparticles and this nano connected with other matrix in pattern like the third layer of the nanoparticles, known as loosely bond layer [13] having low density. This layer is attached with polymer and second layer is attached with second layer of samples containing only polymer matrix.

Surface discharge resistance is influenced by the interaction between nanoparticles and the polymer matrix. Top and bottom nanolayers increase surface discharge resistance and therefore improve electrical properties. Meanwhile, the middle PI layer provides flexibility to improve mechanical breakdown. Furthermore, if the outer nanocomposite layers are discharged resistive then the composite sample becomes discharge resistive as a whole [13].

Electrons are injected from the electrodes and choose an easy path to move inside the sample. Electrons are more accelerated in large free volume regions. But there are many defects and nanoparticles hindrance present in the top and bottom layers, which decelerate them after collision with the nanoparticles, resulting in the increase in breakdown strength [12].

### 5.5 Summary

This final chapter aimed at improving our understanding to predict the dielectric strength of single and multilayer PI/nanocomposite samples by modeling their nonlinear electric field distribution using COMSOL Multiphysics software. The results conclude that a thin layer of PI/nanocomposite in multilayer samples can improve the nanoparticles dispersion and results in improved dielectric strength. The multilayer PI/nanocomposite model was designed on the bases of real experimental boundary conditions obtained after SEM/TEM image processing. A 3D simulation model is used to calculate the electrical field numerically by changing the permittivity and dispersion level of nanoparticles. The influence of nanoparticle permittivity on electric field and space charge density is addressed in this study. An increase in the electric field and polarization density was recorded with an increase of nanoparticles permittivity. In the multilayer model, the electrical field and space charge density are reduced due to homogenous nanoparticles dispersion. On the other hand, for single-layer models (top agglomeration and bottom agglomeration) space charge density and electric field are increased. The proposed modeling method will help the designers to understand the polymeric nanocomposite structure and will allow them to simulate the dielectric behavior of polymeric nanocomposite.



### Conclusion and future perspectives

#### Conclusion

This research concerns the application of high-temperature multilayer polyimide nanodielectric materials for electric motors insulation. Physical properties of polyimide (PI) films and their derived nanocomposites, including the single and multilayer PI/nanocomposite films synthesis process optimization, is studied and described in this thesis. A series of experiments such as lifetime, breakdown strength, corona discharge, space charge and dielectric properties were performed on the synthesized samples. The synthesis of PI nanocomposite is a complex process with several factors that are involved in the process and can change the molecular weight of PAA solution. This complex process can thus influence the overall dielectric properties of the obtained PI/nanocomposite films.

A detailed synthesis process optimization is described to understand this phenomenon. After obtaining the required samples, FTIR spectroscopy was performed for full and half cured PI films to understand the chemical bonds and thermal imidization process. The microscopic morphology characteristics were performed using SEM/TEM scanning to obtain the nanoparticles dispersion and physical condition of samples after applying corona discharge of PWM inverter power pulses. The electrical breakdown strength and lifetime were measured under PWM inverter power pulses conditions, by using a special designed nanoseconds pulse power generator.

The failure mechanism of the PI film after surface discharge is revealed. Factors like interface and voids after electric stresses can influence the electric motor insulation lifetime. The primary reason for PI film aging is the breaking of polymer chains. Discharges release ultraviolet rays and high-energy electrons that increase the surrounding temperature, melt the polymer chain and enhance the electric field locally. The localized electric field enhancement, combined with the temperature, degrades the material chemically and physically. Surface corona discharge initiates material deterioration. Residual charges from last discharge intensity reverse the electric field. Moreover, a decrease in rise time results in an increase of  $dV/dt$ , which is related to the increase of discharge quantity. With the increase in frequency, the charge depletion rate is slow and doesn't have enough time to leave before polarity reverse, thus, the total electric field after each inversion is intensified. The presence of nanoparticles based PI film on the top and bottom surface has played a significant role in improving dielectric and mechanical strength of these films. The multilayer samples with  $\text{SiO}_2$  nanofillers have higher electrical breakdown strength, compared with other types of samples, 30% enhancement compared with multilayer  $\text{Al}_2\text{O}_3$ -PI- $\text{Al}_2\text{O}_3$  films.  $\text{SiO}_2$  additive showed better dispersion. The multilayer structure showed a pronounce improvements on insulation strength within temperature, from  $25^\circ\text{C}$  to  $200^\circ\text{C}$ , which is for example particularly suitable for its application in inverter fed motors, that used in high-speed railway.

## Conclusion and future perspectives

After depositing a thin PI/ nanoparticles layer on both sides of PI film by using spin coating technique, further dielectric properties such as dielectrics constant, dielectric loss, current densities and space charge were measured and investigated on the basis of different type and structure of nano doped PI films. Alumina reinforced samples showed higher dielectric constant and dielectric loss factor, due to interface polarization and higher inheritance of alumina permittivity towards composite than silica particles.

A thermomechanical analysis is performed using a rheological test which tells us the thermal phase changes states (glassy, rubbery) and relaxation peaks of polymer chain process happening for PI and nanocomposite based PI films as a function of temperature. The thermal conductivity of these films was also measured to obtain the heat transfer capacity of these films. The heat in solid materials can be transferred using conduction phenomena by heat-carrying phonons. The nanoparticles have a higher heat transfer rate than polymers. Therefore, higher thermal conductivities are observed in nanoparticles based PI films as compared to pure PI films. To compare the  $T_g$  and mechanical flexibility of these films two dianhydrides were used and compared. The ODPDA based PI films have shown higher mechanical flexibility, but lower  $T_g$  and PMDA based PI films have shown higher  $T_g$  but lower mechanical flexibility. The further thermomechanical test has been demonstrated that the highest  $T_g$  was observed in PI/SiO<sub>2</sub> films. The reduction of the molecular mobility close to the filler induces an increase in the apparent glass transition temperature. The highest  $T_g$  value is taken at the maximum of  $G''$  is about 447 °C.

The conduction mechanism in dielectric films is an essential property to the successful operation of these dielectric films under high voltage applications. In order to understand the polarization and depolarization capabilities of these films, the conduction currents were measured at different temperatures and electric fields and other conduction mechanisms related to charge injection such as Schottky and bulk conduction such as SCLC, Poole-Frenkel and hopping were analyzed using the slope of current/voltage characteristics. At-least one possible conduction of each class, either related to charge injection or bulk conduction should be present to describe the steady-state conduction current. But for some samples such as FPI and PI-PI/SiO<sub>2</sub> two different conduction mechanisms from the same bulk conduction class seem to be present at high temperature 150 °C. This shows that the study of conduction mechanisms in polymeric materials is not easy, and this is even more true when it concerns composite materials. It appears from this study, dominant conduction mechanisms strongly dependent on the electric field and the measurement temperature, whatever the type of studied material.

Space charge accumulation was measured using TSM and PEA techniques. Interfacial interaction of structure and type of nanoparticles were studied to understand charge accumulation and mitigation mechanism. The type of nanoparticle and interface has a significant effect on the charge movements and trap levels of PI/nanocomposite films. The PEA

and TSC results were used to calculate trap levels. The effects of PI/nanocomposite – PI, PI/nanocomposite – PI/nanocomposite, PI – PI interfaces and the type of nanoparticles on the charge trapping and de-trapping were analyzed. The two-layer structure of  $\text{Al}_2\text{O}_3$ - $\text{SiO}_2$  interface acts as traps for electrons, but not for holes. PI/ $\text{Al}_2\text{O}_3$ -PI/ $\text{SiO}_2$  interface accumulates charges with deep level traps, while PI/ $\text{Al}_2\text{O}_3$ -PI-PI/ $\text{Al}_2\text{O}_3$  and PI/ $\text{SiO}_2$ -PI-PI/ $\text{SiO}_2$  charges accumulate at interfaces, then disappear with lower trap energy level. During depolarization, faster charge decay is observed in the three-layer structure, compared to the single-layer structure. From space charge accumulation and trap levels point of view, the order is as follows in five types of samples,  $\text{PI}/\text{Al}_2\text{O}_3\text{-PI}/\text{SiO}_2 > \text{PI}/\text{SiO}_2 > \text{PI}/\text{Al}_2\text{O}_3 > \text{PI}/\text{SiO}_2\text{-PI-PI}/\text{SiO}_2 > \text{PI}/\text{Al}_2\text{O}_3\text{-PI-PI}/\text{Al}_2\text{O}_3$ . The charge distribution in the bulk of the sample strongly depends on the type of nanomaterials. The trap depth is calculated by TSC theoretical model and total charge decay theoretical method; the energy depth of shallow and deep trap levels is between 1.12 eV to 1.26 eV. This part of the research illustrates a broad understanding of the influence of structure and type of nanoparticles on the space charge accumulation, transportation and suppression, which elaborate that the designed multilayer structure can significantly improve the overall performance of polyimide films in high electric field environment applications. The layer interface study is worthwhile, because it can distort the electric field distribution under a high electric field. The space charge accumulation at interface will be a critical parameter to understand electric field distribution in multilayers insulation and to decide whether the breakdown occurs at the interface.

The final chapter of the thesis aimed at improving our understanding to predict the dielectric strength of single and multilayer PI/nanocomposite samples by modeling their nonlinear electric field distribution using COMSOL Multiphysics software. The results conclude that a thin layer of PI/nanocomposite in multilayer samples can improve the nanoparticles dispersion and results in improved dielectric strength. The multilayer PI/nanocomposite model was designed on the bases of real experimental boundary conditions obtained after SEM/TEM image processing. A 3D simulation model is used to calculate the electrical field numerically by changing the permittivity and dispersion level of nanoparticles. The influence of nanoparticle permittivity on electric field and space charge density is addressed in this study. An increase in the electric field and polarization density was recorded with an increase of nanoparticles permittivity. In the multilayer model, the electric field and space charge density are reduced due to homogenous nanoparticles dispersion. On the other hand, for single-layer models (top agglomeration and bottom agglomeration), space charge density and electric field are increased. The proposed modeling method will help the designers to understand the polymeric nanocomposite structure and will allow them to simulate the dielectric behavior of these films.



### **Outcome of the research work**

The electrical properties of the multilayer polyimide films were determined through an iterative comparison between simulation and the experimental results. Our methods will make it possible the prediction of the dielectric strength of insulating materials. New multilayer insulating material will ensure the reliable operation for electric motors and generators, which could be used to increase the lifespan and sustainability of electrical rotating machines. Further research of interface between layers and different thickness of top and bottom layers will be effective to explore their impact on dielectric properties. This method can also provide significant insight to explore the relationship between the surface chemistry of the actual laboratory produced nanocomposite polymer samples and their modeling using real boundary conditions.

- 1) Supervised one to two master degree students for their thesis.
- 2) Published three to five SCI papers during research.
- 3) International research exchange collaboration with IES-GEM lab in Montpellier University France and high voltage laboratory of Sichuan University Chengdu China.
- 4) Attended two international conferences.
- 5) Held small workshops and presentations to undergraduate students of Sichuan University what I have learnt during all my education and experience.

### **Future works**

After completing the project about “High temperature multilayer polyimide nanodielectrics for electric motors insulation used in high speed trains” funded by HEC-Campus France and guided by IES-GEM research institute of the University of Montpellier, France, we still consider that there are several items need to be explored.

The sample manufacturing process could be improved further to obtain a better dispersion of the nanoparticles. Promising results have already been obtained using KH 550 silane coupling agent treatment but still we consider better dispersion technique, such as dispersion using electric and magnetic field orientation can be investigated. On the other hand, parameters such as moisture can influence the properties of nanoparticles; so, in next study, these parameters must be considered while preparing PI/nanocomposite samples. Interesting results can be found when two different types of nanoparticles will be used together. Further detailed study about nanoparticles will help to mix two or more nanoparticles with PI film; it may increase the beneficial impact of the nanoparticles and it is possible to obtain better dielectric properties, such as an increase in breakdown strength or reduced dielectric losses. In our opinion, changing the thickness of top and bottom nanocomposite films in multilayer structure can lead to interesting results. The implementation of the model for fillers with different shapes can also be used for further investigation. COMSOL Multiphysics can be used to simulate different

## Conclusion and future perspectives

thickness multilayer models for electric field distribution and heat transfer. We believed that two-layer structures with high thermal conductive nanoparticles will enhance overall sample thermal conductivity. After being intensively investigated for the last several years, a tendency of creating new types of nanodielectrics can be observed. For these dielectrics, the design of the material at the nano scale, using specific manufacturing procedures is considered. Nevertheless, there is still a bridge to cross between the “lab-prepared” materials and those produced on an industrial scale.

In addition, we can apply same approach to PE based nanodielectric materials for HVDC cables. We can add Polyethylene (PE) based nanocomposite and fluorination layers on high voltage cables to enhance insulation strength, increase the electrical conductivity between interfaces and increase the thermal conductivity to evaporate heat from conductor to atmosphere. It could be very interesting approach to apply this simulation as well as experimental research work to other materials and applications and studied further interfacial mechanism.

Further future perspectives:

- 1) Atomic layer/sputtering deposition and extrusion methods to produce multilayer films.
- 2) Use of plasma modified or hybrid nanoparticles.
- 3) Molecular simulation (energy density, localize electric field and traps between amorphous and crystalline region).
- 4) Simulation and experimental observation for the impact of varying thickness of top and bottom nanocomposite layer on electric field distribution and heat transfer model.
- 5) Apply electric and magnetic field techniques to disperse nanoparticles in single and multilayer PI/nanocomposite films.
- 6) Study the interface between layers and interphase between nanoparticle and PI matrix interaction impact on space charge measurements and their trap levels.
- 7) Moisture absorbance effect of nanoparticles on electrical characterization of single and multilayer PI/nanocomposite films.
- 8) Molecular simulation to calculate energy density, localize electric field and traps between amorphous and crystalline region. Simulation and experimental observation for the impact of varying thickness of top and bottom nanocomposite layer on electric field distribution and heat transfer model. Construction of PI/nanocomposite 3D model based on actual boundary conditions and calculate the nonlinear electric field enhancement factors by changing the nanoparticles position, permittivity and radius.

## Conclusion and future perspectives

- 9) Use high dielectric constant  $k$  nanoparticles to build multilayer PI/nanocomposites sandwich structure with high energy density and high charging-discharging efficiency at high temperatures.



## Acknowledgement

### Acknowledgement

First and foremost, I am most grateful to the Almighty GOD for his countless blessings.

My deepest gratitude goes to my advisors, Prof. Jerome Castellon and Prof. Serge Agnel, the work that I undertook at the University of Montpellier should be used in their way. Without their constant encouragement, support, invaluable guidance, and enormous advice, my doctoral study would hardly have been completed. I have benefited tremendously from their vision, technical insights, and a strong pursuit of excellence.

I am also greatly indebted to my parents and other family members for their incredible love, endless encouragement and heartfelt prayers.

My special thanks are extended to Prof. Jean Pierre Habas from ICGM lab of Montpellier University providing me polymer lab to synthesize my samples. He was always there to provide chemist expert opinion whenever I failed during the synthesis process of PI films.

I also thank all the colleagues in the IES-GEM lab for providing a friendly environment to work. I also express my warmest gratitude to the Frédéric Pichot and Jean Marie Peiris, the staff of Technology Center in Micro and nanoelectronics (CTM), the cleanroom and field microscopy to provide a well-equipped platform for PI film coating and deposition using photolithography techniques.

Study in France would never be accomplished without the financial aid of HEC-Campus France and the Ministry of Higher Education. I also wish to thank Prof. Zhou Kai from Sichuan University, the National Science Foundation of China (NSFC), the Research Program of Chinese Ministry of Education, and the Research Program of Sichuan Province for supporting me in this project.

Last but not least, it is a great pleasure to thank everyone who supported and encouraged me and believed that I could do it.

**Dr. Shakeel Akram**



## References

### References

- [1] “Richard Trevithick | English engineer,” *Encyclopedia Britannica*. <https://www.britannica.com/biography/Richard-Trevithick> (accessed Feb. 05, 2020).
- [2] C. Esveld, *Modern railway track*, 2. ed. Zaltbommel: MRT-Productions, 2001.
- [3] H. I. Andrews, *The principles of railway traction*. Amsterdam; New York: Elsevier Science, 1985.
- [4] S. Iwnicki, Ed., *Handbook of railway vehicle dynamics*. Boca Raton: CRC/Taylor & Francis, 2006.
- [5] “Application Guide for AC Adjustable Speed Drive Systems.” <https://www.nema.org/Standards/Pages/Application-Guide-for-AC-Adjustable-Speed-Drive-Systems.aspx> (accessed Feb. 03, 2020).
- [6] H. A. Toliyat and G. B. Kliman, *Handbook of Electric Motors*. CRC Press, 2018.
- [7] J. C. G. Wheeler, “Effects of converter pulses on the electrical insulation in low and medium voltage motors,” *IEEE Electrical Insulation Magazine*, vol. 21, no. 2, pp. 22–29, Mar. 2005, doi: 10.1109/MEI.2005.1412216.
- [8] “Power Electronics: Converters, Applications, and Design, 3rd Edition | Wiley,” *Wiley.com*. <https://www.wiley.com/en-us/Power+Electronics%3A+Converters%2C+Applications%2C+and+Design%2C+3rd+Edition-p-9780471226932> (accessed Feb. 03, 2020).
- [9] M. K. W. Stranges, G. C. Stone, and D. L. Bogh, “IEC 60034-18-41: a new draft technical specification for qualification and acceptance tests of inverter duty motor insulation,” in *Record of Conference Papers Industry Applications Society 52nd Annual Petroleum and Chemical Industry Conference*, Sep. 2005, pp. 297–302, doi: 10.1109/PCICON.2005.1524566.
- [10] A. Cavallini, D. Fabiani, and G. C. Montanari, “Power electronics and electrical insulation systems - part 2: life modeling for insulation design,” *IEEE Electrical Insulation Magazine*, vol. 26, no. 4, pp. 33–39, Jul. 2010, doi: 10.1109/MEI.2010.5511187.
- [11] M. Melfi, A. M. J. Sung, S. Bell, and G. L. Skibinski, “Effect of surge voltage risetime on the insulation of low-voltage machines fed by PWM converters,” *IEEE Transactions on Industry Applications*, vol. 34, no. 4, pp. 766–775, Jul. 1998, doi: 10.1109/28.703971.
- [12] B. Basavaraja and V. S. S. Siva Sarma, “Analysis of the overvoltages in PWM-inverter fed induction motors,” in *TENCON 2008 - 2008 IEEE Region 10 Conference*, Nov. 2008, pp. 1–6, doi: 10.1109/TENCON.2008.4766404.
- [13] D. R. Johnston, J. T. LaForte, P. E. Podhorez, and H. N. Galpern, “Frequency Acceleration of Voltage Endurance,” *IEEE Transactions on Electrical Insulation*, vol. EI-14, no. 3, pp. 121–126, Jun. 1979, doi: 10.1109/TEI.1979.298211.

## References

- [14] "IEEE Standard for Performance of Adjustable-Speed AC Drives Rated 375 kW and Larger," *IEEE Std 1566-2015 (Revision of IEEE Std 1566-2005)*, pp. 1–74, Feb. 2015, doi: 10.1109/IEEESTD.2015.7051199.
- [15] Weijun Yin, "Dielectric properties of an improved magnet wire for inverter-fed motors," *IEEE Electrical Insulation Magazine*, vol. 13, no. 4, pp. 17–23, Jul. 1997, doi: 10.1109/57.603555.
- [16] E. Persson, "Transient effects in application of PWM inverters to induction motors," in *Conference Record of 1991 Annual Pulp and Paper Industry Technical Conference*, Montreal, Que., Canada, 1991, pp. 228–233, doi: 10.1109/PAPCON.1991.239644.
- [17] "GAMBICA | Motor Insulation Voltage Stresses Under PWM Inverter Operation." <http://www.gambica.org.uk/resourceLibrary/motor-insulation-voltage-stresses-under-pwm-inverter-operation-pdf.html> (accessed Feb. 03, 2020).
- [18] P. Wang, A. Cavallini, and G. C. Montanari, "The influence of repetitive square wave voltage parameters on enameled wire endurance," *IEEE Transactions on Dielectrics and Electrical Insulation*, vol. 21, no. 3, pp. 1276–1284, Jun. 2014, doi: 10.1109/TDEI.2014.6832275.
- [19] R. J. Beeckman, J. J. Harber, and S. J. Wentz, "Studies on magnet wire degradation with inverter driven motors," in *Proceedings: Electrical Insulation Conference and Electrical Manufacturing and Coil Winding Conference*, Sep. 1997, pp. 383–387, doi: 10.1109/EEIC.1997.651158.
- [20] "IEC/TS 60034-18-42 - Rotating electrical machines – Part 18-42: Qualification and acceptance tests for partial discharge resistant electrical insulation systems (Type II) used in rotating electrical machines fed from voltage converters | Engineering360." <https://standards.globalspec.com/std/1105210/iec-ts-60034-18-42> (accessed Feb. 03, 2020).
- [21] *Electrical Insulation for Rotating Machines*, 1st ed. John Wiley & Sons, Ltd, 2014.
- [22] M. Kaufhold, H. Aninger, M. Berth, J. Speck, and M. Eberhardt, "Electrical stress and failure mechanism of the winding insulation in PWM-inverter-fed low-voltage induction motors," *IEEE Transactions on Industrial Electronics*, vol. 47, no. 2, pp. 396–402, Apr. 2000, doi: 10.1109/41.836355.
- [23] S. U. Haq, "A Study on Insulation Problems in Drive Fed Medium Voltage Induction Motors," p. 163.
- [24] A. H. Bonnett and G. C. Soukup, "Cause and analysis of stator and rotor failures in three-phase squirrel-cage induction motors," *IEEE Transactions on Industry Applications*, vol. 28, no. 4, pp. 921–937, Jul. 1992, doi: 10.1109/28.148460.
- [25] "IEEE Guide for Testing Turn Insulation of Form-Wound Stator Coils for Alternating-Current Electric Machines," *IEEE Std 522-2004 (Revision of IEEE Std 522-1992)*, pp. 1–28, Aug. 2004, doi: 10.1109/IEEESTD.2004.94591.



## References

- [26] F. P. Espino-Cortes, Cherney EA, and S. H. Jayaram, "Impact of inverter drives employing fast-switching devices on form-wound AC machine stator coil stress grading," *IEEE Electr. Insul. Mag.*, vol. 23, no. 1, pp. 16–28, Jan. 2007, doi: 10.1109/MEI.2007.288451.
- [27] J. P. Bellomo, P. Castelan, and T. Lebey, "The effect of pulsed voltages on dielectric material properties," *IEEE Transactions on Dielectrics and Electrical Insulation*, vol. 6, no. 1, pp. 20–26, Feb. 1999, doi: 10.1109/94.752005.
- [28] B. K. Gupta, B. A. Lloyd, G. C. Stone, S. R. Campbell, D. K. Sharma, and N. E. Nilsson, "Turn Insulation Capability of Large AC Motors. Part 1 - Surge Monitoring," *IEEE Power Engineering Review*, vol. PER-7, no. 12, pp. 42–42, Dec. 1987, doi: 10.1109/MPER.1987.5526842.
- [29] "IEEE Recommended Practice for Measurement of Power Factor Tip-Up of Electric Machinery Stator Coil Insulation," *IEEE Std 286-2000*, pp. i–29, 2001, doi: 10.1109/IEEESTD.2001.92415.
- [30] P. Wang, A. Cavallini, G. C. Montanari, and G. Wu, "Effect of rise time on PD pulse features under repetitive square wave voltages," *IEEE Transactions on Dielectrics and Electrical Insulation*, vol. 20, no. 1, pp. 245–254, Feb. 2013, doi: 10.1109/TDEI.2013.6451364.
- [31] S. Akram, G. Gao, Y. Liu, J. Zhu, and G. Wu, "Degradation mechanism of Al<sub>2</sub>O<sub>3</sub> nano filled polyimide film due to surface discharge under square impulse voltage," *IEEE Trans. Dielect. Electr. Insul.*, vol. 22, no. 6, pp. 3341–3349, Dec. 2015, doi: 10.1109/TDEI.2015.005059.
- [32] "IEEE Recommended Practice for Voltage-Endurance Testing of Form-Wound Bars and Coils," *IEEE Std 1043-1996*, pp. 1–20, Aug. 1997, doi: 10.1109/IEEESTD.1997.82412.
- [33] W. Chen, G. Gao, and Craig. A. Mouton, "Stator insulation system evaluation and improvement for medium voltage adjustable speed drive applications," in *2008 55th IEEE Petroleum and Chemical Industry Technical Conference*, Sep. 2008, pp. 1–7, doi: 10.1109/PCICON.2008.4663986.
- [34] X. Zhong, A. Shakeel, Y. Yang, G. Gao, and G. Wu, "Preparation and corona-resistance characteristics of double-layer polyimide/Al<sub>2</sub>O<sub>3</sub> nanocomposite film," in *2016 IEEE International Conference on High Voltage Engineering and Application (ICHVE)*, Sep. 2016, pp. 1–4, doi: 10.1109/ICHVE.2016.7800644.
- [35] S. Akram *et al.*, "Influence of nano layer structure of polyimide film on space charge behavior and trap levels," *IEEE Transactions on Dielectrics and Electrical Insulation*, vol. 25, no. 4, pp. 1461–1469, Aug. 2018, doi: 10.1109/TDEI.2018.007506.
- [36] M. F. Fréchette *et al.*, "Nanodielectrics: A 'universal' panacea for solving all electrical insulation problems?," in *2010 10th IEEE International Conference on Solid Dielectrics*, Jul. 2010, pp. 1–3, doi: 10.1109/ICSD.2010.5568070.

## References

- [37] B. X. Du, J. Li, H. Du, and Y. Yin, "Effect of surface fluorination on space charge behavior in multilayered polyimide films," *IEEE Transactions on Dielectrics and Electrical Insulation*, vol. 21, no. 4, pp. 1817–1823, Aug. 2014, doi: 10.1109/TDEI.2014.004306.
- [38] B. X. Du *et al.*, "Dynamic behavior of surface potential on direct-fluorinated polyimide film under low temperature," in *2016 IEEE International Conference on Dielectrics (ICD)*, Jul. 2016, vol. 1, pp. 338–341, doi: 10.1109/ICD.2016.7547613.
- [39] S. Akram, J. Castellon, S. Agnel, and M. Z. Khan, "Space Charge Analysis of Multi-Structure Polyimide Films using TSM," in *2018 IEEE Conference on Electrical Insulation and Dielectric Phenomena (CEIDP)*, Oct. 2018, pp. 34–37, doi: 10.1109/CEIDP.2018.8544870.
- [40] A. V. Kyrlyuk, M. C. Hermant, T. Schilling, B. Klumperman, C. E. Koning, and P. van der Schoot, "Controlling electrical percolation in multicomponent carbon nanotube dispersions," *Nature Nanotech*, vol. 6, no. 6, pp. 364–369, Jun. 2011, doi: 10.1038/nnano.2011.40.
- [41] T. Ramanathan *et al.*, "Functionalized graphene sheets for polymer nanocomposites," *Nature Nanotech*, vol. 3, no. 6, pp. 327–331, Jun. 2008, doi: 10.1038/nnano.2008.96.
- [42] F. Messerer and W. Boeck, "High resistance surface coating of solid insulating components for HVDC metal enclosed equipment," in *1999 Eleventh International Symposium on High Voltage Engineering*, Aug. 1999, vol. 4, pp. 63–66 vol.4, doi: 10.1049/cp:19990793.
- [43] A. P. Kharitonov, "Direct fluorination of polymers—From fundamental research to industrial applications," *Progress in Organic Coatings*, vol. 61, no. 2–4, pp. 192–204, Feb. 2008, doi: 10.1016/j.porgcoat.2007.09.027.
- [44] A. Tressaud, E. Durand, C. Labrugère, A. P. Kharitonov, and L. N. Kharitonova, "Modification of surface properties of carbon-based and polymeric materials through fluorination routes: From fundamental research to industrial applications," *Journal of Fluorine Chemistry*, vol. 128, no. 4, pp. 378–391, Apr. 2007, doi: 10.1016/j.jfluchem.2006.12.015.
- [45] Y. Liu, Z. An, Q. Yin, F. Zheng, Q. Lei, and Y. Zhang, "Characteristics and electrical properties of epoxy resin surface layers fluorinated at different temperatures," *IEEE Transactions on Dielectrics and Electrical Insulation*, vol. 20, no. 5, pp. 1859–1868, Oct. 2013, doi: 10.1109/TDEI.2013.6633718.
- [46] Q. Guo, *Thermosets: Structure, Properties and Applications*. Elsevier, 2012.
- [47] J.-P. Pascault, *Thermosetting polymers*. New York : Marcel Dekker, 2002.
- [48] C. Sikalidis, *Advances in Ceramics - Electric and Magnetic Ceramics, Bioceramics, Ceramics and Environment*. 2011.
- [49] S. Hirose, T. Hatakeyama, and H. Hatakeyama, "Novel Epoxy Resins Derived from Biomass Components," *Procedia Chemistry*, vol. 4, pp. 26–33, Jan. 2012, doi: 10.1016/j.proche.2012.06.004.

## References

- [50] Y. Yang *et al.*, “Self-healing of electrical damage in polymers using superparamagnetic nanoparticles,” *Nature Nanotechnology*, vol. 14, no. 2, pp. 151–155, Feb. 2019, doi: 10.1038/s41565-018-0327-4.
- [51] J. Preston, “Polyimides – a new class of thermally stable polymers,” *Journal of Polymer Science Part B: Polymer Letters*, vol. 9, no. 3, pp. 230–231, 1971, doi: 10.1002/pol.1971.110090315.
- [52] “CORIN® XLS Polyimide.” <http://www.nexolvematerials.com/low-cure-polyimides/corin-xls-polyimide> (accessed Feb. 04, 2020).
- [53] C. E. Sroog, “Polyimides,” *Progress in Polymer Science*, vol. 16, no. 4, pp. 561–694, Aug. 1991, doi: 10.1016/0079-6700(91)90010-l.
- [54] M. Ghosh, *Polyimides: Fundamentals and Applications*. CRC Press, 1996.
- [55] R. Tummala, E. J. Rymaszewski, and A. G. Klopfenstein, *Microelectronics Packaging Handbook: Semiconductor Packaging*, 2nd ed. Springer US, 1997.
- [56] A. Gurses, *Introduction to Polymer-Clay Nanocomposites*. CRC Press, 2015.
- [57] “High-Temperature Properties and Applications of Polymeric Materials, Copyright, 1995 Advisory Board, Foreword,” in *High-Temperature Properties and Applications of Polymeric Materials*, vol. 603, 0 vols., American Chemical Society, 1995, pp. i–iv.
- [58] S.-Y. Yang, *Advanced Polyimide Materials: Synthesis, Characterization, and Applications*. Elsevier, 2018.
- [59] S. H. Wen and J. I. Kim, “Thin Film Wiring for Integrated Electronic Packages,” *MRS Online Proceedings Library Archive*, vol. 108, ed 1987, doi: 10.1557/PROC-108-81.
- [60] R. J. Jensen, “Thin Film Multilayer Interconnection Technologies for Multichip Modules,” in *Multichip Module Technologies and Alternatives: The Basics*, D. A. Doane and P. D. Franzon, Eds. Boston, MA: Springer US, 1993, pp. 255–309.
- [61] D. L. Dunson, “SYNTHESIS AND CHARACTERIZATION OF THERMOSETTING POLYIMIDE OLIGOMERS FOR MICROELECTRONICS PACKAGING,” p. 264.
- [62] G. Tesoro, “Advances in polyimide science and technology, C. Feger and M. M. Khojasteh, Eds., M/S/Htoo technomic publishing, 1993,” *Journal of Polymer Science Part A: Polymer Chemistry*, vol. 31, no. 13, pp. 3501–3501, 1993, doi: 10.1002/pola.1993.080311343.
- [63] C. Stancu, P. V. Notingher, P. Notingher, and M. Lungulescu, “Space charge and electric field in thermally aged multilayer joints model,” *IEEE Transactions on Dielectrics and Electrical Insulation*, vol. 23, no. 2, pp. 633–644, Apr. 2016, doi: 10.1109/TDEI.2015.005363.
- [64] A. K. Jonscher, “Dielectric relaxation in solids,” *J. Phys. D: Appl. Phys.*, vol. 32, no. 14, pp. R57–R70, Jan. 1999, doi: 10.1088/0022-3727/32/14/201.

## References

- [65] A. S. Paramane and K. S. Kumar, "A Review on Nanocomposite Based Electrical Insulations," *Transactions on Electrical and Electronic Materials*, vol. 17, no. 5, pp. 239–251, Oct. 2016, doi: 10.4313/TEEM.2016.17.5.239.
- [66] E. M. Akinoglu, A. J. Morfa, and M. Giersig, "Understanding Anisotropic Plasma Etching of Two-Dimensional Polystyrene Opals for Advanced Materials Fabrication," *Langmuir*, vol. 30, no. 41, pp. 12354–12361, Oct. 2014, doi: 10.1021/la500003u.
- [67] I. Preda *et al.*, "Dielectric response of various partially cured epoxy nanocomposites," *IEEE Trans. Dielect. Electr. Insul.*, vol. 20, no. 2, pp. 580–591, Apr. 2013, doi: 10.1109/TDEI.2013.6508762.
- [68] "KAPTON® fabrication, bags, KAPTON® thermoforming, KAPTON® films, KAPTON® sheets, polyimide," *American Durafilm*. [https://americandurafilm.com/film-distribution/kapton-film/?utm\\_term=kapton%20polyimide&utm\\_campaign=Film+Distributors&utm\\_medium=ppc&utm\\_source=adwords&hsa\\_tgt=kwd-1018173475&hsa\\_ad=200039013521&hsa\\_grp=15646824417&hsa\\_ver=3&hsa\\_mt=p&hsa\\_kw=kapton%20polyimide&hsa\\_net=adwords&hsa\\_src=g&hsa\\_cam=278108217&hsa\\_acc=1571530123&gclid=EAlaIqobChMI5MCZ6-S35wIVxfZRCh2TuwuzEAAYASAAEgLHgPD\\_BwE](https://americandurafilm.com/film-distribution/kapton-film/?utm_term=kapton%20polyimide&utm_campaign=Film+Distributors&utm_medium=ppc&utm_source=adwords&hsa_tgt=kwd-1018173475&hsa_ad=200039013521&hsa_grp=15646824417&hsa_ver=3&hsa_mt=p&hsa_kw=kapton%20polyimide&hsa_net=adwords&hsa_src=g&hsa_cam=278108217&hsa_acc=1571530123&gclid=EAlaIqobChMI5MCZ6-S35wIVxfZRCh2TuwuzEAAYASAAEgLHgPD_BwE) (accessed Feb. 04, 2020).
- [69] J. Simpson, "Fundamental insight on developing low dielectric constant polyimides," *Thin Solid Films*, vol. 308, pp. 480–485, Oct. 1997, doi: 10.1016/S0040-6090(97)00481-1.
- [70] S. Akram, G. Wu, G. Gao, and Y. Liu, "Cavity and Interface effect of PI-Film on Charge Accumulation and PD Activity under Bipolar Pulse Voltage," *Journal of Electrical Engineering and Technology*, vol. 10, no. 5, pp. 2089–2098, Sep. 2015, doi: 10.5370/JEET.2015.10.5.2089.
- [71] Y. Luo, G. Wu, J. Liu, J. Peng, G. Zhu, and G. Gao, "Investigation of temperature effects on voltage endurance for polyimide/Al<sub>2</sub>O<sub>3</sub> nanodielectrics," *IEEE Transactions on Dielectrics and Electrical Insulation*, vol. 21, no. 4, pp. 1824–1834, Aug. 2014, doi: 10.1109/TDEI.2014.004305.
- [72] H. Z. Alisoy and M. Koseoglu, "The Changes in Electrical and Interfacial Properties of Polyimide Exposed to Dielectric Barrier Discharge in SF<sub>6</sub> Medium," *The Scientific World Journal*, 2013. <https://www.hindawi.com/journals/tswj/2013/890454/> (accessed Feb. 04, 2020).
- [73] W. T. Starr, "Polymeric outdoor insulation," *IEEE Transactions on Electrical Insulation*, vol. 25, no. 1, pp. 125–136, Feb. 1990, doi: 10.1109/14.45239.
- [74] F. W. Peek, *Dielectric Phenomena in High Voltage Engineering*. McGraw-Hill Book Company, Incorporated, 1920.
- [75] M. T. Nazir and B. T. Phung, "AC corona resistance performance of silicone rubber composites with micro/nano silica fillers," in *2016 IEEE International Conference on Dielectrics (ICD)*, Jul. 2016, vol. 2, pp. 681–684, doi: 10.1109/ICD.2016.7547707.

## References

- [76] M. T. Nazir, B. T. Phung, S. Yu, and S. Li, "Effects of thermal properties on tracking and erosion resistance of micro-ATH/AlN/BN filled silicone rubber composites," *IEEE Transactions on Dielectrics and Electrical Insulation*, vol. 25, no. 6, pp. 2076–2085, Dec. 2018, doi: 10.1109/TDEI.2018.007125.
- [77] M. T. Nazir, B. T. Phung, S. Li, and S. Yu, "Comparative AC tracking and erosion resistance of micro-AlN and BN filled silicone rubber composites," in *2017 1st International Conference on Electrical Materials and Power Equipment (ICEMPE)*, May 2017, pp. 603–606, doi: 10.1109/ICEMPE.2017.7982169.
- [78] M. F. Frechette, M. L. Trudeau, H. D. Alamdar, and S. Boily, "Introductory remarks on nanodielectrics," *IEEE Transactions on Dielectrics and Electrical Insulation*, vol. 11, no. 5, pp. 808–818, Oct. 2004, doi: 10.1109/TDEI.2004.1349786.
- [79] T. J. Lewis, "Nanometric dielectrics," *IEEE Transactions on Dielectrics and Electrical Insulation*, vol. 1, no. 5, pp. 812–825, Oct. 1994, doi: 10.1109/94.326653.
- [80] G. C. Psarras, "Nanodielectrics: an emerging sector of polymer nanocomposites," *Express Polym. Lett.*, vol. 2, no. 7, pp. 460–460, 2008, doi: 10.3144/expresspolymlett.2008.55.
- [81] I. Capek, *Nanocomposite structures and dispersions: science and nanotechnology--fundamental principles and colloidal particles*, 1st ed. Amsterdam ; Boston: Elsevier, 2006.
- [82] S. Komarneni, J. C. Parker, and H. J. Wollenberger, "Nanophase and nanocomposite materials 2," Sep. 1997, Accessed: Feb. 04, 2020. [Online]. Available: <https://www.osti.gov/biblio/522280-nanophase-nanocomposite-materials>.
- [83] M. R. Society, *Nanophase and Nanocomposite Materials V*. Red Hook, NY: Curran Associates Inc, 2009.
- [84] L. Zhang *et al.*, "Effect of nanoparticle surface modification on breakdown and space charge behavior of XLPE/SiO<sub>2</sub> nanocomposites," *IEEE Transactions on Dielectrics and Electrical Insulation*, vol. 21, no. 4, pp. 1554–1564, Aug. 2014, doi: 10.1109/TDEI.2014.004361.
- [85] Y. Yang, X. Wu, G. Wu, Y. Lei, and J. Liu, "Effect of plasma modified nanoparticles on trap level distribution and dielectric properties of nanocomposites," in *2018 12th International Conference on the Properties and Applications of Dielectric Materials (ICPADM)*, May 2018, pp. 37–40, doi: 10.1109/ICPADM.2018.8401023.
- [86] Y. Yang, X. Zhang, Y. Lei, G. Wu, and G. Hu, "Corona Resistance Improvement of Polyimide Films by Non-Thermal Plasma Modification," in *2018 IEEE International Conference on High Voltage Engineering and Application (ICHVE)*, Sep. 2018, pp. 1–4, doi: 10.1109/ICHVE.2018.8641978.
- [87] D. Tan and P. Irwin, "Polymer Based Nanodielectric Composites," *Advances in Ceramics - Electric and Magnetic Ceramics, Bioceramics, Ceramics and Environment*, Sep. 2011, doi: 10.5772/23012.

## References

- [88] J. H. Koo, *Polymer nanocomposites: processing, characterization, and applications*. McGraw-Hill, 2006.
- [89] T. M. Andritsch, *Epoxy based nanodielectrics for high voltage DC applications: synthesis, dielectric properties and space charge dynamics*. S.l.: s.n., 2010.
- [90] J. P. Critchley, G. J. Knight, and W. W. Wright, *Heat-Resistant Polymers: Technologically Useful Materials*. Springer US, 1983.
- [91] K. L. Mittal, *Polyimides and other high temperature polymers: synthesis, characterization and applications. Volume 2*. VSP, 2003.
- [92] K. Akhtar, S. A. Khan, S. B. Khan, and A. M. Asiri, "Scanning Electron Microscopy: Principle and Applications in Nanomaterials Characterization," in *Handbook of Materials Characterization*, S. K. Sharma, Ed. Cham: Springer International Publishing, 2018, pp. 113–145.
- [93] "Transmission electron microscopy," *Wikipedia*. Jan. 23, 2020, Accessed: Feb. 05, 2020. [Online]. Available: [https://en.wikipedia.org/w/index.php?title=Transmission\\_electron\\_microscopy&oldid=937171234](https://en.wikipedia.org/w/index.php?title=Transmission_electron_microscopy&oldid=937171234).
- [94] P. Goodhew, "General Introduction to Transmission Electron Microscopy (TEM)," in *Aberration-Corrected Analytical Transmission Electron Microscopy*, R. Brydson, Ed. Chichester, UK: John Wiley & Sons, Ltd, 2011, pp. 1–19.
- [95] Yang Yang *et al.*, "Ftir and dielectric studies of electrical aging in polyimide under AC voltage," *IEEE Trans. Dielect. Electr. Insul.*, vol. 19, no. 2, pp. 574–581, Apr. 2012, doi: 10.1109/TDEI.2012.6180252.
- [96] "FTIR Spectroscopy - an overview | ScienceDirect Topics." <https://www.sciencedirect.com/topics/earth-and-planetary-sciences/ftir-spectroscopy> (accessed Feb. 05, 2020).
- [97] "Fourier-transform infrared spectroscopy," *Wikipedia*. Jan. 25, 2020, Accessed: Feb. 05, 2020. [Online]. Available: [https://en.wikipedia.org/w/index.php?title=Fourier-transform\\_infrared\\_spectroscopy&oldid=937496396](https://en.wikipedia.org/w/index.php?title=Fourier-transform_infrared_spectroscopy&oldid=937496396).
- [98] Keysight, "Basics of Measuring the Dielectric Properties of Materials," *Keysight*. <https://www.keysight.com/fr/en/assets/7018-01284/application-notes/5989-2589.pdf> (accessed Feb. 05, 2020).
- [99] V. Saltas, "Dielectric spectroscopy as a tool for the detection of contamination in sandstone," Jan. 2005.
- [100] M. Stranges, G. Stone, and D. Bogh, "Voltage endurance testing," *IEEE Ind. Appl. Mag.*, vol. 15, no. 6, pp. 12–18, Nov. 2009, doi: 10.1109/MIAS.2009.934439.
- [101] Y. Chen, Y. Wang, J. Wu, and Y. Yin, "Study on conduction current characteristics of corona-resistant polyimide film before and after thermal aging," in *2017 International*

## References

- Symposium on Electrical Insulating Materials (ISEIM)*, Sep. 2017, vol. 2, pp. 605–608, doi: 10.23919/ISEIM.2017.8166562.
- [102] J. G. Simmons and M. C. Tam, “Theory of Isothermal Currents and the Direct Determination of Trap Parameters in Semiconductors and Insulators Containing Arbitrary Trap Distributions,” *Phys. Rev. B*, vol. 7, no. 8, pp. 3706–3713, Apr. 1973, doi: 10.1103/PhysRevB.7.3706.
- [103] H. Yahyaoui, P. Notingher, S. Agnel, Y. Kieffel, and A. Girodet, “Analysis of conduction mechanisms in alumina-filled epoxy resin under dc field and temperature,” in *2013 Annual Report Conference on Electrical Insulation and Dielectric Phenomena*, Oct. 2013, pp. 667–670, doi: 10.1109/CEIDP.2013.6748181.
- [104] S. A. Bhumiwat, “Advanced Applications of Polarisation / Depolarisation Current Analysis on Power Transformers,” in *Conference Record of the 2008 IEEE International Symposium on Electrical Insulation*, Jun. 2008, pp. 474–477, doi: 10.1109/ELINSL.2008.4570376.
- [105] Y. B. Zhu and L. K. Ang, “Analytical re-derivation of space charge limited current in solids using capacitor model,” *Journal of Applied Physics*, vol. 110, no. 9, p. 094514, Nov. 2011, doi: 10.1063/1.3658811.
- [106] A. Rose, “Space-Charge-Limited Currents in Solids,” *Phys. Rev.*, vol. 97, no. 6, pp. 1538–1544, Mar. 1955, doi: 10.1103/PhysRev.97.1538.
- [107] “Electronic Processes in Ionic Crystals by N F Mott and R W Gurney - AbeBooks.” <https://www.abebooks.co.uk/book-search/title/electronic-processes-in-ionic-crystals/author/n-f-mott-and-r-w-gurney/> (accessed Feb. 06, 2020).
- [108] M. Ieda, T. Mizutani, and S. Ikeda, “Electrical Conduction and Chemical Structure of Insulating Polymers,” *IEEE Transactions on Electrical Insulation*, vol. EI-21, no. 3, pp. 301–306, Jun. 1986, doi: 10.1109/TEI.1986.349066.
- [109] L. Lan, J. Wu, Y. Yin, X. Li, and Z. Li, “Effect of temperature on space charge trapping and conduction in cross-linked polyethylene,” *IEEE Transactions on Dielectrics and Electrical Insulation*, vol. 21, no. 4, pp. 1784–1791, Aug. 2014, doi: 10.1109/TDEI.2014.004261.
- [110] I. Fofana, H. Hemmatjou, M. Farzaneh, E. Gockenbach, and H. Borsi, “Polarization and Depolarization Current measurements of oil impregnated paper insulation system under thermal runaway,” in *2010 10th IEEE International Conference on Solid Dielectrics*, Jul. 2010, pp. 1–4, doi: 10.1109/ICSD.2010.5568006.
- [111] I. A. Preda, “Modélisation et caractérisation des matériaux nanocomposites par des méthodes diélectriques,” p. 222.
- [112] *Progress in Dielectrics*. Academic Press, 1965.
- [113] I. Preda *et al.*, “Conduction currents and time to frequency domain transformation for epoxy resin nanocomposites,” in *2013 IEEE International Conference on Solid Dielectrics (ICSD)*, Jun. 2013, pp. 1060–1063, doi: 10.1109/ICSD.2013.6619711.

## References

- [114] "DMA - Dynamic Mechanical Analysis :: Anton-Paar.com," *Anton Paar*. <https://www.anton-paar.com/corp-en/products/group/dynamic-mechanical-analysis/> (accessed Feb. 05, 2020).
- [115] "Dynamic Mechanical Analysis (DMA) A Beginner's Guide," p. 23.
- [116] R. E. Taylor, J. Gembarovic, and K. D. Maglic, "Thermal Diffusivity by the Laser Flash Technique," in *Characterization of Materials*, E. N. Kaufmann, Ed. Hoboken, NJ, USA: John Wiley & Sons, Inc., 2002, p. com102.
- [117] W. J. Parker, R. J. Jenkins, C. P. Butler, and G. L. Abbott, "Flash Method of Determining Thermal Diffusivity, Heat Capacity, and Thermal Conductivity," *Journal of Applied Physics*, vol. 32, no. 9, pp. 1679–1684, Sep. 1961, doi: 10.1063/1.1728417.
- [118] "LFA 467 HyperFlash," *NETZSCH Analyzing & Testing*. <https://www.netzsch-thermal-analysis.com/en/products-solutions/thermal-diffusivity-conductivity/lfa-467-hyperflash/> (accessed Feb. 05, 2020).
- [119] "Figure 2 -Schematics of the Netzsch Nanoflash LFA 447/1.," *ResearchGate*. [https://www.researchgate.net/figure/Schematics-of-the-Netzsch-Nanoflash-LFA-447-1\\_fig2\\_262647223](https://www.researchgate.net/figure/Schematics-of-the-Netzsch-Nanoflash-LFA-447-1_fig2_262647223) (accessed Feb. 05, 2020).
- [120] P. Notingham, S. Agnel, and A. Toureille, "Thermal step method for space charge measurements under applied dc field," *IEEE Transactions on Dielectrics and Electrical Insulation*, vol. 8, no. 6, pp. 985–994, Dec. 2001, doi: 10.1109/94.971455.
- [121] S. Agnel, P. Notingham, and A. Toureille, "Space charge measurements under applied DC field by the thermal step method," in *2000 Annual Report Conference on Electrical Insulation and Dielectric Phenomena (Cat. No.00CH37132)*, Oct. 2000, vol. 1, pp. 166–170 vol.1, doi: 10.1109/CEIDP.2000.885253.
- [122] P. Notingham, A. Toureille, S. Agnel, and J . Castellon, "Determination of Electric Field and Space Charge in the Insulation of Power Cables With the Thermal Step Method and a New Mathematical Processing," *IEEE Transactions on Industry Applications*, vol. 45, no. 1, pp. 67–74, Jan. 2009, doi: 10.1109/TIA.2008.2009612.
- [123] K. Fukunaga, "Progress and Prospects in PEA Space Charge Measurement Techniques - [Feature Article]," *IEEE Electrical Insulation Magazine*, vol. 24, no. 3, pp. 26–37, May 2008, doi: 10.1109/MEI.2008.4591432.
- [124] K.- Suh, J. Tanaka, and D. Damon, "What is TSC?," *IEEE Electrical Insulation Magazine*, vol. 8, no. 6, pp. 13–20, Nov. 1992, doi: 10.1109/57.168887.
- [125] "Rheology: Principles, Measurements, and Applications | Wiley," *Wiley.com*. <https://www.wiley.com/en-us/Rheology%3A+Principles%2C+Measurements%2C+and+Applications-p-9780471185758> (accessed Feb. 06, 2020).



## References

- [126] “Viscoelastic Properties of Polymers, 3rd Edition | Wiley,” *Wiley.com*. <https://www.wiley.com/en-us/Viscoelastic+Properties+of+Polymers%2C+3rd+Edition-p-9780471048947> (accessed Feb. 06, 2020).
- [127] R. Kochetov, “Thermal and Electrical Properties of Nanocomposites, Including Material Properties,” *Astrophysical Journal Letters - ASTROPHYS J LETT*, Jan. 2012.
- [128] R. Berman, *Thermal conduction in solids*. Oxford [Eng.]: Clarendon Press, 1976.
- [129] S. Akram, M. T. Nazir, J. Castellon, S. Agnel, K. Zhou, and M. S. Bhutta, “Preparation and distinguish dielectric properties of multi-layer nanoparticles-based polyimide films,” *Mater. Res. Express*, vol. 6, no. 12, p. 125092, Dec. 2019, doi: 10.1088/2053-1591/ab5c40.
- [130] T.-I. Yang and P. Kofinas, “Dielectric properties of polymer nanoparticle composites,” *Polymer*, vol. 48, no. 3, pp. 791–798, Jan. 2007, doi: 10.1016/j.polymer.2006.12.030.
- [131] A. Jimeno, G. Kortaberria, P. Arruti, A. Tercjak, M. Blanco, and I. Mondragon, “Dynamics and dielectric properties of polymer/nanoparticle nanocomposites by dielectric spectroscopy,” 2009, pp. 31–67.
- [132] Z. Wang *et al.*, “Dielectric spectroscopy characterization of relaxation process in Ni/epoxy composites,” *Journal of Alloys and Compounds*, vol. 682, pp. 738–745, Oct. 2016, doi: 10.1016/j.jallcom.2016.05.025.
- [133] M.-J. Brekner and C. Feger, “Curing studies of a polyimide precursor,” *Journal of Polymer Science Part A: Polymer Chemistry*, vol. 25, no. 7, pp. 2005–2020, 1987, doi: 10.1002/pola.1987.080250720.
- [134] N. C. Stoffel, E. J. Kramer, W. Volksen, and T. P. Russell, “Imidization and interdiffusion of poly(amic ethyl ester) precursors of PMDA/3,4'-ODA,” *Journal of Polymer Science Part B: Polymer Physics*, vol. 36, no. 13, pp. 2247–2258, 1998, doi: 10.1002/(SICI)1099-0488(19980930)36:13<2247::AID-POLB1>3.0.CO;2-Q.
- [135] L. S. Schadler, J. K. Nelson, C. Calebrese, A. Travelpiece, and D. L. Schweickart, “High temperature breakdown strength and voltage endurance characterization of nanofilled polyamideimide,” *IEEE Trans. Dielect. Electr. Insul.*, vol. 19, no. 6, pp. 2090–2101, Dec. 2012, doi: 10.1109/TDEI.2012.6396969.
- [136] Y. Yang, J. He, G. Wu, and J. Hu, “‘Thermal Stabilization Effect’ of Al<sub>2</sub>O<sub>3</sub> nano-dopants improves the high-temperature dielectric performance of polyimide,” *Scientific Reports*, vol. 5, no. 1, pp. 1–10, Nov. 2015, doi: 10.1038/srep16986.
- [137] B. P. Singh, D. Singh, R. B. Mathur, and T. L. Dhami, “Influence of Surface Modified MWCNTs on the Mechanical, Electrical and Thermal Properties of Polyimide Nanocomposites,” *Nanoscale Res Lett*, vol. 3, no. 11, pp. 444–453, Nov. 2008, doi: 10.1007/s11671-008-9179-4.
- [138] E. Sili, J. P. Cambronne, N. Naude, and R. Khazaka, “Polyimide lifetime under partial discharge aging: effects of temperature, pressure and humidity,” *IEEE Transactions on*

## References

- Dielectrics and Electrical Insulation*, vol. 20, no. 2, pp. 435–442, Apr. 2013, doi: 10.1109/TDEI.2013.6508745.
- [139] Y. Luo *et al.*, “PD characteristics and microscopic analysis of polyimide film used as turn insulation in inverter-fed motor,” *IEEE Transactions on Dielectrics and Electrical Insulation*, vol. 21, no. 5, pp. 2237–2244, Oct. 2014, doi: 10.1109/TDEI.2014.003868.
- [140] N. A. M. Jamail, M. A. M. Piah, and N. A. Muhamad, “Effects of SiO<sub>2</sub> nanofillers on Polarization and Depolarization Current (PDC) of LLDPE-NR nanocomposite insulating materials,” in *2012 IEEE International Conference on Power and Energy (PECon)*, Dec. 2012, pp. 707–711, doi: 10.1109/PECon.2012.6450306.
- [141] B. X. Du and Y. G. Guo, “Effects of surface fluorination on dielectric properties and surface charge behavior of water absorbed polyimide film,” *IEEE Transactions on Dielectrics and Electrical Insulation*, vol. 22, no. 3, pp. 1369–1375, Jun. 2015, doi: 10.1109/TDEI.2015.7116324.
- [142] S. D. Flora, J. S. Rajan, and M. S. Divekar, “Efforts to improve polarization and depolarization current measurements in paper oil insulation and their interpretation,” in *2015 IEEE 11th International Conference on the Properties and Applications of Dielectric Materials (ICPADM)*, Jul. 2015, pp. 440–443, doi: 10.1109/ICPADM.2015.7295303.
- [143] T. Y. Kim, W. J. Kim, T. H. Lee, J. E. Kim, H. G. Yoon, and K. S. Suh, “Electrical conduction of polyimide films prepared from polyamic acid (PAA) and pre-imidized polyimide (PI) solution,” *e-Polymers*, vol. 8, no. 1, Dec. 2008, doi: 10.1515/epoly.2008.8.1.908.
- [144] J. Castellon, S. Agnel, and P. Notingham, “Review of space charge measurements in high voltage DC extruded cables by the thermal step method,” *IEEE Electrical Insulation Magazine*, vol. 33, no. 4, pp. 34–41, Jul. 2017, doi: 10.1109/MEI.2017.7956631.
- [145] J. Castellon *et al.*, “Electric field and space charge measurements in thick power cable insulation,” *IEEE Electrical Insulation Magazine*, vol. 25, no. 3, pp. 30–42, May 2009, doi: 10.1109/MEI.2009.4977240.
- [146] G. Chen, Y. Tanaka, T. Takada, and L. Zhong, “Effect of polyethylene interface on space charge formation,” *IEEE Transactions on Dielectrics and Electrical Insulation*, vol. 11, no. 1, pp. 113–121, Feb. 2004, doi: 10.1109/TDEI.2004.1266324.
- [147] S. O. Kasap, “The demarcation energy concept in the analysis of charge carrier emission kinetics from deep mobility gap states in amorphous semiconductors,” *J. Phys. D: Appl. Phys.*, vol. 21, no. 5, pp. 841–844, May 1988, doi: 10.1088/0022-3727/21/5/029.
- [148] P. K. Watson, “The transport and trapping of electrons in polymers,” *IEEE Transactions on Dielectrics and Electrical Insulation*, vol. 2, no. 5, pp. 915–924, Oct. 1995, doi: 10.1109/94.469986.
- [149] I. A. Tsekmes, R. Kochetov, P. H. F. Morshuis, and J. J. Smit, “Modeling the thermal conductivity of polymeric composites based on experimental observations,” *IEEE*

## References

- Transactions on Dielectrics and Electrical Insulation*, vol. 21, no. 2, pp. 412–423, Apr. 2014, doi: 10.1109/TDEI.2013.004142.
- [150] L. A. Dissado, V. Griseri, W. Peasgood, E. S. Cooper, K. Fukunaga, and J. C. Fothergill, "Decay of space charge in a glassy epoxy resin following voltage removal," *IEEE Transactions on Dielectrics and Electrical Insulation*, vol. 13, no. 4, pp. 903–916, Aug. 2006, doi: 10.1109/TDEI.2006.1667752.
- [151] R. Chen, "Methods for kinetic analysis of thermally stimulated processes," *J Mater Sci*, vol. 11, no. 8, pp. 1521–1541, Aug. 1976, doi: 10.1007/BF00540887.
- [152] Fuqiang Tian *et al.*, "A new method for direct determination of trap level distribution from TSC measurement," in *2009 IEEE 9th International Conference on the Properties and Applications of Dielectric Materials*, Jul. 2009, pp. 980–983, doi: 10.1109/ICPADM.2009.5252276.
- [153] T. Takada, Y. Hayase, and Y. Tanaka, "Space charge trapping in electrical potential well caused by permanent and induced dipoles for LDPE/MgO nanocomposite," *Dielectrics and Electrical Insulation, IEEE Transactions on*, vol. 15, pp. 152–160, Mar. 2008, doi: 10.1109/T-DEI.2008.4446746.
- [154] T. Tanaka, M. Kozako, N. Fuse, and Y. Ohki, "Proposal of a multi-core model for polymer nanocomposite dielectrics," *IEEE Transactions on Dielectrics and Electrical Insulation*, vol. 12, no. 4, pp. 669–681, Aug. 2005, doi: 10.1109/TDEI.2005.1511092.
- [155] R. Bartnikas and R. M. Eichhorn, *Engineering Dielectrics Volume IIA: Electrical Properties of Solid Insulating Materials: Molecular Structure and Electrical Behavior*. Philadelphia: American Society for Testing and Materials, 1983.
- [156] B. Zazoum, E. David, and A. Ngô, "Simulation and Modeling of Polyethylene/Clay Nanocomposite for Dielectric Application," *TRANSACTIONS ON ELECTRICAL AND ELECTRONIC MATERIALS*, vol. 15, pp. 175–181, Aug. 2014, doi: 10.4313/TEEM.2014.15.4.175.
- [157] G. G. Vogiatzis and D. N. Theodorou, "Multiscale Molecular Simulations of Polymer-Matrix Nanocomposites," *Arch Computat Methods Eng*, vol. 25, no. 3, pp. 591–645, Jul. 2018, doi: 10.1007/s11831-016-9207-y.
- [158] M. T. Nazir *et al.*, "Effect of micro-nano additives on breakdown, surface tracking and mechanical performance of ethylene propylene diene monomer for high voltage insulation," *J Mater Sci: Mater Electron*, vol. 30, no. 15, pp. 14061–14071, Aug. 2019, doi: 10.1007/s10854-019-01771-6.
- [159] T. Tanaka, "Dielectric nanocomposites with insulating properties," *IEEE Transactions on Dielectrics and Electrical Insulation*, vol. 12, no. 5, pp. 914–928, Oct. 2005, doi: 10.1109/TDEI.2005.1522186.

## References

- [160] D. Ma *et al.*, "Influence of nanoparticle surface modification on the electrical behaviour of polyethylene nanocomposites," *Nanotechnology*, vol. 16, no. 6, pp. 724–731, Apr. 2005, doi: 10.1088/0957-4484/16/6/016.
- [161] T. J. Lewis, "Interfaces are the dominant feature of dielectrics at the nanometric level," *IEEE Transactions on Dielectrics and Electrical Insulation*, vol. 11, no. 5, pp. 739–753, Oct. 2004, doi: 10.1109/TDEI.2004.1349779.
- [162] M. Roy, J. K. Nelson, R. K. MacCrone, L. Schadler, C. W. Reed, and R. Keefe, "Polymer Nanocomposite Dielectrics-the Role of the Interface," *Dielectrics and Electrical Insulation, IEEE Transactions on*, vol. 12, pp. 629–643, Sep. 2005, doi: 10.1109/TDEI.2005.1511089.